MECHANISTIC INSIGHTS INTO CHROMATIN MEDIATED GENE REGULATION IN ROTENONE-INDUCED NEURODEGENERATION.

by

Dana M. Freeman

A dissertation submitted to Johns Hopkins University in conformity with the requirements for the degree of Doctor of Philosophy

Baltimore, Maryland
April 2020

Abstract

Rotenone is an organic pesticide and non-selective piscicide that is approved for use in the United States (US). In human epidemiological studies, rotenone exposure increases the risk of Parkinson's disease (PD), the second most common neurodegenerative disorder in the US. Rotenone is a key toxicant used to study gene-environment interactions in neuronal function and aging. In experimental studies, rotenone exposure recapitulates PD cellular pathology at environmentally relevant concentrations. It is a potent complex I inhibitor and promotes the production of reactive oxygen species. Oxidative damage and mitochondrial dysfunction activate critical transcription factors that regulate the cellular stress response. This retrograde signaling pathway alters chromatin structure via epigenetic mechanisms to regulate gene expression. Epigenetic modifications including DNA methylation and histone tail acetylation are persistent and can have a lasting effect on the functionality of a neuron. Investigating the mechanisms and patterning of these epigenetic modifications is critical for understanding the role of the epigenome in maintaining neuronal plasticity during aging. In this dissertation, we examined the molecular signatures of rotenone exposure on the epigenome. We investigated the role of the endogenous protein α-Synuclein (α-Syn), a pathological hallmark of PD, in mediating the effects on chromatin. We discovered that oxidative stress-induced α-Syn interferes with the maintenance of DNA methylation patterns by interfering with the translocation of DNA methyltransferase I. The aggregation of α-Syn activates ATF4 signaling and represses the hypoxic response. We revealed that enhancer enriched PD-associated genetic variants, DNMT1-dependent regions, hypoxia-response elements, and CTCF transcription factor binding motifs were among the genomic elements most vulnerable to rotenone-induced oxidative damage and α-Syn toxicity. We hypothesize that mitochondrial dysfunction activates early

response transcription factors to regulate the balance and activity of DNA modifying enzymes in the nucleus and that α-Syn toxicity drives the direction of this response. There is currently no cure for PD and clinical strategies rely on treating symptoms that occur late after onset of pathology. Epigenetic modifications are persistent, but they are also reversible. This dissertation provides insights into molecular signatures of oxidative stress in the brain and introduces candidate regions for early biological markers and novel pharmaceutical targets.

Advisor:

Zhibin Wang, Associate Professor

Department of Environmental Health & Engineering

Bloomberg School of Public Health

Thesis Committee Chair:

Robert Casero, Professor

Department of Oncology

Sidney Kimmel Comprehensive Cancer Center

Thesis Committee Members:

John Groopman, Professor: Department of Environmental Health & Engineering

Jiou Wang, Associate Professor: Department of Biochemistry & Molecular Biology

James Yager, Professor Emeritus: Department of Environmental Health & Engineering

Thomas Hartung, Professor: Department of Environmental Health & Engineering

Wan-yee Tang, Professor: Department of Environmental Health & Engineering

Preface

I've always loved to learn. When I was younger, my parents made learning an everyday part of our lives. Whether it was a vacation to a historic monument or a fun memorization game on long car rides, my parents always encouraged me to be curious. I'm fortunate to have grown up in an environment where I could be anything I wanted if I worked hard enough and my ethnicity, social class, religion, or sex would not hinder me from that. That privilege I not only recognize but promise to take advantage of for the sake of people less fortunate than me as I move forward with my life and my career. I'd like to dedicate this dissertation to my mother and father for all their sacrifices, love, and support.

When I entered college in 2009, next generation sequencing was at the forefront of the new age of Biology. Almost a decade after the first draft of the human genome was published, I was convinced I would study how our genetic code would cause disease. I started working for Dr. Raquel Lieberman under the supervision of Dr. Rebecca Donegan at Georgia Tech. This experience changed my life. Not only did it give me a passion for research, it gave me the desire to answer a prominent question in the field at that time. Why do we still struggle to comprehend the etiology of most diseases if we know the genetic code and its variation in the human population? After college, I went to the National Center for Environmental Health. I'm grateful for all the wonderful people I met at the Centers for Disease Control and the freedom I was given to explore the vast world of Public Health. It was here that I learned about the idea of gene-environment interactions.

My favorite quote by George Gray describing this phenomenon is

"Genetics loads the gun; the environment pulls the trigger."

I came to Johns Hopkins Bloomberg School of Public Health in August 2015. I am grateful that I began my journey with Lena Smirnova, Georgina Harris, and the Center for Alternatives to Animal Testing. They welcomed me into the department with open arms and taught me invaluable lessons in cell culture technique. Through the help of my cohort, my friends, my lab mates, and mentors; I was able to develop a project that tied together all my interests. I was elated to start working on gene-environment interactions in the brain and understanding the molecular mechanisms involved in exposure driven neurological disorders. I'd like to thank the department for providing me with this amazing opportunity and the NIEHS and NHLBI T32 training grant for funding my education. I'd also like to thank the Frederik Bang Award and the Environmental Health & Engineering Chen Award for believing in my work and providing the funding for me to accomplish this goal.

I want to thank all my friends for their unwavering support. The Lady Scholars Club for keeping me grounded and never allowing me to give up on myself. My friends back home who have over the years become the best family I could ever imagine. Thank you for always reminding me who I am and where I've come from. My dog, Blazer, for always knowing when I need to take a walk break or a nap. He also spent countless evenings with me on the couch while writing. Last, but certainly not least, thank you to my best friend and partner in life Zack Ballew. We've come a long way from being those crazy kids at Tech but you still make me feel connected to that person in all the best ways. I would never have come this far without you. I love you $2 \infty \& \rightarrow$.

Table of Contents

Table of Tables

Table of Figures

INTENDED TO BE BLANK

CHAPTER 1

INTRODUCTION

1.1 Significance

1.1.1 Pesticide usage in the United States

The United States is one of the largest consumers of pesticides in the world with total expenditures accounting for nearly 20% of the global market (Atwood et al. 2017). Unsurprisingly, herbicides constitute approximately half of the pesticides consumed and the agricultural sector accounted for most of the herbicides used between 2008-2012. However, private usage should not be disregarded with individual use in the home and garden consuming 30% of the 680 million pounds of herbicides and insecticides used in 2012 (Atwood et al. 2017). This residential utilization of pesticides can expose susceptible populations including pregnant women and children (Michael and Alavanja 2009; Whyatt et al. 2002). The US regulation on the pesticide industry is more lenient than policies implemented by the European Union (EU) (Donley 2019). In 2016, 322 million pounds of pesticides used in the United States are banned in the EU. One such pesticide is the botanical insecticide rotenone.

Rotenone is an isoflavonoid that is found in many species of plants native to Southeast Asia, East Africa, and some parts of South America (US EPA 2007). It has historically been used in organic farming but registration of rotenone for use on food was cancelled by the EPA starting in 2007 (Islam 2006). Despite this cancellation, rotenone products could be sold until 2011 and currently rotenone is still exempt from a tolerance requirement allowing any amount of residue on food without violation of the law (77 FR 59128, Sept. 26, 2012). The primary use of rotenone today is as a piscicide to terminate invasive or noxious species of fish. Permissible application concentrations can be up to 250 ppb and can be applied to public and recreational waters (US EPA 2007). While it is

highly toxic in humans following acute inhalation or ingestion, the environmental persistence of rotenone is expected to be low and its half-life is estimated between days to weeks in water systems depending on various physiochemical factors including temperature and pH (Dawson et al. 1991; Turner et al. 2007).

The most prominent case study of rotenone toxicity is the accidental poisoning of a young girl with a lethal dose of 40 mg/kg (De Wilde et al. 1986). A separate case study involving an adult woman purposefully consuming 25 mg/kg of rotenone resulted in loss of consciousness and cardiac arrest (Wood et al. 2005). The US EPA has set a chronic reference dose of 4 µg/kg/day to protect vulnerable populations (US EPA 2007). While chronic toxicity studies have indicated developmental and reproductive toxicity, most human studies focus on the potential of rotenone in neurodegeneration (DeLamirande 1992; Khera et al. 1982, US EPA 2007; USDA Forest Service; Uversky, V. 2004; Bertarbet et al. 2000).

1.1.2 Epidemiological evidence of rotenone and neurodegeneration

Rotenone freely crosses cell membranes and targets complex I of the oxidative phosphorylation chain in mitochondria (Greenamyre et al. 2001). Inhibition of complex I in the mitochondria creates deficits in cellular energy production and generates reactive oxygen species causing damage to intracellular lipids and nucleic acids. These features of rotenone toxicity focus on neuronal cells with high metabolic burden and vulnerability to oxidative stress.

Mitochondrial dysfunction and inhibition of complex I have been associated with several neurodegenerative disorders including Parkinson's disease, Alzheimer's disease, Friedreich's ataxia, Huntington's disease, Amyotrophic lateral sclerosis, Leber's optic neuropathy, and axonal peripheral neuropathies (Beal et al. 1998, Brown et al. 1992, Benienda et al. 2013). Inhibition of mitochondrial respiration in Parkinson's disease (PD) became a focal point in the literature after a group of young adults developed symptoms

of Parkinsonism after injecting 1-methyl-4-phenyl-1,2,3,6-tetrahydropyridine (MPTP), a by-product and contaminant of synthetic heroin (Langston et al. 1984). These effects on mitochondrial function and oxidative phosphorylation were mirrored in idiopathic PD (Schapira et al. 2010, Parker et al. 2008). To examine these mechanisms of mitochondrial dysfunction and ATP depletion in PD, Betarbet (2000) used rotenone to inhibit complex I in-vivo and reproduced the neuropathological features of PD. This association of chronic pesticide exposure and nigrostriatal pathology initiated epidemiological studies to assess the risk of life-time exposure of rotenone with idiopathic PD. The Agricultural Health Study (AHS) is a prospective cohort of agricultural workers and their families organized with the intent to quantify disease risks from exposure to pesticides and agricultural chemicals (Alavanja et al. 1996). The Farming and Movement Evaluation Study is a nested case-control study within the AHS which followed private applicators of pesticides and their spouses to determine the risk of lifetime pesticide use with PD diagnosis (Tanner et al. 2011). Rotenone was the mitochondrial toxicant with the greatest association of PD with an odds ratio of 2.5 (95% CI, 1.3-4.7). While there are inconsistencies with the results from human data stemming from the limitations in assessing exposure and misdiagnosed Parkinson's disease, most studies report a positive association in agricultural workers with ever use of pesticides and the onset of PD (Kamel et al. 2007; Dhillon et al. 2008; Firestone et al. 2005; Gorrell et al. 1998, Freire and Hoifman 2012). Users of rotenone were 2.5 times more likely to develop PD as nonusers and this association was consistent even when exposure was truncated as many as 15 years before diagnosis (Tanner et al. 2011). Not only pesticide applicators are at risk but children living in rural environments and in residential areas that apply pesticides are also found to have increased risk of early-onset PD even without prior genetic history (Semchuk et al. 1991, Simcox et al. 1995, Lu et al. 2000, Hancock et al. 2008).

1.1.3 Parkinson's disease in the United States

Parkinson's disease (PD) is a chronic and highly progressive disorder with global incidence rates ranging from 10-18 per 100,000 person-years (Pringsheim et al. 2014). Industrialized nations see higher prevalence due to increased longevity with 1% of people affected over the age of 60. These numbers are only expected to increase with projections that worldwide prevalence will rise by 50% in 2030 (Dorsey et al. 2007). The estimated annual burden of Parkinson's disease in the United States is over $20 billion and projected to exceed $50 billion after 2050 (Findley et al. 2007). Due to the heterogeneous nature and rapid progressivity of its symptoms, there is not a proficient strategy to treat Parkinson's disease (Kalia and Lang 2015). Clinical strategies rely on the treatment of individual symptoms with the use of L-dopa, dopamine receptor stimulants, anti-psychotics, or anti-inflammatory agents. This type of intervention strategy while moderately improving the quality of life for patients can significantly contribute to the economic burden of the disease and does little to impact disease trajectory.

1.2 Background

1.2.1 Clinical and molecular features of Parkinson's disease

The classical symptoms of PD involve loss of motor control resulting in tremors, muscle rigidity, and the reduced ability to initiate movement (bradykinesia). These symptoms stem from the loss of dopaminergic neurons in the substantia nigra of the midbrain (Kalia and Lang 2016). Neuronal death does not only occur in this region, however, but in other regions of the brain as well including the amygdala, the hypothalamus, and the hippocampus (Yang and Yu 2016). This creates disturbances in other dopamine pathways that result in non-motor symptoms including psychosis, sleep disorders, and olfactory impairment. These alternative symptoms typically occur prodromal and can predate the first signs of motor dysfunction by decades. Historically, however, the diagnosis of PD has been dependent upon the motor features of PD and the relative effectiveness of dopamine precursors in treatment (Marsili et al. 2018). This

causes serious limitations in the treatment of PD since the development of motor features such as bradykinesia is concurrent with approximately 60% of dopaminergic loss in the brain (Cheng et al. 2010). It also leads to misdiagnoses with up to 25% of PD patients diagnosed with idiopathic PD having a “Parkinson’s-like” syndrome that results from a separate cause such as Alzheimer’s, focal brain lesions, brain injury, or neuroleptic drug usage (Litvan et al. 1998). Recently, the Movement Disorder Society (MDS) released new criteria for diagnosing PD that considers prodromal and non-motor symptoms but the success of the MDS criteria strategy remains to be determined because of lack of adoption by physicians and the lack of pathological validation (Postuma et al. 2015, Marsili et al. 2018).

While the pervasive destruction of dopamine secreting neurons is central to pathology, the exact mechanism causing cell death has not been identified. Several cellular processes have been highlighted in PD pathogenesis including metabolism, protein trafficking, inflammation, synaptic transmission, and controlled degradation pathways (Dauer and Przedborski 2003, Michel et al. 2013). These processes can be linked to two prominent molecular features of PD pathogenesis: mitochondrial dysfunction and protein aggregation. Mitochondrial dysfunction has been well characterized in patients with both familial and sporadic forms of PD (Belsa et al. 2015, Bose and Beal 2016). Mutations or impairment of proteins involved in mitochondrial metabolism and mitochondrial stress response results in lowered ATP production, increased oxidative stress, promotion of inflammatory cytokines, and the initiation of apoptosis (Pickrell et al. 2015). Alternatively, the oligomerization of mutated or mis-regulated proteins can lead to the formation of toxic insoluble fibrils known as inclusion bodies, or Lewy bodies (Kasten et al. 2013). Lewy bodies obstruct the secretion of dopamine and modify synaptic plasticity. They also inhibit intracellular degradation pathways that eliminate damaged or dysfunctional cell products and maintain cellular integrity. The failure of these pathways

to clear aggregated proteins promotes oxidative stress. Lewy bodies not only damage the host cell but may transfer toxic byproducts across synapses to neighboring cells causing local inflammation. Reactive oxygen species (ROS) are produced by mitochondrial dysfunction and Lewy body formation. ROS can also initiate or promote mitochondrial dysfunction and Lewy body formation (Anderson 2004, Hashimoto et al. 1998). Therefore, oxidative stress is a hallmark of PD creating a positive feedback loop between the weakening of homeostatic mechanisms and the propagation of pathological mechanisms. Oxidative stress can result from genetic mutations, inherited susceptibility genes, endogenous processes, and exogenous exposures.

1.2.2 Etiology of Parkinson's disease

Epidemiological evidence supports a Mendelian component to PD with approximately 5-10% of total cases resulting from monogenetic inheritance (Ascherio and Schwarzschild 2016). These genes referred to as causative genes have low prevalence in the population but when inherited can lead to the aggressive onset of symptoms at younger ages (Farrer 2006, Shulte and Gasser 2011). Of these causative genes, the first identified was *SNCA*. *SNCA* is the gene that encodes alpha-Synuclein (α-Syn). The endogenous role for α-Syn is not well understood but there is evidence to suggest that it functions at the pre-synaptic terminal to regulate secretion and promote synaptic plasticity (Benskey et al. 2016). α-Syn has also been identified as the major component of Lewy bodies. Mutations in *SNCA* can promote Lewy body formation by altering the protein conformation to one with a greater propensity to aggregate. Other mutations in *SNCA* can increase the expression and accumulation of α-Syn by strengthening its promoter site for transcription and increasing its resistance to degradation pathways (Kasten et al. 2013).

While genetics play a role in the onset of PD, 90% of diagnosed cases cannot be explained by genetics alone. In fact, less than 1% of early onset cases can be explained by any of the genes identified in GWAS studies (Ascherio and Schwarzschild 2016,

Schulte and Gasser 2011). However, no single causative factor has been identified in epidemiological studies. Therefore, the scientific community largely agrees that Parkinson's disease is likely caused by the complex interaction of genetics and environmental exposures (Zanon et al. 2018).

1.2.3 Rotenone-induced models of Parkinson's disease

Multiple criteria are used to assess the value of environmentally induced animal models of PD including: (1) the presence of motor impairment stemming from loss of nigrostriatal neurons, (2) the responsiveness of the motor condition to dopamine agonists, (3) the formation of inclusion bodies, (4) and damage in other structures of the brain resulting in non-motor disturbances (Cicchetti et al. 2009). Rotenone exposure in rodent models of PD has been shown to replicate motor symptoms including bradykinesia and postural instability (Betarbet et al. 2000, Cannon et al. 2009). Furthermore, the severity of motor impairment correlated with striatal lesions and the loss of dopaminergic neurons caused by rotenone treatment (Betarbet et al. 2000, Cannon et al. 2009, Lapointe et al. 2004). Motor behavior in rotenone-induced models is generally considered to be responsive to dopamine agonists (Betarbet et al. 2000, Cicchetti et al. 2009). However, inconsistencies remain with the specificity of rotenone toxicity to the central nervous system and the localization of lesions within nigrostriatal tissues (Ferrante et al. 1997, Lapointe et al. 2004, Benienda et al. 2013). While this non-specificity may be advantageous in reproducing non-motor symptoms such as sleeplessness, it could be more relevant to atypical PD than idiopathic PD (Garcia-Garcia et al. 2005). There are limitations of the model based on route of exposure. Most studies have relied on intravenous or subcutaneous injections of rotenone, but this exposure route can result in high rates of mortality in rodents (Sherer et a. 2003, Hooglinger et al. 2006). Though more recent studies have been able to overcome these challenges by intrastriatal infusion of rotenone (Carriere et al. 2014; Carriere et al. 2016), oral administration of rotenone

provides a more relevant approach. Low chronic exposures via ingestion have also been shown to increase locomotor deficits and reduce dopaminergic neurons in the striatum (Inden et al. 2011, Liu et al. 2017). However, interspecies variability in metabolism remains a limitation when extrapolating to humans in these studies.

Rotenone is a potent inhibitor of complex I of the mitochondrial respiratory chain and prevents the generation of ATP (Franco et la. 2010). The unavailability of an electron carrier from NADH to ubiquinone generates reactive oxygen species which can damage DNA, modify protein function, and degrade cellular lipids. This mechanism is mirrored in PD patients with reduced activity of complex I observed in the substantia nigra (Hoglinger et al. 2006). Mitochondrial damage can induce the release of cytochrome C and activate caspase mediated apoptosis. However, rotenone-induced cellular apoptosis is not dependent on complex I inhibition indicating other critical pathways of toxicity (Cabeza-Arvelaiz and Schiestl 2012, Choi et al. 2008).

Rotenone alters the expression of genes in one-carbon metabolism which is essential for purine and pyrimidine biosynthesis in cell proliferation (Smirnova et al. 2016). Metabolic reprogramming occurs from deficits in cellular respiration but there exists a complex I independent pathway for rotenone-induced changes in metabolism (Cabeza-Arvelaiz and Schiestl 2012). Rotenone destabilization of microtubules and the closure of mitochondrial voltage-dependent anion channels (VDACS) by disassembled tubulin are possible mechanisms to explain the effect of rotenone on mitochondrial membrane permeability independent of its effects on cellular respiration. Microtubules are key drivers of PD pathogenesis (Cartelli and Cappelletti 2017). Microtubule dynamics affect neurite outgrowth which is impaired in rotenone models of PD (Smirnova et al. 2016). The stabilization of microtubules also affects axonal transport and neurotransmission of dopamine in the striatum (Cartelli and Cappelletti 2017).

Rotenone treatment *in-vivo* and *in-vitro* can promote the accumulation of α-Syn and the formation of Lewy bodies (Cannon et al. 2009, Franco et al. 2011, Sala et al. 2016; Yuan et al. 2015). Aggregation of α-Syn is associated with multiple adverse effects including endoplasmic reticulum stress, proteasome obstruction, autophagy dysfunction, and neurotransmission interference. The formation of α-Syn inclusion bodies is often attributed to oxidative damage from the mitochondria but can also result from the down regulation of endoplasmic reticulum chaperone proteins and the fluctuation of intracellular calcium ion concentrations (Sala et al. 2016; Yuan et al. 2015). Intracellular α-Syn is considered a critical factor in PD-associated neuronal cell death and may be the key to understanding gene-environment interactions in idiopathic PD.

1.2.4 Epigenetic mechanisms mediate gene-environment interactions

Epigenetic mechanisms work at the interface of gene-environment interactions and are defined by heritable modifications of gene expression. Epigenetic modifications do not change the DNA sequence but rather regulate gene expression by modifying the accessibility of DNA to DNA binding proteins required for the initiation and/or elongation of transcription. Euchromatin, or open chromatin, is active and allows the binding of transcription factors at target genes. Heterochromatin, or closed chromatin, prevents the binding of the transcription machinery and silences genes. Epigenetic regulation is essential for proliferation, migration, and differentiation into individual cell types during development. Different timepoints of development are known as windows of susceptibility and exposures that occur during these windows of susceptibility cause disturbances in organ systems marked by epigenetic signatures. These signatures are then subjected to continuous editing in response to lifetime experiences modifying the risk of disease in adulthood (Martos et al. 2015). The most commonly studied of these epigenetic signatures are DNA methylation and histone tail modifications.

DNA methylation refers to the addition of a methyl group to the 5' position of the cytosine ring (5mC). 5mC represents between 2-5% of all cytosines in the human genome and most commonly occurs when a cytosine is adjacent to a guanine (CG site) (Millar et al. 2003). DNA hypomethylation at gene promoters is generally associated with open chromatin and increased expression. DNA methylation at gene encoding regions can be complementary or skewed toward one allele which may determine the interaction of an environmental factor with a specific genotype (Kanthasamy et al. 2012). However, DNA methylation also occurs frequently at non-coding regions and at repetitive elements (Yang et al. 2004). DNA methylation changes at these regions can also cause genomic instability by changing the activation state of transposable elements that foster widespread changes in genetic expression (Hou et al. 2012, Li et al. 2015).

Histone proteins package DNA and control the organization of DNA into structural units known as nucleosomes. Histone tails are enriched with positively charged amino acid residues lysine (K) and arginine (R). Histone tails can be covalently modified by acetylation to influence chromatin structure and the expression of genes (Wang et al. 2008). Histone 3 (H3) is the most commonly modified histone protein and acetylation of histone 3 lysine 27 (H3K27ac) is pursued in the scientific community because it is known to distinguish active enhancers from “poised” enhancers which may become active after an external cue (Chen et al. 2017, Creyghton et al. 2010).

1.2.5 Epigenetic insights in Parkinson’s disease

Several studies have shown that blood, serum, and tissue samples from patients diagnosed with PD have differential methylation patterns than neurologically normal controls (reviewed in Lu et al. 2013, Labbe et al. 2016, Jakubowskia and Labriea 2017). One study looking at post-mortem brain tissue of PD patients showed lower global levels of methylation than controls (Matsumoto et al. 2010). These differential patterns varied between different regions of the brain and between different stages of disease. A later

study using DNA chip arrays to analyze the DNA methylome across three different regions in the spinal cord and brain confirmed differential methylation in PD cases that varied by region (Young et al. 2019). Two primary mechanistic explanations for global hypomethylation have been studied thus far in patients: (1) reductions in DNA methyltransferases and (2) increases in TET enzymes. DNA Methyltransferase 1 (DNMT1), the enzyme predominately responsible for the maintenance of DNA methylation patterns, is reduced in the post mortem brain tissue samples from patients with PD (Desplats et al. 2011). There are also reports that levels of 5-hydroxymethylcytosine (5hmC), which is mediated by the TET1 enzyme and antagonizes 5mC, were higher in the cerebellum of PD patients (Stoger et al. 2017, Kaut et al. 2019). Further, a recent study revealed that reducing TET activity can protect human neurons from mitochondrial toxicant exposure *in-vitro* and rescue PD-associated motor phenotypes in mice (Wu et al. 2020).

Complementary to global methylation changes above, the methylation status of PD-relevant genes has been investigated in PD pathogenesis. The hypomethylation of several relevant genes including *CYP2E1 (*cytochrome p450 metabolic enzymes), *TNF* (Tumor Necrosis Factor inflammatory transcription factor), and PD-risk genes PARK2/PINK1 (mitochondrial damage sensors) (Cai et al. 2010, Kaut et al. 2012, Pieper et al 2008). In addition, clock genes (*PER, CRY, BMAL1,* and NPAS2) encode proteins that regulate circadian rhythms essential to main physiological homeostasis during aging. Blood samples from PD patients had decreased DNA methylation patterns and this altered expression of clock genes may contribute to the accelerated aging phenotype described by Horvath's epigenetic clock (Horvath et al. 2013, Horvath and Ritz 2015, Lin et al. 2012, Mao et al. 2018). Additionally, α-Syn encoding gene *SNCA* has been shown to have decreased methylation in the first intron which resulted in increased expression of the protein involved in the formation of Lewy bodies (Ai et al. 2014, Tan et al. 2014, De Boni

et al. 2011). The effect of reduced DNA methylation at *SNCA* intronic regions was reversed with administration of synthetic dopamine suggesting a role in dopaminergic neuronal activity with DNA methylation (Schmitt et al. 2015).

Histone acetylation codes are critical for maintaining neuronal function and regulating cell death (Saha and Pahan 2006). Hyperacetylation of histones has been observed in the post-mortem brain tissues of human patients and in toxicant-induced models of PD (Harrison et al. 2018). Studies have proposed that increased degradation of histone deacetylaces (HDACs) (Park et al. 2016) or lack of recruitment of HDACs to PD associated genes (Soldner et al. 2016, Hwang et al. 2017). The latter is evidenced by disrupted DNA binding of repressive complexes including REST and EMX2 and likely then also alter the methylation of histone proteins to silence chromatin (van Heesbeen and Smidt et al. 2019). HDAC inhibitor nicotinamide exacerbates motor symptoms and dopaminergic cells loss in rats (Harrison et al. 2019). Additionally, valproic acid, the HDAC inhibitor and psychiatric drug, has been associated with increased PD risk in elderly patients and withdrawal of the drug resulted in alleviated symptoms (Mahmoud and Tampi, 2011). However, histone hyperacetylation varies depending on the brain region and cell type (Park et al. 2016). The acetylome in primary fibroblasts from PD patients can also vary by etiology of PD with genetic and idiopathic cases being characterized by hyperacetylation and hypoacetylation, respectively (Yakhine-Diop et al. 2018). This interdependence of disease subtype and histone pathological state may then explain conflicting reports that HDAC inhibitors have neuroprotective potential in clinical trials (Harrison et al. 2018).

Regions affected by DNA hypomethylation and histone hyperacetylation result in the differential expression of genes involved in metabolism, inflammation, and autophagy (Labbe et al. 2016). Large disturbances in expression profiles of these genes drives cellular pathology by orchestrating several adverse events within neurons until cumulative

damage triggers cell death. These widespread changes in gene expression are persistent and neurons which survive the initial “hit” may retain a kind of “epigenetic memory” of the stressor which makes them more vulnerable to future stress (Smirnova et al. 2015). This explains the long latency period in disease onset and the delayed manifestation of motor symptoms.

1.2.6 *Epigenetic modifications in rotenone-induced models of PD*

Rotenone causes oxidative damage to DNA and is associated with modified DNA epigenetic patterns. Histone modifications are the most well-studied in rotenone models of PD. For example, pesticides paraquat and dieldrin are reported to cause hyperacetylation of lysine tails on histones (Song et al. 2010, Labbe et al. 2016). Similarly, complex I inhibitors, rotenone and MPTP, are associated with hyperacetylation and reduced histone deacetylase activity (Feng et al. 2015, Labbe et al. 2016, Sokhna et al. 2019). The reduced activity in HDAC complex enzymes may be mediated by stress induced autophagy and the pharmacological HDAC activator Resveratrol is neuroprotective in rotenone treated neuronal cells *in-vitro* (Feng et al. 2015, Wang et al. 2018, Park et al. 2016). Ketone bodies such as β-hydroxybutyrate produced from compensatory metabolic mechanisms due to deficient respiratory chain ATP generation have also been shown to affect HDAC activity levels (Sankha et a. 2014, Imamura et al. 2006). However, these observations on global histone acetylation levels have not been consistent between models (Sokhna et al. 2019). For example, several studies have reported a protective effect of HDAC inhibitors from rotenone that rescues neurons from α-Syn related toxicity (Labbe et al. 2016, Sokhna et al. 2019, Zhang et al. 2016, Singh et al. 2017, Outeiro et al. 2007). Regardless the direction, it seems a delicate balance between HAT and HDAC activity must be maintained to fortify neuronal health during aging.

DNA methylation is correlated with chronic chemical exposure and neurodegeneration (Collota et al. 2013, Kwok et al. 2010). Mitochondrial dysfunction from chronic chemical exposure has long term effects on nuclear DNA methylation levels and complex I inhibition is associated with altered DNA methylation (5-mC) and DNA hydroxymethylation (5hmC) *in-vitro* (Bellizzi et al. 2012, Scola et al. 2014). Furthermore, DNA hypomethylation from pesticide exposure has been reported in human peripheral blood leukocytes which correlates with the DNA methylation patterns observed in PD patients (Kim et al. 2010, Hou et al. 2011). While fewer studies have examined the methylome in result of rotenone exposure, there is evidence to suggest that DNA methylation inhibition exacerbates PD pathology and α-Syn toxicity in dopaminergic neurons exposed to rotenone (Wang et al. 2013).

There are epigenetic processes that regulate gene expression on the transcript level. Small, non-coding RNAs known as microRNAS (miRNA) bind complementary sequences on messenger RNAs to prevent translation. miRNAs are critical for PD associated gene expression and are required to maintain neurons during aging (Labbe et al. 2016). Though the post-trascriptional regulation of gene expression is important to understand gene-environment interactions in neurotoxicity, it will not be the focus of this dissertation. Instead, this dissertation will focus on gene regulation that occurs at the chromatin level by studying DNA methylation and histone modifications.

1.3 Overview of Specific Aims

The goal of this dissertation is to investigate chromatin-mediated gene regulation in rotenone induced neurotoxicity. Rotenone pathways of toxicity with respect to PD pathogenesis have been of significant interest in the scientific community for the past two decades and thus this dissertation will focus primarily on mechanisms of chromatin regulation in PD. However, it should be noted that these mechanisms are not considered

dopaminergic neuron specific and may have implications for other neuronal subtypes including peripheral neurons.

DNA 5-methylcytosine methylation and histone tail lysine acetylation are two examples of chromatin-mediated gene regulation. Because these epigenetic patterns are influenced by both genetic variability and environmental exposure, epigenetic mechanisms can bridge the gap to understanding gene-environment interactions in rotenone induced neurotoxicity. I hypothesizethat rotenone induced α-Syn accumulation and mitochondrial damage creates large disturbances in gene expression profiles that orchestrate cellular pathways of toxicity and cues cell-mediated apoptosis. To address this hypothesis, I propose the following three specific aims:

1. To determine changes in chromatin-mediated gene regulation in human cells exposed to rotenone.
2. To investigate the role of oxidative stress induced α-Synuclein accumulation in mediating epigenetic response to Rotenone.
3. To investigate the role of mitochondrial damage on histone acetylation and chromatin accessibility in Rotenone-Induced cellular models of Parkinson's disease.

1.4 Innovation and Impact

Multiple studies have been published using environmental exposures to observe pathological events within a cell. Furthermore, with advancements in the accessibility of high content technologies, the number of studies characterizing the transcriptome of exposed neurons via RNA-sequencing have increased. These "omics" studies have identified several molecular pathways, proteins, and genes as important players in neurodegeneration and PD. It is widely accepted that epigenetic mechanisms including DNA methylation and histone modifications are critical in mediating gene-environment interactions in PD, which is particularly critical in considering the interactions for 90-95% of PD cases. However, few studies have investigated the role of these mechanisms in

toxicant induced models of PD. Additionally, almost no studies to date aim to understand the mechanisms for how changes in these epigenetic patterns occur as a result of exposure. We take an innovative approach to studying gene-environment interactions by using a relevant exogenous exposure to investigate epigenetic mechanisms in neurons. In this dissertation, we use three separate human cell lines (*HEK293*, *SH-5YSY*, and *LUHMES)* which are commonly used to model neurobiology *in-vitro*. Each cell line adds a new layer of complexity with *HEK293* being the simplest model. *HEK293* is a human immortalized cell line derived originally from primary embryonic kidney cells but have been found to have a genetic signature similar to neurons (Stepanenko and Dmitrenko 2015). The *SH-5YSY* cell line is also an immortalized cell but neuronal in origin. The cells were derived from a metastatic neuroblastoma and display a catecholaminergic phenotype with the ability to synthesize dopamine (Xicoy et al. 2017). Lastly, the *LUHMES* cell line represents the most specific model for rotenone induced PD as it originates from non-cancerous embryonic mesencephalic (midbrain) tissue and differentiates into fully mature differentiated dopaminergic neurons (Smirnova et al. 2016). While rotenone has toxic effects in multiple cell types, dopaminergic neurons are especially vulnerable to rotenone induced oxidative stress (Harris et al. 2018). Furthermore, degeneration of dopaminergic neurons is a primary feature of PD and it's the loss of dopamine in the midbrain that causes motor deficits. We tested our proposed mechanisms for rotenone changes at multiple stages of neuronal maturation to determine which epigenetic modifications may be more important during exposures at early stages of development and which are more meaningful during adult exposures. This thesis will take an in depth look at gene expression, DNA methylation, histone acetylation, transcription factor binding, and chromatin accessibility to interpret rotenone mechanisms of toxicity and its implications in neurodegeneration. It will also highlight vulnerable regions of the genome and link these regions to their effects in cellular processes. These data can provide mechanistic insights

into the role of the epigenome on the aging brain and can inform clinical strategies for the diagnosis and treatment of neurodegenerative disorders such as PD.

1.5 References

1. Ai S, Xu Q, Hu Y, Song C, Guo J, Shen L et al. 2014. Hypomethylation of SNCA in blood of patients with sporadic Parkinson's disease. J Neurol Sci 337(1-2):123-128.
2. Alavanja MC. 2009. Introduction: Pesticides use and exposure, extensive worldwide. Rev Environ Health 24(4):303-310.
3. Alavanja MC, Sandler DP, McMaster SB, Zahm SH, McDonnell CJ, Lynch CF et al. 1996. The agricultural health study. Environ Health Perspect 104(4):362-369; doi: 10.1289/ehp.96104362 [doi].
4. Andersen JK. 2004. Oxidative stress in neurodegeneration: Cause or consequence? Nat Med 10(7):S18-S25.
5. Ascherio A, Schwarzschild MA. 2016. The epidemiology of Parkinson's disease: Risk factors and prevention. The Lancet Neurology 15(12):1257-1272.
6. Atwood D, Paisley-Jones C. 2017. Pesticides industry sales and usage: 2008–2012 market estimates. US Environmental Protection Agency, Washington, DC 20460.
7. Beal MF. 1998. Mitochondrial dysfunction in neurodegenerative diseases. Biochimica et Biophysica Acta (BBA)-Bioenergetics 1366(1-2):211-223.
8. Bellizzi D, D'Aquila P, Giordano M, Montesanto A, Passarino G. 2012. Global DNA methylation levels are modulated by mitochondrial DNA variants. Epigenomics 4(1):17-27.
9. Benskey MJ, Perez RG, Manfredsson FP. 2016. The contribution of alpha synuclein to neuronal survival and function–Implications for Parkinson's disease. J Neurochem 137(3):331-359.
10. Betarbet R, Sherer TB, MacKenzie G, Garcia-Osuna M, Panov AV, Greenamyre JT. 2000. Chronic systemic pesticide exposure reproduces features of parkinson's disease. Nat Neurosci 3(12):1301.
11. Binienda ZK, Sarkar S, Mohammed-Saeed L, Gough B, Beaudoin MA, Ali SF et al. 2013. Chronic exposure to rotenone, a dopaminergic toxin, results in peripheral neuropathy associated with dopaminergic damage. Neurosci Lett 541:233-237.
12. Blesa J, Trigo-Damas I, Quiroga-Varela A, Jackson-Lewis VR. 2015. Oxidative stress and Parkinson's disease. Frontiers in neuroanatomy 9:91.
13. Bose A, Beal MF. 2016. Mitochondrial dysfunction in parkinson's disease. J Neurochem 139:216-231.
14. Brown MD, Voljavec AS, Lott MT, MacDonald I, Wallace DC. 1992. Leber's hereditary optic neuropathy: A model for mitochondrial neurodegenerative diseases. FASEB J 6(10):2791-2799; doi: 10.1096/fasebj.6.10.1634041 [doi].
15. Cabeza-Arvelaiz Y, Schiestl RH. 2012. Transcriptome analysis of a rotenone model of parkinsonism reveals complex I-tied and-untied toxicity mechanisms common to neurodegenerative diseases. PloS one 7(9):e44700.
16. Cai M, Tian J, Zhao G, Luo W, Zhang B. 2011. Study of methylation levels of parkin gene promoter in parkinson's disease patients. Int J Neurosci 121(9):497-502; doi: 10.3109/00207454.2011.580866.
17. Cannon JR, 3Tapias V, Na HM, Honick AS, Drolet RE, Greenamyre JT. 2009. A highly reproducible rotenone model of parkinson's disease. Neurobiol Dis 34(2):279-290.
18. Carriere CH, Kang NH, Niles LP. 2016. Chronic low-dose melatonin treatment maintains nigrostriatal integrity in an intrastriatal rotenone model of Parkinson's disease. Brain Res 1633:115-125.

19. Carriere C, Kang N, Niles L. 2014. Neuroprotection by valproic acid in an intrastriatal rotenone model of Parkinson's disease. Neuroscience 267:114-121.
20. Cartelli D, Cappelletti G. 2017. Microtubule destabilization paves the way to Parkinson's disease. Mol Neurobiol 54(9):6762-6774.
21. Chen D, Jin C. 2019. Histone variants in environmental-stress-induced DNA damage repair. Mutation Research/Reviews in Mutation Research 780:55-60.
22. Cheng H, Ulane CM, Burke RE. 2010. Clinical progression in parkinson disease and the neurobiology of axons. Ann Neurol 67(6):715-725.
23. Choi WS, Kruse SE, Palmiter RD, Xia Z. 2008. Mitochondrial complex I inhibition is not required for dopaminergic neuron death induced by rotenone, MPP+, or paraquat. Proc Natl Acad Sci U S A 105(39):15136-15141; doi: 10.1073/pnas.0807581105 [doi].
24. Cicchetti F, Drouin-Ouellet J, Gross RE. 2009. Environmental toxins and parkinson's disease: What have we learned from pesticide-induced animal models? Trends Pharmacol Sci 30(9):475-483.
25. Collotta M, Bertazzi P, Bollati V. 2013. Epigenetics and pesticides. Toxicology 307:35-41.
26. Creyghton MP, Cheng AW, Welstead GG, Kooistra T, Carey BW, Steine EJ et al. 2010. Histone H3K27ac separates active from poised enhancers and predicts developmental state. Proc Natl Acad Sci U S A 107(50):21931-21936; doi: 10.1073/pnas.1016071107 [doi].
27. Dawson V, Gingerich W, Davis R, Gilderhus P. 1991. Rotenone persistence in freshwater ponds: Effects of temperature and sediment adsorption. N Am J Fish Manage 11(2):226-231.
28. De Boni L, Tierling S, Roeber S, Walter J, Giese A, Kretzschmar HA. 2011. Next-generation sequencing reveals regional differences of the α-synuclein methylation state independent of lewy body disease. Neuromolecular medicine 13(4):310-320.
29. DE LAMIRANDE E, GAGNON C. 1992. Reactive oxygen species and human spermatozoa: I. effects on the motility of intact spermatozoa and on sperm axonemes. J Androl 13(5):368-378.
30. Desplats P, Spencer B, Coffee E, Patel P, Michael S, Patrick C et al. 2011. Alpha-synuclein sequesters Dnmt1 from the nucleus: A novel mechanism for epigenetic alterations in lewy body diseases. J Biol Chem 286(11):9031-9037; doi: 10.1074/jbc.C110.212589 [doi].
31. Dhillon AS, Tarbutton GL, Levin JL, Plotkin GM, Lowry LK, Nalbone JT et al. 2008. Pesticide/environmental exposures and parkinson's disease in east texas. J Agromed 13(1):37-48.
32. Donley N. 2019. The USA lags behind other agricultural nations in banning harmful pesticides. Environ Health 18(1):44.
33. Dorsey ER, Constantinescu R, Thompson JP, Biglan KM, Holloway RG, Kieburtz K et al. 2007. Projected number of people with parkinson disease in the most populous nations, 2005 through 2030. Neurology 68(5):384-386; doi: 01.wnl.0000247740.47667.03 [pii].
34. Farrer MJ. 2006. Genetics of parkinson disease: Paradigm shifts and future prospects. Nature Reviews Genetics 7(4):306-318.
35. Feng Y, Liu T, Dong S, Guo Y, Jankovic J, Xu H et al. 2015. Rotenone affects p53 transcriptional activity and apoptosis via targeting SIRT 1 and H3K9 acetylation in SH-SY 5Y cells. J Neurochem 134(4):668-676.
36. Ferrante RJ, Schulz JB, Kowall NW, Beal MF. 1997. Systemic administration of rotenone produces selective damage in the striatum and globus pallidus, but not in the substantia nigra. Brain Res 753(1):157-162.

37. Firestone JA, Smith-Weller T, Franklin G, Swanson P, Longstreth W, Checkoway H. 2005. Pesticides and risk of parkinson disease: A population-based case-control study. Arch Neurol 62(1):91-95.
38. Franco R, Li S, Rodriguez-Rocha H, Burns M, Panayiotidis MI. 2010. Molecular mechanisms of pesticide-induced neurotoxicity: Relevance to parkinson's disease. Chem Biol Interact 188(2):289-300.
39. Freire C, Koifman S. 2012. Pesticide exposure and parkinson's disease: Epidemiological evidence of association. Neurotoxicology 33(5):947-971.
40. García-García F, Ponce S, Brown R, Cussen V, Krueger JM. 2005. Sleep disturbances in the rotenone animal model of parkinson disease. Brain Res 1042(2):160-168.
41. Gorell JM, Johnson CC, Rybicki BA, Peterson EL, Richardson RJ. 1998. The risk of parkinson's disease with exposure to pesticides, farming, well water, and rural living. Neurology 50(5):1346-1350; doi: 10.1212/wnl.50.5.1346 [doi].
42. Greenamyre JT, Sherer TB, Betarbet R, Panov AV. 2001. Complex I and parkinson's disease. IUBMB Life 52(3-5):135-141.
43. Hancock DB, Martin ER, Mayhew GM, Stajich JM, Jewett R, Stacy MA et al. 2008. Pesticide exposure and risk of parkinson's disease: A family-based case-control study. BMC neurology 8(1):6.
44. Harrison IF, Smith AD, Dexter DT. 2018. Pathological histone acetylation in Parkinson's disease: Neuroprotection and inhibition of microglial activation through SIRT 2 inhibition. Neurosci Lett 666:48-57.
45. Harrison IF, Powell NM, Dexter DT. 2019. The histone deacetylase inhibitor nicotinamide exacerbates neurodegeneration in the lactacystin rat model of parkinson's disease. J Neurochem 148(1):136-156; doi: 10.1111/jnc.14599 [doi].
46. Hashimoto M, Hsu LJ, Xia Y, Takeda A, Sisk A, Sundsmo M et al. 1999. Oxidative stress induces amyloid-like aggregate formation of NACP/α-synuclein in vitro. Neuroreport 10(4):717-721.
47. Hoöglinger G, Oertel W, Hirsch E. 2006. The rotenone model of parkinsonism—the five years inspection. In: Parkinson's Disease and Related Disorders:Springer, 269-272.
48. Horvath S. 2013. DNA methylation age of human tissues and cell types. Genome Biol 14(10):R115-2013-14-10-r115; doi: gb-2013-14-10-r115 [pii].
49. Horvath S, Ritz BR. 2015. Increased epigenetic age and granulocyte counts in the blood of parkinson's disease patients. Aging (Albany NY) 7(12):1130-1142; doi: 100859 [pii].
50. Hou L, Zhang X, Wang D, Baccarelli A. 2012. Environmental chemical exposures and human epigenetics. Int J Epidemiol 41(1):79-105.
51. Hwang JY, Aromolaran KA, Zukin RS. 2017. The emerging field of epigenetics in neurodegeneration and neuroprotection. Nat Rev Neurosci 18(6):347-361; doi: 10.1038/nrn.2017.46 [doi].
52. Imamura K, Takeshima T, Kashiwaya Y, Nakaso K, Nakashima K. 2006. D-β-hydroxybutyrate protects dopaminergic SH-SY5Y cells in a rotenone model of parkinson's disease. J Neurosci Res 84(6):1376-1384.
53. Inden M, Kitamura Y, Abe M, Tamaki A, Takata K, Taniguchi T. 2011. Parkinsonian rotenone mouse model: Reevaluation of long-term administration of rotenone in C57BL/6 mice. Biological and Pharmaceutical Bulletin 34(1):92-96.
54. Jakubowski JL, Labrie V. 2017. Epigenetic biomarkers for parkinson's disease: From diagnostics to therapeutics. J Parkinsons Dis 7(1):1-12; doi: 10.3233/JPD-160914 [doi].
55. Kalia LV, Lang AE. 2016. Parkinson disease in 2015: Evolving basic, pathological and clinical concepts in PD. Nature reviews Neurology 12(2):65.

56. Kalia L, Lang A. Parkinson's disease.Lancet [Internet].2015; 386 (9996): 896–912.
57. Kamel F, Engel L, Gladen B, Hoppin J, Alavanja MC, Sandler D. 2007. Neurologic symptoms in licensed pesticide applicators in the agricultural health study. Hum Exp Toxicol 26(3):243-250.
58. Kanthasamy A, Jin H, Anantharam V, Sondarva G, Rangasamy V, Rana A et al. 2012. Emerging neurotoxic mechanisms in environmental factors-induced neurodegeneration. Neurotoxicology 33(4):833-837.
59. Kasten M, Klein C. 2013. The many faces of alpha-synuclein mutations. Movement Disorders 28(6):697-701.
60. Kaut O, Kuchelmeister K, Moehl C, Wullner U. 2019. 5-methylcytosine and 5-hydroxymethylcytosine in brains of patients with multiple system atrophy and patients with parkinson's disease. J Chem Neuroanat 96:41-48; doi: S0891-0618(18)30210-2 [pii].
61. Kaut O, Schmitt I, Wullner U. 2012. Genome-scale methylation analysis of parkinson's disease patients' brains reveals DNA hypomethylation and increased mRNA expression of cytochrome P450 2E1. Neurogenetics 13(1):87-91; doi: 10.1007/s10048-011-0308-3 [doi].
62. Kim KY, Kim DS, Lee SK, Lee IK, Kang JH, Chang YS et al. 2010. Association of low-dose exposure to persistent organic pollutants with global DNA hypomethylation in healthy koreans. Environ Health Perspect 118(3):370-374; doi: 10.1289/ehp.0901131 [doi].
63. Kwok JB. 2010. Role of epigenetics in Alzheimer's and Parkinson's disease. Epigenomics 2(5):671-682.
64. Labbé C, Lorenzo-Betancor O, Ross OA. 2016. Epigenetic regulation in Parkinson's disease. Acta Neuropathol 132(4):515-530.
65. Langston JW, Ballard P, Tetrud JW, Irwin I. 1983. Chronic parkinsonism in humans due to a product of meperidine-analog synthesis. Science 219(4587):979-980; doi: 10.1126/science.6823561 [doi].
66. Lapointe N, St-Hilaire M, Martinoli M, Blanchet J, Gould P, Rouillard C et al. 2004. Rotenone induces non-specific central nervous system and systemic toxicity. The FASEB journal 18(6):717-719.
67. Li Z, Dai H, Martos SN, Xu B, Gao Y, Li T et al. 2015. Distinct roles of DNMT1-dependent and DNMT1-independent methylation patterns in the genome of mouse embryonic stem cells. Genome Biol 16:115-015-0685-2; doi: 10.1186/s13059-015-0685-2 [doi].
68. Lin Q, Ding H, Zheng Z, Gu Z, Ma J, Chen L et al. 2012. Promoter methylation analysis of seven clock genes in parkinson's disease. Neurosci Lett 507(2):147-150; doi: 10.1016/j.neulet.2011.12.007 [doi].
69. Litvan I, MacIntyre A, Goetz C, Wenning G, Jellinger K, Verny M et al. 1998. Accuracy of the clinical diagnoses of lewy body disease, parkinson disease, and dementia with lewy bodies: A clinicopathologic study. Arch Neurol 55(7):969-978.
70. Liu H, Ho PW, Leung GC, Lam CS, Pang SY, Li L et al. 2017. Combined LRRK2 mutation, aging and chronic low dose oral rotenone as a model of Parkinson's disease. Scientific reports 7(1):1-15.
71. Lu C, Fenske RA, Simcox NJ, Kalman D. 2000. Pesticide exposure of children in an agricultural community: Evidence of household proximity to farmland and take home exposure pathways. Environ Res 84(3):290-302.
72. Mahmoud F, Tampi RR. 2011. Valproic acid-induced parkinsonism in the elderly: A comprehensive review of the literature. Am J Geriatr Pharmacother 9(6):405-412; doi: 10.1016/j.amjopharm.2011.09.002 [doi].

73. Mao W, Zhao C, Ding H, Liang K, Xue J, Chan P et al. 2018. Pyrosequencing analysis of methylation levels of clock genes in leukocytes from parkinson's disease patients. Neurosci Lett 668:115-119; doi: S0304-3940(18)30027-2 [pii].
74. Marsili L, Rizzo G, Colosimo C. 2018. Diagnostic criteria for Parkinson's disease: From james parkinson to the concept of prodromal disease. Frontiers in neurology 9:156.
75. Martos SN, Tang W, Wang Z. 2015. Elusive inheritance: Transgenerational effects and epigenetic inheritance in human environmental disease. Prog Biophys Mol Biol 118(1-2):44-54.
76. Matsumoto L, Takuma H, Tamaoka A, Kurisaki H, Date H, Tsuji S et al. 2010. CpG demethylation enhances alpha-synuclein expression and affects the pathogenesis of parkinson's disease. PLoS One 5(11):e15522; doi: 10.1371/journal.pone.0015522 [doi].
77. Michel PP, Hirsch EC, Hunot S. 2016. Understanding dopaminergic cell death pathways in parkinson disease. Neuron 90(4):675-691.
78. Millar DS, Holliday R, Grigg GW. 2003. Five not four: History and significance of the fifth base. The Epigenome: Molecular Hide and Seek:1-20.
79. Outeiro TF, Kontopoulos E, Altmann SM, Kufareva I, Strathearn KE, Amore AM et al. 2007. Sirtuin 2 inhibitors rescue alpha-synuclein-mediated toxicity in models of parkinson's disease. Science 317(5837):516-519; doi: 1143780 [pii].
80. Park G, Tan J, Garcia G, Kang Y, Salvesen G, Zhang Z. 2016. Regulation of histone acetylation by autophagy in parkinson disease. J Biol Chem 291(7):3531-3540; doi: 10.1074/jbc.M115.675488 [doi].
81. Parker Jr WD, Parks JK, Swerdlow RH. 2008. Complex I deficiency in parkinson's disease frontal cortex. Brain Res 1189:215-218.
82. Pickrell AM, Youle RJ. 2015. The roles of PINK1, parkin, and mitochondrial fidelity in Parkinson's disease. Neuron 85(2):257-273.
83. Pieper HC, Evert BO, Kaut O, Riederer PF, Waha A, Wullner U. 2008. Different methylation of the TNF-alpha promoter in cortex and substantia nigra: Implications for selective neuronal vulnerability. Neurobiol Dis 32(3):521-527; doi: 10.1016/j.nbd.2008.09.010 [doi].
84. Postuma RB, Berg D, Stern M, Poewe W, Olanow CW, Oertel W et al. 2015. MDS clinical diagnostic criteria for parkinson's disease. Movement Disorders 30(12):1591-1601.
85. Pringsheim T, Jette N, Frolkis A, Steeves TD. 2014. The prevalence of parkinson's disease: A systematic review and meta-analysis. Movement disorders 29(13):1583-1590.
86. Saha R, Pahan K. 2006. HATs and HDACs in neurodegeneration: A tale of disconcerted acetylation homeostasis. Cell Death & Differentiation 13(4):539-550.
87. Sala G, Marinig D, Riva C, Arosio A, Stefanoni G, Brighina L et al. 2016. Rotenone down-regulates HSPA8/hsc70 chaperone protein in vitro: A new possible toxic mechanism contributing to Parkinson's disease. Neurotoxicology 54:161-169.
88. Schapira A. 2010. Complex I: Inhibitors, inhibition and neurodegeneration. Exp Neurol 224(2):331-335.
89. Schmitt I, Kaut O, Khazneh H, deBoni L, Ahmad A, Berg D et al. 2015. L-dopa increases alpha-synuclein DNA methylation in parkinson's disease patients in vivo and in vitro. Mov Disord 30(13):1794-1801; doi: 10.1002/mds.26319 [doi].
90. Schulte C, Gasser T. 2011. Genetic basis of parkinson's disease: Inheritance, penetrance, and expression. Appl Clin Genet 4:67-80; doi: 10.2147/TACG.S11639 [doi].
91. Scola G, Kim HK, Young LT, Salvador M, Andreazza AC. 2014. Lithium reduces the effects of rotenone-induced complex I dysfunction on DNA methylation and

hydroxymethylation in rat cortical primary neurons. Psychopharmacology (Berl) 231(21):4189-4198.
92. Semchuk KM, Love EJ, Lee RG. 1992. Parkinson's disease and exposure to agricultural work and pesticide chemicals. Neurology 42(7):1328-1335; doi: 10.1212/wnl.42.7.1328 [doi].
93. Sherer TB, Betarbet R, Testa CM, Seo BB, Richardson JR, Kim JH et al. 2003. Mechanism of toxicity in rotenone models of parkinson's disease. J Neurosci 23(34):10756-10764; doi: 23/34/10756 [pii].
94. Simcox NJ, Fenske RA, Wolz SA, Lee IC, Kalman DA. 1995. Pesticides in household dust and soil: Exposure pathways for children of agricultural families. Environ Health Perspect 103(12):1126-1134; doi: 10.1289/ehp.951031126 [doi].
95. Singh P, Hanson PS, Morris CM. 2017. Sirtuin-2 protects neural cells from oxidative stress and is elevated in neurodegeneration. Parkinson’s Disease 2017.
96. Smirnova L, Harris G, Leist M, Hartung T. 2015. Cellular resilience. ALTEX 32(4):247-260; doi: 10.14573/altex.1509271 [doi].
97. Smirnova L, Harris G, Delp J, Valadares M, Pamies D, Hogberg HT et al. 2016. A LUHMES 3D dopaminergic neuronal model for neurotoxicity testing allowing long-term exposure and cellular resilience analysis. Arch Toxicol 90(11):2725-2743.
98. Soldner F, Stelzer Y, Shivalila CS, Abraham BJ, Latourelle JC, Barrasa MI et al. 2016. Parkinson-associated risk variant in distal enhancer of alpha-synuclein modulates target gene expression. Nature 533(7601):95-99; doi: 10.1038/nature17939 [doi].
99. Song C, Kanthasamy A, Anantharam V, Sun F, Kanthasamy AG. 2010. Environmental neurotoxic pesticide increases histone acetylation to promote apoptosis in dopaminergic neuronal cells: Relevance to epigenetic mechanisms of neurodegeneration. Mol Pharmacol 77(4):621-632; doi: 10.1124/mol.109.062174 [doi].
100. StÃ¶ger R, Scaife PJ, Shephard F, Chakrabarti L. 2017. Elevated 5hmC levels characterize DNA of the cerebellum in parkinson's disease. NPJ Parkinsons Dis 3:6-017-0007-3. eCollection 2017; doi: 10.1038/s41531-017-0007-3 [doi].
101. Tan Y, Wu L, Zhao Z, Wang Y, Xiao Q, Liu J et al. 2014. Methylation of α-synuclein and leucine-rich repeat kinase 2 in leukocyte DNA of parkinson's disease patients. Parkinsonism Relat Disord 20(3):308-313.
102. Tanner CM, Kamel F, Ross GW, Hoppin JA, Goldman SM, Korell M et al. 2011. Rotenone, paraquat, and parkinson's disease. Environ Health Perspect 119(6):866-872; doi: 10.1289/ehp.1002839 [doi].
103. Turner L, Jacobson S, Shoemaker L. 2007. Risk assessment for piscicidal formulations of rotenone. Compliance Services International, Lakewood:25.
104. Uversky VN. 2004. Neurotoxicant-induced animal models of Parkinson’s disease: Understanding the role of rotenone, maneb and paraquat in neurodegeneration. Cell Tissue Res 318(1):225-241.
105. van Heesbeen HJ, Smidt MP. 2019. Entanglement of genetics and epigenetics in Parkinsonâ€™s disease. Frontiers in Neuroscience 13:277.
106. Wang H, Dong X, Liu Z, Zhu S, Liu H, Fan W et al. 2018. Resveratrol suppresses rotenone-induced neurotoxicity through activation of SIRT1/Akt1 signaling pathway. Anat Rec 301(6):1115-1125.
107. Wang Y, Wang X, Li R, Yang Z, Wang Y, Gong X et al. 2013. A DNA methyltransferase inhibitor, 5-Aza-2′-Deoxycytidine, exacerbates neurotoxicity and upregulates Parkinson's Disease-Related genes in dopaminergic neurons. CNS neuroscience & therapeutics 19(3):183-190.

108. Wang Z, Zang C, Rosenfeld JA, Schones DE, Barski A, Cuddapah S et al. 2008. Combinatorial patterns of histone acetylations and methylations in the human genome. Nat Genet 40(7):897.
109. Whyatt RM, Camann DE, Kinney PL, Reyes A, Ramirez J, Dietrich J et al. 2002. Residential pesticide use during pregnancy among a cohort of urban minority women. Environ Health Perspect 110(5):507-514; doi: sc271_5_1835.
110. Worth AJ, Basu SS, Snyder NW, Mesaros C, Blair IA. 2014. Inhibition of neuronal cell mitochondrial complex I with rotenone increases lipid beta-oxidation, supporting acetyl-coenzyme A levels. J Biol Chem 289(39):26895-26903; doi: 10.1074/jbc.M114.591354.
111. Wu TT, Liu T, Li X, Chen YJ, Chen TJ, Zhu XY et al. 2020. TET2-mediated Cdkn2A DNA hydroxymethylation in midbrain dopaminergic neurons injury of Parkinson's disease. Hum Mol Genet; doi: ddaa022.
112. Yakhine-Diop SMS, Martinez-Chacon G, Uribe-Carretero E, Niso-Santano M, Gonzalez-Polo RA, Fuentes JM. 2019. The paradigm of protein acetylation in Parkinson's disease. Neural Regen Res 14(6):975-976; doi: 10.4103/1673-5374.250575.
113. Yang AS, Estécio MR, Doshi K, Kondo Y, Tajara EH, Issa JJ. 2004. A simple method for estimating global DNA methylation using bisulfite PCR of repetitive DNA elements. Nucleic Acids Res 32(3):e38-e38.
114. Yang W, Yu S. 2017. Synucleinopathies: Common features and hippocampal manifestations. Cellular and molecular life sciences 74(8):1485-1501.
115. Young JI, Sivasankaran SK, Wang L, Ali A, Mehta A, Davis DA et al. 2019. Genome-wide brain DNA methylation analysis suggests epigenetic reprogramming in Parkinson disease. Neurol Genet 5(4):e342; doi: 10.1212/NXG.0000000000000342.
116. Yuan Y, Yan W, Sun J, Huang J, Mu Z, Chen N. 2015. The molecular mechanism of rotenone-induced α-synuclein aggregation: Emphasizing the role of the calcium/GSK3β pathway. Toxicol Lett 233(2):163-171.
117. Zanon A, Pramstaller PP, Hicks AA, Pichler I. 2018. Environmental and genetic variables influencing mitochondrial health and Parkinson's disease penetrance. Parkinson's Disease 2018.
118. Zhang J, Deng Y, Zhang M, Su H, Qu Q. 2016. SIRT3 acts as a neuroprotective agent in rotenone-induced Parkinson's cell model. Neurochem Res 41(7):1761-177.

CHAPTER 2

ROTENONE INDUCED CHANGES OF EPIGENETIC PATTERNS AT CIS-ACTING REGULATORY REGIONS.

CHAPTER 2[1]

PART A. Rotenone regulates chromatin by modifying global levels of DNA 5-methylcytosine and Histone 3 Lysine 27 acetylation.

2A.1 Abstract

Epigenetic modifications can vary individual behavior by influencing neuronal gene expression and neural activity. Pesticide exposure is associated with epigenetic modifications that can impair neurite outgrowth, obstruct axonal transport, and diminish synaptic plasticity. These adverse effects hinder the cellular stress response in neurons making them more vulnerable to environmental factors and degeneration. Pesticides reduce global DNA methylation and rotenone is expected to have a similar response. Pathological histone hyperacetylation and increased enhancer activation is also caused by rotenone neurotoxicity. Therefore, rotenone toxicity may result from widespread changes in gene expression caused from the opening of chromatin and the unregulated binding of DNA transcription factors. In Part A of this chapter, we measured the cellular response to rotenone treatment after 24h and analyzed changes in chromatin mediated gene regulation. Rotenone reduced DNA methylation and increased histone H3 lysine 27 acetylation (H3K27ac) globally across the human cell line *HEK293*. These epigenetic modifications were associated with the altered expression of over 2,000 genes (>1.5 fold change, FDR<0.05) which were largely involved in the oxidative stress response, transcription factor DNA binding activity, and chromatin organization. We hypothesize that rotenone-induced global chromatin changes cause instability that targets vulnerable regions of the genome and tampers with the expression of genes required to preserve neuronal function.

[1] Parts of this chapter have been submitted for publication in *Frontiers in Genetics*. D.M. Freeman and Z. Wang (2020).

2A.2 Introduction

Rotenone is a pesticide commonly used as a Parkinson's disease model toxicant and has been shown to robustly replicate the physiological and molecular features of human PD in animal models (Cannon et al. 2009). It is estimated that chronic exposure to concentrations of approximately 20-30 nM of rotenone is enough to cause degeneration of dopaminergic neurons in the midbrain (Greenamyre et al. 2003). While rotenone is a potent inhibitor of complex I in the electron transport chain of mitochondria, higher doses of rotenone (>30nM) have off target effects by binding alternative proteins (Greenamyre et al. 1996, Harris et al. 2018). Therefore, rotenone is toxic to neurons outside of its role as a complex I inhibitor (Choi et al. 2008, Cabeza-Arvelaiz and Schiestl 2012). For instance, rotenone can cause mitochondrial dysfunction indirectly through the production of ROS via activation of microglia (Shaikh and Nicholson 2009) and may also reduce mitochondrial membrane potential by blockading voltage dependent anion channels on the outer mitochondrial membrane (Cabeza-Arvelaiz and Schiestl 2012). Rotenone also induces chromatin mediated gene regulation which can vary the expression of genes involved in neural activity and ultimately lead to changes in behavior (Kanthasamy et al. 2012).

Mitochondrial damage by rotenone provides feedback to the nucleus via two primary routes. The first involves the activation of transcription factors which initiate the transcription of genes involved in compensatory mechanisms (Wang et al. 2018). The transcriptomic response to rotenone has been well characterized and transcription factors including ATF4, NEF2L2, and p53 are activated to regulate cell proliferation, the oxidative stress response, and intrinsic apoptosis (Smirnova et al. 2016, Harris et al. 2018, Cabeza-Arvelaiz and Shiestl 2012, Huang and Lou et al. 2019). The second route for mitochondrial feedback to the nucleus is through metabolic flux. One example is the metabolite Acetyl-CoA which is used in the Krebs cycle to generate energy-rich ATP. Acetyl-CoA is also the

substrate for histone acetyltransferase enzymes which acetylate lysine-rich histone tails to regulate the transcription of genes (Mews et al. 2017). Acetyl CoA is variable and optimal acetyl-CoA concentrations are required to maintain the expression of functional genes in neurons.

As discussed in *Chapter 1.2*, DNA methylation and histone acetylation are epigenetic modifications implicated in both genetic and sporadic Parkinson's disease as well as in rotenone induced neurotoxicity. DNA hypomethylation has been reported in response to pesticide exposure (Hou et al. 2012) but no information exists on the effect of rotenone on global DNA methylation and chromosome stability. More information is known about histone acetylation patterns which are tightly coupled to gene expression and enhancer activation (Wang et al. 2008). Most studies agree that rotenone induced neurodegeneration is associated with pathological hyperacetylation as a result of impaired homeostatic activity of HATs and HDACs. (Song et al. 2010, Feng et al. 2015, Harrison et al. 2018, Huang and Lou et al. 2019, Park et al. 2016). This part of chapter 2 examines the effect of rotenone on cellular viability, metabolic capacity, and intracellular ROS after 24h exposure in human cell line *HEK293*. It explores the enrichment of gene ontologies and pathways involved in rotenone exposure and it analyzes the effects of rotenone treatment on global levels of DNA 5-methylcytosine (5mC) and histone lysine 27 acetylation (H3K27ac). While it has been shown that rotenone induced neurotoxicity is associated with changes in the epigenome, there is little information on what regions of the genome are susceptible to rotenone exposure and the effect of differential expression of these regions on pathogenesis. Part B of this chapter will cover the effects of rotenone induced epigenetic changes at CTCF insulating motifs within cis-regulatory regions of PD associated genes.

2A.3 Materials and Methods

2A.3.1 Cell culture and treatment of human cell line HEK293

All media reagents and chemicals in cell culture were purchased from Sigma (St. Louis, MO). Human cell line HEK293 was grown in Dulbecco's Modified Eagle Medium with high glucose, L-glutamine, and sodium pyruvate. Media was supplemented with 10% (v/v) heat inactivated fetal bovine serum and 1% (v/v) Penicillin-Streptomycin. HEK293 cells were confirmed by ATCC. Cells were treated at approximately 70% confluency with rotenone or DMSO vehicle control (<0.001%) for 24 hours. Cell viability was measured with trypan blue (0.4%) staining and cells were counted manually with a hematocytometer. Mitochondrial viability was estimated with the Presto Blue viability reagent (ThermoFisher, Waltham, MA). The reagent was added at 10% (v/v) and incubated for 1h at 37°C before measuring fluorescence (excitation 530 nm/ emission 590 nm). Intracellular reactive oxygen species (ROS) were measured with the DCFDA intracellular ROS assay according to kit instructions (Abcam, Cambridge, UK). Statistical hypothesis testing was done with a one-way ANOVA and post-hoc pairwise t-test calculation with p-value correction using the false discovery rate (FDR) adjustment method.

2A.3.2 RNA extraction and RNA sequencing library construction

Total RNA was extracted from two replicates of DMSO or rotenone treated HEK293 using the trizol method (Invitrogen, Carlsbad, CA). A total of 2ug per sample was used for library construction using the TruSeq Sample Preparation kit from Ilumina (San Diego, CA). Poly-A containing mRNA molecules were isolated from total RNA using oligo-dT attached magnetic beads. Isolated mRNA was then fragmented and synthesized into double stranded cDNA according to kit instructions. Ligation of unique Ilumina adapter indices was completed for each sample before bead purification. Libraries were loaded onto a 2% agarose gel and library products between 200-800 bp were purified using the

mini-Elute gel extraction kit from Qiagen (Hilden, Germany). Approximately 150 ng was sent for sequencing on a HiSeq 2000 platform with 100 bp paired-end reads.

2A.3.3 RNA sequencing data analysis

Adapter sequences were removed from the raw sequencing data and individual libraries were converted to the fastq format. Sequencing reads were aligned to the human genome (hg19) with TopHat2 (v2.0.9) (Kim et al. 2013). For mRNA analyses, the RefSeq database (Build 37.3) was chosen as the annotation references. Read counts of annotated genes were obtained by the Python software HTSeq-count (Anders et al. 2015). The read counts of each transcript were normalized to the length of the individual transcript and to the total mapped fragment counts in each sample and expressed as fragments per kilobase of exon per million fragments mapped (FPKM) of mRNAs in each sample. Differentially expressed genes were defined as those with a 1.5 fold change in expression using a FDR<0.05 from the edgeR package (Robinson et al. 2010). Gene Ontology annotation was done with Gorilla online platform and visualized with Revigo and Cytoscape (Eden et al. 2009; Supek et al. 2011; Otasek et al. 2019). Biological pathway enrichment was done with reactome (Fabregat et al. 2018). The top 5 pathways were reported though their enrichment was not significant after p-value correction with the false discovery rate method. Lastly, we used the Ingenuity Pathway Analysis tool (Qiagen, Hilden, Germany) for further pathway and functional annotation.

(https://www.qiagenbioinformatics.com/products/ingenuitypathway-analysis)

2A.3.4 Global DNA methylation analysis

Genomic DNA was extracted from two replicates of DMSO or rotenone treated HEK293 using Phenol: Chloroform: Isoamyl alcohol (1:1 ratio) (Sigma, St. Louis, MO). Global DNA methylation was first measured by dot blot analysis. Bisulfite treated DNA (30-60 ng/uL) was denatured at 95°C for 5 minutes and then cooled at 4°C for 5 minutes in a conventional thermocycler (Mycycler; Bio-Rad; Herclues, CA). DNA was spotted onto

0.45 micron nitrocellulose paper as 1 or 2 µL drops and dried for 30 minutes at room temperature. The membrane was UV crosslinked at 3000 Hz and incubated in anti-5mC primary antibody overnight at 4°C (Epigenetek 33D3; Farmingdale, NY). The membrane was washed with TBST and incubated with secondary antibody conjugated to HRP for 1 hour at room temperature (Santa-Cruz Biotechnology anti-mouse IgG sc-2005; Dallas, TX). The membrane was washed again with TBST after secondary incubation and visualized with chemiluminescence (ProSignal Femto; Promethus; Raleigh, NC).

2A.3.5 Western Blot for global H3K27ac

HEK293 cells were collected after 24 hours treatment and histones were extracted using the Abcam Histone Extraction kit according to kit instructions (Cambridge, UK). Histone protein concentration was measured by Qubit Protein Assay from ThermoFisher (Waltham, MA). Protein (5 ug) was loaded onto 4-15% Bio-Rad Page Gels and transferred to 0.45 um nitrocellulose (Bio-Rad, Hercules, CA). The blots were incubated with H3K27ac primary antibody (1:1000; Abcam ab4729) overnight at 4°C and anti-rabbit IgG conjugated secondary antibody (1:5000, Santa Cruz Biotechnology Sc-2357) for 1h at room temperature. The histone protein was normalized to total histone 3 (H3; Abcam ab1791) and quantified with Image J software. We tested significance by comparing the ratio of H3K27ac/H3 with a two-tailed Student's paired t-test.

2A.4 Results

2A.4.1 Rotenone exposure in human cells

We tested three doses of rotenone (100-300 nM) for 24h and measured cell viability with two independent assays. The trypan blue exclusion assay measures plasma membrane integrity and there was no change in the penetrance of trypan blue between control and treatments (Figure 2.1). The Presto Blue viability assay measures cellular capacity to reduce resazurin to resorufin. This measurement was used as a proxy for mitochondrial status and we observed a decrease in reductive capacity in all treatment

groups compared to the control but only 200-300 nM was significant compared to the vehicle DMSO control (Figure 2.1). Finally, we measured the production of intracellular reactive oxygen species, a hallmark of complex I inhibition and a common cellular phenotype in neuronal cell death. Rotenone treatment significantly increased intracellular oxygen species only in the rotenone 200 nM group after 24h treatment (Figure 2.1). We used rotenone 200 nM for 24h for the rest of experiments based on these molecular responses.

2A.4.2 Rotenone changes in gene expression

We used RNA-seq analyses to identify over 2000 differentially expressed genes (DEGs) in response to rotenone (Figure 2.2). To gain insights of impacted biological processes, we performed gene ontology enrichment analysis on 1853 of these DEGs with known HUGO (hgnc) symbol and cell description using a p-value threshold of $p<10^{-3}$ (Supplemental File 1). Among enriched biological processes, we observed a significant induction of the oxidative stress response, transcription factor activity, and chromatin organization ($<10^{-3}$) (Figure 2.3). We observed a significant enrichment of genes involved in nucleic acid binding ($<10^{-7}$) and DNA binding ($<10^{-5}$) with the nuclear cell component being most represented ($<10^{-5}$) (Figure 2.3). We analyzed pathway enrichment of the top 200 genes with the largest change in expression using reactome pathways (Fabregat et al. 2018) (Table 2.1). Three of the top 5 pathways enriched in our data were major transcription factor pathways including SMAD, NOTCH, and TP53 which have implications in Parkinson's disease reviewed in the discussion section. The Ingenuity Pathway analysis revealed the unfolded protein response and histone deacetylase Sirtuin signaling were additional canonical pathways affected by rotenone exposure (Table 2.2).

2A.4.2 Rotenone changes in global epigenetic patterns

We used dot blot method to qualitatively assess changes in DNA methylation levels in cells exposed to rotenone. The total 5mC level was detected with anti-5mC

antibody and visualized using chemiluminescence. After 24h, 5mC levels were strikingly reduced in genomic DNA (Figure 2.4). Next, we asked the extent to which rotenone exposure impacted histone acetylation. To investigate histone acetylation at active enhancers with PD-relevant SNPs, we selected H3K27ac mark (Wang et al. 2008) and examined H3K27ac levels from extracted histones using Western blot. We measured a significant 1.3-fold increase in H3K27ac in rotenone-treated cells compared to the DMSO vehicle control ($p<0.05$) (Figure 2.4).

2A.5 Discussion

We selected rotenone based on its ability to model gene-environment interactions in rodents and non-mammalian models of PD (Cannon and Greenamyre 2013; Johnson and Bobrovskaya 2015). We observed reduced mitochondrial viability and increased ROS after rotenone (200 nM) treatment for 24h. Our lowest dose of rotenone (100nM) for 24 hours reduced mitochondrial viability but did not change levels of ROS (Figure 2.1). Interestingly, we observed the same trend for our highest dose of rotenone (Figure 2.1). We surmise that increased ROS was not observed in the highest dose because of the rapid reduction of oxidative metabolites from the induction and recruitment of antioxidant enzymes following a large dose.

Intriguingly, rotenone has been shown to cause neurodegeneration by mechanisms unrelated to its effect on complex I (Sherer et al. 2007; Choi et al. 2008). The transcriptome and its regulation have become a focus for understanding these mechanisms outside of the electron transport chain (Cabeza-Arvelaiz and Shiestl 2012). We observed large scale changes in gene expression profiles and many of these genes were enriched in processes involved in gene regulation and chromatin organization (Figure 2.3). The pathway analysis of differentially expressed genes also revealed a large involvement in major intracellular transcription factor pathways (Table 2.1). For instance, SMAD proteins are critical for transducing signals from the transforming growth factor

(TGFβ) receptors at the plasma membrane which are essential for midbrain dopaminergic survival (Hegarty et al. 2014). Notch signaling is known have an important role in regulating genes involved in nervous system development and synaptic plasticity (Ables et al. 2011). Lastly, the TP53 pathway is perhaps the most well-known of the toxicant induced signaling mechanisms to control cell cycle progression and cellular survival. It is thus a critical regulator of programmed cell death in Parkinson's disease and rotenone induced neurotoxicity (Venderova and Park 2012).

Several studies have investigated transcriptomic changes in mammalian cells following rotenone treatment and reported changes in DNA damage repair and cell cycle progression (Cabeza-Arvelaiz and Shiestl 2012, Smirnova et al. 2016, Harris et al. 2018, Huang and Lou et al. 2019). One study focused on rotenone induced changes in the expression of genes involved in microtubule dynamics (Cabeza-Arvelaiz and Shiestl 2012). Microtubules play a critical role in several neuronal processes including myelination, axonal transport, and neurite outgrowth. Rotenone has been shown to impair neurite outgrowth in dopaminergic neurons (Harris et al. 2018). Furthermore, rotenone inhibited axonal transport in an α-Synuclein (α-Syn) mutant induced pluripotent stem cell (iPSC) model of Parkinson's disease by indirectly nitrating microtubules through increased nitrosative stress (Stykel et al. 2018). Our data show increases in the gene (*TPPP*) encoding tubulin-polymerizing promoting protein which under homeostatic conditions promotes myelination and the insulation of axons (Olah and Ovadi et al. 2019). However, unregulated *TPPP* can stimulate protein-protein interactions and has been associated with α-Synuclein formation of Lewy body inclusions.

Protein aggregation resulting from the accumulation of disordered proteins initiates the endoplasmic reticulum mediated unfolded protein response. Our Ingenuity Pathway (IPA) analysis identified this response as our top canonical pathway (Table 2.2). We

observed a significant increase in its transcription factor ATF3 and its target genes. The cyclic AMP response element-binding (CREB) family transcription factors ATF3 and ATF4 can be activated by both endoplasmic reticulum and mitochondrial stress. Their role in the stress response to rotenone and other mitochondrial complex I inhibitors has been well established (Krug et al. 2014, Smirnova et al. 2016, Harris et al. 2018). However, the role of CREB transcription factors and their recruitment of the p300/CBP histone acetyltransferase complex has yet to be fully explored in rotenone induced models of PD. Interestingly, our second top canonical pathway identified by IPA was the Sirtuin signaling pathway (Table 2.2). Sirtuins act as mitochondrial sensors and respond to mitochondrial stress by deacetylating lysine residues on DNA histone tails. This data supports an important role of the ATF stress response in maintaining the balance in histone acetyltransferase and deacetylase activity in neurons.

Lastly, we compared our gene expression data to data generated in a complementary model of mitochondrial dysfunction. The rat dopaminergic neural cell line N27 was used to generate a knockout of the mitochondrial transcription factor A protein (TFAM) (Huang et al. 2019). *TFAM* regulates mitochondrial biogenesis and has been shown to closely mimic rotenone effects on chromatin *in-vitro*. In the N27 rotenone and the N27 *TFAM* knockout model, the NF-kβ inflammatory pathway was significantly down-regulated (Huang et al. 2019). We also observed a significant decrease (-0.8 LFC, FDR<0.05) in the NF-kβ encoding gene (*NFKB1*) as well as a significant increase (0.7 LFC, FDR<0.05) in its inhibitor protein (*NFKBIB*). NF-kβ has an interesting role in mediating the crosstalk between histone lysine acetylation and methylation which determines the expression of inflammatory genes (Karin et al. 2002). The effect of NF-kβ inhibition in rotenone treated cells on global histone patterns may also play a role in the accessibility of transcription factor binding sites in non-inflammatory pathways.

To determine if the gene expression changes discussed above were due to changes in global levels of epigenetic patterns, we performed a dot blot and Western blot to examine global levels of 5mC and H3K27ac (Figure 2.4). DNA methylation is the best studied epigenetic modification and small changes in methylation at regulatory regions of the genome can have substantial effects on genome integrity during aging. As seen with other pesticide models, we observed a global decrease in DNA methylation in response to rotenone. We also chose to look at global H3K27ac levels because it is tightly correlated with gene expression and vulnerable to environmentally driven enhancer activation (Wang et al. 2008). We observed a significant increase in H3K27ac across the genome. H3K27ac is not only an important mark to distinguish poised from active enhancers in bivalent chromatin, but it is also a critical epigenetic modulator in post-mitotic cells including dopaminergic neurons (Maze et al. 2015).

In summary, rotenone is a complex I inhibitor that impairs the mitochondrial electron transport chain resulting in increases in oxidative stress. However, the effect of rotenone on mitochondria, oxidative species, and cellular viability is not limited to its affinity to complex I. We hypothesize that rotenone induced mitochondrial dysfunction causes large-scale changes to gene expression profiles. These changes in expression are mediated by the opening of chromatin structure through reduced DNA methylation and increased activation of enhancers via H3K27ac. The perturbance of global chromatin structure causes a loss of genomic integrity and results in the orchestration of multiple adverse cellular events until cumulative damage signals for intrinsic apoptosis.

2A.6 References

1. Ables JL, Breunig JJ, Eisch AJ, Rakic P. 2011. Not(ch) just development: Notch signaling in the adult brain. Nature Reviews Neuroscience 12(5):269.
2. Cabeza-Arvelaiz Y, Schiestl RH. 2012. Transcriptome analysis of a rotenone model of parkinsonism reveals complex I-tied and-untied toxicity mechanisms common to neurodegenerative diseases. PloS one 7(9):e44700.
3. Cannon JR, Greenamyre JT. 2013. Gene–environment interactions in Parkinson's disease: Specific evidence in humans and mammalian models. Neurobiol Dis 57:38-46.
4. Cannon JR, Tapias V, Na HM, Honick AS, Drolet RE, Greenamyre JT. 2009. A highly reproducible rotenone model of Parkinson's disease. Neurobiol Dis 34(2):279-290.
5. Choi WS, Kruse SE, Palmiter RD, Xia Z. 2008. Mitochondrial complex I inhibition is not required for dopaminergic neuron death induced by rotenone, MPP+, or paraquat. Proc Natl Acad Sci U S A 105(39):15136-15141; doi: 10.1073/pnas.0807581105.
6. Feng Y, Liu T, Dong S, Guo Y, Jankovic J, Xu H et al. 2015. Rotenone affects p53 transcriptional activity and apoptosis via targeting SIRT 1 and H3K9 acetylation in SH-SY 5Y cells. J Neurochem 134(4):668-676.
7. Greenamyre JT, Betarbet R, Sherer TB. 2003. The rotenone model of Parkinson's disease: Genes, environment and mitochondria. Parkinsonism Relat Disord 9:59-64.
8. Harris G, Eschment M, Orozco SP, McCaffery JM, Maclennan R, Severin D et al. 2018. Toxicity, recovery, and resilience in a 3D dopaminergic neuronal in vitro model exposed to rotenone. Arch Toxicol 92(8):2587-2606.
9. Harrison IF, Smith AD, Dexter DT. 2018. Pathological histone acetylation in Parkinson's disease: Neuroprotection and inhibition of microglial activation through SIRT 2 inhibition. Neurosci Lett 666:48-57.
10. Hegarty SV, Collins LM, Gavin AM, Roche SL, Wyatt SL, Sullivan AM et al. 2014. Canonical BMP–Smad signaling promotes neurite growth in rat midbrain dopaminergic neurons. Neuromolecular medicine 16(2):473-489.
11. Higgins DS,Jr, Greenamyre JT. 1996. Dihydrorotenone binding to NADH: Ubiquinone reductase (complex I) of the electron transport chain: An autoradiographic study. J Neurosci 16(12):3807-3816.
12. Hou L, Zhang X, Wang D, Baccarelli A. 2012. Environmental chemical exposures and human epigenetics. Int J Epidemiol 41(1):79-105.
13. Huang M, Lou D, Charli A, Kong D, Jin H, Anantharam V et al. 2019. Mitochondrial dysfunction induces epigenetic dysregulation by H3K27 hyperacetylation to perturb active enhancers in Parkinson's disease models. bioRxiv:808246.
14. Johnson ME, Bobrovskaya L. 2015. An update on the rotenone models of Parkinson's disease: Their ability to reproduce the features of clinical disease and model gene–environment interactions. Neurotoxicology 46:101-116.
15. Kanthasamy A, Jin H, Anantharam V, Sondarva G, Rangasamy V, Rana A et al. 2012. Emerging neurotoxic mechanisms in environmental factors-induced neurodegeneration. Neurotoxicology 33(4):833-837.
16. Karin M, Cao Y, Greten FR, Li Z. 2002. NF-κB in cancer: From innocent bystander to major culprit. Nature reviews cancer 2(4):301-310.
17. Krug AK, Gutbier S, Zhao L, Pöltl D, Kullmann C, Ivanova V et al. 2014. Transcriptional and metabolic adaptation of human neurons to the mitochondrial toxicant MPP. Cell death & disease 5(5):e1222-e1222.
18. Maze I, Wenderski W, Noh K, Bagot RC, Tzavaras N, Purushothaman I et al. 2015. Critical role of histone turnover in neuronal transcription and plasticity. Neuron 87(1):77-94.

19. Mews P, Donahue G, Drake AM, Luczak V, Abel T, Berger SL. 2017. Acetyl-CoA synthetase regulates histone acetylation and hippocampal memory. Nature 546(7658):381-386.
20. Oláh J, Ovádi J. 2019. Pharmacological targeting of α-synuclein and TPPP/p25 in Parkinson's disease: Challenges and opportunities in a nutshell. FEBS Lett 593(13):1641-1653.
21. Park G, Tan J, Garcia G, Kang Y, Salvesen G, Zhang Z. 2016. Regulation of histone acetylation by autophagy in parkinson disease. J Biol Chem 291(7):3531-3540; doi: 10.1074/jbc.M115.675488.
22. Shaikh SB, Nicholson LF. 2009. Effects of chronic low dose rotenone treatment on human microglial cells. Molecular neurodegeneration 4(1):55.
23. Sherer TB, Richardson JR, Testa CM, Seo BB, Panov AV, Yagi T et al. 2007. Mechanism of toxicity of pesticides acting at complex I: Relevance to environmental etiologies of Parkinson's disease. J Neurochem 100(6):1469-1479.
24. Smirnova L, Harris G, Delp J, Valadares M, Pamies D, Hogberg HT et al. 2016. A LUHMES 3D dopaminergic neuronal model for neurotoxicity testing allowing long-term exposure and cellular resilience analysis. Arch Toxicol 90(11):2725-2743.
25. Song C, Kanthasamy A, Anantharam V, Sun F, Kanthasamy AG. 2010. Environmental neurotoxic pesticide increases histone acetylation to promote apoptosis in dopaminergic neuronal cells: Relevance to epigenetic mechanisms of neurodegeneration. Mol Pharmacol 77(4):621-632; doi: 10.1124/mol.109.062174.
26. Stykel MG, Humphries K, Kirby MP, Czaniecki C, Wang T, Ryan T et al. 2018. Nitration of microtubules blocks axonal mitochondrial transport in a human pluripotent stem cell model of Parkinson's disease. The FASEB Journal 32(10):5350-5364.
27. Venderova K, Park DS. 2012. Programmed cell death in Parkinson's disease. Cold Spring Harb Perspect Med 2(8):10.1101/cshperspect.a009365; doi: 10.1101/cshperspect.a009365.
28. Wang H, Lou D, Wang Z. 2018. Crosstalk of genetic variants, allele-specific DNA methylation, and environmental factors for complex disease risk. Frontiers in genetics 9:695. doi:10.3389/fgene.2018.00695
29. Wang Z, Zang C, Rosenfeld JA, Schones DE, Barski A, Cuddapah S et al. 2008. Combinatorial patterns of histone acetylations and methylations in the human genome. Nat Genet 40(7):897.

2A.7 Tables

Table 2.1 Top pathway enrichment from Reactome pathways

Pathway name	Entities			
	found	ratio	p-value	FDR*
SMAD2/SMAD3:SMAD4 heterotrimer regulates transcription	5 / 39	0.003	7.12e-04	0.235
Pre-NOTCH Transcription and Translation	7 / 89	0.006	0.001	0.235
Interaction With Cumulus Cells And The Zona Pellucida	3 / 12	8.31e-04	0.001	0.235
TP53 Regulates Transcription of Genes Involved in Cytochrome C Release	4 / 33	0.002	0.003	0.316
Transcriptional activity of SMAD2/SMAD3:SMAD4 heterotrimer	5 / 55	0.004	0.003	0.316
Pre-NOTCH Expression and Processing	7 / 113	0.008	0.004	0.366

Table 2.2 Top canonical pathways from Ingenuity Pathways Analysis

Top Canonical Pathways

Name	p-value	Overlap
Unfolded protein response	2.19E-03	19.6 % 11/56
Sirtuin Signaling Pathway	2.80E-03	12.0 % 35/292
Mouse Embryonic Stem Cell Pluripotency	3.31E-03	15.5 % 16/103
Epoxysqualene Biosynthesis	5.37E-03	100.0 % 2/2
Notch Signaling	5.50E-03	21.1 % 8/38

2A.8 Figures

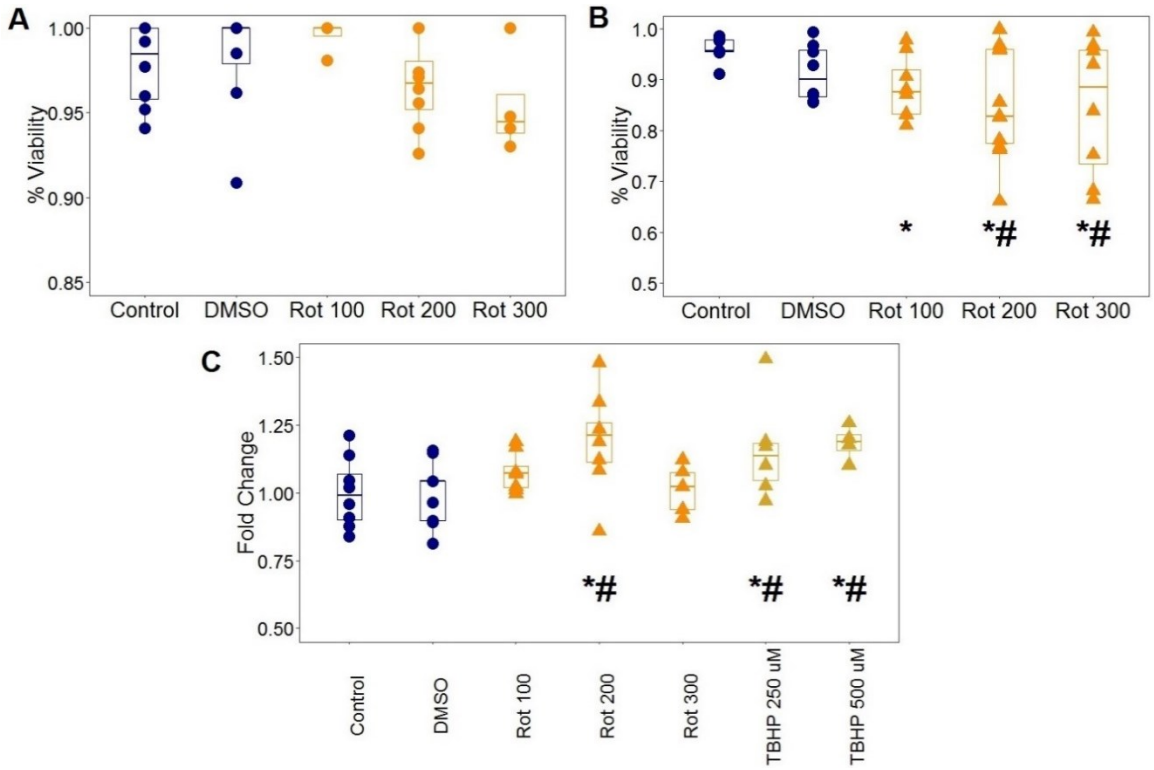

Figure 2.1 Cellular phenotype of *HEK293* cells treated with rotenone (100, 200, 300 nM) for 24h.

A) Cell viability measured with the trypan blue exclusion assay expressed as percent viability relative to the control. DMSO is the vehicle control. B) Metabolic viability measured by the reductive capacity of mitochondria and expressed as percent viability relative to the control. DMSO is the vehicle control. C) Intracellular ROS was measured with DCFDA fluorescence assay and expressed as the fold change in fluorescence relative to the control. DMSO is the vehicle control and TBHP (250/500 uM) is the positive control. Significance testing was done with ANOVA. *$p<0.05$ compared to non-treated control. #$p<0.05$ compared to vehicle control (DMSO).

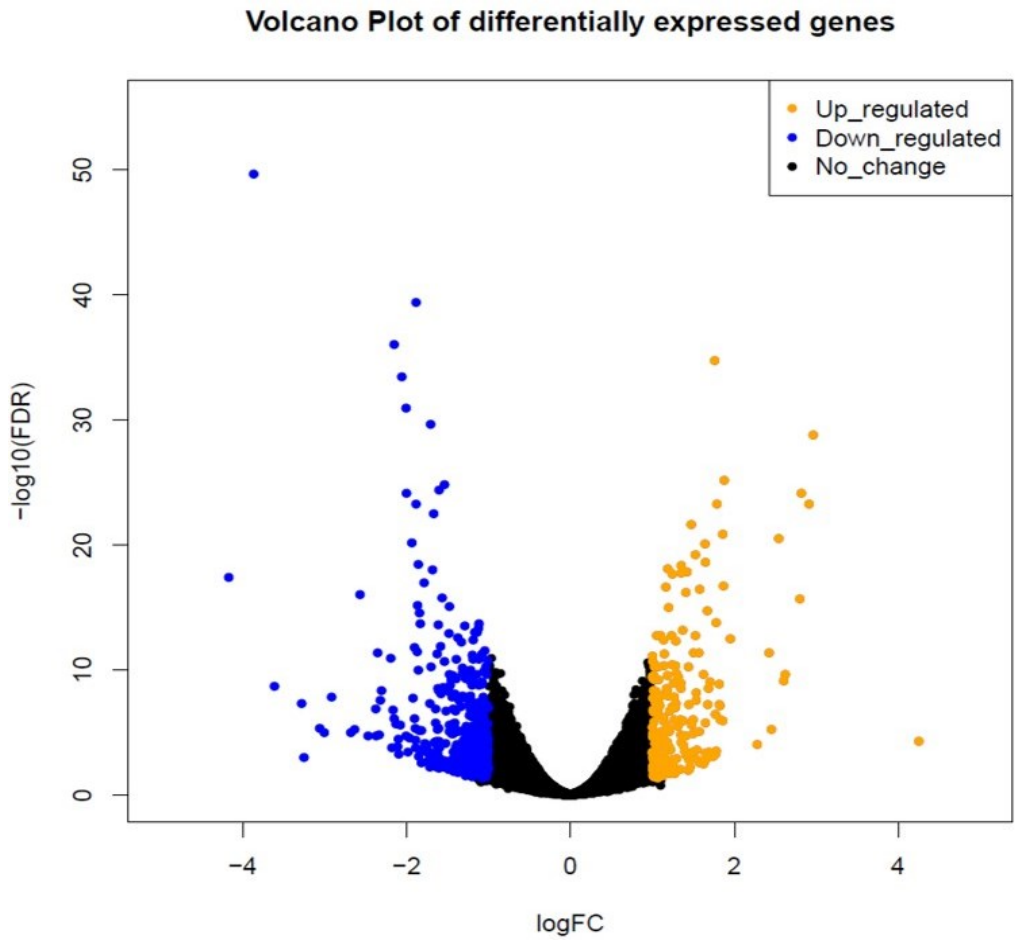

Figure 2.2 Volcano plot of differentially expressed genes in *HEK293* exposed to rotenone.
The volcano plot displays differentially expressed genes (>1.5 fold change; FDR<0.05) in *HEK293* cells exposed to rotenone (200nM, 24h). The x-axis represents the change in expression (log2 fold change) and the y-axis represents the significance of that fold change by p-value adjusted by the false discovery rate method. 1853 genes were differentially expressed and used for downstream analysis with 1039 genes down-regulated and 814 genes up-regulated.

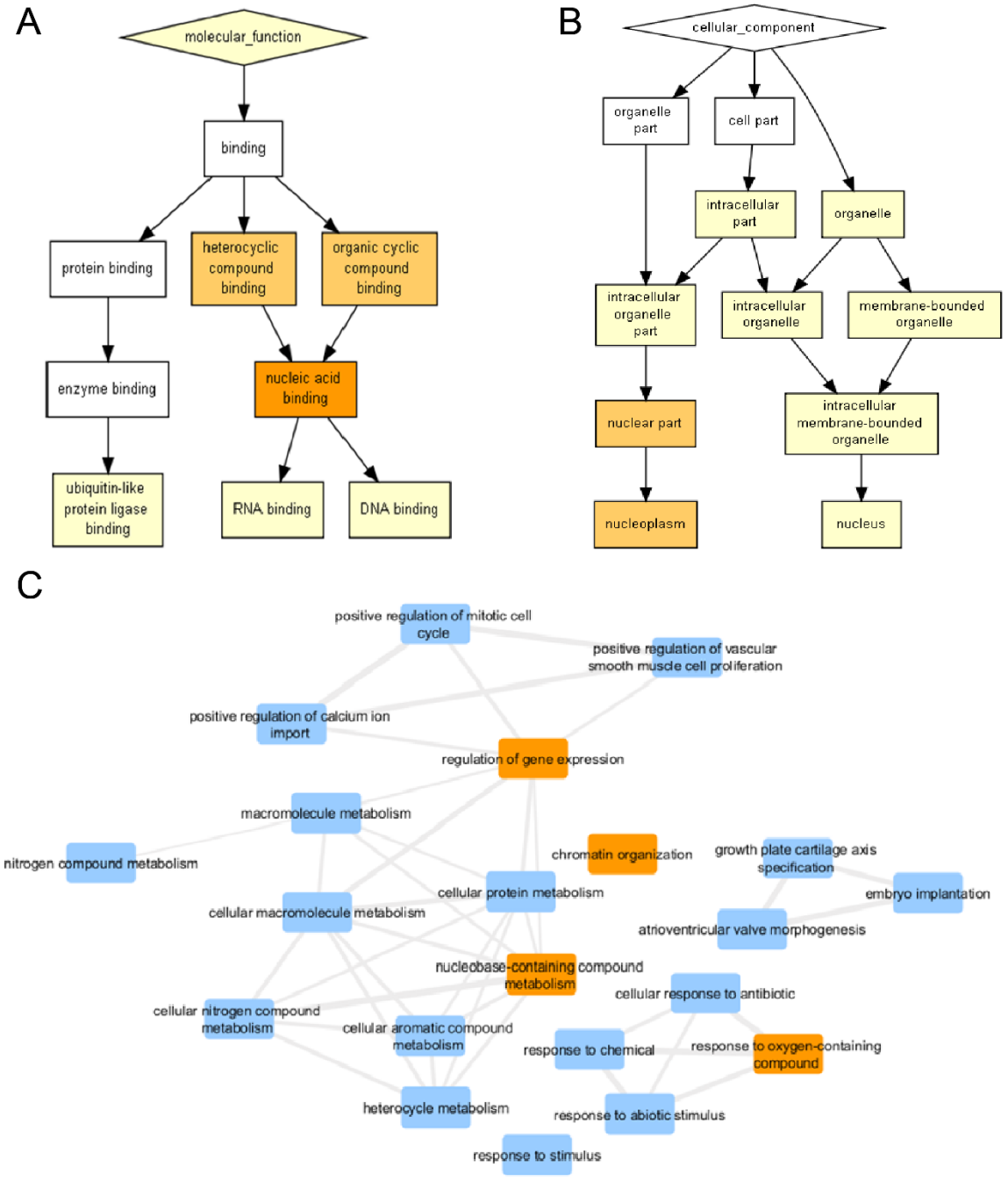

Figure 2.3 Gene Ontology enrichment analysis of RNA-sequencing data.
A) Gene Ontology molecular function enriched in our differentially expressed genes from rotenone treated *HEK293* cells. B) Gene Ontology cellular component enriched. Color gradient indicate enrichment p-value: white $<10^{-3}$; yellow 10^{-3}-10^{-5}; light orange 10^{-5}-10^{-7}). C) Network analysis of significantly enriched biological processes. Blue boxes enrichment p-value$<10^{-3}$ and orange boxes enrichment p-value$<10^{-5}$.

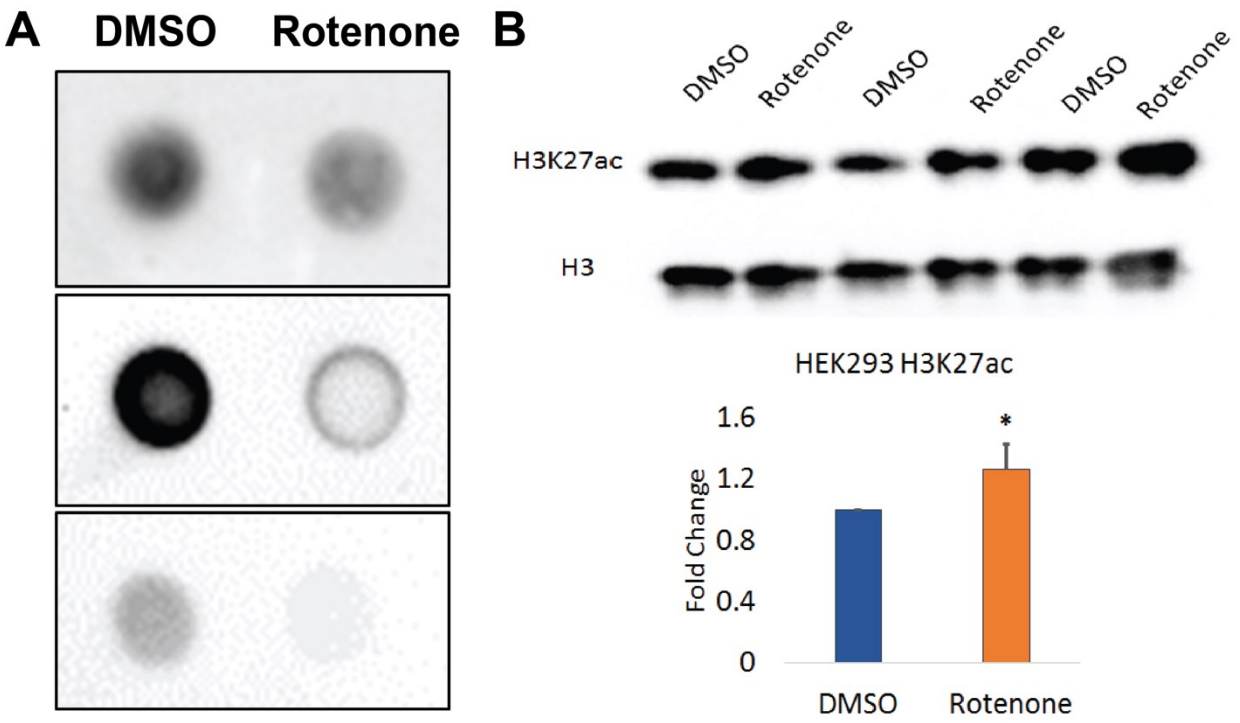

Figure 2.4 Global epigenetic patterns in rotenone treated *HEK293* cells.
A) Global DNA methylation was visualized by dot blot method using anti-5mC antibody. Three biological replicates are shown in this image. B) Global histone H3K27ac levels were measured from total extracted histones using Western blot. Total histone H3 was used as the loading control. Three biological replicates are shown in this image. This Western blot was quantified using Image J software and is shown as the fold change in the amount of H3K27ac relative to the vehicle (DMSO) control. * $p<0.05$ using a paired Student's t-test with the ratio of H3K27ac/H3.

CHAPTER 2[2]

PART B. Epigenetic vulnerability of insulator CTCF motifs at Parkinson's disease-associated genes in response to environmental rotenone.

2B.1 Abstract

CCCTC-binding factor (CTCF) is a regulatory protein that binds DNA to control spatial organization and transcription. The sequence-specific binding of CTCF is variable and is impacted by nearby epigenetic patterns. It has been demonstrated that non-coding genetic variants cluster with CTCF sites in topological associating domains and thus can affect CTCF activity on gene expression. Therefore, environmental factors that alter epigenetic patterns at CTCF binding sites may dictate the interaction of non-coding genetic variants with regulatory proteins. To test this mechanism, we treated human cell line HEK293 with rotenone for 24h and characterized its effect on global epigenetic patterns specifically at regulatory regions of Parkinson's disease (PD) risk loci. We used RNA sequencing to examine changes in global transcription and identified over 2,000 differentially expressed genes (DEGs, >1.5-fold change, FDR<0.05). Among these DEGs, 14 were identified as PD-associated genes according to GWAS meta-data. We focused on eight genes that have non-coding risk variants and a prominent CTCF binding site. We analyzed methylation of a total of 165 CGs surrounding CTCF binding sites and detected differential methylation (|>1%|, q<0.05) in 45 CGs at 7 PD-associated genes. Of these 45 CGs, 47% were hypomethylated and 53% were hypermethylated. Interestingly, 5 out of the 7 genes had correlated gene upregulation with CG hypermethylation at CTCF and gene downregulation with CG hypomethylation at CTCF. We also investigated active H3K27ac surrounding the same CTCF binding sites within these 7 genes. We observed a significant increase in H3K27ac in 4 genes (FDR<0.05). Three genes (PARK2, GPRIN3, FER) showed increased CTCF binding in response to rotenone. Our data indicate that rotenone

[2] This chapter has been submitted for publication in *Frontiers in Genetics*. D.M. Freeman and Z. Wang (2020).

alters regulatory regions of PD-associated genes through changes in epigenetic patterns and these changes impact high order chromatin organization to increase the influence of noncoding variants on genome integrity and cellular survival.

2B.2 Introduction

Parkinson's disease (PD) is the second most common neurodegenerative disorder in the United States (de Lau and Breteler 2006). More than 800 genetic association studies have been conducted to interpret genetic contribution to PD etiology (Coetzee et al. 2016; Lill et al 2012). Genome Wide Association Studies (GWAS) evaluate the association of common genetic variants to a phenotype or disease outcome. Since 2005, thousands of variants have been identified to have a significant association with a disease and more than 1,600 single nucleotide polymorphisms (SNPs) have been identified as genetic risk variants for PD (Lill et al. 2012). However, unlike rare monogenetic associations, the functional consequence of most of these variants have yet to be determined. Over 90% of all indexed SNPs including those associated with PD occur in non-coding regions of the genome (Maurano et al. 2012, Verstraeten et al. 2015). This discovery led to the hypothesis that SNPs in the human genome interact with regulatory elements to control gene expression (Wang et al. 2019). This is supported by expression of quantitative trait loci (eQTLs) defined as genetic regions that are enriched at positive GWAS sites and explain variability in the expressivity of a gene (Nica et al. 2010). Despite these advances, it remains a challenge to determine which genetic variants in a broad region of variants is the driver of gene expression changes particularly when regulatory element interactions are long range (Do et al. 2016). SNPs cluster within enhancers and can modify PD risk. These observations of PD-associated SNPs have been described in multiple cell types (Coetzee et al. 2016). With this new evidence, studies are now focusing on interactions of regulatory elements to understand how genetic associations trigger disease biology within the brain.

CTCF can play a long-range cis-regulatory role that insulates genes from their surrounding signaling environment by directing chromatin looping (Phillips and Corces 2009). Functional CTCF binding sites are required for the formation of distinct structural domains within three-dimensional chromosomal organization (Ong and Corces 2014; Tang et al. 2015). CTCF binding is dependent upon DNA sequence (CCGCGNGGNGGCAG) and allelic hypomethylation (Wang et al. 2012). Thus, genetic variants and epigenetic patterns within binding sites can contribute to dysfunctional CTCF allele-specific binding (Tang et al. 2015; Wang et al. 2019).

Approximately 85% of PD cases cannot be explained by genetic predisposition alone (Verstraeten et al. 2015; Labbé et al. 2016; Franco et al. 2010). Therefore, it is likely that most cases are caused by the interplay of common SNPs with environmental factors. Environmental factors can modulate the association of a genetic variant with a disease (Lee et al. 2011). For instance, exposures that impact allele-specific methylated regions in the genome can influence CTCF binding and thus influences non-coding variants effect on genetic expression (Wang et al. 2019) (Figure 2.5). GWAS association signals are complex in that they can cover a broad region of DNA with several polymorphisms, so we focused on environmentally induced epigenetic changes in CTCF binding regions nearby risk associated genes to explore mechanisms of gene-environment interactions in PD.

In our pesticide-induced cellular model, we used rotenone, a naturally occurring insecticide and potent inhibitor of complex I in the mitochondrial electron transport chain. Rotenone is a widely accepted PD toxicant and can robustly replicate pathology via depletion of ATP, generation of reactive oxygen species, damage of nigrostriatal tissues, and death of dopamine producing cells in the midbrain (Cicchetti et al. 2009; Dawson et al. 2002). It has also been shown to cause these types of cellular pathology in HEK293 (Orth et al. 2003; Teixeira et al. 2018). DNA methylation and histone acetylation are epigenetic modifications implicated in rotenone induced neurotoxicity (Huang et al. 2019).

DNA hypomethylation has been reported in response to pesticide exposure (Hou et al. 2012) and we discovered that rotenone reduces DNA methylation at DNMT1-dependent regions in the human genome (Freeman et al. 2020). Histone acetylation patterns have been more extensively studied in rotenone-induced PD due to its high correlation with gene expression and enhancer activation (Wang et al. 2008). Most studies agree that rotenone-induced neurodegeneration is associated with pathological hyperacetylation as a result of impaired homeostatic activity of HATs and HDACs (Feng et al. 2015, Harrison et al. 2018, Wang et al. 2018, Park et al. 2016, Huang and Lou 2019).

In this study, we examined rotenone-induced changes in DNA methylation and histone acetylation patterns at CTCF binding sites adjacent to PD-associated genes. Eight selected genes all had identified disease risk SNPs in a non-coding region and were indexed by a meta-data analysis of over seven million human polymorphisms (Lill et al. 2012). We hypothesize that rotenone exposure modifies epigenetic patterns at CTCF binding motifs and affects its allele-specific transcription factor binding. We postulate that this mechanism could mediate the interchange between genetic variants and regulatory elements controlling transcription and genomic stability.

2B.3 Materials and Methods

2B.3.1 Cell culture and treatment of human cell line HEK293

HEK293 cells were treated with rotenone (200 nM) for 24h according to the protocol in Chapter 2A.3.1.

2B.3.2 RNA sequencing library construction and analysis

The RNA sequencing data used for this subchapter was the same data reported in Chapter 2A.3.2-2A.3.3.

2B.3.3 RNA sequencing validation with quantitative reverse transcription-PCR

RNA was converted to cDNA with the PrimeScript RT reagent kit according to kit instructions outline in Chapter 2B.3.6. We selected ten genes for quantitative PCR (qRT-

PCR) analysis using primers listed in Table 2.3. The change in expression was normalized to the GAPDH housekeeping gene and expressed as fold change ($2^{-\Delta\Delta CT}$).

2B.3.4 Identification and selection of Parkinson's disease associated genes

We identified Parkinson's disease-associated genes using the National Health Genomic Research Institute GWAS Catalog (Buniello et al. 2019). We searched for all associations both reported and mapped using the trait "Parkinson's disease" (EFO_0002508) which included 39 publications investigating genomic signatures of both familial and environmentally driven Parkinson's disease as well as Lewy body pathology and Parkinsonism in frontotemporal lobe dementia. We calculated the frequency for various region types (non-coding, regulatory, coding) within the 246 known genetic variants provided by GWAS Catalog (Figure 2.5). We compared 399 reported and mapped genes to our list of differentially expressed genes. We then cross referenced these genes with the PD gene online resource which analyzed over 800 publications and seven million polymorphisms (Lill et al. 2012). We selected 5 genes that remained significant in the PD gene meta-analysis, were represented in at least 2 studies, and had their most significant variant in a non-coding region (Table 2.4). We also selected three additional genes from the PD gene database that were represented in our RNA sequencing data (Table 2.4). The first, *UBOX5*, was among the most significant polymorphisms identified by the meta-analysis (Lill et al. 2012; Nalls et al. 2014). The other two, *PARK2* and *CHCHD2*, have significant polymorphisms according to the PD gene database but are also reported to have autosomal mutations that contribute to familial disease cases (Lill, C. 2016).

2B.3.5 Region selection for bisulfite and ChIP primer design

CTCF transcription factor binding was observed using the Uniform Transcription Factor Binding data found in the ENCODE Regulation super track in UCSC Genome Browser. We selected all CTCF transcription factor binding sites detected with ChIP-Seq experiments from the ENCODE consortium from 2007-2012 (ENCODE 2012). We also

predicted which cytosine would overlap the binding motif using the CTCF binding prediction tool database v2.0 (Ziebarth and Bhattacharya 2013). Primer design was focused on CTCF binding sites for both Bisulfite sequencing and ChIP-PCR experiments (further described below).

2B.3.6 Bisulfite-DNA conversion and Bisulfite-amplicon sequencing library construction

Genomic DNA was extracted from two replicates of DMSO or rotenone treated HEK293 using Phenol: Chloroform: Isoamyl alcohol (Sigma, St. Louis, MO). A total of 200 ng DNA was Bisulfite-converted using the Sigma DNA Imprint Modification kit two-step protocol. Bisulfite-converted DNA (BS-DNA) was amplified with primers for selected regions designed with MethPrimer (Li and Dahiya 2002) (Table 2.5). Amplified BS-DNA products were run on a 2% EtBr agarose gel and purified using the mini-Elute gel extraction kit from Qiagen (Hilden, Germany). Purified products for each sample were pooled together and 1 ng was used for library preparation using the Ilumina Nextera DNA Library Preparation kit. Each sample was tagged with a unique Nextera XT adapter (San Diego, CA). Sequencing libraries were quality checked via Bioanalyzer and run on an Ilumina MiSeq platform to generate 150 bp paired end reads.

2B.3.7 Bisulfite-amplicon sequencing analysis

The raw fastq files were imported into the Galaxy web platform (Afgan 2016). Reads with quality score >30 were trimmed with Trim Galore (Krueger 2015). Reads were mapped to amplified sequences in the human genome (hg19) using bwa-meth (Pederson et al. 2014). MethylDackel was used for methylation calling and per-cytosine contexts were merged into per-CPG metrics (https://github.com/dpryan79/MethylDackel). Duplicates and singletons identified in alignment were ignored from the methylation call. Minimum and maximum per-base depths were 1000x and 100,000x, respectively. The output was selected for methylKit format. Coverage statistics and differentially methylated regions were calculated for CpG sites with methylKit installed in R (v3.5) (Akalin et al.

2012). Differentially methylated cytosines were defined as being present in both biological replicates, having a minimum absolute difference of 1% using the coverage weighted mean, and having a SLIM adjusted q-value<0.01 using the methylKit logistic regression model (Ning et al. 2011). The change in mean percent methylation (Δme) for all CpG sites within a defined region was calculated by taking the mean number of methylated versus non-methylated CpG sites from the pooled control and treated samples and using Fisher's exact test FDR <0.05.

2B.3.8 HEK293 Chromatin Immunoprecipitation

All chemicals were purchased from Sigma unless otherwise noted (St. Louis, MO). *HEK293* were harvested after 24 hours treatment and resuspended in fresh media at $10x10^6$ cells/ mL in a conical tube. Cells were fixed with 1% formaldehyde for 10 minutes at room temperature. Reaction was stopped with 0.2 M glycine and incubation at room temperature for 5 minutes. Fixed cells were centrifuged for 5 minutes at 300xg 4°C and washed with 1 mL cold PBS. Fixed cell pellet was stored at -80°C until chromatin immunoprecipitation (ChIP).

Cell pellets were resuspended at approximately $1x10^6$ cells/ 0.1 mL with PBS + 0.5 % Triton-X + 1% protease inhibitor cocktail and incubated on ice for 10 minutes prior to centrifugation for 5 minutes at 400xg 4°C. The pellet was resuspended in TE buffer pH 8.0 with protease inhibitor and PMSF. Cells were sonicated at high intensity for 30s on/ 60s off until DNA fragments were within 200-800 bp as checked by 2% agarose gel. After sonication, samples were centrifuged for 15 minutes at 14,000xg 4°C to pellet insoluble material. Sheared chromatin was transferred to RIPA buffer and approximately 10% was saved for input DNA extraction.

ChIP was done with Dynabeads Protein A (Invitrogen, Carlsbad, CA) and 4 ug of primary ChIP grade antibody (H3K27ac Abcam ab4729; CTCF Millipore 07-729; Rabbit IgG Santa Cruz Biotechnology sc-2025). Beads were washed with lithium chloride (LiCl

0.25M) buffer and immunoprecipitated DNA was extracted from beads using phenol: chloroform method. DNA was quantified using Qubit dsDNA high sensitivity assay (Thermo Fisher, Waltham, MA).

2B.3.9 HEK293 ChIP PCR analysis

We selected eight genes for quantitative real-time PCR (qRT-PCR) analysis using primers listed in Table 2.6. Primers were designed with NCBI Primer Blast at H3K27ac peaks surrounding the predicted CTCF binding site (Ye et al. 2012). All qRT-PCR reactions were performed on a 7500 Real-Time PCR system from Applied Biosystems (Foster City, CA) using the iTaq Universal SYBR Green Supermix from Bio-Rad (Hercules, CA). H3K27ac and CTCF enrichment was calculated from the Ct threshold value as a percent of the total input DNA. Rabbit IgG samples were used as a negative control.

2B.4 Results

2B.4.1 Alteration of PD-associated genes stands out upon rotenone exposure

The GWAS Catalog is a public database of approximately 72,000 variant-trait associations from over 3500 publications (Buniello et al. 2019). Out of 246 PD-associated variants with genetic sequence context information, 220 variants (89%) were in noncoding regions (intron, intergenic, regulatory, and exon) (Figure 2.5) Intronic variants constituted most of the known polymorphisms. We searched our DEGs for PD-associated genes and identified 14 genes from the GWAS Catalog (Appendix Table 1). Of these genes, 13 were also considered significant PD-associated genes according to meta-analysis data in PDgene (Lill et al. 2012). We validated the RNA sequencing results for 10 of these genes and were able to validate 8 of them with qPCR analysis (R^2=0.96) (Figure 2.6). We selected five genes (*ITGA8*, *GPRIN3*, *FER*, *CNKSR3*, *BMP4*) and three additional genes from the PD gene meta-analysis (*UBOX5*, *PARK2*, *CHCHD2*) for further analysis (Table 2.4).

2B.4.2 Selected genes contain prominent CTCF binding sites in their regulatory non-coding regions

To examine any potential CTCF motifs within these selected genes, we visualized CTCF binding using experimental data from ENCODE and the CTCF binding prediction tool from the Cui Lab at the University of Tennessee (ENCODE 2012; Ziebarth and Bhattacharya 2013). Intriguingly, all selected genes had at least one prominent CTCF binding site in their regulatory non-coding region. We designed both bisulfite primers and ChIP primers at these sites using ENCODE regulation data from the Broad Institute (ENCODE 2012). The polymorphisms in these regions that were recognized by the SNP database (dbSNP; http://www.ncbi.nlm.nih.gov/SNP) were also analyzed with Regulomedb, a database that annotates SNPs with known or predicted interactions with regulatory elements in intergenic regions (Boyle et al. 2012). We determined SNPs within selected regions at 2 genes, *GPRIN3* and *FER*, were present at CTCF binding sites and were active in the brain (Table 2.7). The rank of a single nucleotide polymorphism represents the number of available datasets for that polymorphism and the score is generated based on the integrated results from available datasets. In this analysis, the polymorphism listed at each gene were present in datasets from experimental transcription factor binding, matched transcription factor position-weight matrix (PWM), and DNase footprinting. We checked the *HEK293* genome using the online database (http://hek293genome.org/v2/) and did not find either variant in our cells (Lin et al. 2014). This information provides additional evidence that CTCF binding sites among common non-coding variants may be critical in disease pathogenesis.

2B.4.3 Rotenone alters DNA methylation patterns at CTCF binding sites in regulatory regions of PD-associated genes.

Because CTCF binding is methylation sensitive and changes of CG methylation correlate to disease risks (Wang et al. 2018), we next examined a total of 284 CG

nucleotides from 8 regions surrounding our selected genes. Our amplicon-sequencing results demonstrated that 233 of these nucleotides met our minimum requirement of 1000x coverage (Figure 2.7). From all CGs with >1000x coverage, 68 were differentially methylated across 7 of 8 genes (> l1%l, q<0.01). We focused our analysis on 165 CG sites that met minimum coverage requirements and overlapped predicted CTCF binding motifs at 7 of the selected genes. There were 45 differentially methylated CG sites and 53% were hypermethylated (Table 2.8). Two of these CG sites, *FER* cg143 at chr5:102025097 and CHCHD2 cg217 at chr7:56174103, were significantly hypomethylated (*FER cg143*Δ=-4.4) and hypermethylated (*CHCHD2 cg217*Δ=1.7) at the predicted CTCF binding sequence (Figure 2.8). Two genes, *PARK2* and *UBOX5*, were significantly hypomethylated (*PARK2* Δ=-1.3) and hypermethylated (*UBOX5*Δ= 0.33) across the entire CTCF binding region with p<0.05 but did not remain significant after multiple hypothesis testing (FDR>0.05) (Figure 2.8). Collectively, we conclude that methylation of CTCF binding motifs was vulnerable to rotenone exposure.

2B.4.4 Rotenone alters histone acetylation patterns at CTCF binding sites in regulatory regions of Parkinson's disease associated genes.

Histone acetylation especially H3K27 acetylation is associated with regions of active chromatin and is critical in maintaining chromatin organization. We observed an increase in total H3K27ac levels in rotenone treated cells (1.3-fold change, p=0.02) (Chapter 2A Figure 2.4). We used ChIP-PCR to test whether local H3K27ac enrichment overlapped CTCF binding sites in PD associated genes. Four genes (*GPRIN3*, *UBOX5*, *FER*, *BMP4*) had significantly increased H3K27ac at CTCF binding motifs with FDR<0.05. One gene, *CNKSR3*, had reduced H3K27ac at its CTCF binding motif but was not statistically significant (p=0.07; FDR=1) (Figure 2.9). Interestingly, the H3K27 region amplified in qPCR overlapped at least one differentially methylated cytosine for all four significantly enhanced genes (Table 2.9). Only one of the genes without H3K27ac enrichment, *CHCHD2*, also had differentially methylated cytosines within the amplified region. These genes had both increased and decreased changes in percent methylation.

2C.4.5 Rotenone increases CTCF binding at three PD-associated genes.

To determine whether altered DNA methylation and H3K27ac patterns would affect CTCF binding, we measured CTCF enrichment at its binding motif at 7 PD associated genetic loci. CTCF binding was increased at 3 genes (*PARK2, GPRIN3*, *BMP4*) (Figure 2.10). *BMP4* had one hypomethylated CG and increased H3K27ac within our selected region. There was an increase in CTCF binding and mRNA expression. *PARK2* had two hypomethylated CGs but no increase in H3K27ac in its CTCF binding domain. In this region, CTCF binding increased and mRNA expression decreased. *GPRIN3*, unlike the other two genes, had more hypermethylated CGs within its CTCF binding motif but the closest CG to its consensus sequence was also hypomethylated. There was increased H3K27ac enrichment at *GPRIN3* and increased CTCF binding. *GPRIN3* mRNA was significantly up-regulated in response to rotenone.

2B.5 Discussion

Rotenone has been shown to cause neurodegeneration by mechanisms unrelated to its effect on complex I (Sherer et al. 2007; Choi et al. 2008). The transcriptome and its regulation have become a focus for understanding these mechanisms outside of the electron transport chain (Cabeza-Arvelaiz and Shiestl 2012). We observed large scale changes in gene expression profiles and many of these genes were enriched in processes involved in gene regulation and chromatin organization (Chapter 2A Figure 2.3). We searched the differentially expressed genes for non-coding risk variants associated with PD. We discovered 13 genes with significant association to PD using GWAS meta-data. We focused on eight genes (*ITGA8*, *GPRIN3*, *FER*, *CNKSR3*, *BMP4*, *UBOX5*, *PARK2*, and *CHCHD2*) that remained significantly associated in at least two studies with their most significant variant lying in a non-coding region (PDGene; Lill et al. 2014). *UBOX5* was the most significantly associated variant according to GWAS meta-data. Furthermore, *UBOX5* was the only identified gene with its most significant non-coding variant having known interactions with regulatory elements such as CTCF (Regulomedb; Boyle et al. 2012).

UBOX5 is predicted to have a role in the ubiquitin proteasome system, a well-known PD pathway involved in protein quality control and cellular detoxification (McNaught and Jenner 2001; McNaught et al. 2003). This pathway is involved in the function of multiple PD-associated genes most notably *PARK2* which encodes a ubiquitin ligase. Mutations in *PARK2* account for approximately 50% of familial early onset PD but the frequency of these mutations decrease with age (Bekris et al. 2010). These mutations generally occur at exon sequences but other less penetrant but significantly associated polymorphisms with higher frequency in the population occur more often at intronic or regulatory sequences of the gene.

Each of the selected genes had a CTCF binding site determined by ENCODE and the CTCF prediction tool (ENCODE 2012; Ziebarth and Bhattacharya 2013). We used the online tool, Regulomedb, to investigate whether single nucleotide polymorphisms in these CTCF binding regions had evidence of an interaction with CTCF (Table 2.7). There was evidence of a CTCF interaction in the brain in 2 of the selected genes *GPRIN3* and *FER*. This rank score generated by Regulomedb is indicative of the strength of the evidence for this interaction with 1 being the greatest.

CTCF binds regions with allele specific methylation and preferentially binds the unmethylated allele (Wang et al. 2018). The methylation status of these allele specific methylated regions is critical to functional CTCF binding and can explain as much as 41% of its variability (Wang et al. 2012). We have previously identified allele specific methylated regions in the human genome and verified their sensitivity to rotenone exposure (Martos et al. 2017; Freeman et al. 2020). Therefore, we hypothesized that CTCF binding sites at PD associated genes would also be vulnerable to rotenone. Out of 165 CG sites that met minimum coverage requirements and overlapped predicted CTCF binding motifs, we detected 45 differentially methylated cytosines (Table 2.9). In two of the genes, the cytosine within the CTCF consensus sequence were differentially methylated but not in any consistent direction (*FER*- hypomethylated; *CHCHD2*- hypermethylated) (Figure 2.7). We saw a similar trend in *PARK2* and *UBOX5* which had differential methylation across the whole binding region but did not change in a consistent direction (*PARK2*- hypomethylated) and (*UBOX5*-hypermethylated) (Figure 2.7). Overall there was a slight increase in hypermethylated cytosines (53%) indicating a potential decrease in CTCF binding capacity.

One of the primary functions of CTCF is to act as an insulator by blocking enhancer-promoter interactions (Phillips and Corces 2009). CTCF is thus tightly correlated with enhancer activity and its interaction with active enhancers topologically is much

greater than with silent regions of the genome (Ren et al. 2017). Histone acetylation patterns also determine chromatin structure and the histone mark H3K27ac is correlated with active enhancer regions (Creyghton et al. 2010; Wang et al. 2009). p300 is one of the primary histone acetyltransferase enzymes and loads the acetyl group onto the lysine tail of histone 3 at active regions. CTCF binding sites are often located next to at least one p300 binding site and interacts with p300 at chromatin with active acetylation (Ren et al. 2017).

Histone acetylation patterns are vulnerable to environmental factors and like DNA methylation are heritable (Chinnusamy et al. 2009; Dai and Wang 2014; Zhu et al. 2018). It is likely that histone acetylation patterns also contribute to the role of genetic variants in disease pathogenesis. We tested H3K27ac levels at CTCF binding sites to determine if acetylation patterns were also sensitive to rotenone at PD-associated genes. We saw an increase in H3K27ac at four of the eight identified genes suggesting strong chromatin interactions with CTCF (FDR<0.05) (Figure 2.8). Notably, all four genes with H3K27ac also overlapped a differentially methylated cytosine within the CTCF binding region. This suggests a crosstalk mechanism with DNA methylation patterns and H3K27ac enrichment at CTCF binding sites to control chromosomal organization and SNP impacted gene expression.

We observed increased CTCF binding at 3 differentially expressed PD associated genes (Figure 2.18). *PARK2* is a well-known genetic factor in PD as described earlier. Increased CTCF binding at its upstream enhancer decreased its expression thereby affecting its role in the ubiquitin proteasome system. *BMP4* is a gene that encodes bone morphogenetic protein 4 and it regulates neurite outgrowth and axonal transport through the activation of the TGFβ/Smad pathway which is disrupted according to RNA sequencing reactome enrichment data (Chapter 2A Table 2.1). Increased CTCF binding was associated with increased *BMP4* promoter expression which is essential for

dopaminergic neuron differentiation and survival (Hegarty et al. 2013, Hegarty et al. 2014). *GPRIN3* encodes a protein involved in microtubule dynamics and neurite outgrowth which are both impaired in rotenone induced neurotoxicity (Cabeza-Arvelaiz and Schiestl 2012). Interestingly, increased CTCF binding occurred at *GPRIN3* within an active transcription start site in the substantia nigra (Doyle et al. 2012). It is also associated with a fully penetrant Parkinson's disease mutation causing a triplication of this loci and doubling of *GPRIN3* mRNA transcripts (Devine et al. 2011). This observed increase in mRNA transcripts in a mature dopaminergic neuron differentiated from a patient was comparable to the observed 1.5-fold change increase in our rotenone treated cells.

The maintenance of CTCF binding is critical to genomic stability. These sites are not only vulnerable to environmental factors but are also enriched with disease associated genetic variants that accumulate proximal to CTCF in three dimensional domains (Wang et al. 2018; Sadowski et al. 2019). Our data explores gene-environment interactions in Parkinson's disease by focusing on epigenetic patterns at vulnerable allele specific CTCF binding sites adjacent to PD associated genes. We conclude that both DNA methylation and histone acetylation patterns are vulnerable to environmental rotenone and rotenone induced chromatin opening results in increased CTCF binding. This may unlock the functional mechanisms explaining how non-coding genetic variants can dysregulate gene expression and promote disease pathology. It supports previous reports of rotenone being an effective toxicant to study gene-environment interactions in the brain (Cannon and Greenamyre 2010; Johnson and Bobrovskaya 2015). Lastly, it promotes the ongoing movement to include the environment and epigenetic regulation in population studies to predict the risk of developing complex, age-related diseases.

2B.6 References

1. Ables JL, Breunig JJ, Eisch AJ, Rakic P. 2011. Not (ch) just development: Notch signalling in the adult brain. Nature Reviews Neuroscience 12(5):269.
2. Afgan E, Baker D, Van den Beek M, Blankenberg D, Bouvier D, Čech M et al. 2016. The galaxy platform for accessible, reproducible and collaborative biomedical analyses: 2016 update. Nucleic Acids Res 44(W1):W3-W10.
3. Akalin A, Kormaksson M, Li S, Garrett-Bakelman FE, Figueroa ME, Melnick A et al. 2012. methylKit: A comprehensive R package for the analysis of genome-wide DNA methylation profiles. Genome Biol 13(10):R87.
4. Anders S, Pyl PT, Huber W. 2015. HTSeq—a python framework to work with high-throughput sequencing data. Bioinformatics 31(2):166-169.
5. Bhattacharya A, Ziebarth JD, Cui Y. 2013. PolymiRTS database 3.0: Linking polymorphisms in microRNAs and their target sites with human diseases and biological pathways. Nucleic Acids Res 42(D1):D86-D91.
6. Boyle AP, Hong EL, Hariharan M, Cheng Y, Schaub MA, Kasowski M et al. 2012. Annotation of functional variation in personal genomes using RegulomeDB. Genome Res 22(9):1790-1797; doi: 10.1101/gr.137323.112.
7. Buniello A, MacArthur JAL, Cerezo M, Harris LW, Hayhurst J, Malangone C et al. 2018. The NHGRI-EBI GWAS catalog of published genome-wide association studies, targeted arrays and summary statistics 2019. Nucleic Acids Res 47(D1):D1005-D1012.
8. Cabeza-Arvelaiz Y, Schiestl RH. 2012. Transcriptome analysis of a rotenone model of parkinsonism reveals complex I-tied and-untied toxicity mechanisms common to neurodegenerative diseases. PloS one 7(9):e44700.
9. Cannon JR, Greenamyre JT. 2011. The role of environmental exposures in neurodegeneration and neurodegenerative diseases. Toxicological Sciences 124(2):225-250.
10. Chinnusamy V, Zhu J. 2009. Epigenetic regulation of stress responses in plants. Curr Opin Plant Biol 12(2):133-139.
11. Choi WS, Kruse SE, Palmiter RD, Xia Z. 2008. Mitochondrial complex I inhibition is not required for dopaminergic neuron death induced by rotenone, MPP+, or paraquat. Proc Natl Acad Sci U S A 105(39):15136-15141; doi: 10.1073/pnas.0807581105.
12. Cicchetti F, Drouin-Ouellet J, Gross RE. 2009. Environmental toxins and Parkinson's disease: What have we learned from pesticide-induced animal models? Trends Pharmacol Sci 30(9):475-483.
13. Coetzee SG, Pierce S, Brundin P, Brundin L, Hazelett DJ, Coetzee GA. 2016. Enrichment of risk SNPs in regulatory regions implicate diverse tissues in Parkinson's disease etiology. Scientific reports 6:30509.
14. Creyghton MP, Cheng AW, Welstead GG, Kooistra T, Carey BW, Steine EJ et al. 2010. Histone H3K27ac separates active from poised enhancers and predicts developmental state. Proc Natl Acad Sci U S A 107(50):21931-21936; doi: 10.1073/pnas.1016071107.
15. Dai H, Wang Z. 2014. Histone modification patterns and their responses to environment. Current environmental health reports 1(1):11-21.
16. Dawson TM, Mandir AS, Lee MK. 2002. Animal models of PD: Pieces of the same puzzle? Neuron 35(2):219-222.
17. De Lau LM, Breteler MM. 2006. Epidemiology of Parkinson's disease. The Lancet Neurology 5(6):525-535.

18. Devine MJ, Ryten M, Vodicka P, Thomson AJ, Burdon T, Houlden H et al. 2011. Parkinson's disease induced pluripotent stem cells with triplication of the α-synuclein locus. Nature communications 2(1):1-10.
19. Do C, Lang CF, Lin J, Darbary H, Krupska I, Gaba A et al. 2016. Mechanisms and disease associations of haplotype-dependent allele-specific DNA methylation. The American Journal of Human Genetics 98(5):934-955.
20. Eden E, Navon R, Steinfeld I, Lipson D, Yakhini Z. 2009. GOrilla: A tool for discovery and visualization of enriched GO terms in ranked gene lists. BMC Bioinformatics 10(1):48.
21. ENCODE Project Consortium. 2012. An integrated encyclopedia of DNA elements in the human genome. Nature 489(7414):57.
22. Franco R, Li S, Rodriguez-Rocha H, Burns M, Panayiotidis MI. 2010. Molecular mechanisms of pesticide-induced neurotoxicity: Relevance to Parkinson's disease. Chem Biol Interact 188(2):289-300.
23. Freeman DM, Lou D, Li Y, Martos SN, Wang Z. 2020. The conserved DNMT1 dependent methylation regions in human cells are vulnerable to environmental rotenone. Epigenetics & Chromatin, 13(1), 1-16.
24. Hegarty SV, Collins LM, Gavin AM, Roche SL, Wyatt SL, Sullivan AM et al. 2014. Canonical BMP–Smad signalling promotes neurite growth in rat midbrain dopaminergic neurons. Neuromolecular medicine 16(2):473-489.
25. Johnson ME, Bobrovskaya L. 2015. An update on the rotenone models of Parkinson's disease: Their ability to reproduce the features of clinical disease and model gene–environment interactions. Neurotoxicology 46:101-116.
26. Kim D, Pertea G, Trapnell C, Pimentel H, Kelley R, Salzberg SL. 2013. TopHat2: Accurate alignment of transcriptomes in the presence of insertions, deletions and gene fusions. Genome Biol 14(4):R36.
27. Krueger F. 2015. Trim galore. A wrapper tool around Cutadapt and FastQC to consistently apply quality and adapter trimming to FastQ files.
28. Labbé C, Lorenzo-Betancor O, Ross OA. 2016. Epigenetic regulation in Parkinson's disease. Acta Neuropathol 132(4):515-530.
29. Lee YC, Lai CQ, Ordovas JM, Parnell LD. 2011. A database of gene-environment interactions pertaining to blood lipid traits, cardiovascular disease and type 2 diabetes. J Data Mining Genomics Proteomics 2(1):10.4172/2153-0602.1000106; doi: 106.
30. Li L, Dahiya R. 2002. MethPrimer: Designing primers for methylation PCRs. Bioinformatics 18(11):1427-1431.
31. Lill CM. 2016. Genetics of Parkinson's disease. Mol Cell Probes 30(6):386-396.
32. Lill CM, Roehr JT, McQueen MB, Kavvoura FK, Bagade S, Schjeide BM et al. 2012. Comprehensive research synopsis and systematic meta-analyses in Parkinson's disease genetics: The PDGene database. PLoS genetics 8(3):e1002548.
33. Lin Y, Boone M, Meuris L, Lemmens I, Van Roy N, Soete A et al. 2014. Genome dynamics of the human embryonic kidney 293 lineage in response to cell biology manipulations. Nature communications 5(1):1-12.
34. Martos SN, Li T, Ramos RB, Lou D, Dai H, Xu J et al. 2017. Two approaches reveal a new paradigm of 'switchable or genetics-influenced allele-specific DNA methylation'with potential in human disease. Cell Discovery 3:17038.
35. Maurano MT, Humbert R, Rynes E, Thurman RE, Haugen E, Wang H et al. 2012. Systematic localization of common disease-associated variation in regulatory DNA. Science 337(6099):1190-1195; doi: 10.1126/science.1222794.
36. McNaught KSP, Belizaire R, Isacson O, Jenner P, Olanow CW. 2003. Altered proteasomal function in sporadic Parkinson's disease. Exp Neurol 179(1):38-46.

37. McNaught KSP, Jenner P. 2001. Proteasomal function is impaired in substantia nigra in Parkinson's disease. Neurosci Lett 297(3):191-194.
38. Nalls MA, Pankratz N, Lill CM, Do CB, Hernandez DG, Saad M et al. 2014. Large-scale meta-analysis of genome-wide association data identifies six new risk loci for parkinson's disease. Nat Genet 46(9):989.
39. Nica AC, Montgomery SB, Dimas AS, Stranger BE, Beazley C, Barroso I et al. 2010. Candidate causal regulatory effects by integration of expression QTLs with complex trait genetic associations. PLoS genetics 6(4):e1000895.
40. Ning Y, Yang J, Ma G, Chen P. 2011. Modelling rock blasting considering explosion gas penetration using discontinuous deformation analysis. Rock Mech Rock Eng 44(4):483-490.
41. Ong C, Corces VG. 2014. CTCF: An architectural protein bridging genome topology and function. Nature reviews Genetics 15(4):234.
42. Orth M, Tabrizi S, Schapira A, Cooper J. 2003. α-Synuclein expression in HEK293 cells enhances the mitochondrial sensitivity to rotenone. Neurosci Lett 351(1):29-32.
43. Otasek D, Morris JH, Bouças J, Pico AR, Demchak B. 2019. Cytoscape automation: Empowering workflow-based network analysis. Genome Biol 20(1):1-15.
44. Phillips JE, Corces VG. 2009. CTCF: Master weaver of the genome. Cell 137(7):1194-1211.
45. Ren G, Jin W, Cui K, Rodrigez J, Hu G, Zhang Z et al. 2017. CTCF-mediated enhancer-promoter interaction is a critical regulator of cell-to-cell variation of gene expression. Mol Cell 67(6):1049-1058. e6.
46. Robinson MD, McCarthy DJ, Smyth GK. 2010. edgeR: A bioconductor package for differential expression analysis of digital gene expression data. Bioinformatics 26(1):139-140.
47. Sadowski M, Kraft A, Szalaj P, Wlasnowolski M, Tang Z, Ruan Y et al. 2019. Spatial chromatin architecture alteration by structural variations in human genomes at the population scale. Genome Biol 20(1):148.
48. Sherer TB, Richardson JR, Testa CM, Seo BB, Panov AV, Yagi T et al. 2007. Mechanism of toxicity of pesticides acting at complex I: Relevance to environmental etiologies of Parkinson's disease. J Neurochem 100(6):1469-1479.
49. Supek F, Bošnjak M, Škunca N, Šmuc T. 2011. REVIGO summarizes and visualizes long lists of gene ontology terms. PloS one 6(7):e21800.
50. Tang Z, Luo OJ, Li X, Zheng M, Zhu JJ, Szalaj P et al. 2015. CTCF-mediated human 3D genome architecture reveals chromatin topology for transcription. Cell 163(7):1611-1627.
51. Teixeira J, Basit F, Swarts HG, Forkink M, Oliveira PJ, Willems PH et al. 2018. Extracellular acidification induces ROS-and mPTP-mediated death in HEK293 cells. Redox biology 15:394-404.
52. Venderova K, Park DS. 2012. Programmed cell death in parkinson's disease. Cold Spring Harb Perspect Med 2(8):10.1101/cshperspect.a009365; doi: 10.1101/cshperspect.a009365 [doi].
53. Verstraeten A, Theuns J, Van Broeckhoven C. 2015. Progress in unraveling the genetic etiology of parkinson disease in a genomic era. Trends in Genetics 31(3):140-149.
54. Wang H, Lou D, Wang Z. 2018. Crosstalk of genetic variants, allele-specific DNA methylation, and environmental factors for complex disease risk. Frontiers in genetics 9.
55. Wang Z, Zang C, Rosenfeld JA, Schones DE, Barski A, Cuddapah S et al. 2008. Combinatorial patterns of histone acetylations and methylations in the human genome. Nat Genet 40(7):897.

56. Wang H, Maurano MT, Qu H, Varley KE, Gertz J, Pauli F et al. 2012. Widespread plasticity in CTCF occupancy linked to DNA methylation. Genome Res 22(9):1680-1688; doi: 10.1101/gr.136101.111.
57. Ye J, Coulouris G, Zaretskaya I, Cutcutache I, Rozen S, Madden TL. 2012. Primer-BLAST: A tool to design target-specific primers for polymerase chain reaction. BMC Bioinformatics 13(1):134.
58. Zhu Y, Li Y, Lou D, Gao Y, Yu J, Kong D et al. 2018. Sodium arsenite exposure inhibits histone acetyltransferase p300 for attenuating H3K27ac at enhancers in mouse embryonic fibroblast cells. Toxicol Appl Pharmacol 357:70-79.

2B.7 Tables

Table 2.3 qRT-PCR primers for RNA seq Validation

PARK2	GTGTTTGTCAGGTTCAACTCCA
	GAAAATCACACGCAACTGGTC
ITGA8	AGAATGGAGACCTTATTGTGGGA
	GAGCCACTTCCGTCTGCTTT
CHCHD2	ACACATTGGGTCACGCCATTA
	GCACCTCATTGAAACCCTCACA
GPRIN3	AGGGCACCTCCACCATTTG
	GACACTAACACGCCGAAGTCA
FER	TGCTTCTGGACTCCTTACAAAAG
	TTAGCAGCCGTTGTTCTGTGA
CNSKR3	GACTGCCTGCAACAATATGTCC
	CTGGTGTCCAATCCGTGTGAC
UBOX5	CAAGTGGTGTTTAGCCACAGG
	GAAAGAGCCCCTTTATTCCAGAG
BMP4	ATGATTCCTGGTAACCGAATGC
	CCCCGTCTCAGGTATCAAACT
WNT3	AGGGCACCTCCACCATTTG
	GACACTAACACGCCGAAGTCA

Table 2.4 Selected non-coding genetic variants

HGNC	Log 2 FC	FDR	SNP	# studies	p-value	Cell Function
FER	-0.86	6.21E-07	rs13178668	13	<0.05	Tyrosine kinase activates cell surface signalling.
Park2	-0.82	3.55E-03	rs4388272	13	<0.05	E3 ubiquitin ligase targets proteins for degradation.
ITGA8	-0.78	7.24E-06	rs10737104	15	2.70E-06	Transmembrane receptor activates various cell signaling.
BMP4	0.59	1.16E-02	rs148491084	3	<0.05	Secreted regulatory protein regulates development.
GPRIN3	0.60	3.31E-04	rs10014765	15	6.48E-05	G-protein regulates neurite outgrowth.
CNKSR3	0.65	2.44E-05	rs145160741	12	<0.05	Scaffold protein signals membrane dynamics.
UBOX5	0.65	6.46E-04	rs55785911	21	3.30E-10	Interacting protein signals ubiquitin proteasome pathway.
CHCHD2	0.90	2.00E-04	rs11978209	12	<0.05	DNA binding protein signals oxidative stress response.

Table 2.5 BS-PCR primers for amplicon sequencing

CHCHD2	TTTTATATTTTTTTAATATAGGTTTTA
	AATAAACCACAAAAACTTCC
CNKSR3	GTTTATATGTGGTTTGAAAATGTAG
	AAAAATAAAAATAACCTTTCTATAAC
UBOX5	TTGAAGTTTTTATTATAGTTAGGTTTG
	TCCAAAAAAATATTTTCCCTCTACA
ITGA8	GTATTTGGAATATTTAGGATTTG
	CTAAATAACAACCACCCACC
PARK2-CTCF	TTTAGTTATAGTTTTGTTGGAAGGA
	CAAAAACACAAAAAACAAAAAAACA
GPRIN3	TAAAGGATTTTTGTGTAAAATGTGG
	AAACTCTCACCTCCAAACTAACTCTAC
FER	TTAGTTTAGGGTTTAAGTTTTGTTTT
	CCCAACCAAAAATACTCTACTAC
BMP4	TTATTTTTTTTGGATTTTAGAGT
	CTAAATATCTAACTTATCTCCCC

Table 2.6 ChIP-PCR primers

BMP4	CAGGTAGCCTTGCTCACCAT
	CCGGAAGCTAGGTGAGTGTG
UBOX5	CTGAAGTTCTCACCACAGCCA
	GAGGAGCCAGTATCTGTGTCG
GPRIN3	TCGCATATCCCAAGCACCG
	ATGAACAGTCGGGCAAGTGA
FER	TCAGGTTCTAGGTAGGTGCGT
	GGGAGGATGAGCGGATGAC
CNKSR3	CCTGGCGCAAATGCTATGG
	CCGAGCCTGTCTGTTTTTGTT
PARK2	CCTGCTGCTTTGAGCCTTTTT
	TCAAAGGCTGTTGCTTGCTT
CHCHD2	ACGTTCAATCTACCCCCGC
	TCTACTGGGGCAATGACGC

Table 2.7 Regulomedb results for SNPs within selected regions

Gene	chr:start	SNP ID	Rank	Score
GPRIN3	chr4:90228735	rs2116326	2a	0.96
FER	chr5:108084548	rs113728457	2a	0.92

Table 2.8 Differentially methylated CG sites at PD-associated genes

CHR_GENE	CG	pvalue	qvalue	delta
chr14_54422869_54423420_BMP4	54423352	5.48E-08	5.60E-08	-3.3
chr20_3140226_3140678_UBOX5	3140420	2.59E-27	9.41E-27	2.3
chr20_3140226_3140678_UBOX5	3140429	3.46E-34	1.62E-33	3.6
chr4_90228647_90229070_GPRIN3	90228692	2.37E-07	2.24E-07	-1.1
chr4_90228647_90229070_GPRIN3	90228700	1.87E-13	3.06E-13	1.3
chr4_90228647_90229070_GPRIN3	90228702	3.42E-13	5.41E-13	1.2
chr4_90228647_90229070_GPRIN3	90228709	1.23E-33	5.49E-33	-2.5
chr4_90228647_90229070_GPRIN3	90228753	2.38E-09	2.82E-09	1.1
chr4_90228647_90229070_GPRIN3	90228761	1.33E-13	2.29E-13	1.7
chr4_90228647_90229070_GPRIN3	90228764	4.10E-07	3.73E-07	1.0
chr4_90228647_90229070_GPRIN3	90228792	2.58E-11	3.61E-11	-1.2
chr4_90228647_90229070_GPRIN3	90228822	4.03E-16	8.78E-16	1.7
chr4_90228647_90229070_GPRIN3	90228849	1.47E-36	8.03E-36	2.7
chr4_90228647_90229070_GPRIN3	90228860	3.23E-44	2.88E-43	1.8
chr5_108084418_108084954_FER	102025087	1.53E-06	1.26E-06	-1.6
chr5_108084418_108084954_FER	102025097	5.23E-76	8.56E-75	-4.4
chr5_108084418_108084954_FER	102025117	1.62E-140	1.59E-138	-4.9
chr5_108084418_108084954_FER	102025151	2.40E-14	4.62E-14	-1.3
chr5_108084418_108084954_FER	102025176	2.79E-12	4.14E-12	1.6
chr5_108084418_108084954_FER	102025225	1.05E-16	2.39E-16	1.9
chr5_108084418_108084954_FER	102025228	1.12E-19	2.98E-19	3.4
chr5_108084418_108084954_FER	102025231	1.23E-11	1.79E-11	-2.8
chr5_108084418_108084954_FER	102025234	1.56E-15	3.26E-15	1.7
chr5_108084418_108084954_FER	102025251	4.73E-03	2.52E-03	-1.8
chr5_108084418_108084954_FER	102025320	5.38E-07	4.77E-07	1.9
chr5_108084418_108084954_FER	102025330	3.76E-04	2.32E-04	1.3
chr5_108084418_108084954_FER	102025334	2.60E-04	1.67E-04	-1.7
chr5_108084418_108084954_FER	102025341	1.36E-15	2.90E-15	2.7
chr5_108084418_108084954_FER	102025408	2.37E-07	2.24E-07	2.1
chr5_108084418_108084954_FER	102025430	2.26E-03	1.28E-03	-1.4
chr6_154830537_154830958_CNKSR3	154830543	8.22E-22	2.44E-21	-2.5
chr6_154830537_154830958_CNKSR3	154830584	1.66E-24	5.63E-24	1.8
chr6_154830537_154830958_CNKSR3	154830770	2.43E-59	2.65E-58	-1.5
chr6_154830537_154830958_CNKSR3	154830810	1.02E-43	8.35E-43	1.7
chr6_154830537_154830958_CNKSR3	154830817	3.60E-14	6.66E-14	-1.1
chr6_154830537_154830958_CNKSR3	154830837	1.41E-93	6.93E-92	3.3
chr6_154830537_154830958_CNKSR3	154830863	8.54E-20	2.33E-19	-1.0
chr6_163277806_163278291_PARK2	163277841	3.89E-04	2.38E-04	-1.7
chr6_163277806_163278291_PARK2	163277943	8.27E-07	7.12E-07	-2.0
chr7_56173886_56174373_CHCHD2	56174016	1.67E-08	1.76E-08	-1.1

chr7_56173886_56174373_CHCHD2	56174033	4.52E-04	2.75E-04	-1.9
chr7_56173886_56174373_CHCHD2	56174103	1.71E-05	1.29E-05	1.7
chr7_56173886_56174373_CHCHD2	56174107	1.01E-08	1.11E-08	-1.1
chr7_56173886_56174373_CHCHD2	56174149	2.07E-04	1.37E-04	1.6
chr7_56173886_56174373_CHCHD2	56174179	3.24E-04	2.05E-04	1.2

Table 2.9 Differentially methylated CG sites within H3K27ac enriched regions

CHR_GENE	CG	pvalue	qvalue	delta
chr14_54422869_54423420_BMP4	54423352	5.48E-08	5.60E-08	-3.3
chr20_3140226_3140678_UBOX5	3140420	2.59E-27	9.41E-27	2.3
chr20_3140226_3140678_UBOX5	3140429	3.46E-34	1.62E-33	3.6
chr4_90228647_90229070_GPRIN3	90228822	4.03E-16	8.78E-16	1.7
chr4_90228647_90229070_GPRIN3	90228849	1.47E-36	8.03E-36	2.7
chr4_90228647_90229070_GPRIN3	90228860	3.23E-44	2.88E-43	1.8
chr5_108084418_108084954_FER	1.02E+08	1.05E-16	2.39E-16	1.9
chr5_108084418_108084954_FER	1.02E+08	1.12E-19	2.98E-19	3.4
chr5_108084418_108084954_FER	1.02E+08	1.23E-11	1.79E-11	-2.8
chr5_108084418_108084954_FER	1.02E+08	1.56E-15	3.26E-15	1.7
chr5_108084418_108084954_FER	1.02E+08	4.73E-03	2.52E-03	-1.8
chr5_108084418_108084954_FER	1.02E+08	5.38E-07	4.77E-07	1.9
chr5_108084418_108084954_FER	1.02E+08	3.76E-04	2.32E-04	1.3
chr5_108084418_108084954_FER	1.02E+08	2.60E-04	1.67E-04	-1.7
chr5_108084418_108084954_FER	1.02E+08	1.36E-15	2.90E-15	2.7
chr5_108084418_108084954_FER	1.02E+08	2.37E-07	2.24E-07	2.1
chr5_108084418_108084954_FER	1.02E+08	2.26E-03	1.28E-03	-1.4

2B.8 Figures

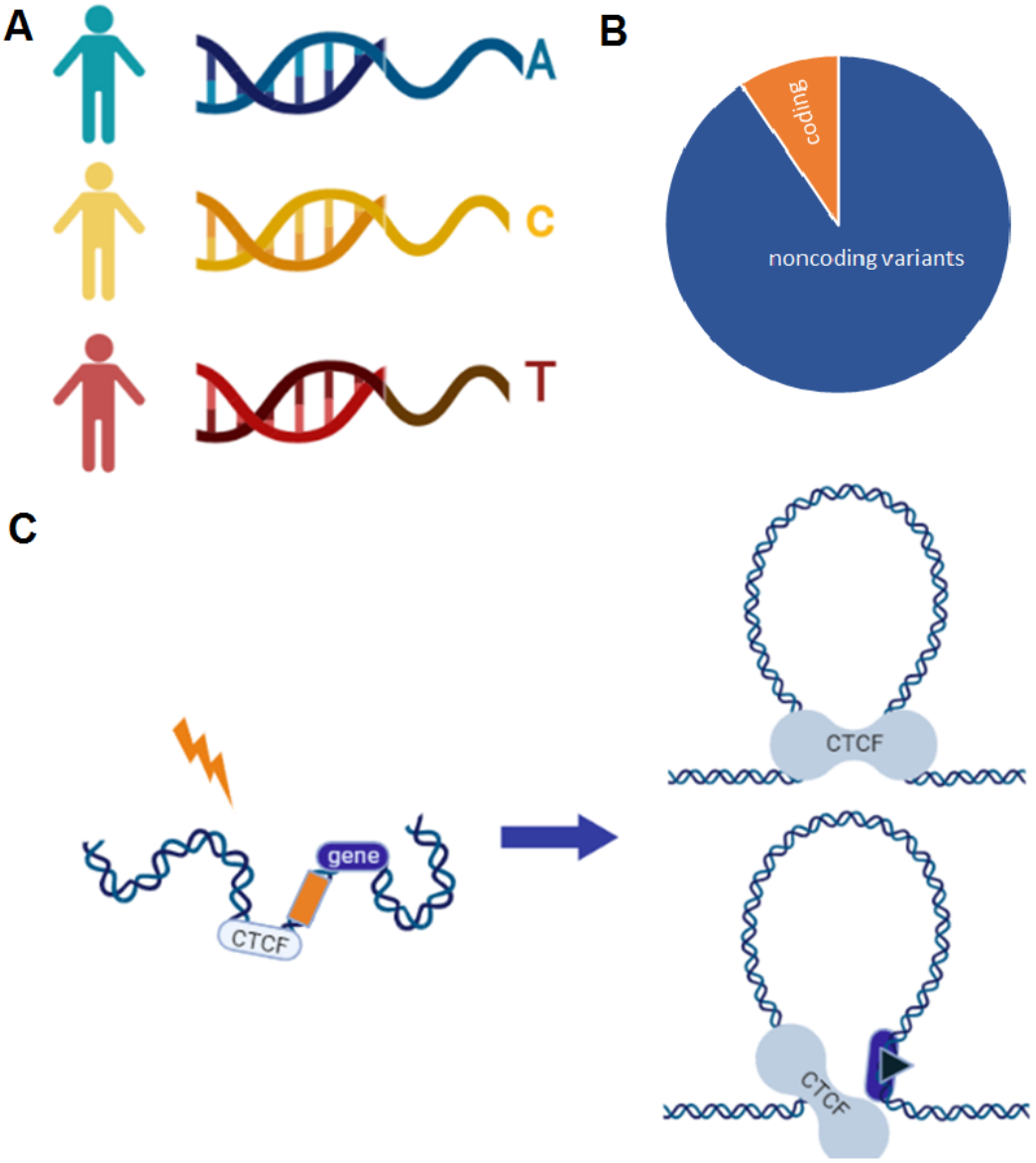

Figure 2.5 Environmental factors alter CTCF interaction with non-coding variants. A) Genome wide association studies (GWAS) assess predisposition for disease by using unbiased genetic screens to associate single nucleotide polymorphisms (SNP) with complex traits. B) Parkinson's disease-associated genetic variants were identified using the GWAS catalog and 90% (220 polymorphisms) were in non-coding regions of the genome. C) In cells exposed to environmental stress, cis-epigenetic mechanisms at CTCF binding motifs impact CTCF transcription factor binding and insulator activity. This can affect enhancer enriched SNPs and their interactions with gene regulatory regions.

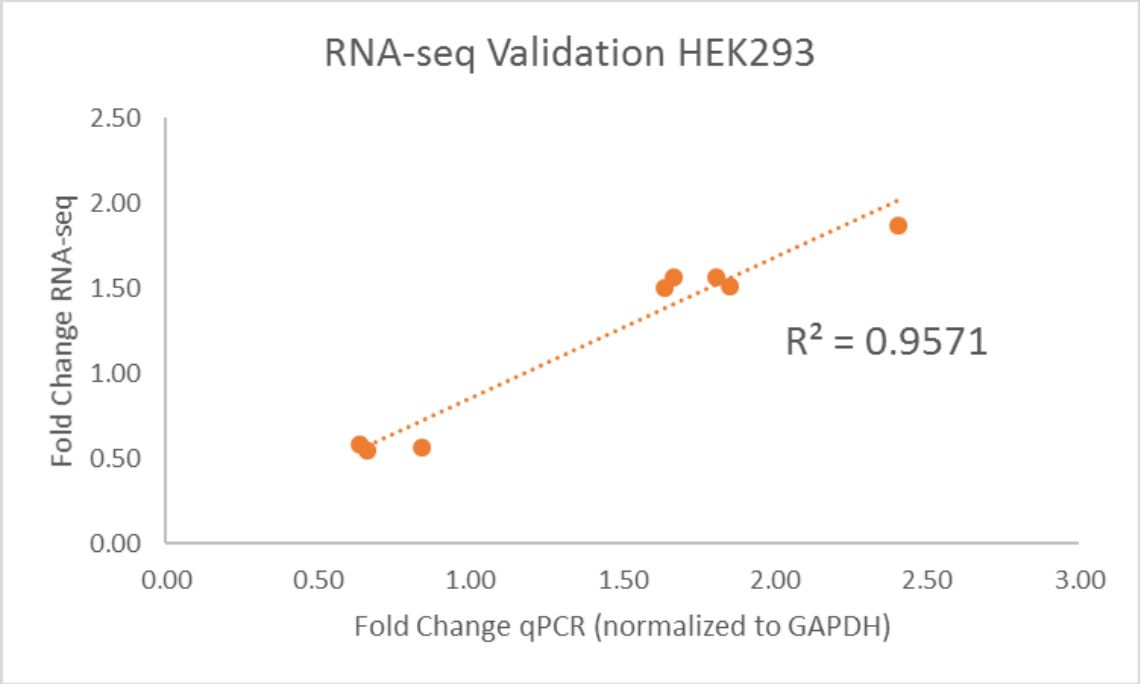

Figure 2.6 RNA sequencing validation with qRT-PCR. Linear calibration curve of RNA sequencing results with qRT-PCR results expressed as fold change in expression.

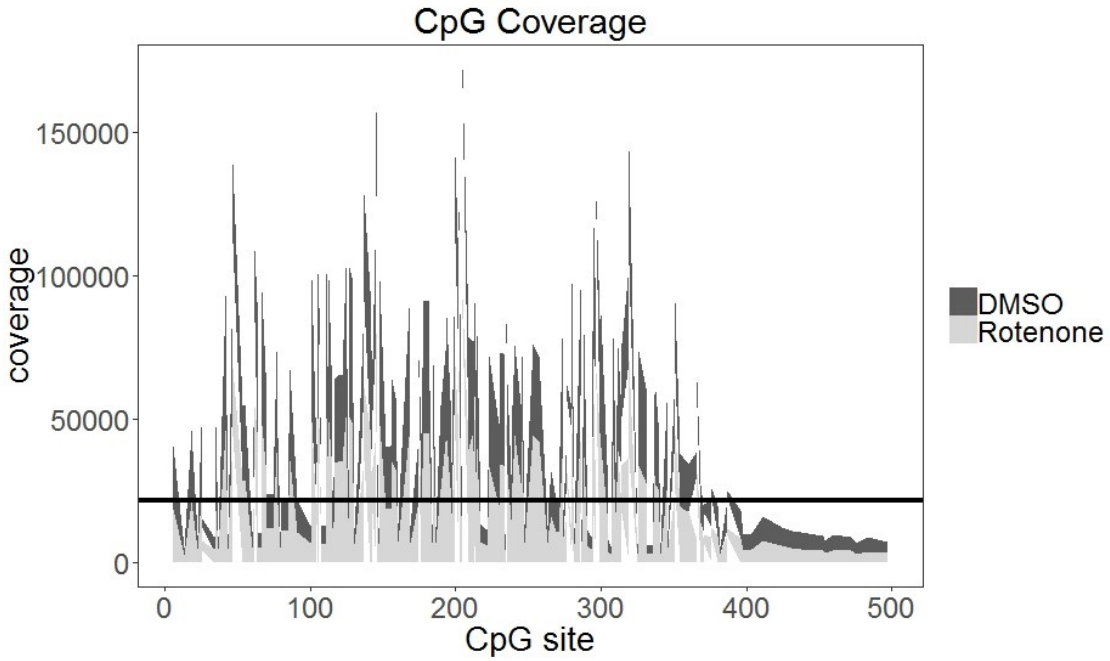

Figure 2.7 BS sequencing coverage of CpG sites within amplified regions at PD-associated genes. The average total coverage for all CpG sites within the amplified region is indicated by the straight line.

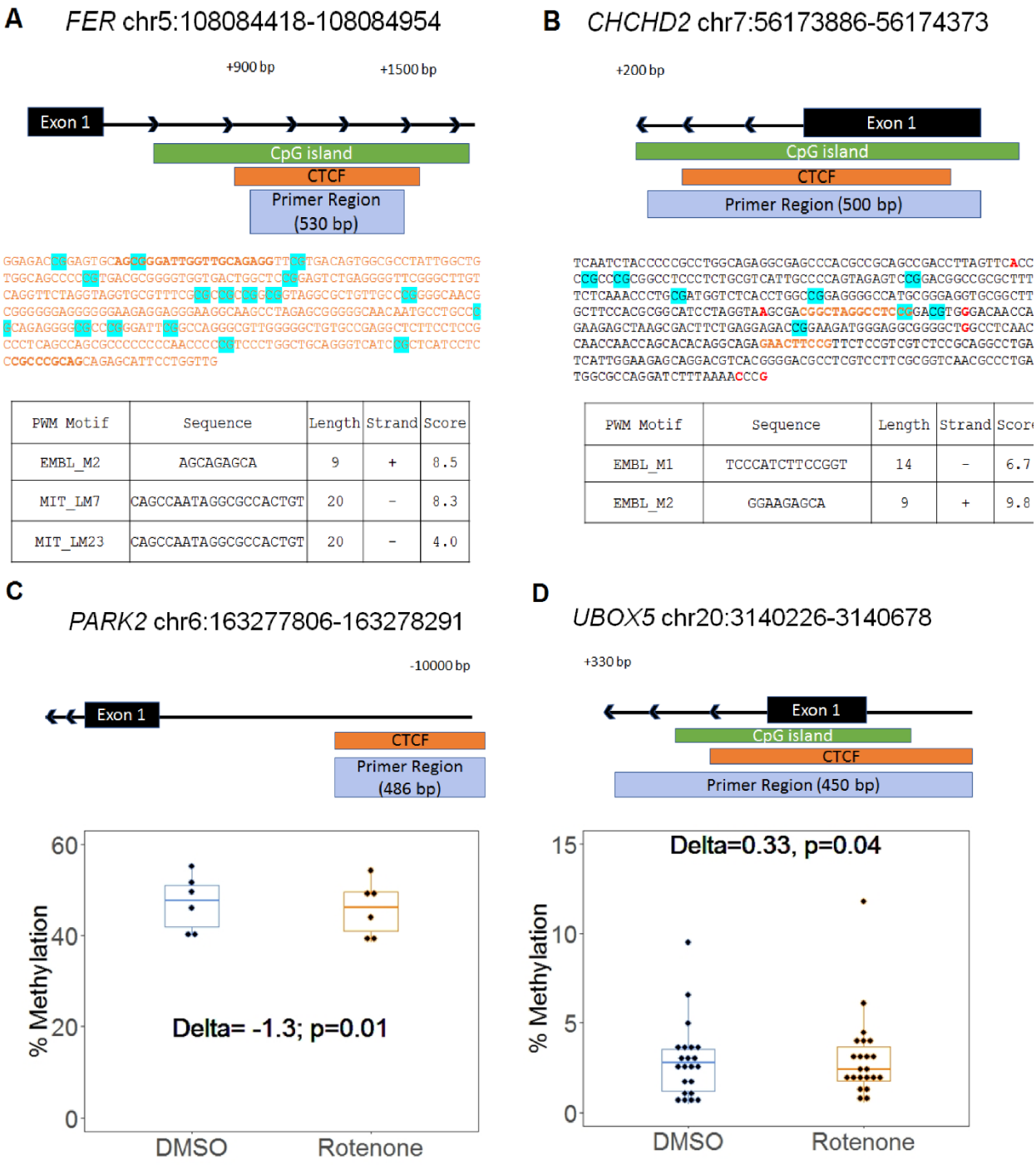

Figure 2.8 Differential methylation within CTCF motifs at PD-associated genes
A-B) Two genes, *FER and CHCHD2*, had differential methylation at CG sites within their predicted CTCF binding motif. The amplified region at both genes covered the first exon and intron. The highlighted blue CG sites are all with significant differential methylation (> |1%|; q-value<0.05). Red text emphasizes a common SNP. Orange text represents CTCF binding sites in the human genome identified by ENCODE. The bold orange text is the sequence motif predicted by the Cui Lab CTCF prediction tool (Ziebarth and Bhattacharya

2013). The output of the CTCF binding prediction tool is listed in the table with the name of the position weight matrix motif, motif sequence, motif length, strand orientation, and the integrated output score. C-D) Two genes, *PARK2* and *UBOX5*, had significantly different methylation across the region. Each dot represents a CG within the region. Delta indicates the change in the mean CpG methylation percentage and the associated p-value from Fisher's exact test.

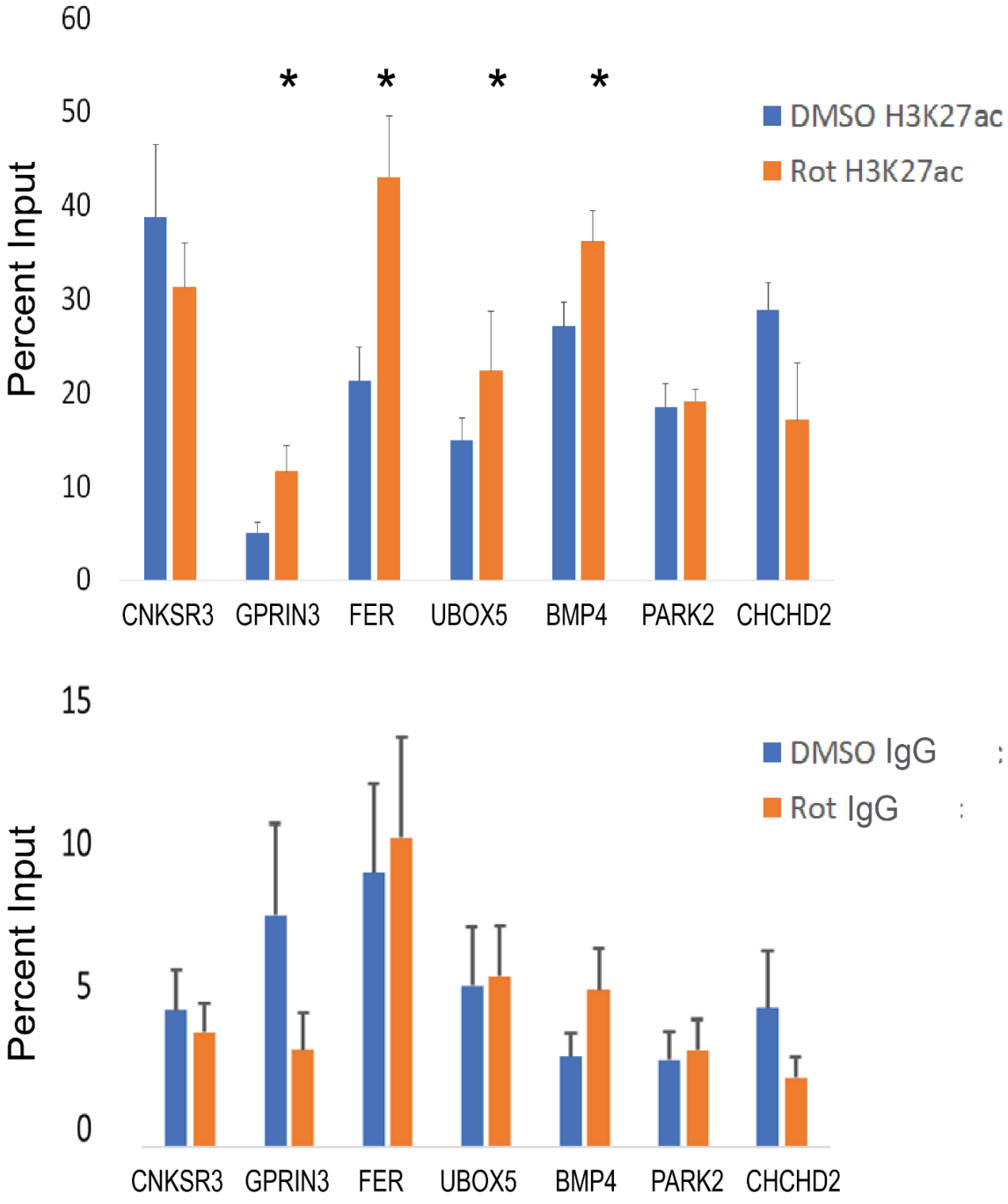

Figure 2.9 CTCF site histone acetylation patterns in response to rotenone.
The local abundance of H3K27ac within CTCF binding sites at Parkinson's disease associated genes was measured with ChIP-PCR and expressed as the percent of total DNA input used for immunoprecipitation. The negative control for ChIP analysis was Rabbit IgG (shown in bottom panel). Significance was tested with paired student's t-test using the percent input of vehicle (DMSO) vs rotenone and post-hoc analysis for multiple hypotheses was done using the false discovery method. * FDR<0.05.

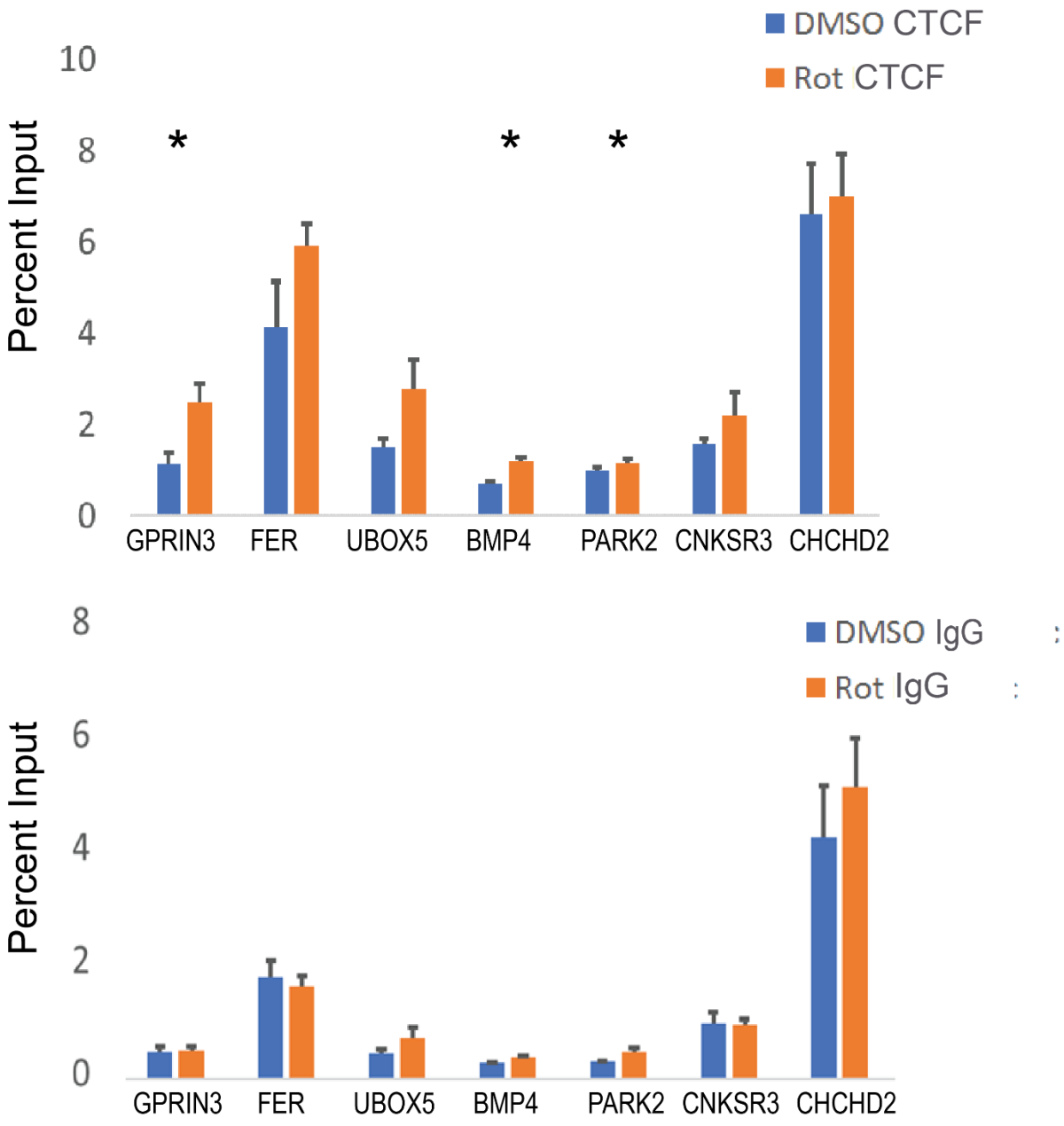

Figure 2.10 CTCF binding at PD-associated genes in response to rotenone.
The local abundance of CTCF binding at Parkinson's disease associated genes was measured with ChIP-PCR and expressed as the percent of total DNA input used for immunoprecipitation. The negative control for ChIP analysis was Rabbit IgG (shown in Supplemental Figure 6). Significance was tested with paired student's t-test using the percent input of vehicle (DMSO) vs rotenone and post-hoc analysis for multiple hypotheses was done using the false discovery method. * FDR<0.05

CHAPTER 3[3]

THE CONSERVED DNMT1-DEPENDENT METHYLATION REGIONS IN HUMAN CELLS ARE VULNERABLE TO NEUROTOXICANT ROTENONE EXPOSURE.

3.1 Abstract

Allele-specific DNA methylation (ASM) describes genomic loci that maintain CpG methylation at only one inherited allele rather than having coordinated methylation across both alleles. The most prominent of these regions are germline ASMs (gASMs) that control the expression of imprinted genes in a parent of origin- dependent manner and are associated with disease. However, our recent report reveals numerous ASMs at non-imprinted genes. These non-germline ASMs are dependent on DNA methyltransferase 1 (DNMT1) and strikingly show the feature of random, switchable monoallelic methylation patterns in the mouse genome. The significance of these ASMs to human health has not been explored. Due to their shared allelicity with gASMs, herein, we propose that non-traditional ASMs are sensitive to exposures in association with human disease. We first explore their conservancy in the human genome. Our data show that our putative non-germline ASMs were in conserved regions of the human genome and located adjacent to genes vital for neuronal development and maturation. We next tested the hypothesized vulnerability of these regions by exposing human embryonic kidney cell HEK293 with the neurotoxicant rotenone for 24h. Indeed,14 genes adjacent to our identified regions were differentially expressed from RNA-sequencing. We analyzed the base-resolution methylation patterns of the predicted non-germline ASMs at two neurological genes, *HCN2* and *NEFM,* with potential to increase the risk of neurodegeneration. Both regions

[3] This chapter has been accepted for publication in *Epigenetics and Chromatin*. D.M. Freeman (2020). Co-authors: Dan Lou, Yangqiang Li, Suzanne Martos. Corresponding author: Z. Wang.

were significantly hypomethylated in response to rotenone. Our data indicate that non-germline ASMs seem conserved between mouse and human genomes, overlap important regulatory factor binding motifs, and regulate the expression of genes vital to neuronal function. These results support the notion that ASMs are sensitive to environmental factors such as rotenone and may alter the risk of neurological disease later in life by disrupting neuronal development.

3.2 Introduction

DNA methylation refers to the addition of a methyl group (CH3) to the cytosine base of DNA by DNA methyltransferases. This predominately occurs at cytosine-guanine adjacent sites known as CpG sites. For most genomic loci, DNA methylation is coordinated across both inherited alleles. However, some loci maintain CpG methylation at only one allele and these regions are described to have allele-specific methylation (ASM; previously known as differentially methylated region DMR) (Bartolomei and Tilghman 1997). The most well-known of these regions are germline ASMs which control the expression of imprinted genes in a parent of origin-dependent manner. Imprinted genes are crucial in development and are commonly associated with genetic disorders such as Beckwith-Wiedemann, Angelman, and Prader-Willi syndromes (Butler 2009). In addition to the control of imprinted gene expression, DNA methylation is key to maintain genome stability via silencing retrotransposons (Chen et al., 2007; Walsh et al., 1998).

Investigations demonstrate that two types of genomic regions, imprinted germline ASMs and intracisternal A-particle (IAP)-like retrotransposons, seem vulnerable to environmental factors. Therefore, these two regions are proposed to be pivotal for understanding human disease in response to exposure and popularly pursued in animal and epidemiological studies (Jirtle and Skinner 2007; Murphy and Hoyo 2013). The former is attractive because exposure altered ASMs are anticipated to be faithfully transmitted to somatic cells during rounds of global demethylation and remethylation in early embryos

(Barlow and Bartolomei 2014; Kacem and Feil 2009). As a result, parental exposure can be epigenetically inherited to modify offspring phenotype (Freeman and Wang 2019). The latter is exemplified in mice by the bisphenol A-hypomethylated IAP at the *agouti* gene for variations of coat color and obesity, as well as by altered methylation of IAPs at $Axin^{Fu}$ for tail kinkiness (Rakyan et al. 2003; Zhou et al. 2007).

In our recent work, we developed two approaches, no-rescued DMRs (NORED) and methylation mosaicity analyses (MethylMosaic), to identify numerous genomic loci bearing potential ASMs (Martos et al. 2017). Both the known imprinted germline ASMs and newly identified ASMs are dependent on DNA methyltransferase 1 (DNMT1)(Li et al. 2015). Many of these novel ASMs are presumably sequence (single nucleotide polymorphism; SNP)-influenced ASMs (Kerkel et al. 2008). For example, in a reciprocal cross between 129S1/SvlmJ and Cast/EiJ or between C57BL/6NJ and Cast/EiJ, the Cast allele with SNP C of *Hcn2* ASM is always hypomethylated (i.e., independent of parental origin), whereas the 129 allele or the C57 allele with SNP A is always hypermethylated. Standing out of the previously appreciated sequence-dependent ASMs, a new paradigm of switchable ASMs that shows equal chances of either paternal or maternal allele to be methylated was revealed by our report (Martos et al. 2017). Importantly, the switchable feature seems also conserved in the human genome. At the *DLGAP2* locus, independent evidence confirms a maternally imprinted ASM during pre-implantation switched to a random ASM in somatic tissues during gestation (Monteagudo-Sánchez et al. 2018). Collectively, the mouse genome or human genome contains more ASMs (including both sequence-dependent and switchable ASMs) than previously appreciated (Deng et al. 2014, Martos et al. 2017, Monteagudo-Sanchez et al. 2018, Onuchic et al. 2018). The newly revealed random, switchable ASMs remind us of features in X chromosome inactivation, leading to a proposed hypothesis of regional autosomal chromosome inactivation (Wang et al. 2018).

Currently, germline ASMs are being increasingly considered in human disease; however, less studied are non-germline ASMs, which maintain CpG methylation at one allele independent of the parent of origin (Zhang et al. 2009, Deng et al. 2014, Martos et al. 2017). These regions regulate the expression of non-imprinted genes and these genes are hypothesized to have random monoallelic expression. Due to their predicted monoallelicity (DNA methylation and transcripts), we hypothesize that these regions are also targets for environmental factors and associated with disease like germline ASMs (Susiarjo et al. 2013).

The goal of this study was to determine whether our identified candidate ASMs in the mouse genome were in conserved regions of the human genome and to explore the possible adverse effects of differential methylation in these regions by examining their tissue expressivity and functional enrichment. Lastly, we tested our hypothesis that genes adjacent to non-germline ASMs would be vulnerable to environmental factors by exposing human embryonic kidney *HEK293* cells to the pesticide rotenone for 24h. We used whole transcriptome RNA-sequencing and targeted bisulfite-amplicon sequencing to evaluate changes in expression of adjacent genes and DNA methylation at candidate ASMs in response to rotenone. Indeed, our data demonstrate the vulnerability of these new, non-traditional ASMs to environmental exposure (Freeman et al. 2020).

3.3 Materials and Methods

3.3.1 Identification of conserved DNMT1-dependent regions in the human genome

Whole Genome Bisulfite Sequencing (WGBS) was used to analyze base resolution methylomes of a series of *Dnmt1* (-/-), *Dnmt3a* (-/-), and *Dnmt3b* (-/-) murine embryonic stem cell lines (wild-type J1) as described previously (Li et al. 2015, Martos et al. 2017). DNMT1-dependent regions termed “NORED” were defined as regions with near complete loss of methylation in *Dnmt*1(-/-) compared to wild-type J1 that remained unable to recover methylation after the addition of exogenous *Dnmt1* cDNA. To identify the conserved

DNMT1-dependent regions in the human genome, we used the UCSC Genome Browser LiftOver software to locate regions in the hg19 assembly from the mouse mm10 assembly. A text file of the chromosome positions (chr: start-end) for each putative ASM was uploaded into LiftOver and converted to the human hg19 assembly with a minimum ratio of 0.1 bases mapping for each region. The genomic location of each conserved region was analyzed in the UCSC Genome Browser window with NCBI RefSeq annotations. Transcription factor binding was observed using the Uniform Transcription Factor Binding data found in the ENCODE Regulation super track. We selected all transcription factor binding sites in H1-human embryonic stem cells (H1-hESCs) detected with ChIP-Seq experiments from the ENCODE consortium from 2007-2012 (ENCODE 2012). Imprinted genes from mouse and human genome were identified from the Jirtle Laboratory GeneImprint database (http://www.geneimprint.org/).

3.3.2 Functional and tissue enrichment for candidate DNMT1-dependent genes in the human genome

We restricted functional enrichment analysis of conserved human regions to those that had >70% base pair match for over 90% of the span of the identified region (Table 1). Pathway enrichment and network interactions for human genes nearest to these regions were calculated using the STRING database (Szklarczyk et al. 2014). Gene Ontology was used for functional annotations and significance was measured using Fisher's exact test with a false discovery rate (FDR) <0.05. Network interactions were clustered using Cytoscape based on gene functional annotations in the reactome pathways (Fabregat et al. 2018).

The human DNMT1-dependent genes (Table 3.1) were used for tissue enrichment in EnrichR (Chen et al. 2013) using the ArchS4 database (Lachmann et al. 2018). The top six human tissues were reported with a p-value <0.01 adjusted using their correction for the Fisher's exact test (Chen et al. 2013). Enrichment of tissue-specific genes was

performed using the TissueEnrich R package which uses gene expression data from the Human Protein Atlas (Jain and Tuteja 2018). Genes with an expression level of at least one transcript per million (TPM) were defined as tissue enriched when expression was at least five-fold higher in a distinct tissue compared to the expression of any other individual tissue and tissue enhanced when expression was at least five-fold higher in a distinct tissue compared to the total average expression of all other tissues. Group enriched genes were defined as genes with an expression level of at least one TPM and had at least five-fold higher expression in a group of tissues compared to all tissues. These definitions were taken from TissueEnrich.

3.3.3 Cell culture and treatment of human cell line HEK293

HEK293 cells were treated with rotenone (200 nM) for 24h according to the protocol in Chapter 2A.3.1.

3.3.4 RNA sequencing library construction and analysis

The RNA sequencing data used for this subchapter was the same data reported in Chapter 2A.3.2-2A.3.3.

3.3.5 Selection and tissue expression analysis of human DNMT1 dependent regions

We examined differentially expressed genes in RNA-seq in common with the genes nearest to the conserved DNMT1-dependent regions in the human genome with >70% base pair match for over 90% of the span of the identified region in the mouse genome. Overlapping genes were entered into the Genotype-Tissue Expression (GTEx) database using the multi-gene query tool (GTEx Consortium 2013). Parkinson's disease brain regions associated with motor function including the cerebellum, cortex, frontal cortex, spinal cord, substantia nigra, and basal ganglia were selected for further expression analysis.

3.3.6 RNA sequencing validation with quantitative reverse transcription-PCR

Total RNA was extracted from an additional replicate of HEK293 treated with DMSO or rotenone using the same procedure as stated above. A total of 500ng RNA was converted to cDNA with the PrimeScript RT reagent kit with gDNA eraser from Takara (Kusatsu, Japan). We selected seven out of fourteen overlapping genes for quantitative PCR (qRT-PCR) analysis using primers listed in Table 3.2. All qRT-PCR reactions were performed on a 7500 Real-Time PCR system from Applied Biosystems (Foster City, CA) using the iTaq Universal SYBR Green Supermix from Bio-Rad (Hercules, CA). The change in expression was normalized to the GAPDH housekeeping gene and expressed as fold change ($2^{-\Delta\Delta CT}$).

3.3.7 Bisulfite-DNA conversion and Bisulfite-amplicon sequencing library construction

Bisulfite DNA conversion and library preparation was done according to the exact same protocol in *Chapter 2B 3.6-3.7* with primers designed to amplify DNMT1-dependent regions in Table 3.1. Primer sequences are listed in Table 3.3.

3.4 Results

3.4.1 DNMT1-dependent regions in the mouse and human genome.

Two approaches, NORED and MethylMosaic, independently identified over 2,000 regions with DNMT1 dependency and allele-specific methylation. To simplify future interpretation, we focused on 207 overlapped regions (i.e., 'NORED+MethylMosaic' regions) to initiate our investigation. We compared these 207 regions from mouse and observed 145 of these regions were conserved in the human genome. Most regions identified in the human genome were highly conserved with >70% matched bases for more than 90% of the entire span of the region (Figure 3.1). Analyzing these regions in the genome browser, we noted that 70% of the conserved regions in the human genome were located in the gene body and approximately 50% of them had transcription factor binding sites in human embryonic stem cells (Figure 3.1). The two transcription factors that were the most significantly enriched were POL2RA and TAF1 with binding sites at 19% of

conserved DNMT1 regions. Both were concentrated around transcription start sites and regulate RNA polymerase II binding and processivity in gene transcription. The third most enriched transcription factor was CTCF with binding motifs in 17% of conserved regions and most often found within intragenic regions. The top transcription factors with binding motifs found in intergenic sites were CTCF, SIN3A, and RAD21. All three transcription factors are crucial in regulating chromatin structure to repress gene transcription and inhibition of these factors are closely associated with human disease (Davis et al. 2018; Witteveen et al. 2016; Zuin et al. 2014). We searched conserved human genes for known imprinted genes at germline ASMs using the GeneImprint database and found 20 known imprinted genes (Figure 3.1). Most of the human genes found at conserved DNMT1-dependent regions had an unknown imprinted status and thus were considered candidate non-germline ASMs. Prior examination of DNA methylation in four independent mouse embryonic stem cell lines validated our hypothesis at one conserved gene (*HCN2*) that non-germline ASMs can exhibit a random, switchable pattern (Martos et al. 2017).

3.4.2 Human DNMT1-dependent genes are enriched in cellular processes associated with cell-cell signaling.

Out of the 145 regions identified in the human genome, we selected 97 of the most highly conserved regions compared to the mouse genome. The genes nearest to these regions on the same allele (112 genes) were used for functional enrichment analyses (Table 3.1). We used Gene Ontology functional annotations to gain insights into the cellular processes associated with these genes and significance was determined from the Fisher's exact test with p-value adjustment using false discovery rate method (FDR<0.05). We observed adjacent genes were highly associated with cell to cell interactions and signaling. The number of genes involved in this biological process as well as the significance of its enrichment (expressed as log base 2 false discovery rate) are shown in Figure 3.2. Genes regulating cell-cell adhesion belonged primarily to the cadherin protein

family. This agrees with previous reports showing monoallelic expression of protocadherins in Purkinje neurons (Esumi 2005). Gene Ontology of cellular components describe the subcellular compartments where enriched cellular processes and molecular functions occur. The plasma membrane and the pre-synapse were significantly enriched in our dataset in accordance with the enrichment of cell-cell interactions and calcium ion binding (FDR<0.05, Table 3.4).

The interaction of the proteins encoded by DNMT1-dependent genes was analyzed using the STRING database (Figure 3.2). The STRING database is a commonly used platform that summarizes the functional associations of a group of proteins. Out of the 112 selected protein encoding genes in humans, 98 nodes with 109 edges were detected with a medium confidence interaction score (>0.4). The interaction p-value (PPI) was less than $1x10^{-16}$, indicating that the number of associations was significant. We manually clustered genes with interactions using functional gene annotations. The largest cluster consisted of genes involved in cell-cell signaling including cadherins and cell surface adhesion molecules, cell trafficking chaperones, cytoskeleton proteins, and voltage-gated ion channels. Other significant pathways included developmental pathways of the nervous system and the vascular system.

3.4.3 Human DNMT1-dependent genes are enriched in tissues of the brain.

Given the evidence that DNMT1-dependent genes may play an important role in cell-cell adherence and communication as well as in nervous system development, we hypothesized that DNMT1-dependent genes may be highly expressed in the brain. We analyzed the enrichment of tissue expression using the ARCHS4 human tissue database in EnrichR. The ARCHS4 database reports publicly available RNA-sequencing across all tissues and cell types in approximately 85,000 human samples (Lachmann et al. 2018). Significant expression of the DNMT1-dependent genes in the adult and developing brain was observed ($p < 0.01$, Figure 3.3). We also observed enrichment in the regions of the

brain associated with motor function control. These include structures such as the cerebellum, spinal cord, and the striatum which are directly involved with motor coordination as well as the superior frontal gyrus which contains the supplementary motor area activated in complex movements (Li et al. 2013, Sang et al. 2015).

To further determine if these genes were specific to neuronal tissues or if they have functionality across several tissues, we analyzed DNMT1-dependent genes for tissue specific enrichment using the TissueEnrich R package (Jain and Tuteja 2018). Genes with increased expression in one tissue compared to the expression in any other tissue were defined as tissue enriched while genes with increased expression in one tissue compared to the average of all tissues were defined as tissue enhanced. Group enriched genes were defined as genes that have increased expression in a group of tissues compared to all other tissues. Our analysis demonstrates that DNMT1-dependent genes conserved in the human genome have a significant abundance of tissue enhanced and group enriched genes within the brain, but not tissue enriched genes (Figure 3). From these data, we conclude that DNMT1-dependent genes are likely important in cellular processes in the fetal and adult brain.

3.4.4 Five DNMT1-dependent genes are represented in genes for potential PD blood biomarkers in patients.

To further explore the significance of identified human DNMT1-dependent genes, we evaluated the recent literature on potential blood biomarkers in Parkinson's disease (PD) patients. Encouragingly, we observed five differentially methylated genes in these studies within our conserved human regions (Henderson-Smith et al 2018; Wang et al. 2019). They are *COL9A2*, *SCNN1A*, *AMICA1*, *SLC16A3*, and *DLK1*. One of these genes, *COL9A2*, was also found to be differentially expressed in our rotenone treated cells (Henderson-Smith et al. 2018) (described below). Given that candidate PD biomarkers

and our DNMT1-dependent genes were selected by differing criteria, we consider five overlapping genomic regions to be promising toward our hypothesis.

3.4.5 Human DNMT1-dependent genes are differentially expressed in response to rotenone in human cells.

We have shown that DNMT1-dependent regions have conserved sequences in the human genome and are enriched at genes involved in cell to cell interactions. These genes have enhanced expression in the brain and may contribute to neurological dysfunction and disease in response to environmental stress. To test the hypothesized contribution, we focus on rotenone exposure. Rotenone is a mitochondrial complex I inhibitor that is known to disrupt neuronal cell function in Parkinson's disease associated brain regions (Tanner 2011). These brain regions include the cerebellum, spinal cord, striatum, and basal ganglia. We treated human cell line HEK293 with rotenone (200 nM) for 24h. This dose was chosen based on previous reports in HEK293 and other neuronal cell models (Harris et al. 2018, Orth et al. 2003, Teixeria et al. 2018).

Rotenone treatment had a substantial effect on the expression levels of over 2,000 genes (≥1.5 fold, FDR≤0.05). We examined these differentially expressed genes with our identified human DNMT1-dependent genes and discovered 14 of them had been changed upon rotenone treatment (Table 3.5). We validated the expression of 7 these genes with qRT-PCR (R^2= 0.69, Figure 3.4). We investigated whether these genes may contribute to rotenone-induced Parkinson's disease by observing their expression in Parkinson's disease tissues (Figure 3.5). All 14 genes were expressed in Parkinson's disease regions (>1 TPM[4]) and 8 of the genes (*PPFIA4, NEFM, HCN2, ADRA2C, COL9A2, LRRC8D, EML2,* and *KDM7A/JHDM1D*) had pronounced expression in Parkinson's disease regions (>35 TPM). Two genes, *NEFM* and *HCN2*, had significant expression (>100 TPM) in all

[4] TPM is abbreviated for transcript per one million reads.

selected regions and were identified by our tissue specific enrichment analysis as tissue enhanced and tissue enriched, respectively (Figure 3.5). We therefore selected *NEFM* and *HCN2* for targeted methylation analysis based on their regional expression and significant up-regulation from both RNAseq and qRT-PCR analyses. The relevance and significance of *HCN2* and *NEFM* in human development and diseases are detailed later in the discussion.

3.4.6 DNMT1-dependent regions at HCN2 and NEFM are differentially methylated in response to rotenone in human cells.

Previously, germline ASMs are especially vulnerable to environmental exposure, thereby altering imprinted gene expression (Susiarjo et al. 2013). Herein, we determined the potential methylation changes of the defined DNMT1-dependent region at these two genes, *NEFM* and *HCN2*, with significant up-regulation in response to rotenone. We completed base-resolution bisulfite sequencing of these regions amplified with bisulfite PCR. After filtering of low-quality reads, approximately 42% of reads were mapped uniquely to the amplified regions. We observed high correlation between biological replicates and similar average coverage between control and treated samples (Figures 3.6). The average CpG coverage for both genes in all samples was >15,000x. Of the 23 predicted CpG sites within the amplified DNMT1-dependent region on exon 8 of *HCN2*, 21 CpGs had adequate coverage (>1000x) in all samples and 14 CpGs were differentially methylated (Figure 3.7; Table 3.6). The mean percent methylation of all CpGs within the amplified DNMT1-dependent region was also significantly hypomethylated (Δme of -1.84%, FDR<0.05) (Figure 3.7).

We saw a similar trend in the DNMT1-dependent region at exon 1 of *NEFM*. Of the 39 predicted CpG sites within the amplified DNMT1-dependent region, 35 CpGs had adequate coverage in all samples and 13 of these CpGs were differentially methylated. A slight majority (54%) of these differentially methylated cytosines were hypomethylated

(Supplemental Figure 4). The overall change in methylation ratio for the entire region was significant but very low (<0.1% absolute difference, FDR<0.01). As a result, we decided to focus on the first 200 bp of the 500 bp amplified region, which overlap both the CpG island at exon 1 as well as a CTCF transcription factor binding site reported by ENCODE (ENCODE 2012). In this region, there was a slightly higher change in methylation (Δme of -0.12%, FDR<0.05). Additionally, we used the CTCF binding site prediction tool to determine the exact CpG sites within the CTCF binding motif (Ziebarth and Bhattacharya 2013). One of the top hits predicted CpG binding on the negative strand at CpG sites 89-96 within the defined *NEFM* region (Figure 3.8, Table 3.7). Three of these four CpG sites were differentially methylated with half of them having >2% reduced methylation.

These data enable us to conclude that the methylation status of DNMT1-dependent regions in the human genome are vulnerable to the neurotoxicant rotenone. We found that the coding regions and transcription factor binding motifs may be among the DNA elements that are particularly susceptible to exposure. The changes in methylation we observed were similar in scale to observed differential methylation at gene-encoding regions in the blood and brain of Parkinson's disease patients (Masliah et al. 2013; Navarro-Sanchez et al. 2018; Henderson-Smith et al. 2018; Wang et al. 2019). Both *HCN2* and *NEFM* are regionally expressed in Parkinson's disease tissues and their function has a critical role in neuronal plasticity and survival detailed in the discussion.

3.5 Discussion

Our previous work identified DNMT1-dependent putative non-germline ASMs in the mouse genome. In this study, we analyzed these regions and found that 70% were in highly conserved regions with the human genome. In the human genome, our candidate loci were often located at gene-coding regions and half of them overlapped transcription factor binding sites (Figure 3.1). Our observations agreed with another recent study which identified genome-wide ASMs in human samples from a Norfolk Island genetic isolate (Benton et al. 2019). Methylated cytosines alter gene expression by influencing the binding of transcription factors to DNA. We listed the top transcription factor binding sites within our identified candidate regions in human embryonic stem cells using ENCODE experimental data (Figure 3.1). Unsurprisingly, three of these transcription factors were TAF1, TBP, and POL2RA which all have an essential role in initializing transcription. We were interested to see SIN3A and RBBP5 which both interact with histone modifying enzymes to regulate chromatin accessibility and are critical during neurodevelopment (Gabriele et al. 2018). Furthermore, SIN3A is recruited to the methyl-CpG binding protein MeCP2 to silence transcription. Mutations in MeCP2 cause an X-linked neurodevelopmental disorder known as Rett Syndrome and similarly impairment of SIN3A expression also causes developmental cognitive deficits (Witteveen et al. 2016). MeCP2 and SIN3A have been linked to the establishment and maintenance of imprinting control regions but their effect on the expression of neighboring imprinted genes remains to be determined (Ma et al. 2015).

CTCF is another transcription factor of interest with 17% of the DNMT1-dependent human regions overlapping the CCCTC-binding motif. CTCF is also critical in neurodevelopment and chromatin organization (Franco et al. 2014, Davis et al. 2018). CTCF mediates the formation of chromatin loops and thus can promote widespread changes in gene expression (Hou et al. 2008, Phillips and Corces 2009). When bound to

sequences known as insulator sequences, CTCF represses transcription by blockading promoter-enhancer interactions (Bell et al. 2000, Hark et al. 2000). CTCF and the stabilizing protein cohesion bind at numerous imprinted control regions (Rubio et al. 2008, Prickett et al. 2013). CTCF has been reported to preferentially bind unmethylated chromatin but binding affinity depends not only on the methylation status of the motif itself but the surrounding CpG sites as well (Li et al. 2017, Wang et al. 2012).

Given the importance of imprinted gene clusters in development, we analyzed functional enrichment of our non-germline ASMs in the human genome. The most significant biological process associated with our gene set was cell to cell adhesion (Figure 3.2). We observed a significant group of cadherins at DNMT1-dependent regions on chromosome 5. Cadherin proteins are expressed on the membrane of embryonic stem cells and are critical for their self-renewal by forming tight intracellular niches (Pieters and Frans van Roy 2014). The expression of cadherin subtypes on embryonic stem cells is variable and the patterning of cadherin expression also controls their differentiation. Protocadherins are involved in neuronal connectivity and this function extends from neural progenitors during development into postmitotic neurons in the adult brain (Sams et al. 2016). Intriguingly, protocadherin is regulated by CTCF and deletion of CTCF in mice caused deficits in hippocampal learning and memory via dysregulation of protocadherin expression (Sams et al. 2016). The most significant molecular function was calcium ion binding and the pre-synaptic axon terminal was one of two most significant cellular components represented. This agreed with our network analyses where multiple genes were involved in cell trafficking and synaptic activity (Figure 3.2). We investigated whether developmental genes were specific to an individual tissue or group of tissues. These genes from DNMT1-dependent regions have significant enrichment of genes expressed in the cerebral cortex from two separate databases, EnrichR ArchS4 and Tissue Enrich Human Protein Atlas (Figure 3.3). Our data suggests that DNMT1-dependent non-

germline ASMs have enhanced expression in the brain, which could be important for neurological development and cellular communication function.

In our previous work, we characterized non-germline ASMs in the mouse genome at two genes, *Hcn2* and *Park7*, with potential in Parkinson's disease (Bonifati et al. 2003, Kim et al. 2005, Martos et al. 2017). The proper maintenance of the epigenome throughout aging is believed to have a major impact on the risk of neurodegeneration later in life (Gapp et al. 2014, Labbe et al. 2016). The influence of germline-ASMs on neurodegeneration has recently been of interest in the literature given their involvement in neurodevelopment but the effect of non-imprinted ASMs have not been well characterized (Gapp et al. 2014). To experimentally examine the association of identified ASMs in the human genome with Parkinson's disease, we used human embryonic kidney cells with a neuronal lineage phenotype and treated them with rotenone for 24h (Stepanenko and Dmitrenko 2015). We observed several of our candidate genes were affected in response to rotenone treatment and half of these genes have regional expression in Parkinson's disease associated regions (Figure 3.4). Among these genes, *HCN2* and *NEFM* were determined from our tissue enrichment analysis to have a higher expression level in the brain than any other tissue. Additionally, experimental analysis of *Hcn2* in the mouse genome suggests a random, switchable allele-specific methylation pattern that was independent of the parent-of-origin (Martos et al. 2017). We selected these two genes for methylation analysis to determine if conserved non-germline ASMs in the human genome were sensitive to environmental factors associated with Parkinson's disease.

The *HCN2* gene encodes an isoform of the hyperpolarization-activated cyclic nucleotide-gated channel located on the membrane of neurons in the central and peripheral nervous system. HCN channels regulate neuronal plasticity and have the advantage of using both voltage dependent mechanisms as well as cAMP intracellular

signaling mechanisms (DiFrancesco et al. 1999). In the midbrain, these channels control the spontaneous activity of dopaminergic neurons and their dysfunction has been linked to the depletion of dopamine in Parkinson's disease (Chen et al. 2011, DiFrancesco and DiFrancesco 2015, Good et al. 2011). In the human genome (hg19), the conserved DNMT1-dependent locus identified was 321 bp at a CpG island on exon 8 of the gene. We observed significant upregulation of mRNA expression levels (1.6-fold change, FDR<0.01) that correlated with DNA hypomethylation (-1.8%, FDR<0.05) of a 450 bp site surrounding the region of interest (Table 3.5; Figure 3.7; Table 3.6). Dysregulated *HCN2* expression could affect HCN2 channel activity leading to disrupted regulation of dopaminergic excitability.

The *NEFM* gene encodes a subunit of neuron-specific intermediate filaments known as neurofilaments. Neurofilaments are primary components of myelinated axons and are essential for synaptic function (Yuan et al. 2017). Neurofilament subunit expression is tightly regulated to maintain proper stoichiometry. As such, aberrant expression of *NEFM* likely disrupts axonal growth and transport. Interestingly, neurofilament subunits including the NEFM protein are considered promising neurodegeneration biomarkers due to their cell specificity and sensitivity to neuronal damage (Khalil et al. 2018). In Parkinson's disease patients, neurofilament proteins have been detected at higher levels in the cerebral spinal fluid, and more recently, in the blood (Abdo et al. 2007, Rosengren et al. 1996, Rojas et al. 2016). In our data, the conserved DNMT1-dependent locus covered a 150 bp region in exon 1 as well as a 1,650 bp region spanning exon 1 to intron 2. We observed significant upregulation of mRNA (1.7-fold change, FDR<0.01) and hypomethylation of a 200 bp section of the identified region at exon 1 (-0.12%, FDR<0.05). While the total change in percent methylation was relatively small, the selected region contained a CTCF binding site. Several CpG sites located within this CTCF binding motif had higher changes in methylation (>1%, adjusted q-value<0.01)

(Figure 3.8; Table 3.7). As mentioned previously, CTCF is hypersensitive to changes in DNA methylation and approximately 41% of CTCF binding variability has been attributed to DNA methylation (Wang et al. 2012). The lack of repressive signaling from CTCF could contribute to the observed increases in NEFM reported in Parkinson's disease patients and the observed overexpression of *NEFM* associated with cytoplasmic inclusions in motor-impaired mice (Sosa et al. 2003, Liu et al. 2011, Wong et al. 1995).

We evaluated the recent literature on candidate blood biomarkers in Parkinson's disease patients and observed five differentially methylated genes (*COL9A2*, *SCNN1A*, *AMICA1*, *SLC16A3*, and *DLK1*) in these studies within our conserved human regions (Henderson-Smith et al 2018; Wang et al. 2019). Of these genes, *COL9A2* was differentially expressed in our rotenone treated cells and was determined to have high regional expression in the substantia nigra (Table 2, Figure 4) (Henderson-Smith et al. 2018). This observation is strengthened with another study that has found that differentially methylated genes in the blood have high concordance with differentially methylated genes in the brain (Masliah et al. 2013). These data partially support our hypothesis that environmentally induced changes in DNMT1-dependent ASMs in the human brain can alter the risk of neurodegeneration.

DNMT1 expression in neural stem cells is essential for adult neurogenesis and the survival of adult neurons in the brain (Noguchi et al. 2015). We've shown that non-germline ASMs are dependent on DNMT1 in mice. The goal of this study was to identify conserved DNMT1-dependent regions and putative non-germline ASMs in the human genome and test the vulnerability of these regions to a neurotoxicant associated with Parkinson's disease. Our work identified candidate, non-germline ASMs with DNMT1 dependence as enriched in the human brain. We discovered 14 genes have altered expression (>1.5-fold change) at predicted ASMs in response to rotenone. We quantified methylation of 2 identified regions at adjacent genes (*HCN2* and *NEFM*) known to increase the risk for

Parkinson's disease and observed significant hypomethylation. In the future, a larger panel of these identified regions in the human genome will be tested in other cells lines at varying points in neuronal differentiation to determine the role of non-germline ASMs on neuronal development and its maintenance with age.

3.6 References

1. Abdo WF, Bloem BR, Van Geel WJ, Esselink RA, Verbeek MM. 2007. CSF neurofilament light chain and tau differentiate multiple system atrophy from parkinson's disease. Neurobiol Aging 28(5):742-747.
2. Afgan E, Baker D, Van den Beek M, Blankenberg D, Bouvier D, Čech M et al. 2016. The galaxy platform for accessible, reproducible and collaborative biomedical analyses: 2016 update. Nucleic Acids Res 44(W1):W3-W10.
3. Akalin A, Kormaksson M, Li S, Garrett-Bakelman FE, Figueroa ME, Melnick A et al. 2012. methylKit: A comprehensive R package for the analysis of genome-wide DNA methylation profiles. Genome Biol 13(10):R87.
4. Anders S, Pyl PT, Huber W. 2015. HTSeq—a python framework to work with high-throughput sequencing data. Bioinformatics 31(2):166-169.
5. Barlow DP, Bartolomei MS. 2014. Genomic imprinting in mammals. Cold Spring Harb Perspect Biol 6(2):10.1101/cshperspect.a018382; doi: 10.1101/cshperspect.a018382 [doi].
6. Bartolomei MS, Tilghman SM. 1997. Genomic imprinting in mammals. Annu Rev Genet 31(1):493-525.
7. Bell AC, Felsenfeld G. 2000. Methylation of a CTCF-dependent boundary controls imprinted expression of the Igf2 gene. Nature 405(6785):482.
8. Benton MC, Lea RA, Macartney-Coxson D, Sutherland HG, White N, Kennedy D, Mengerson K, Haupt LM, Griffiths LR. 2019. Genome-wide allele-specific methylation is enriched at gene regulatory regions in a multi-generation pedigree from the Norfolk Island isolate. Epigenetics and Chromatin 12(60); doi:10.1186/s13072-019-0304-7.
9. Bonifati V, Rizzu P, van Baren MJ, Schaap O, Breedveld GJ, Krieger E et al. 2003. Mutations in the DJ-1 gene associated with autosomal recessive early-onset parkinsonism. Science 299(5604):256-259; doi: 10.1126/science.1077209 [doi].
10. Butler MG. 2009. Genomic imprinting disorders in humans: A mini-review. J Assist Reprod Genet 26(9-10):477-486.
11. Chen, T., Hevi, S., Gay, F., Tsujimoto, N., He, T., Zhang, B., Ueda, Y., and Li, E. (2007). Complete inactivation of DNMT1 leads to mitotic catastrophe in human cancer cells. Nat Genet 39, 391-396.
12. Chen EY, Tan CM, Kou Y, Duan Q, Wang Z, Meirelles GV et al. 2013. Enrichr: Interactive and collaborative HTML5 gene list enrichment analysis tool. BMC Bioinformatics 14(1):128.
13. Chen L, Xu R, Sun F, Xue Y, Hao X, Liu H et al. 2015. Hyperpolarization-activated cyclic nucleotide-gated (HCN) channels regulate firing of globus pallidus neurons in vivo. Molecular and Cellular Neuroscience 68:46-55.
14. Davis L, Onn I, Elliott E. 2018. The emerging roles for the chromatin structure regulators CTCF and cohesin in neurodevelopment and behavior. Cellular and Molecular Life Sciences 75(7):1205-1214.
15. Deng Q, Ramskold D, Reinius B, Sandberg R. 2014. Single-cell RNA-seq reveals dynamic, random monoallelic gene expression in mammalian cells. Science 343(6167):193-196; doi: 10.1126/science.1245316 [doi].
16. DiFrancesco D. 1999. Dual allosteric modulation of pacemaker (f) channels by cAMP and voltage in rabbit SA node. J Physiol (Lond) 515(2):367-376.
17. Dolinoy DC, Weidman JR, Waterland RA, Jirtle RL. 2006. Maternal genistein alters coat color and protects avy mouse offspring from obesity by modifying the fetal epigenome. Environ Health Perspect 114(4):567-572; doi: 10.1289/ehp.8700 [doi].
18. ENCODE Project Consortium. 2012. An integrated encyclopedia of DNA elements in the human genome. Nature 489(7414):57.

19. Esumi S, Kakazu N, Taguchi Y, Hirayama T, Sasaki A, Hirabayashi T et al. 2005. Monoallelic yet combinatorial expression of variable exons of the protocadherin-α gene cluster in single neurons. Nat Genet 37(2):171.3
20. Fabregat A, Korninger F, Viteri G, Sidiropoulos K, Marin-Garcia P, Ping P et al. 2018. Reactome graph database: Efficient access to complex pathway data. PLoS computational biology 14(1):e1005968.
21. Franco MM, Prickett AR, Oakey RJ. 2014. The role of CCCTC-binding factor (CTCF) in genomic imprinting, development, and reproduction. Biol Reprod 91(5):125, 1-9.
22. Freeman, D. M., & Wang, Z. 2019. Towards the molecular mechanisms of transgenerational epigenetic inheritance: insights from transgenic mice. In Transgenerational Epigenetics (pp. 137-156). Academic Press.
23. Freeman DM, Lou D, Li Y, Martos SN, Wang Z. 2020. The conserved DNMT1 dependent methylation regions in human cells are vulnerable to environmental rotenone. Epigenetics & Chromatin, 13(1), 1-16.
24. Gabriele M, Tobon AL, D'Agostino G, Testa G. 2018. The chromatin basis of neurodevelopmental disorders: Rethinking dysfunction along the molecular and temporal axes. Prog Neuro-Psychopharmacol Biol Psychiatry 84:306-327.
25. Gapp K, Woldemichael BT, Bohacek J, Mansuy IM. 2014. Epigenetic regulation in neurodevelopment and neurodegenerative diseases. Neuroscience 264:99-111.
26. Good CH, Hoffman AF, Hoffer BJ, Chefer VI, Shippenberg TS, Bäckman CM et al. 2011. Impaired nigrostriatal function precedes behavioral deficits in a genetic mitochondrial model of parkinson's disease. The FASEB journal 25(4):1333-1344.
27. Hark AT, Schoenherr CJ, Katz DJ, Ingram RS, Levorse JM, Tilghman SM. 2000. CTCF mediates methylation-sensitive enhancer-blocking activity at the H19/Igf2 locus. Nature 405(6785):486.
28. Harris G, Eschment M, Orozco SP, McCaffery JM, Maclennan R, Severin D et al. 2018. Toxicity, recovery, and resilience in a 3D dopaminergic neuronal in vitro model exposed to rotenone. Arch Toxicol 92(8):2587-2606.
29. Henderson-Smith A, Fisch KM, Hua J, Liu G, Ricciardelli E, Jepsen K et al. 2019. DNA methylation changes associated with Parkinson's disease progression: Outcomes from the first longitudinal genome-wide methylation analysis in blood. Epigenetics 14(4):365-382.
30. Hou C, Zhao H, Tanimoto K, Dean A. 2008. CTCF-dependent enhancer-blocking by alternative chromatin loop formation. Proc Natl Acad Sci U S A 105(51):20398-20403; doi: 10.1073/pnas.0808506106 [doi].
31. Jain A, Tuteja G. 2018. TissueEnrich: Tissue-specific gene enrichment analysis. Bioinformatics 35(11):1966-1967.
32. Jirtle RL, Skinner MK. 2007. Environmental epigenomics and disease susceptibility. Nature reviews genetics 8(4):253.
33. Kacem S, Feil R. 2009. Chromatin mechanisms in genomic imprinting. Mammalian genome 20(9-10):544-556.
34. Kappil M, Lambertini L, Chen J. 2015. Environmental influences on genomic imprinting. Current environmental health reports 2(2):155-162.
35. Kerkel K, Spadola A, Yuan E, Kosek J, Jiang L, Hod E et al. 2008. Genomic surveys by methylation-sensitive SNP analysis identify sequence-dependent allele-specific DNA methylation. Nat Genet 40(7):904.
36. Khalil M, Teunissen CE, Otto M, Piehl F, Sormani MP, Gattringer T et al. 2018. Neurofilaments as biomarkers in neurological disorders. Nature Reviews Neurology 14(10):577-589.

37. Kim D, Pertea G, Trapnell C, Pimentel H, Kelley R, Salzberg SL. 2013. TopHat2: Accurate alignment of transcriptomes in the presence of insertions, deletions and gene fusions. Genome Biol 14(4):R36.
38. Kim RH, Smith PD, Aleyasin H, Hayley S, Mount MP, Pownall S et al. 2005. Hypersensitivity of DJ-1-deficient mice to 1-methyl-4-phenyl-1, 2, 3, 6-tetrahydropyrindine (MPTP) and oxidative stress. Proceedings of the National Academy of Sciences 102(14):5215-5220.
39. Krueger F. 2015. Trim galore. A wrapper tool around Cutadapt and FastQC to consistently apply quality and adapter trimming to FastQ files.
40. Labbé C, Lorenzo-Betancor O, Ross OA. 2016. Epigenetic regulation in Parkinson's disease. Acta Neuropathol 132(4):515-530.
41. Lachmann A, Torre D, Keenan AB, Jagodnik KM, Lee HJ, Wang L et al. 2018. Massive mining of publicly available RNA-seq data from human and mouse. Nature communications 9(1):1366.
42. Li L, Dahiya R. 2002. MethPrimer: Designing primers for methylation PCRs. Bioinformatics 18(11):1427-1431.
43. Li W, Qin W, Liu H, Fan L, Wang J, Jiang T et al. 2013. Subregions of the human superior frontal gyrus and their connections. Neuroimage 78:46-58.
44. Li Z, Dai H, Martos SN, Xu B, Gao Y, Li T et al. 2015. Distinct roles of DNMT1-dependent and DNMT1-independent methylation patterns in the genome of mouse embryonic stem cells. Genome Biol 16(1):115.
45. Liu Q, Xie F, Alvarado-Diaz A, Smith MA, Moreira PI, Zhu X et al. 2011. Neurofilamentopathy in neurodegenerative diseases. Open Neurol J 5:58-62; doi: 10.2174/1874205X01105010058 [doi].
46. Lonsdale J, Thomas J, Salvatore M, Phillips R, Lo E, Shad S et al. 2013. The genotype-tissue expression (GTEx) project. Nat Genet 45(6):580.
47. Ma P, de Waal E, Weaver JR, Bartolomei MS, Schultz RM. 2015. A DNMT3A2-HDAC2 complex is essential for genomic imprinting and genome integrity in mouse oocytes. Cell reports 13(8):1552-1560.
48. Martos SN, Li T, Ramos RB, Lou D, Dai H, Xu J et al. 2017. Two approaches reveal a new paradigm of 'switchable or genetics-influenced allele-specific DNA methylation'with potential in human disease. Cell discovery 3:17038.
49. Masliah E, Dumaop W, Galasko D, Desplats P. 2013. Distinctive patterns of DNA methylation associated with parkinson disease: Identification of concordant epigenetic changes in brain and peripheral blood leukocytes. Epigenetics 8(10):1030-1038.
50. Monteagudo-Sánchez A, Sánchez-Delgado M, Guara Ciurana S, Medrano J, Poo-Llanillo ME, Ishida M et al. 2018. Epigenetic asymmetry of DLGAP2: Pre-implantation maternal methylation switches to a random monoallelic profile in somatic tissues. OBM genetics. OBM Genetics 10.
51. Murphy SK, Hoyo C. 2013. Sculpting our future: Environmental nudging of the imprintome. In: Environmental Epigenomics in Health and Disease:Springer, 51-73.
52. Navarro-Sánchez L, Águeda-Gómez B, Aparicio S, Pérez-Tur J. 2018. Epigenetic study in Parkinson's disease: A pilot analysis of DNA methylation in candidate genes in brain. Cells 7(10):150.
53. Ning Y, Yang J, Ma G, Chen P. 2011. Modelling rock blasting considering explosion gas penetration using discontinuous deformation analysis. Rock Mech Rock Eng 44(4):483-490.
54. Noguchi H, Kimura A, Murao N, Matsuda T, Namihira M, Nakashima K. 2015. Expression of DNMT1 in neural stem/precursor cells is critical for survival of newly generated neurons in the adult hippocampus. Neurosci Res 95:1-11.

55. Onuchic V, Lurie E, Carrero I, Pawliczek P, Patel RY, Rozowsky J et al. 2018. Allele-specific epigenome maps reveal sequence-dependent stochastic switching at regulatory loci. Science 361(6409):10.1126/science.aar3146. Epub 2018 Aug 23; doi: eaar3146 [pii].
56. Orth M, Tabrizi S, Schapira A, Cooper J. 2003. α-Synuclein expression in HEK293 cells enhances the mitochondrial sensitivity to rotenone. Neurosci Lett 351(1):29-32.
57. Pedersen BS, Eyring K, De S, Yang IV, Schwartz DA. 2014. Fast and accurate alignment of long bisulfite-seq reads. arXiv preprint arXiv:1401.1129.
58. Phillips JE, Corces VG. 2009. CTCF: Master weaver of the genome. Cell 137(7):1194-1211.
59. Pieters T, van Roy F. 2014. Role of cell-cell adhesion complexes in embryonic stem cell biology. J Cell Sci 127(Pt 12):2603-2613; doi: 10.1242/jcs.146720 [doi].
60. Prickett AR, Barkas N, McCole RB, Hughes S, Amante SM, Schulz R et al. 2013. Genome-wide and parental allele-specific analysis of CTCF and cohesin DNA binding in mouse brain reveals a tissue-specific binding pattern and an association with imprinted differentially methylated regions. Genome Res 23(10):1624-1635; doi: 10.1101/gr.150136.112 [doi].
61. Rakyan VK, Chong S, Champ ME, Cuthbert PC, Morgan HD, Luu KV et al. 2003. Transgenerational inheritance of epigenetic states at the murine axin(fu) allele occurs after maternal and paternal transmission. Proc Natl Acad Sci U S A 100(5):2538-2543; doi: 10.1073/pnas.0436776100 [doi].
62. Robinson MD, McCarthy DJ, Smyth GK. 2010. edgeR: A bioconductor package for differential expression analysis of digital gene expression data. Bioinformatics 26(1):139-140.
63. Rojas JC, Karydas A, Bang J, Tsai RM, Blennow K, Liman V et al. 2016. Plasma neurofilament light chain predicts progression in progressive supranuclear palsy. Annals of clinical and translational neurology 3(3):216-225.
64. Rosengren LE, Karlsson J, Karlsson J, Persson LI, Wikkelsø C. 1996. Patients with amyotrophic lateral sclerosis and other neurodegenerative diseases have increased levels of neurofilament protein in CSF. J Neurochem 67(5):2013-2018.
65. Rubio ED, Reiss DJ, Welcsh PL, Disteche CM, Filippova GN, Baliga NS et al. 2008. CTCF physically links cohesin to chromatin. Proc Natl Acad Sci U S A 105(24):8309-8314; doi: 10.1073/pnas.0801273105 [doi].
66. Sams DS, Nardone S, Getselter D, Raz D, Tal M, Rayi PR et al. 2016. Neuronal CTCF is necessary for basal and experience-dependent gene regulation, memory formation, and genomic structure of BDNF and arc. Cell reports 17(9):2418-2430.
67. Sang L, Zhang J, Wang L, Zhang J, Zhang Y, Li P et al. 2015. Alteration of brain functional networks in early-stage Parkinson's disease: A resting-state fMRI study. PloS one 10(10):e0141815.
68. Sosa MAG, Friedrich Jr VL, DeGasperi R, Kelley K, Wen PH, Senturk E et al. 2003. Human midsized neurofilament subunit induces motor neuron disease in transgenic mice. Exp Neurol 184(1):408-419.
69. Stepanenko A, Dmitrenko V. 2015. HEK293 in cell biology and cancer research: Phenotype, karyotype, tumorigenicity, and stress-induced genome-phenotype evolution. Gene 569(2):182-190.
70. Susiarjo M, Sasson I, Mesaros C, Bartolomei MS. 2013. Bisphenol a exposure disrupts genomic imprinting in the mouse. PLoS genetics 9(4):e1003401.
71. Susiarjo M, Sasson I, Mesaros C, Bartolomei MS. 2013. Bisphenol a exposure disrupts genomic imprinting in the mouse. PLoS genetics 9(4):e1003401.

72. Szklarczyk D, Franceschini A, Wyder S, Forslund K, Heller D, Huerta-Cepas J et al. 2014. STRING v10: Protein–protein interaction networks, integrated over the tree of life. Nucleic Acids Res 43(D1):D447-D452.
73. Tanner CM, Kamel F, Ross GW, Hoppin JA, Goldman SM, Korell M et al. 2011. Rotenone, paraquat, and parkinson's disease. Environ Health Perspect 119(6):866-872; doi: 10.1289/ehp.1002839 [doi].
74. Teixeira J, Basit F, Swarts HG, Forkink M, Oliveira PJ, Willems PH et al. 2018. Extracellular acidification induces ROS-and mPTP-mediated death in HEK293 cells. Redox biology 15:394-404.
75. Walsh, C.P., Chaillet, J.R., and Bestor, T.H. (1998). Transcription of IAP endogenous retroviruses is constrained by cytosine methylation. Nat Genet 20, 116-117.
76. Wang C, Chen L, Yang Y, Zhang M, Wong G. 2019. Identification of potential blood biomarkers for Parkinson's disease by gene expression and DNA methylation data integration analysis. Clinical epigenetics 11(1):24.
77. Wang H, Lou D, Wang Z. 2018. Crosstalk of genetic variants, allele-specific DNA methylation, and environmental factors for complex disease risk. Frontiers in genetics 9.
78. Wang H, Maurano MT, Qu H, Varley KE, Gertz J, Pauli F et al. 2012. Widespread plasticity in CTCF occupancy linked to DNA methylation. Genome Res 22(9):1680-1688; doi: 10.1101/gr.136101.111 [doi].
79. Witteveen JS, Willemsen MH, Dombroski TC, Van Bakel NH, Nillesen WM, Van Hulten JA et al. 2016. Haploinsufficiency of MeCP2-interacting transcriptional co-repressor SIN3A causes mild intellectual disability by affecting the development of cortical integrity. Nat Genet 48(8):877.
80. Wong PC, Marszalek J, Crawford TO, Xu Z, Hsieh ST, Griffin JW et al. 1995. Increasing neurofilament subunit NF-M expression reduces axonal NF-H, inhibits radial growth, and results in neurofilamentous accumulation in motor neurons. J Cell Biol 130(6):1413-1422; doi: 10.1083/jcb.130.6.1413 [doi].
81. Yuan A, Rao MV, Veeranna, Nixon RA. 2017. Neurofilaments and neurofilament proteins in health and disease. Cold Spring Harb Perspect Biol 9(4):10.1101/cshperspect.a018309; doi: a018309 [pii].
82. Zhang Y, Rohde C, Reinhardt R, Voelcker-Rehage C, Jeltsch A. 2009. Non-imprinted allele-specific DNA methylation on human autosomes. Genome Biol 10(12):R138.
83. Zhou W, Bouhassira EE, Tsai HM. 2007. An IAP retrotransposon in the mouse ADAMTS13 gene creates ADAMTS13 variant proteins that are less effective in cleaving von willebrand factor multimers. Blood 110(3):886-893; doi: blood-2007-01-070953 [pii].
84. Ziebarth JD, Bhattacharya A, Cui Y. 2012. CTCFBSDB 2.0: A database for CTCF-binding sites and genome organization. Nucleic Acids Res 41(D1):D188-D194.
85. Zuin J, Dixon JR, van der Reijden MI, Ye Z, Kolovos P, Brouwer RW et al. 2014. Cohesin and CTCF differentially affect chromatin architecture and gene expression in human cells. Proc Natl Acad Sci U S A 111(3):996-1001; doi: 10.1073/pnas.1317788111 [doi].

3.7 Tables

Table 3.1 Predicted human DNMT1-dependent loci and genes

chr1:203012544-203013111	*PPFIA4*	chr1:151762641-151762866	*TDRKH*
chr9:130633077-130634324	*AK1*	chr1:40769328-40769695	*COL9A2*
chr20:2736325-2736555	*EBF4*	chr1:23789986-23792384	*ASAP3*
chr20:30133018-30134961	*MCTS2P/ HM13*	chr1:20569708-20569903	*UBXN10/VWA5B1/LINC01757*
chr20:30134986-30135324	*MCTS2P/ HM13*	chr1:17570695-17571208	*PADI1*
chr20:36149063-36149960	*NNAT/BLCAP*	chr4:3809685-3810214	*ADRA2C*
chr20:36150645-36151532	*NNAT/BLCAP*	chr4:6575638-6576768	*MAN2B2*
chr20:37356947-37357083	*SLC32A1*	chr4:24982328-24982857	*CCDC149/LGI2*
chr20:57424303-57428479	*GNAS*	chr1:90308879-90309031	*LRRC8D*
chr20:57429454-57430628	*GNAS*	chr1:90309136-90309398	*LRRC8D*
chr20:57428494-57429364	*GNAS*	chr12:120031502-120031941	*TMEM233*
chr20:57430647-57430802	*GNAS*	chr12:117146822-117147291	*C12orf49*

chr12:113400413-113400788	*OAS3*
chr7:94284623-94285630	*SGCE*
chr7:94285746-94285993	*PEG10*
chr7:94286061-94286219	*PEG10*
chr7:94286263-94287973	*PEG10*
chr7:130126204-130127042	*MEST*
chr7:130129122-3130129865	*MEST*
chr7:130130320-130132940	*MEST*
chr7:130133202-130135402	*MEST*
chr7:134955283-134955477	*STRA8*
chr7:139942121-139942907	*KDM7A/SLC37A3*
chr4:89618037-89618988	*NAP1L5/HERC3*
chr3:3842722-3843091	*LRRN1/SUMF1*

chr12:6451268-6451802	*TNFRSF1A/SCNN1A*
chr12:14518500-14518687	*ATF7IP*
chr19:55677470-55677864	*DNAAF3*
chr19:57349655-57353647	*PEG3/ZIM2/MIMT1*
chr19:47138150-47139513	*GNG8*
chr19:46148498-46149609	*EML2/GIPR*
chr19:45260696-45260939	*BCL3*
chr19:44008046-44008221	*PHLDB3*
chr19:42810915-42811210	*PRR19*
chr11:2018645-2019501	*H19*
chr11:2718814-2720223	*KCNQ1OT1/KCNQ1*
chr11:2720461-2722038	*KCNQ1OT1/KCNQ1*
chr4:175134957-175135614	*AK125257/FBXO8*

chr16:56624355-56625029	*MT3*
chr16:67313281-67313411	*PLEKHG4*
chr16:72698159-72698950	*AK201563/LINC01572*
chr16:81297176-81297683	*BCMO1*
chr16:89258400-89259894	*CDH15*
chr12:1100277-1100455	*ERC1*
chr19:10250933-10251636	*DNMT1*
chr11:118050777-118051248	*SNC2B/AMICA1*
chr15:79574796-79575831	*ANKRD34C*
chr3:147111981-147112692	*ZIC4*
chr6:144328582-144329817	*PLAGL1*
chr19:616132-616452	*HCN2*
chr7:50850069-50850216	*GRB10*

chr2:63271636-63272171	*EHBP1*
chr1:228612850-228612928	*HIST3H3/TRIM17*
chr17:10551758-10552335	*MYH3*
chr17:75723668-75724123	*LINC01987*
chr17:76133291-76133628	*TMC8*
chr17:80187539-80188383	*SLC16A3*
chr17:80797978-80799678	*TBCD*
chr14:74814669-74815870	*VRTN*
chr14:101275797-101278087	*MEG3/DLK1/MIR2392*
chr14:101290612-101291411	*MEG3*
chr14:101292483-101292929	*MEG3*
chr14:101292955-101294422	*MEG3*
chr6:656305-657021	*HUS1B/EXOC2*

chr6:18121790-18122423	*NHLRC1*
chr9:94123015-94123883	*AUH*
chr13:22246327-22246913	*FGF9*
chr8:28196773-28197118	*PNOC*
chr8:24771898-24773551	*NEFM*
chr8:24771655-24771790	*NEFM*
chr13:53423771-53424148	*PCDH8*
chr3:185795915-185797093	*ETV5*
chr6:158422346-158423188	*SYNJ2*
chr6:159084156-159084536	*SYTL3*
chr5:172306505-172306903	*ERGIC1*
chr6:36237727-36237965	*PNPLA1*
chr6:38997730-38998017	*DNAH8*

chr2:43058554-43059906	*HAAO*
chr4:11280093-11280328	*MIR572/HSTS31*
chr18:34823790-34823894	*CELF4*
chr5:140175896-140176159	*PCDHA2/PCDHA1*
chr5:140228130-3140228418	*PCDHA1-9*
chr5:140250568-140251167	*PDDHA1-11*
chr5:140554155-140554621	*PCDHB7*
chr18:56664106-56665166	*ZNF532/OACYLP*

Table 3.2 qRT-PCR primers for RNAseq validation in human cells

PPFIA4_For	CTCTGCGGATGTTGTCTCCC
PPFIA4_Rev	ATGCTGCCACTGGTTACACG
DNAAF3-For	GGGCTCAAGTCATTCACCCC
DNAAF3-Rev	GGTTGGGCACATGATAGGC
LRRC8D-For	ATGACATTCAGCCAACTTACCG
LRRC8D-Rev	TACTGGCAAACAGACCACCTG
9ADRA2C-For	GCCTCAACGACGAGACCTG
ADRA2C-Rev	CCCAGCCCGTTTTCGGTAG
EML2-For	CTCCGTAGCCGTGCTATACAG
EML2-Rev	CCAAGCATTTGATGTCATCGTTG
HCN2-For	AGAAGGGCATTGACTCCGAG
HCN2-Rev	TAGCGGATCAGGCGTGAGA
NEFM-For	GCTCGTCATTTGCGCGAATAC
NEFM-Rev	TTTCTGTACGCAGCGATTTCTAT
GAPDH-For	ACAACTTTGGTATCGTGGAAGG
GAPDH-Rev	GCCATCACGCCACAGTTTC

Table 3.3 BS-PCR primers for amplicon sequencing in human cells

HCN2-For	TGAGATTATTTTGGTTAATATGGTGAA
HCN2-Rev	CAAAAAAATAAAATTCTTCTTACCTAC
NEFM-For	GGTATTAAGGAGTTTTTGGAG
NEFM-Rev	CTAACCTAACCATTCCCATCTAAAC

Table 3.4 Gene Ontology cell component enrichment analysis

GO Term	Cellular Component	Gene Ratio	FDR
GO:0005886	plasma membrane	0.008	0.024
GO:0098793	presynapse	0.023	0.028

Table 3.5 Human DNMT1-dependent Genes Altered by rotenone*

Gene	Log2FC	FDR	Region Type	Function/Process
MYH3	-1.62	3.31E-09	intragenic	myosin protein; cell movement and transport
PPFIA4	-1.37	2.59E-13	intragenic	neurotransmitter release synaptic function
COL9A2	-0.79	1.53E-04	intragenic	collagen; extracellular matrix organization
DNAAF3	-0.78	3.59E-02	intragenic	dynein protein assembly; cell movement
LRRC8D	-0.78	8.42E-05	intragenic	ion channel protein; neurotransmission
PLEKHG4	-0.65	2.74E-03	intragenic	guanine exchange factor; cell signaling
ADRA2C	0.59	2.93E-02	intergenic	neurotransmitter release synaptic function
EML2	0.62	5.99E-05	promoter	microtubule protein; synaptic function
HCN2	0.66	1.10E-03	intragenic	voltage gated ion channel; action potential

KDM7A	0.67	1.16E-04	intergenic	histone demethylase; neurodevelopment
PHLDB3	0.76	3.75E-04	intragenic	enzyme binding; cell growth and proliferation
GIPR	0.76	2.37E-02	promoter	gastric inhibitory peptide; insulin release
BCL3	0.78	2.00E-02	intragenic	proto-oncogene; cell growth and proliferation
NEFM	0.80	4.33E-07	intragenic	neurofilament; synaptic function

***** Log2FC is the log base 2 fold change of the FPKM read counts of the rotenone treated *HEK293* relative to the vehicle control. FDR is the adjusted p-value using the false discovery rate correction method.

Table 3.6 CpG Methylation *HCN2*

CpG site	q-value	Δme
42	6.8E-18	-7.0
54	5.4E-06	-2.6
58	3.3E-04	-1.8
78	1.7E-04	-1.7
140	8.3E-19	-3.9
142	3.6E-13	-3.3
160	2.5E-25	-6.0
164	7.6E-17	-5.0
180	3.0E-13	-4.9
364	5.0E-05	-1.2
406	2.3E-04	1.0
420	1.2E-12	1.7
444	5.4E-06	1.5
450	2.1E-08	-2.7

Table 3.7 CpG Methylation *NEFM*

CpG site	q-value	Δme
42	6.8E-18	-7.0
54	5.4E-06	-2.6
58	3.3E-04	-1.8
78	1.7E-04	-1.7
140	8.3E-19	-3.9
142	3.6E-13	-3.3
160	2.5E-25	-6.0
164	7.6E-17	-5.0
180	3.0E-13	-4.9
364	5.0E-05	-1.2
406	2.3E-04	1.0
420	1.2E-12	1.7
444	5.4E-06	1.5
450	2.1E-08	-2.7

3.8 Figures

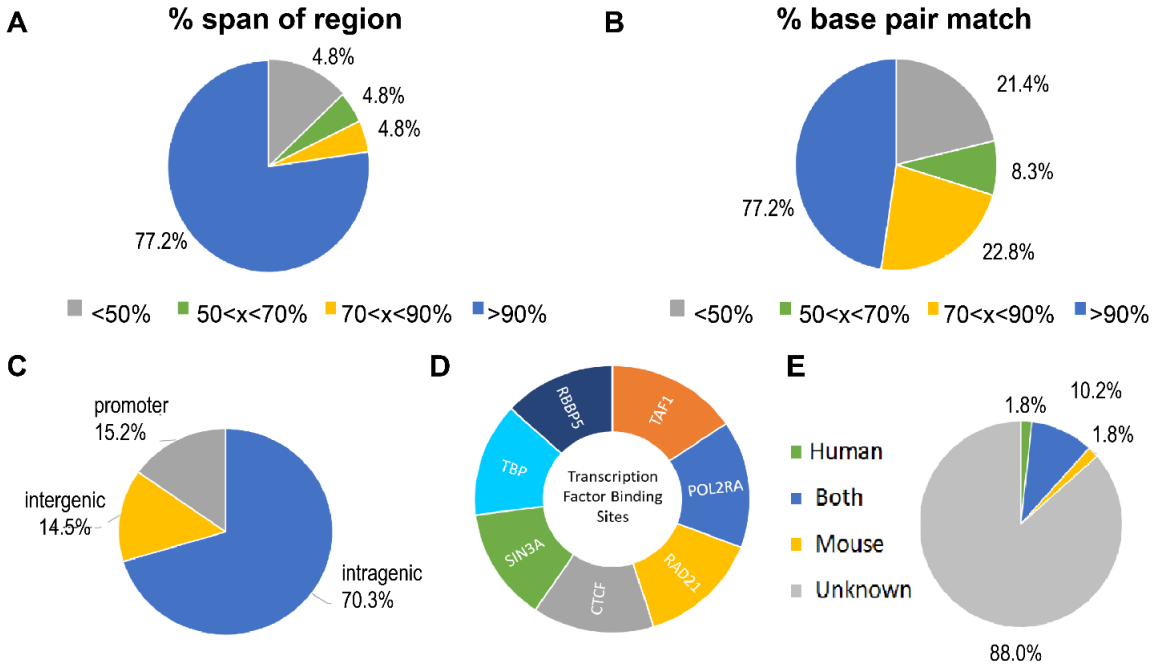

Figure 3.1 Characterization of DNMT1-dependent regions from mouse conserved in human genome.
A) The percent span of the DNMT1-dependent regions in mouse covered by the identified human conserved regions. Pie chart represents the percentage of all identified conserved regions in the human genome that fall into each category. B) The percent base pair match of the DNMT1-dependent regions in mouse with the identified human conserved regions. Pie chart represents the percentage of all conserved regions in the human genome that fall into each category. C) The percentage of all conserved regions in the human genome that are located within the promoter, the gene body, or in non-coding intergenic regions. D) The top transcription factor binding sites found within all human conserved regions. E) The percentage of known germline ASMs in our conserved DNMT1-dependent regions separated by genome.

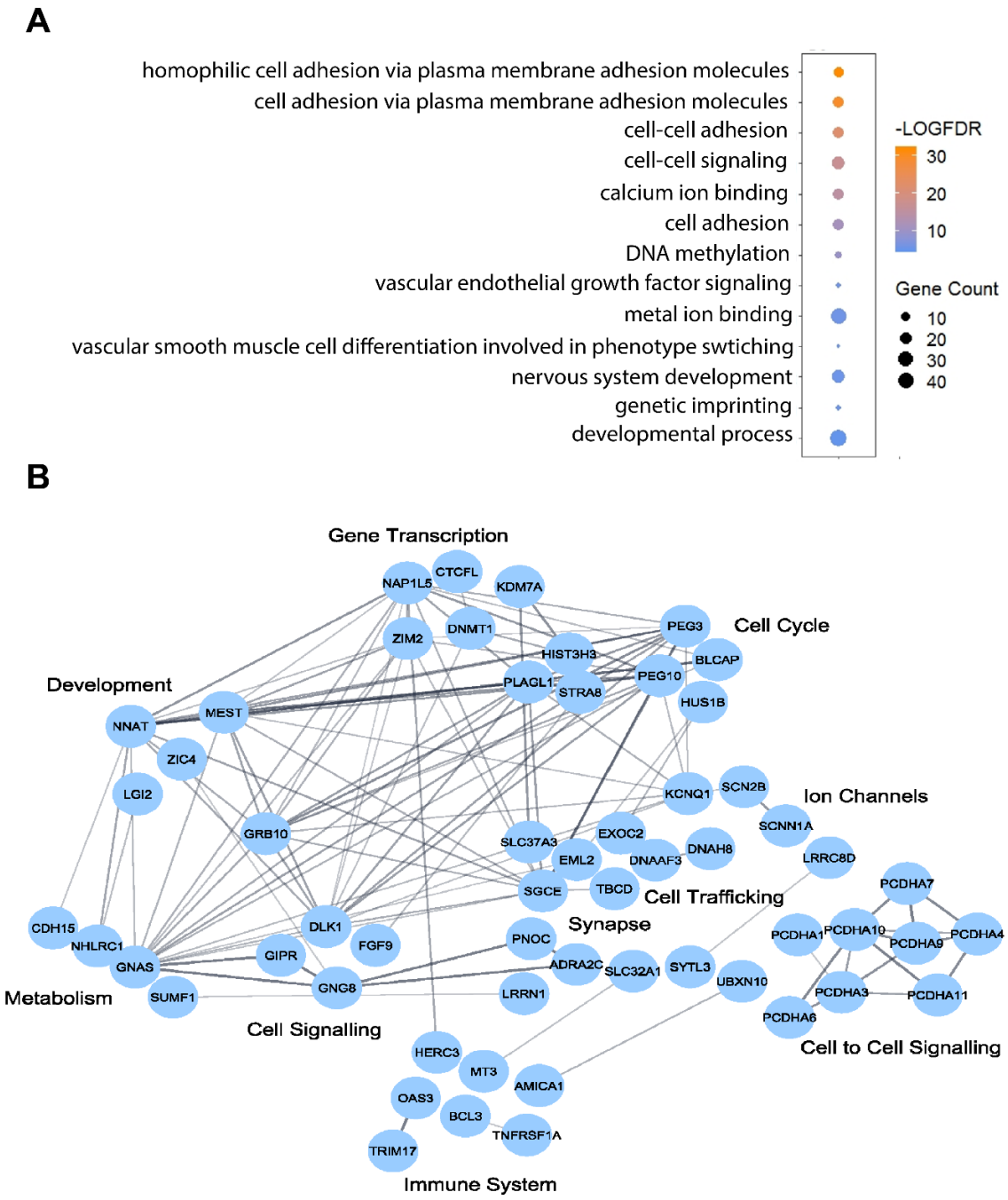

Figure 3.2 Functional enrichment analysis of DNMT1-dependent genes conserved in the human genome.

A) Gene Ontology enrichment for cellular processes and molecular functions from the 112 selected human DNMT1-dependent genes (adjusted p-value; false discovery rate FDR<0.05). B) Network interactions from STRING database with an interaction enrichment p-value < $1x\ 10^{-16}$. Genes are clustered based on functional gene annotations from reactome pathways.

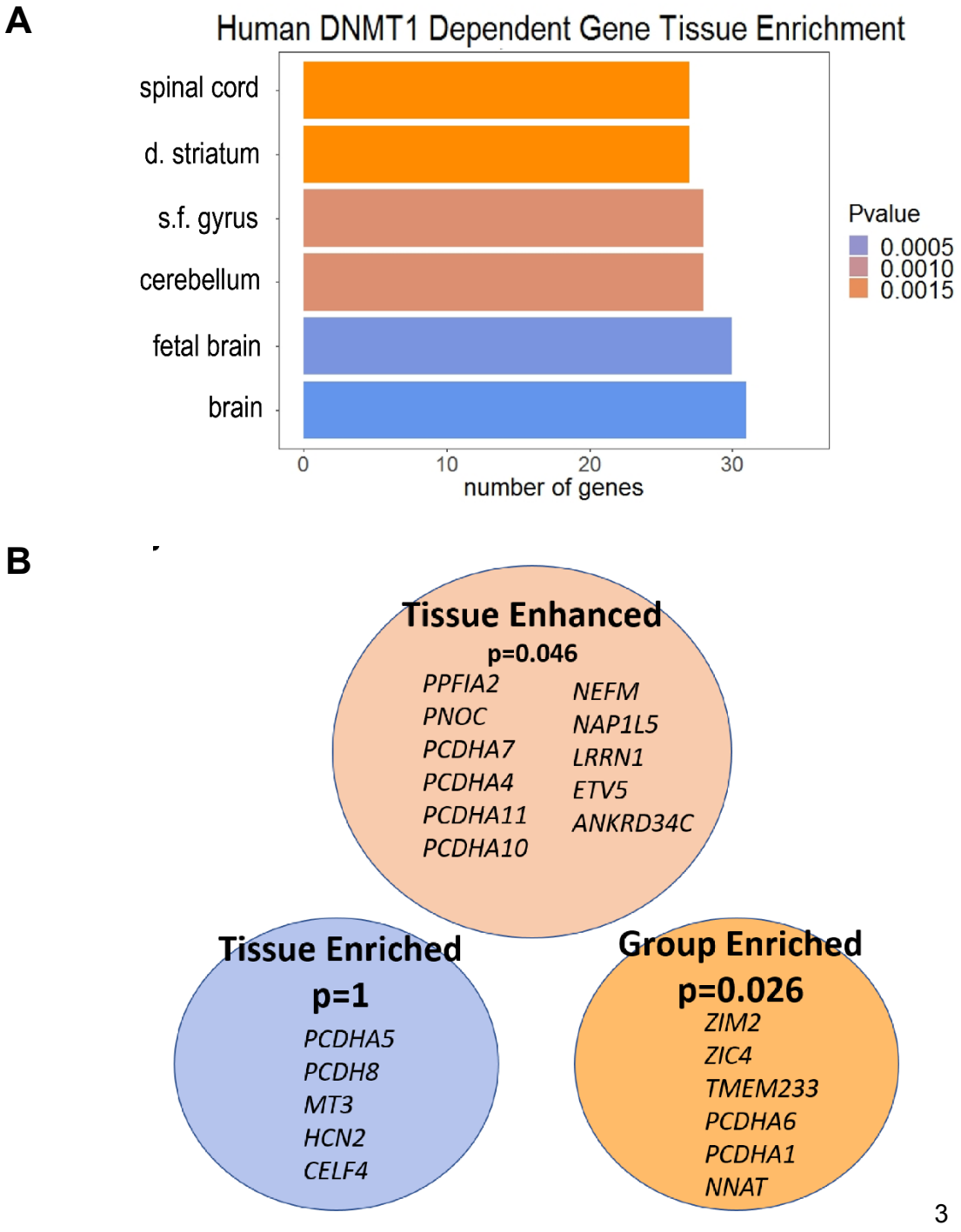

Figure 3.3 Tissue enrichment analysis of DNMT1-dependent genes conserved in the human genome.

A) The top 6 tissues represented from the 112 selected human DNMT1-dependent genes (adjusted p-value<0.01) scored from Enrich R using the ArchS4 human tissue database (s.f. gyrus = superior frontal gyrus; d. striatum= dorsal striatum). B) DNMT1 human genes

that are tissue-enriched, tissue-enhanced, or group-enriched genes within the cerebral cortex from Tissue Enrich (adjusted p-value shown).

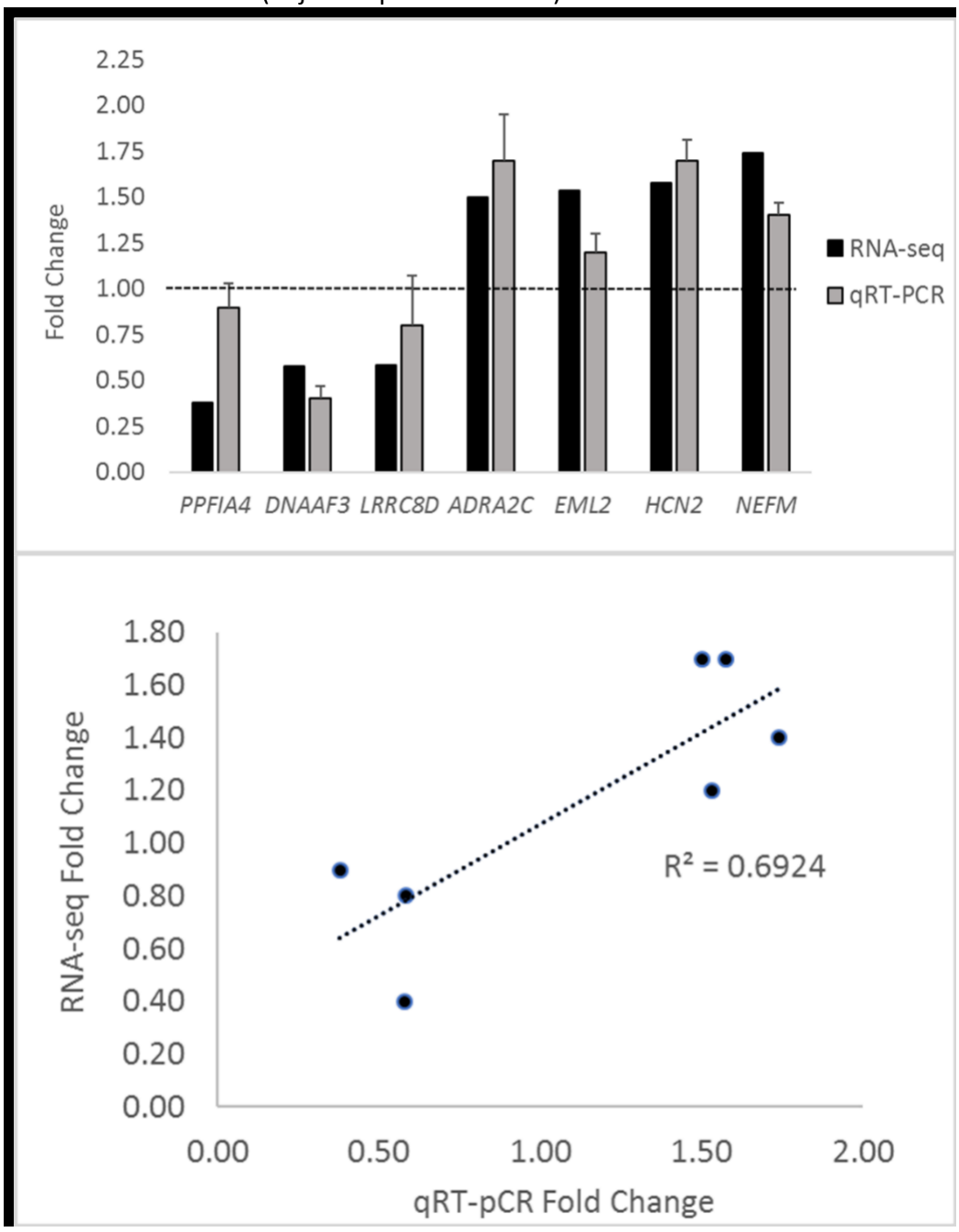

Figure 3.4 RNA sequencing validation with qRT-PCR.
Fold change comparison of RNA sequencing results versus qRT-PCR results and the linear calibration curve of RNA sequencing results with qRT-PCR results expressed as fold change in expression.

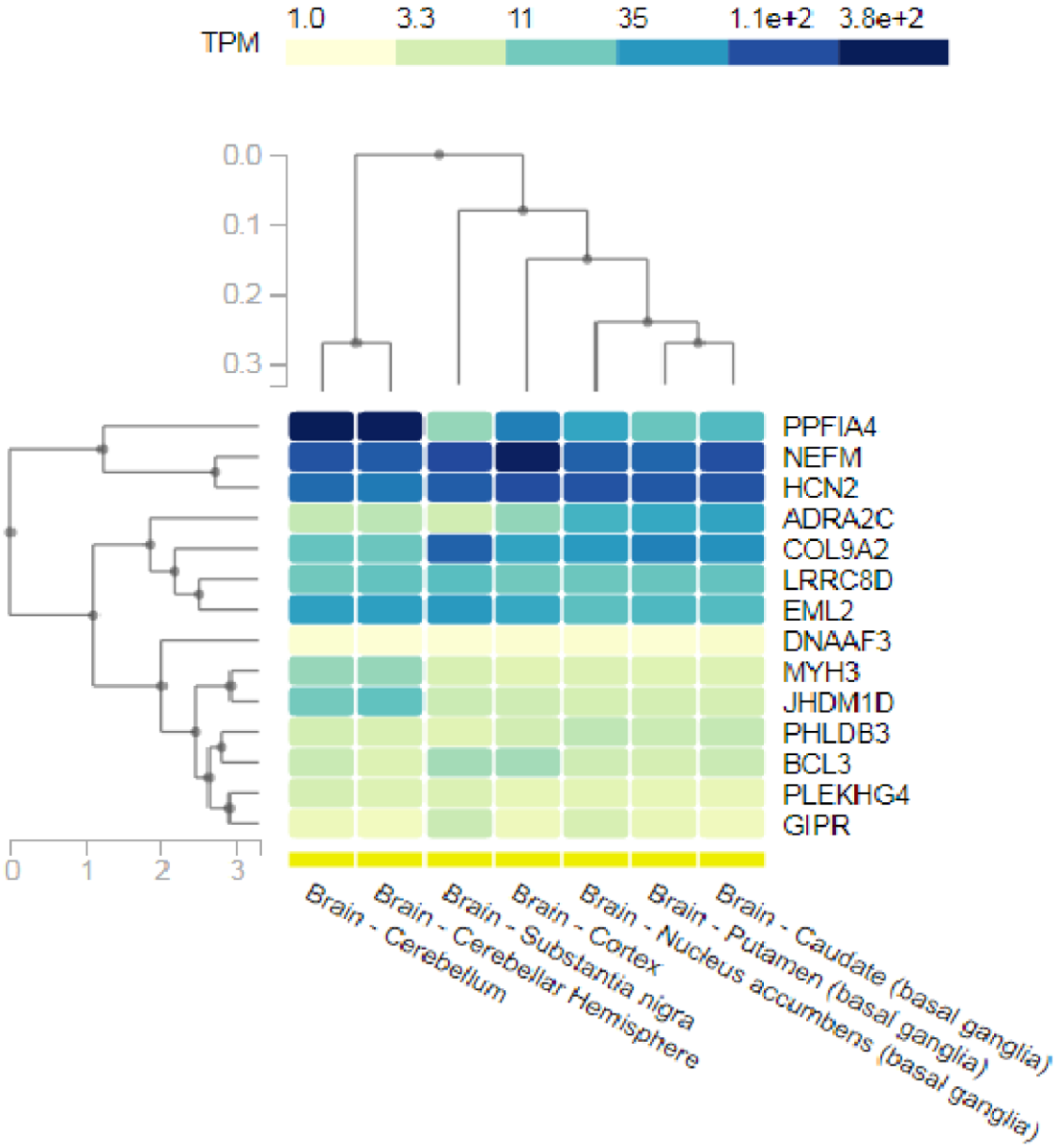

Figure 3.5 Regional expression of DNMT1-dependent genes altered by rotenone. Human DNMT1-dependent genes that were differentially expressed (≥1.5 fold change, false discovery rate FDR≤0.05) in response to rotenone were used for regional expression analysis in the Genotype-Tissue Expression (GTex) database. Brain regions selected are associated with Parkinson's disease pathogenesis and important for motor function control. The heat map was generated using GTex and organization is clustered by gene function and tissue function. The color of each square indicates the level of expression of the gene in the selected region in transcripts per kilobase million (TPM).

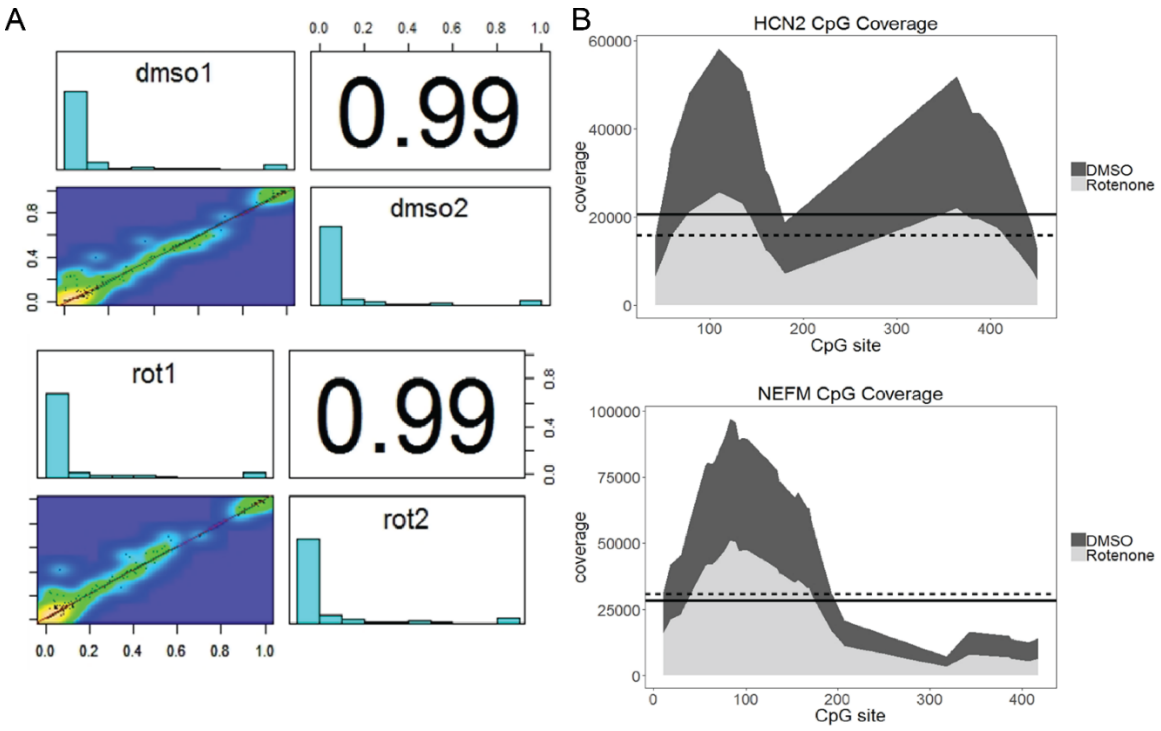

Figure 3.6 Bisulfite amplicon sequencing analysis
A) Correlation coefficients of Bisulfite sequencing data between biological replicates of control and rotenone treated samples. B) Sequencing coverage of CpG sites within amplified regions at *HCN2* and *NEFM*. The average total coverage for all CpG sites within the amplified region is indicated by the straight line for DMSO and the dash line for rotenone.

-

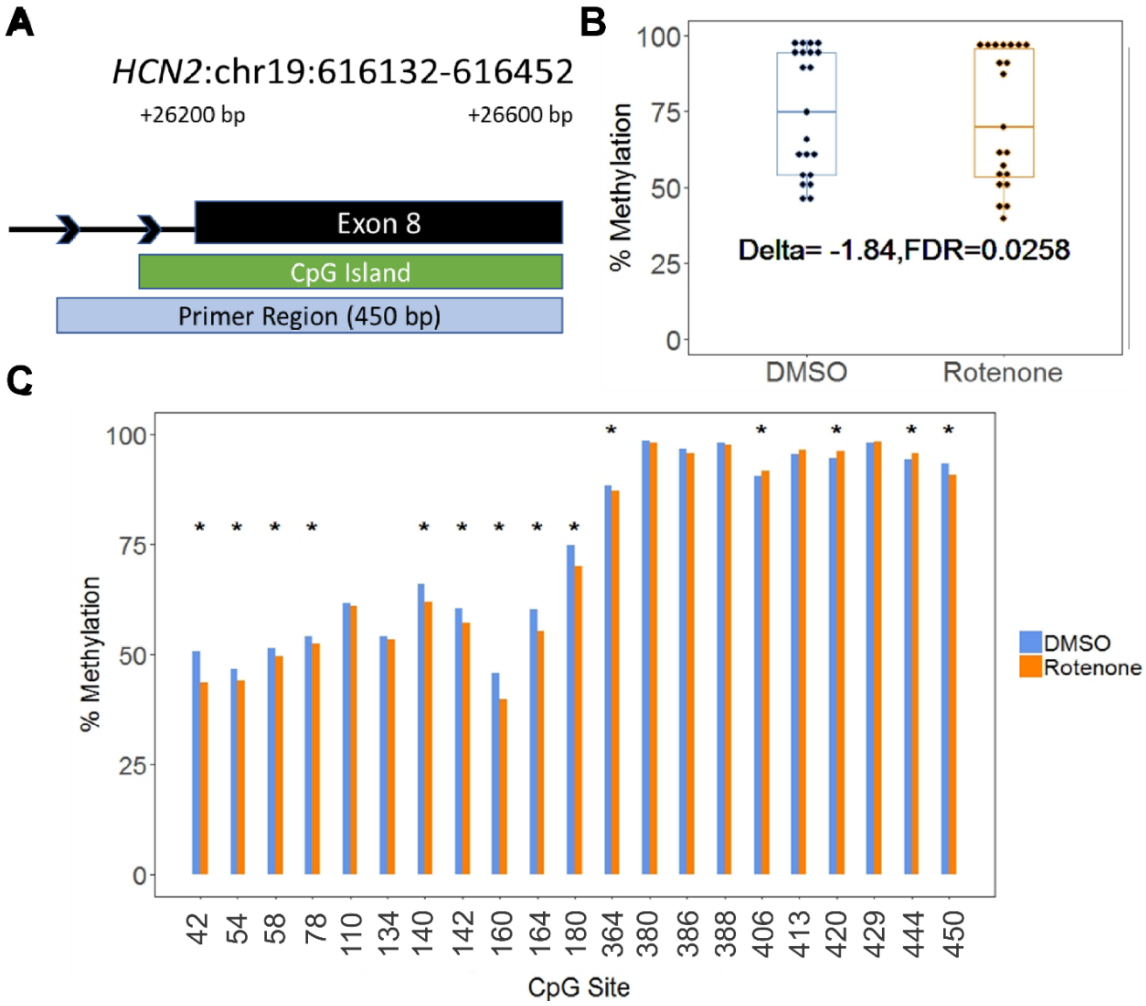

Figure 3.7 Altered CpG methylation at HCN2 human DNMT1-dependent locus. A) Genomic location of identified *HCN2* DNMT1-dependent region. The DNA element and distance from the transcription start site is annotated in black. The primer region box indicates the amplified region for Bisulfite-sequencing. B) The percent methylation of all CpG sites within the amplified region. Delta indicates the change in the mean CpG methylation percentage and the associated false discovery rate. C) The percent methylation of individual CpG sites within the amplified region. Significant differentially methylated cytosines are indicated by * (Δ>1%; q-value<0.01).

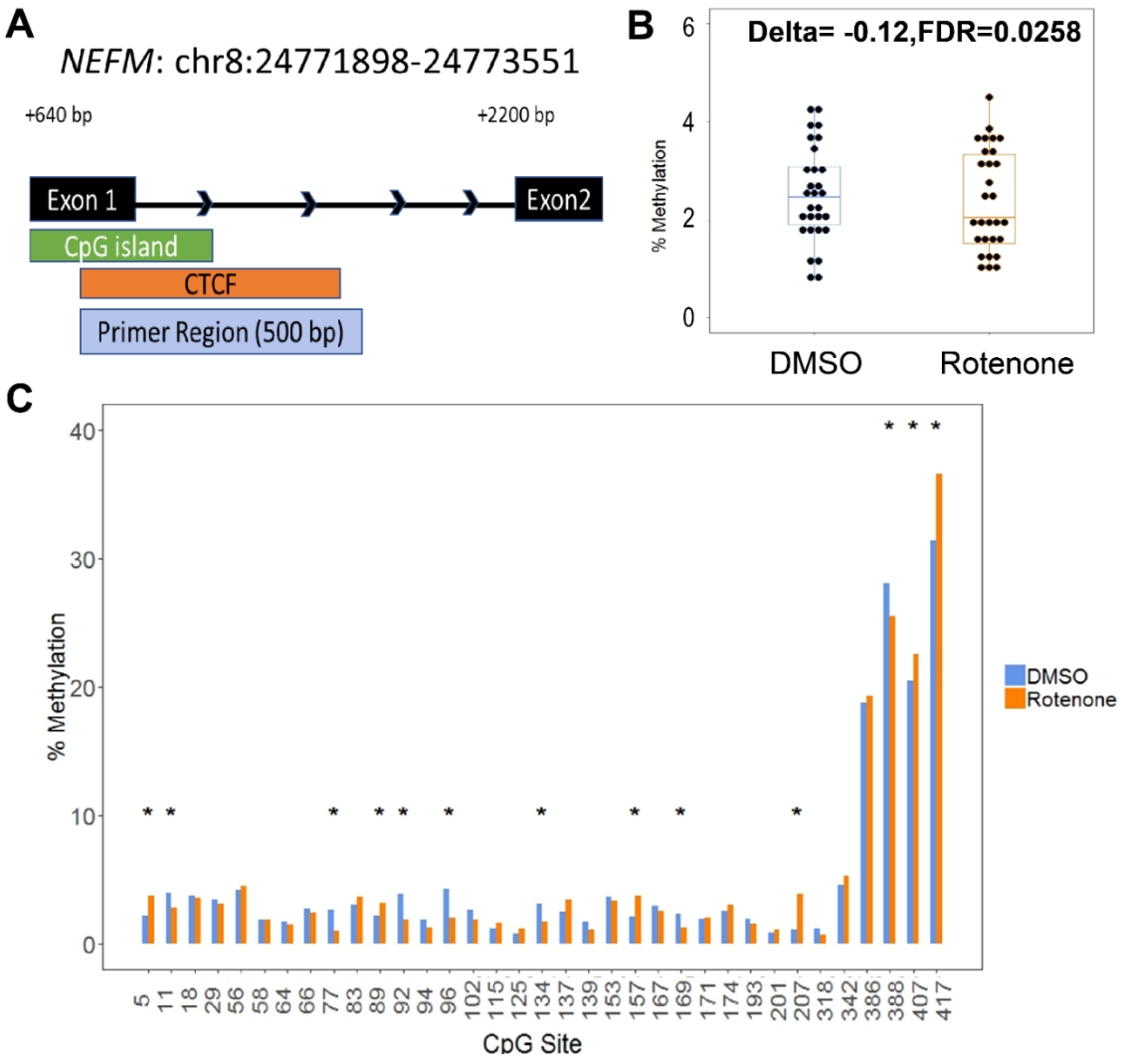

Figure 3.8 Altered CpG methylation at NEFM human DNMT1-dependent locus.
A) Genomic location of identified *NEFM* DNMT1-dependent region. The DNA element and distance from the transcription start site is annotated in black. The transcription factor binding site for CTCF was annotated from ENCODE v2 and ENCODE Uniform TFBS tracks in Genome Browser. The primer region box indicates the amplified region for Bisulfite-sequencing. B) The percent methylation of all CpG sites within the first 200 base pairs of the amplified region. Delta indicates the change in the mean CpG methylation percentage and the associated false discovery rate. C) The percent methylation of individual CpG sites within the amplified region. Significant differentially methylated cytosines are indicated by * (Δ>1%; q-value<0.01).

CHAPTER 4

ALPHA-SYNUCLEIN MEDIATES CHANGES IN DNA METHYLATION PATTERNS IN HUMAN NEURONS BY INTERFERING WITH DNMT1 TRANSLOCATION AND MAINTENANCE OF THE EPIGENOME.

4.1 Abstract

The aggregation of the neural protein α-Synuclein (α-Syn) is a hallmark of Parkinson's disease (PD) pathology and has become an attractive target for pharmaceutical intervention. Our data indicate that rotenone promotes α-Syn accumulation, and our previous study demonstrated vulnerability of DNA methylation patterns at allele-specific methylated regions and CTCF binding sites to the PD toxicant rotenone. Herein we hypothesized that rotenone-induced α-Syn mediates changes in DNA methylation patterns, causing global epigenetic reprogramming and genomic instability. To test our hypothesis, we treated human neuronal cell line SH-5YSY with rotenone for 24h and reported that rotenone induced α-Syn interacts with DNA methyltransferase1 (DNMT1). This interaction was associated with reduced DNMT1 translocation to the nucleus and global reductions in DNA 5-methylcytosine. Reduction of α-Syn expression significantly increased nuclear levels of DNMT1 (1.3-fold, $p<0.05$) and fortified mitochondria to rotenone exposure. Analysis of transcriptomic changes caused by rotenone exposure in control α-Syn and knockdown α-Syn neurons revealed a significant increase in the cellular defense response ($p<10^{-3}$) and the differential expression of genes that regulate p53 activation, dopamine synthesis, neurogenesis, and one-carbon metabolism. Intriguingly, α-Syn accumulation suppressed the hypoxic response to rotenone in SH-5YSY and altered the expression of prominent DNMT1-dependent imprinted genes. We discovered that targeting α-Syn partially rescued the hypoxic response and up-regulated the expression of hypoxia inducible factor (HIF1α) target

genes. The rescue of the hypoxic response can activate DNA methyltransferases and has the potential to increase DNA methylation patterns at imprinted control regions of DNMT1-dependent genes. We concluded that α-Syn knockdown did in fact rescue methylation patterns at both hypoxic response elements and in allele-specific methylated regions indicating a critical role for α-Syn mediating the epigenome.

4.2 Introduction

Alpha-synuclein (α-Syn) is an endogenous protein that localizes to the pre-synaptic membrane and associates with synaptic vesicles to facilitate neurotransmission (Ghiglieri et al. 2018). The structure of α-Syn consists of a lysine-rich, lipid-binding amino terminus and a disordered, acidic carboxyl terminus which interacts with synaptic proteins including the SNARE complex and the dopamine active transporter (Lashuel et al. 2013). The expression of α-Syn requires tight regulation. A lack of α-Syn can induce behavioral motor deficits (Abeliovich et al. 2000) and leads to a reduction of dopaminergic neurons in the substantia nigra during development (Garcia-Reitboeck et al. 2013). However, overexpression of α-Syn can drive oligomerization and disrupt neuronal function preventing proper neurotransmission (Scott et al. 2010). α-Syn aggregation into inclusion bodies (i.e. Lewy bodies) is associated with a disease phenotype known as a synucleinopathy and is a prominent feature in PD.

The gene encoding α-Syn is *SNCA,* and it was among the first genetic risk factors for PD (Singleton et al. 2004). Point mutations in the gene can promote misfolding and accumulation (Scott et al. 2010, Ghiglieri et al. 2018). Copy number variations are also associated with pathological Lewy bodies (Singleton et al. 2003) and reported to have a dose-response relationship with the risk of PD (Singleton et al. 2004). Oxidative stress and mitochondrial dysfunction can induce Lewy body formation in experimental models making α-Syn a powerful driver of both familial and sporadic PD (Uversky et al. 2001).

α-Syn also regulates gene expression and affects the expression of genes involved in the cellular stress response, epigenome editing, and dopamine synthesis (Baptista et al. 2003, Desplats et al. 2011, Motyl et al. 2018). DNA methylation regulates *SNCA* expression (Jowaed et al. 2010) and regulatory methylation has been reported at intron 1 of the *SNCA* gene (de Boni et al. 2015). Levodopa, the current primary treatment for PD, replaces dopamine in the brain and is associated with increased DNA methylation (Lu et al. 2013). DNA methylation and α-Syn aggregation are inversely correlated but the nature of their interaction remains a challenge to characterize (Jowaed et al. 2010, Kantor et al. 2018). However, it has been demonstrated in a genetic model of PD, that α-Syn aggregation can inhibit the functional role of DNA methyltransferases (DNMTs) *in-vitro* (Desplats et al. 2011).

Rotenone-induced oxidative stress causes a conformational change in α-Syn and accelerates its fibrillization *in-vitro* (Uversky et al. 2001). Our previous data demonstrate that rotenone causes global decreases in DNA methylation and affects methylation patterns at allele-specific methylated regions with dependence on DNA methylation enzyme, DNA methyltransferase I (DNMT1) (Freeman et al. 2020). We have also examined altered DNA methylation within CTCF binding motifs at PD associated genes that modified CTCF binding and insulator activity (*Chapter 2B*). These changes can have widespread effects on chromatin organization and genomic stability.

The first goal of this study was to examine the association of rotenone-induced α-Syn with DNMT1 activity in a human neuronal cell line. Our data revealed that accumulated α-Syn reduced global DNA methylation patterns in SH-5YSY cells (Figure 4.2). Our data agreed with another study in *SH-5YSY* that used viral induced overexpression of α-Syn to show decreases in global DNA methylation (Desplats et al. 2011). Studies have shown that inhibition of DNMT1 with the pharmacological inhibitor 5-Aza-2′-deoxycytidine increases the sensitivity of neurons to rotenone (Wang et al. 2013)

and that knockdown of *SNCA* expression makes neurons less susceptible to oxidative damage (Zharikov et al. 2015). Our next goal was to investigate the consequences of these findings by analyzing changes in the transcriptome and methylome of neuronal cells to rotenone both with and without α-Syn (using RNAi knockdown in *SH-5YSY*) influence. Our hypothesis is that rotenone-induced α-Syn mediates dysregulated maintenance of the methylome in neurons by impacting DNMT1 translocation to the nucleus (Figure 4.1).

4.3 Materials and Methods

4.3.1 Cell culture and treatment of human cell line SH-5YSY

All media reagents and chemicals in cell culture were purchased from Sigma (St. Louis, MO). SH-5YSY were grown in Dulbecco's Modified Eagle Medium with high glucose, L-glutamine, and sodium pyruvate. Media was supplemented with 10% (v/v) heat inactivated fetal bovine serum and 1% (v/v) Penicillin-Streptomycin. SH-5YSY cells were confirmed by ATCC. Cells were treated at approximately 60% confluency with rotenone (200 nM) or DMSO vehicle control (<0.001%) for 24h.

4.3.2 Rotenone induced α-Syn accumulation

SH-5YSY cells were collected after 24 hours treatment and cells were lysed with Pierce IP lysis buffer (ThermoFisher, Waltham, MA) with 1% protease inhibitor cocktail (P8340, Sigma, St. Louis, MO). Protein concentration from lysate was measured by Qubit Protein Assay from ThermoFisher (Waltham, MA). Protein (30 μ~~u~~g) was loaded onto 4-15% Bio-Rad Page Gels and transferred to 0.45 um nitrocellulose (Bio-Rad, Hercules, CA). The blots were incubated with α-Syn primary antibody (1:2500; Abcam ab138501) or GAPDH (1:5000; Sigma G9545) overnight at 4°C and anti-rabbit IgG conjugated secondary antibody (1:5000, Santa Cruz Biotechnology Sc-2357) for 1h at room temperature. Blots were visualized with chemiluminescence using ECL from GE Healthcare (Sigma, St. Louis, MO). We normalized α-Syn protein to GAPDH and

quantified with Image J software. We tested significance by comparing the ratio of α-Syn/GAPDH with a two-tailed Student's paired t-test.

4.3.3 Global DNA methylation analysis

Genomic DNA was extracted from three replicates of DMSO- or rotenone-treated SH-5YSY using 1:1:1 Phenol: Chloroform: Isoamyl alcohol (Sigma, St. Louis, MO). Global DNA methylation was first measured by dot blot analysis. Bisulfite treated DNA (30-60 ng/μL) was denatured at 95°C for 5 minutes and then cooled at 4°C for 5 minutes in a conventional thermocycler (Mycycler; Bio-Rad; Herclues, CA). DNA was spotted onto 0.45 micron nitrocellulose paper as 1 or 2 uL drops and dried for 30 minutes at room temperature. The membrane was UV crosslinked at 3000 Hz and incubated in anti-5mC primary antibody overnight at 4°C (Epigenetek 33D3; Farmingdale, NY). The membrane was washed with TBST and incubated with secondary antibody conjugated to HRP at room temperature (Santa-Cruz Biotechnology anti-mouse IgG sc-2005; Dallas, TX). The membrane was washed again with TBST after secondary incubation and visualized with chemiluminescence using Promethus ProSignal Femto-ECL Reagent (20-302, Genesee Scientific, San Diego, CA).

4.3.4 Co-immunoprecipitation of DNMT1 with α-Syn

SH-5YSY cells were collected after 24 h treatment and cells were lysed in Gibco phosphate buffer saline (PBS) pH 7.4 (ThermoFisher, Waltham, MA). PBS was supplemented with 1.25 M sucrose, 0.5 M EDTA (E9884), 0.5 M EGTA (E3889), 1% protease inhibitor cocktail (P8340), and 0.5% Triton-X (T8787) (Sigma, St. Louis, MO). Protein concentration from lysate was measured by Qubit Protein Assay from ThermoFisher (Waltham, MA). Protein input (10%) was saved before co-immunoprecipitation. We bound 4 μg α-Syn (Abcam 13850) and rabbit IgG (negative control, Cell Signaling Technologies 2729) at room temperature before being incubated

with protein lysate (0.5-1 mg) at 4°C overnight. After incubation, beads were washed and resuspended in the lysis buffer with 4x Laemmli.

Samples were denatured with bead at 95°C for 5 minutes and then loaded onto 4-15% Bio-Rad Page Gels (Bio-Rad, Hercules, CA). We transferred the proteins to 0.45 µm nitrocellulose membrane and incubated with α-Syn (1:2500; Abcam ab138501) and DNMT1 (1:1000, Imgenex IMG-261A) overnight at 4°C. We incubated with secondary anti-rabbit and anti-mouse IgG (1:5000, Santa Cruz Biotechnology sc-2357 & sc-2005) for 1h at room temperature. The blots were visualized by chemiluminescence with Promethus ProSignal Femto-ECL Reagent (20-302, Genesee Scientific, San Diego, CA).

4.3.5 siRNA transfection and treatment of human cell line SH-5YSY

SH-5YSY cells were plated in regular cell culture (*4.3.1*) until they reached 40% confluency. The media was then replaced with Opti-MEM with no additional supplements and transfected with lipofectamine RNAiMAX (ThermoFisher, Waltham, MA). The siRNA for SNCA knockdown was purchased with the TriFECTa DsiRNA Kit (ID hs.Ri.SNCA.13) from IDT Technologies (Coralville, IA). We first tested transfection conditions after 24h with the TYE 563 transfection control provided by the TriFECTa kit at 10nM concentration. We tested three separate double-stranded siRNA for *SNCA* knockdown after 24h post-transfection using qRT-PCR (details *4.3.10)* using primers for *SNCA* (F: GCAGCCACTGGCTTTGTCAA; R: AGGATCCACAGGCATATCTTCCA). We ran Western blot after 48h post-transfection to ensure α-Syn protein level was also reduced after knockdown (details *4.3.2*). We chose siRNA-2 (hs.Ri.SNCA.13.2) at 10 nM and used a scramble siRNA at the same concentration for the negative control (Neg Ctrl). Cells were treated based on Table 4.1. After transfection (36h), the media was replaced with fresh Opti-MEM containing treatment (DMSO or 200 nM rotenone), lipofectamine RNAiMAX, and 5 nM siRNA (scramble or SNCA) for 24h.

4.3.6 Toxicity assays on control and α-Syn knockdown SH-5YSY cells

Mitochondrial viability was estimated with the Presto Blue viability reagent (ThermoFisher, Waltham, MA). The reagent was added at 10% (v/v) and incubated for 1h at 37°C before measuring fluorescence (excitation 530 nm/ emission 590 nm). Intracellular reactive oxygen species (ROS) were measured with the DCFDA intracellular ROS assay according to kit instructions (Abcam, Cambridge, UK). Mitochondrial number was estimated with Mitotracker Red FM (Invitrogen, M22425). Following treatment, cells were incubated with Mitotracker (500 nM) for 1h at 37 °C. Cells were fixed with 1.5% formaldehyde for 10 mins at room temperature before fluorescence was measured at 580/640 nm. Mitochondrial DNA (mtDNA) copy number was estimated from 5 ng total DNA using a qPCR method published by Grady et al. 2014. We compared the mitochondrial gene ND1 (F: ATGGCCAACCTCCTACTCCT; R: GCGGTGATGTAGAGGGTGAT) to genomic genes *BECN1* (F: CGAGGCTCAAGTGTTTAGGC; R: ATGTACTGGAAACGCCTTGG) and *B2M* (F: CCAGCAGAGAATGGAAAGTCAA, R: TCTCTCTCCATTCTTCAGTAAGTCAACT). Statistical hypothesis testing with results from toxicity assays was done with a one-way ANOVA and the post-hoc Tukey honest significant differences test to correct for multiple hypotheses. The expression data from mtDNA quantification was analyzed with a one-way ANOVA and post-hoc pairwise t-test calculation with p-value correction using the false discovery rate (FDR) adjustment method.

4.3.7 Nuclear localization of DNMT1 in response to rotenone

Cells were lysed with PBS lysis buffer (from *4.3.4*) with only 0.05% Triton-X. Whole cell lysate (20%) was saved to test nuclear isolation. Cells were centrifuged at 600 x g for 6 minutes at 4°C and the supernatant was removed from the nuclei. Nuclei were washed in lysis buffer without supplementation and resuspended in fresh PBS lysis buffer with 0.5% Triton-X. Whole cell lysate and nuclear lysate was sonicated in an Ultrasonic Bath Sonicator three times for ten seconds each. We ran 15 µg of the whole cell lysate versus

the nuclear lysate on Western blot with nuclear marker H3 (1:1000, ab1791), cytoplasmic marker GAPDH (1:1000, G9549), and DNMT1 (1:1000, IMG-261A). We quantified DNMT1 in both whole cell lysate and nuclear lysate relative to H3 using Image J software. We tested significance by comparing the ratio of DNMT1/H3 with a two-tailed Student's paired t-test and a post-hoc false-discovery p-value correction.

4.3.8 RNA extraction and RNA sequencing library construction

Total RNA was extracted from two replicates of SH-5YSY using the Trizol method (Invitrogen, Carlsbad, CA). A total of 2 µg per sample was used for library construction using the TruSeq Sample Preparation kit from Ilumina (San Diego, CA). Poly-A containing mRNA 3molecules were isolated from total RNA using oligo-dT attached magnetic beads. Isolated mRNA was then fragmented and synthesized into double stranded cDNA according to kit instructions. Ligation of unique Ilumina adapter indices was completed for each sample before bead purification. Libraries were loaded onto a 2% agarose gel and library products between 200-800 bp were purified using the mini-Elute gel extraction kit from Qiagen (Hilden, Germany). Approximately 150 ng was sent for sequencing on a HiSeq-X platform with 100 bp paired-end reads.

4.3.9 RNA sequencing analysis

The raw BCL files were converted into FastQ files using CASAVA 1.8.2 (CASAVA). Raw sequencing reads were processed using TaRGETII RNA-seq pipeline which was prepared for large size RNA-seq sample processing (https://github.com/ShaopengLiu1/RNA-seq_QC_analysis). Cutadapt (V2.8) (Martin 2011) was used to remove any remaining adapter sequences from the high throughput sequencing reads. Sequencing reads were aligned to the human genome (hg38) with STAR aligner (v2.5.4b) (Dobin et al. 2013). For mRNA analyses, the Gencode database (Gencode version 27) was chosen as the annotation reference. Read counts of annotated genes were counted using featureCount from the SubRead package (Liao et al. 2013).

The raw read counts of each transcript were normalized by library size, then further normalized based on empirical controls using RUVg from the RUVseq package (REF-PMID: 25150836). Differentially expressed genes were defined as those with a 1.5-fold change in expression using an FDR<0.05 from the edgeR package (Robinson et al. 2010). Gene Ontology annotation was done with the GOrila and the EnrichR online platforms and visualized with Revigo (Eden et al. 2009; Chen et al. 2013; Supek et al. 2011). Biological pathway analysis was done with KEGG Human Pathways 2019 and reactome pathway analysis (Kaneisha et al. 2019; Fabregat et al. 2018).

4.3.10 qRT-PCR validation

Total RNA was extracted from an additional replicate of control and α-Syn knockdown. Both control and knockdown SH-5YSY cells treated with DMSO or rotenone were used using the same procedures as stated above. A total of 500 ng RNA was converted to cDNA with the PrimeScript RT reagent kit with gDNA eraser from Takara (Kusatsu, Japan). We selected twelve genes for quantitative PCR (qRT-PCR) analysis using primers listed in Table 4.2. All qRT-PCR reactions were performed on a 7500 Real-Time PCR system from Applied Biosystems (Foster City, CA) using the iTaq Universal SYBR Green Supermix from Bio-Rad (Hercules, CA). The change in expression was normalized to the *GAPDH* housekeeping gene and expressed as fold change ($2^{-\Delta\Delta CT}$).

4.3.11 Bisulfite-DNA conversion and Bisulfite-amplicon sequencing library construction

Genomic DNA was extracted from two replicates of DMSO or rotenone-treated SH-5YSY using Phenol: Chloroform: Isoamyl alcohol (Sigma, St. Louis, MO). A total of 200 ng DNA was Bisulfite-converted using the Sigma DNA Imprint Modification kit two-step protocol. Bisulfite-converted DNA (BS-DNA) was amplified with primers for selected DNMT1-dependent regions and hypoxic pathway regions designed in MethPrimer (Li and Dahiya 2002) (Table 4.3). Amplified BS-DNA products were run on a 2% EtBr agarose gel and purified using the mini-Elute gel extraction kit from Qiagen (Hilden, Germany). Purified

products for each sample were pooled together and 1 ng was used for library preparation using the Ilumina Nextera DNA Library Preparation kit. Each sample was tagged with a unique Nextera XT adapter (San Diego, CA). Sequencing libraries were quality checked via Bioanalyzer and run on an Ilumina NovaSeq platform to generate 150 bp paired end reads.

4.4.12 Bisulfite-amplicon sequencing analysis

The raw fastq files were imported into the Galaxy web platform (Afgan 2016). Reads with quality score >30 were trimmed with Trim Galore (Krueger 2015). Reads were mapped to amplified sequences in the human genome (hg38) using bwa-meth (Pederson et al. 2014). MethylDackel was used for methylation calling and per-cytosine contexts were merged into per-CPG metrics (https://github.com/dpryan79/MethylDackel). Duplicates and singletons identified in alignment were ignored from the methylation call. Minimum and maximum per-base depths 3were 1000x and 100,000x, respectively. The output was selected for methylKit format. Coverage statistics and differentially methylated regions were calculated for CpG sites with methylKit installed in R (v3.5) (Akalin et al. 2012). Differentially methylated cytosines were defined as being present in both biological replicates, having a minimum absolute difference of 0.1% using the coverage weighted mean, and having a SLIM adjusted q-value<0.05 using the methylKit logistic regression model (Ning et al. 2011). The change in mean percent methylation (Δme) for all CpG sites within a defined region was calculated by taking the mean number of methylated versus non-methylated CpG sites from the pooled control and treated samples and using Fisher's exact test $p<0.05$.

4.5 Results

4.5.1 Rotenone-induced a-Syn accumulation is associated with DNA hypomethylation.

We selected a rotenone dose of 200 nM for 24h based on our results in *HEK293* (Chapter 2A.4.1). This dose was also shown by other labs to induce endogenous protein

levels of α-Syn in SH-5YSY cells (Sala et al. 2013, Chorfa et al. 2013). We checked with Western blot and observed significant accumulation of α-Syn (1.3-fold change, $p<0.05$) (Figure 4.2). We examined global DNA methylation with dot blot and observed genome-wide reductions like those found in *HEK293* cells (Chapter 2 Figure 2.4) *(*Figure 4.2). Together, we conclude that rotenone exposure-induced α-Syn leads to DNA demethylation.

4.5.2 Co-immunoprecipitation of DNMT1 occurs only in rotenone treated cells.

To explore the mechanism behind changes in global DNA methylation after exposure, we tested our hypothesis that accumulated α-Syn impacts DNMT1 from maintaining methylation patterns. Co-immunoprecipitation of α-Syn pulled down DNMT1 only in rotenone-treated cells but not in control cells, thus providing evidence that endogenous α-Syn can interact with DNMT1 inside the cell after exposure (Figure 4.3). Because rotenone exposure induced more α-Syn within treated cells, it may suggest that either increased protein level of α-Syn or exposure-altered conformation changes of α-Syn (or both) initiated protein-protein interaction.

4.5.3 siRNA transfection and knockdown of SNCA in SH-5YSY neuronal cell line.

Given the fact that copy number variations of the *SNCA* gene linearly increases risks for familial PD (Singleton et al. 2004), it suggests that dysregulated α-Syn (presumably over a threshold) plays a causal role in PD pathogenesis. To explore the hypothesized role of accumulated α-Syn in PD, we aim to use RNAi to reduce rotenone-induced α-Syn, and then check cellular responses. We optimized transfection conditions by using visual transfection of the TYE-563 fluorescent dye with fluorescence microscopy (Figure 4.4). We tested *SNCA* knockdown with three independent siRNAs provided by the IDT TriFECTa kit using qRT-PCR and chose hs.Ri.SNCA.13.2 based on its ability to significantly reduce both *SNCA* transcripts and α-Syn protein in non-treated and rotenone treated SH-5YSY cells (Figure 4.4). The knockdown efficiency of siRNA in qRT-PCR was

0.07-fold in non-treated cells and 0.16-fold in rotenone treated cells ($p<0.01$). The protein level of α-Syn was reduced -1.0-fold in non-treated cells and -0.8-fold in rotenone treated cells ($p<0.05$).

4.5.4 α-Syn knockdown cells were resistant to rotenone toxicity in-vitro.

To determine the extent to which α-Syn knockdown cells were resistant to rotenone toxicity, we used four independent tests of mitochondrial viability and function (Figure 4.5). We used the Presto Blue viability assay to measure mitochondrial reduction capacity as a proxy for mitochondrial viability. α-Syn knockdown resulted in significantly higher viability of mitochondria treated with rotenone when compared to the negative control cells. Oxidative stress is a common result of mitochondrial damage and we observed increases in intracellular ROS in rotenone-treated *HEK293* cells (*Chapter 2A.4.1).* In our SH-5YSY model, rotenone increased intracellular ROS only in control cells. There was an increase in ROS in negative control cells (1.2-fold change) but it was not significant. There was no observed increase in oxidative species in knockdown cells. The number of mitochondria was estimated with the Mitotracker FM Red fluorescent dye. Both control and negative control cells had reduced mitochondrial fluorescence signal in response to rotenone (0.5-fold and 0.6-fold, respectively) ($p<0.05$). There was no change in fluorescence in rotenone treated knockdown cells. Lastly, we used mtDNA copy number as a surrogate for mitochondrial function using the relative abundance of genes encoded by nuclear DNA (*BECN1* and *B2M*) with a gene encoded only in mitochondria *(ND1*). Mitochondrial gene, *ND1*, encodes the mitochondrial electron transport chain complex I which is targeted by rotenone. This region is highly conserved in mitochondria and reported to be closely associated with mitochondrial respiratory function (Grady et al. 2014). We observed a significant decrease in mtDNA copy number in control and negative control cells but not in α-Syn knockdown cells. This was consistent regardless of which genomic gene was used to estimate relative copy number. Therefore, our data demonstrate that targeting α-

Syn protects neuronal cell line SH-5YSY viability by fortifying mitochondria from propagated oxidative damage induced by rotenone (Figure 4.5). Altogether, we conclude that α-Syn plays a critical role in mediating the effects of the mitochondrial stress response on chromatin structure in neurons.

4.5.5 DNMT1 nuclear protein in response to rotenone is increased in α-Syn knockdown neurons.

We showed that rotenone-induced α-Syn can interact with DNMT1 in control SH-5YSY cells. To investigate whether this interaction can obstruct DNMT1 from translocating to the nucleus, we measured nuclear levels of DNMT1 protein in control and knockdown cells exposed to rotenone (Figure 4.6). In control cells, rotenone did not affect whole cell concentrations of DNMT1 protein but decreased nuclear protein (control: 0.56-fold; negative control: 0.68-fold). In α-Syn knockdown cells, rotenone did not affect whole cell or nuclear concentrations of DNMT1. Nuclear DNMT1 level was increased in rotenone-treated α-Syn knockdown compared to the negative control ($p<0.05$).

4.5.6 Rotenone alters the expression of genes involved in mitochondrial and neuronal health.

To gain insights of rotenone alteration at the transcriptomic level, we examined changes in the transcriptome of rotenone treated control cells using RNA sequencing. RNA-seq analyses identified 526 genes differentially expressed in response to exposure (FDR<0.05). Most of the genes identified are involved in functions within the nucleosome or at the neuronal synapse (Figure 4.7). Another cellular structure involved in the cellular response was the axolemma which is the membrane of the neuronal axon responsible for maintaining the action potential to support neurotransmission. The biological processes significantly altered were involved in glucose metabolism, ATP generation, and the cellular response to hypoxia (Figure 4.7). We focused on which of these processes were up-regulated versus down-regulated in our dataset using a ranked list of our genes separated

by log2FC and ordered by significance (FDR) (Figure 4.7). Processes involved in cell death and the mitochondrial mediated intrinsic apoptotic pathway were among those up-regulated. We also observed TP53 activation, DNA damage response, and cell cycle arrest in our pathway enrichment analysis using reactome ($p<0.01$). In contrast, neurogenesis and neuronal development and maturation were down-regulated. We highlighted four genes with a key role in these pathways in Figure 4.7. The significance of these genes is in the discussion section.

4.5.7 Rotenone treatment in α-Syn knockdown cells alters the oxidative stress response.

We identified 128 genes that were differentially expressed in response to rotenone in knockdown cells. The axon remained a primary cellular component for these genes. Only three biological processes were significantly enriched (FDR<0.05) (Figure 4.7). These biological processes are relevant to the hypoxic response and are hypothesized to have a role in neurodegeneration as discussed in the discussion section. Among up-regulated genes, central nervous system neuronal differentiation and the bone morphogenesis pathway were represented using Gene Ontology annotations ($p<0.05$). The down-regulated genes were enriched in biological processes associated with cell migration and mesenchymal cell proliferation (Figure 4.7).

We also analyzed the enriched molecular functions in knockdown cells exposed to rotenone ($p<0.05$) (Figure 4.7). The top molecular functions represented ($p<0.001$) included carbonic anhydrase activity in the antioxidant response and transmembrane transporter activity. Carbonic anhydrases are regulators of the oxidative metabolism of glucose and thus play a part in the propagation of damage induced by intracellular ROS (Shah et al. 2013). Transmembrane water and ammonia transporters are also critical to maintain cellular homeostasis under cellular stress. For instance, dysregulated intracellular concentrations of ammonia initiate mitochondrial permeability in apoptosis (Rama et al. 2005). While α-Syn knockdown does not prevent oxidative stress caused by

rotenone inhibition of mitochondrial respiration, we did not discover the same associated effects on ATP generation, neurogenesis, or neuronal differentiation. This agrees with our earlier conclusion that targeting α-Syn confers resistance by strengthening mitochondria from propagated oxidative damage caused by rotenone complex I inhibition (Figure 4.5).

4.5.8 α-Syn knockdown increases the expression of genes in the cellular defense response.

Out of the 526 genes differentially expressed in rotenone-treated negative control cells and 129 genes in rotenone-treated α-Syn knockdown cells, 73 genes overlapped both datasets. These concordant genes were involved in endothelial cell migration, mesenchymal transition, and transporter activity as noted in the knockdown cells (Figure 4.7). To compare the differences in the cellular response to rotenone, we analyzed differential gene expression between rotenone-treated negative control cells and rotenone-treated α-Syn knockdown cells. There were 190 altered genes that altered the cellular response to rotenone. We analyzed the functional annotation of all differentially expressed genes as a single rank list in the order of expression (high Log2FC to low Log2FC) and revealed the enrichment the cellular defense response mediated by α-Syn knockdown ($p<0.001$) (Figure 4.8). We analyzed the pathways involved in these 190 genes with the 2019 KEGG Human pathway database (Figure 4.8). The top pathways with $p<0.001$ were one-carbon metabolism and HIF-1α signaling. We looked at which pathways were associated with up-regulated versus down-regulated genes. We discovered that HIF-1α signaling was correlated with up-regulated genes ($p<0.001$) and TGF-β signaling was correlated with down-regulated genes ($p<0.05$). HIF-1α signaling in the hypoxic response to rotenone was significantly increased in α-Syn knockdown cells even after p-value adjustment for multiple hypotheses ($p<0.001$, $q<0.05$). We selected 12 genes from Tables 4.4 and 4.5 for validation by qRT-PCR. We observed similar trends in

expression between datasets and the linear curve had a correlation coefficient (R^2) of 0.66 (Figure 4.9).

In general, the ischemic response mediated by HIF1α results in DNA hypermethylation due to the activation of DNA methyltransferases (Tothova et al. 2018). HIF1α depletion is also associated with increased homocysteine levels which lowers methylation capacity. Protein unfolding is associated with HIF1α repression therefore we hypothesize the effect of rotenone on hypoxia response via α-Syn aggregation. We examined DNA methylation patterns at hypoxia-response elements (HRE) in the promoter regions of differentially expressed hypoxia response genes to determine if α-Syn down-regulation was mediated by its interaction with DNMT1 (Table 4.4).

4.5.9 DNMT1-dependent genes with allele-specific methylated regions are differentially expressed in α-Syn knockdown cells.

We previously investigated DNMT1-dependent regions in the human genome and showed that DNA methylation patterns in two of these PD associated regions, at *HCN2* and *NEFM*, were vulnerable to rotenone exposure (Freeman et al. 2020). Similarly, we tested the extent to which DNMT1-dependent genes would also be affected in our rotenone-treated SH-5YSY cells and α-Syn knockdown would reverse altered DNA methylation patterns due to uninhibited DNMT1 nuclear translocation. We discovered 5 genes in our rotenone treated negative control cells but none of these overlapped DNMT1-dependent genes altered in rotenone treated *HEK293* (Chapter 3; Table 3.5). Three genes (*IGF2, KCNQ101T1, NNAT*) were significantly up-regulated in α-Syn knockdown cells compared to the negative control. All three genes are imprinted and have neurological significance which is detailed in the discussion section.

4.5.10 Differential methylation patterns in α-Syn knockdown cells exposed to rotenone.

DNA methylation at regions within HIF1-α transcription factor binding sites and within DNMT1-dependent regions was used to investigate genomic resilience to rotenone

treatment as a result of α-Syn knockdown (Table 4.3). We examined a total of 175 CG nucleotides from 10 regions surrounding 8 genes between rotenone treated negative control cells and rotenone treated α-Syn knockdown cells. From these nucleotides, 96 CGs from 4 genes met our minimum coverage requirement >1000x in all four samples (Figure 4.10). We determined 91 CGs were differentially methylated (> | 0.1% |, q<0.01). We first focused on 3 genes involved in the hypoxic response (*NDRG1*, *ID2*, *CDKN1A*). All three genes had 36 differentially methylated CGs from a total of 43 CGs covering each hypoxic response element bound by HIF1α (Table 4.6). All three genes were significantly hypomethylated across each region ($p=2x10^{-16}$) from Fisher's Exact test (Figure 4.11). The decrease in DNA methylation at hypoxic response elements was correlated with the increase in the expression of genes *NDRG1* and *ID2* but not *CDKN1A*. We conclude that the increase in cellular defense via hypoxia response was partially mediated by DNA methylation at HIF1α binding elements in α-Synuclein knockdown cells exposed to rotenone. In the future, ChIP analysis of HIF1α binding will be useful in further examining this proposed effect of α-Syn on the hypoxic response.

We next examined DNMT1-dependent regions which were previously shown to be vulnerable to rotenone (Chapter 3). We measured DNA methylation at five DNMT1-dependent genes identified by RNAseq (Table 4.5). Of these five genes, *DLK1* and *GNAS* had differentially methylated CGs that met our criteria (Table 4.7). One gene, *NNAT*, was measured when we loosened the criteria to calculate differential methylation of all CG sites with adequate coverage in at least one replicate. The other two genes, *IGF2* and *KCNQ101T1*, did not have adequate CG coverage after normalization.

For *DLK1*, all 13 CGs within the DNMT1-dependent region in the gene body were differentially methylated and 70% were hypomethylated compared to the rotenone treated control cells (Table 4.7). Interestingly, methylation across the entire DNMT1-dependent

region was hypermethylated albeit the changes were small (delta= 0.33%, $p=8x10^{-10}$) (Figure 4.12). DNA hypermethylation of the gene body at *DLK1* has been reported in the blood of PD patients in a cross-sectional analysis (delta= 0.2%, $p=1x10^{-6}$). This suggests that the methylation state of the DNMT1 dependent region at *DLK1* may be important in PD pathogenesis and could serve as a biomarker.

For, GNAS the DNMT1-dependent region covered the promoter/intron 1 as well as the exon 1 sequences. We measured significant differential methylation at 42 of the 50 CGs within this region and 71% of them were hypermethylated (Table 4.7). To determine if the entire region was differentially methylated, we divided it into two separate 500 bp amplicons and compared percent methylation with Fisher's Exact test ($p<0.05$). The region covering the promoter and intron 1 was significantly hypermethylated (delta = 2.3%, $p=3X10^{-7}$) while the region at exon 1 was not changed (delta= 0.55%, p=0.3) (Figure 4.12).

Despite *NNAT* not being adequately covered in all replicates, we tested whether differential methylation correlated with the increased mRNA expression observed in α-Syn knockdown cells (Table 4.7). Like *GNAS*, we divided the entire DNMT1-dependent region at *NNAT* into two amplicons covering the promoter and intron 1. Out of the 28 CGs analyzed in the first region (chr20:37520661-37521558), 21 CGs met our criteria in at least one replicate and 86% of those CGs were hypomethylated (Table 4.7). The change in DNA methylation across the region was a striking -11.6% ($p=2x10^{16}$). These results support our hypothesis that rotenone-induced α-Syn accumulation mediates changes in DNA methylation at vulnerable loci such as DNMT1-dependent regions. DNA methylation changes create genomic instability and can alter the expression of genes critical to maintain neuronal function.

4.6 Discussion

SH-5YSY neuroblastoma cells were treated with rotenone 200 nM for 24 h to induce features of Parkinson's cellular pathology including reduced viability, decreased mitochondria and mtDNA copy number, increased oxidative stress, and dysfunction in metabolic state. While the SH-5YSY cell line is not specific to dopaminergic neurons, it is commonly used to model dopaminergic neurotoxicity *in-vitro* and genomics approaches have verified that genes associated with neuronal function and PD pathology are in-tact (Krishna et al. 2014). Importantly, we use PD as a model system to study rotenone's effects on the neuronal epigenome because it's association with pathology is well-studied in both human and animal models (as discussed in Chapter 1.1 and 1.2). However, rotenone toxicity is not specific to dopaminergic neurons (Betarbet et al. 2000, Zagoura et al. 2017, Pamies et al. 2018) and neither is α-synucleinopathy (Braak et al. 1995). The most commonly recognized α-synucleinopathy outside of the substantia nigra is Lewy body dementia in which toxic aggregation of α-Syn occurs within hippocampal neurons and causes cognitive deficits (Vekrellis and Stefanis 2012, Hall et al. 2014). Other central nervous system cells that can be affected by α-Syn accumulation are glial cells which regulate neuroinflammation and oligodendrocytes that maintain axonal integrity (Leushel et al. 2013). Peripheral spinal cord neurons are also vulnerable to α-Syn overexpression. Synucleinopathy has been described in elderly patients and it was postulated that α-Syn toxicity may have originated in peripheral neurons before moving into the nigrostriatal tissues (Braak et al. 2007, Sumikura et al. 2015, Feng et al. 2016). This postulation is supported by the Braak theory of PD progression in which the disease initiates in the periphery in the brain stem and moves in temporal pattern through susceptible regions of the midbrain and the cortex (Braak et al. 2003). With this evidence, SH-5YSY was considered a suitable model to understand the role of α-Syn in mediating changes to DNA methylation patterns at early stages of disease pathogenesis (Figure 4.1).

Consistent with previous studies in SH-5YSY, we observed a significant increase in α-Syn protein accumulation after rotenone treatment (Figure 4.2) and this result was comparable to the accumulation caused by common *SNCA* point mutations (A30P and G51D) in *in-vitro* dopaminergic neurons (Ysselstein et al. 2015). This increase was also comparable to the increase seen in PD patients with a triplication of the *SNCA* locus and 2-fold increases in *SNCA* transcripts (Miller et al. 2004). This increase in α-Syn protein correlated with observed decreases in global DNA methylation patterns in the same cells (Figure 4.2). Genome-wide DNA hypomethylation was also observed in our *HEK293* cell model (*Chapter 2A Figure 2.4*). This evidence agrees with DNA hypomethylation observed as a result of exposure with alternative pesticides (Collota et al. 2013) and with human epidemiological studies reporting DNA hypomethylation in the post-mortem brain tissues of PD patients (Matsumoto et al. 2010, Desplats et al. 2011, Lu et al. 2013, Labbe et al. 2016).

DNMT1 depletion and mis-localization in post-mortem human cortex samples from patients with PD and Lewy body dementia was reported to be associated with DNA hypomethylation at CpG islands regulating the expression of PD associated genes including the gene encoding α-Syn, *SNCA* (Desplats et al. 2011). This same study used lentiviral overexpression of α-Syn in rat dopaminergic neurons in culture and discovered that DNMT1 mis-localization may be mediated by the association of α-Syn with DNMT1 in the cytoplasm of neurons thereby sequestering from its role in the nucleus. We used our rotenone induced α-Syn model in human SH-5YSY cells and assessed the proposed interaction with co-immunoprecipitation (Figure 4.3). Our data supported the hypothesis that accumulation of α-Syn can interact with DNMT1. We also observed a trend of decreased nuclear DNMT1 protein that was significantly increased with the knockdown of *SNCA* expression by RNAi but not in overall protein levels measured in the whole cell (Figure 4.6).

Inhibition of DNA methylation activates the expression of *SNCA (*(Jowaed et al. 2010) and thus we hypothesize that exposure creates a positive feedback loop of α-Syn accumulation and sequestration of DNMT1. Therefore, α-Syn is an attractive target to interfere with rotenone's toxic effects on the methylome. Studies have reported the increased resilience of PD toxicant models in response to targeting α-Syn. For instance, α-Syn knockout mice had more dopamine in nigrostriatal tissues than wild-type mice exposed to the mitochondrial complex I inhibitor MPTP (Thomas et al. 2011). This was also replicated in SH-5YSY cells in which knockdown of the *SNCA* gene increased cellular viability and attenuated mitochondrial dysfunction in response to the same chemical (Wu et al. 2009). This resilience of α-Syn silencing is mirrored in rotenone inhibition of complex I (Zharikov et al. 2015). Targeting α-Syn with short hairpin RNA (shRNA) improved nigrostriatal integrity and motor function in rats exposed to rotenone via intraperitoneal (i.p.) injection. We investigated mitochondrial resistance to rotenone exposure in our SH-5YSY cell model and found significant improvement of mitochondrial function and viability in rotenone treated α-Syn knockdown cells compared to negative control cells (Figure 4.5).

Since α-Syn expression is correlated with the oxidative stress response and apoptosis in SH-5YSY cells (Habig et al. 2009), we compared the transcriptome of α-Syn knockdown cells to the negative control cells after treatment. We observed similar results to Habig et al. that decreased α-Syn was associated with less p53-mediated apoptosis activation in response to oxidative stress. We showed the significant up-regulation of two of these genes, *CDKN1A* and *BBC3*, in relation to this pathway in Figure 4.7. The cyclin-dependent kinase inhibitor, p21, is encoded by the *CDKN1A* gene and promotes cell cycle arrest in response to oxidative damage. The Bcl-2 binding component, or better known as PUMA, is encoded by *BBC3* and is a transcriptional target of p53. PUMA induces cytochrome c release in apoptosis by activating apoptotic factors to increase the outer mitochondrial membrane permeability. Neither of these genes were altered in rotenone

treated α-Syn knockdown cells but they were also not up-regulated in the rotenone treated knockdown versus the negative control cells indicating that the decrease in p53 activation may be small.

It is also established that α-Syn regulates dopaminergic neurogenesis and the expression of genes involved in dopamine synthesis (Baptista et al. 2003, Garcia-Reitboeck et al. 2013). In our rotenone-treated negative control cells, neurogenesis and neuronal differentiation were among the processes associated with down-regulated genes (Figure 4.7). We showed the significant suppression of two genes involved in these processes, *TH* and *IGF2* (Figure 4.7). Tyrosine hydroxylase is an enzyme encoded by the *TH* gene and is the rate limiting step in dopamine synthesis. It serves as a dopaminergic marker in the central nervous system and Parkinson's disease patients have reductions in TH-positive cells in the substantia nigra. A study in murine dopaminergic neurons revealed that overexpressed α-Syn reduces the immunoreactivity of tyrosine hydroxylase and nigrostriatal cell loss over time (Alerte et al. 2009). Rotenone treatment only suppressed tyrosine hydroxylase expression in negative control cells and suggests that rotenone-induced α-Syn accumulation reduces the amount of dopamine in the central nervous system. We hypothesize that α-Syn is inversely correlated with the expression of tyrosine hydroxylase as a result of oxidative stress restructuring of chromatin architecture. We predict this relationship is also affected by metabolic conditions as amino acid deprivation can induce the repression of HIF1α via the unfolded protein response (Tothova et al. 2018).

IGF2 encodes the insulin-like growth factor 2 protein hormone that stimulates nervous system development and enhances neurite outgrowth (Jeong et al. 2013). It is a gene of interest in the epigenetics community because of its monoallelic expression pattern and the established presence of an intergenic control region (ICR) that regulates its expression through DNA methylation. *IGF2* is also interesting because of its role in the

hippocampus to control proliferation of neural stem cells and thus is critical in adult neurogenesis (Bracko et al. 2012). For decades, evidence of adult neurogenesis was lacking especially within the striatum. However, recent advances in lineage tracing techniques have allowed us to observe dopaminergic neuronal regeneration from precursor cells and uncover new insights into neuronal loss in aging (Morrison 2016). Intriguingly, we discovered significant up-regulation of *IGF2* gene expression in rotenone treated α-Syn knockdown cells compared to rotenone treated control cells. Therefore, it is possible that α-Syn knockdown confers cellular resilience to PD toxicants through manipulation of DNA methylation at regulatory regions of the *IGF-2* locus.

In both negative control and knockdown cells, we detected biological processes related to the oxidative stress response (Figure 4.7). For example, mesenchymal cell proliferation and transition can promote tissue regeneration and thus be protective against oxidative damage in the brain (Bui et al. 2009). This process was diminished regardless of α-Syn status in rotenone-treated neurons. Therefore, we predict that the oxidative stress response to mitochondrial complex I inhibition initiates changes in chromatin regulation to induce the expression of genes against oxidative damage.

We detected a significant change in the defense response of cells exposed to rotenone in α-Syn knockdown cells (Figure 4.8). For example, the hypoxia response pathway was influenced by α-Syn accumulation (Figure 4.8). We discovered significant enrichment of target genes involved in HIF-1α transcription factor signaling in all datasets (Table 4.4). We also discovered a significant up-regulation of almost all these target genes with α-Syn knockdown. We concluded that rotenone toxicity interferes with the cellular response to hypoxia and that α-Syn had a role in that effect. It is currently unclear if α-Syn accumulation directly impedes HIF-1α transcription factor activity or indirectly modulates its activity through the induction of p53 (Sermeus and Michiels 2011). This is further supported by a recent study reporting that stimulation of the hypoxic response is

neuroprotective in a rotenone-induced model of PD in rats (Kandil et al. 2019). Given our previous data that rotenone affects DNA methylation patterns at allele specific transcription factor binding sites, we chose to investigate the role of α-Syn mediated DNA methylation changes at the hypoxia response element regulatory binding motifs at differentially expressed target genes *NDRG1*, *ID2,* and *CDKN1A*.

We examined DNA methylation at 43 CG nucleotides overlapping the HIF1α response element at three hypoxia target genes and discovered differential methylation at 36 CGs (Table 4.6). All three genes were significantly hypomethylated in response to rotenone in α-Syn knockdown cells (Figure 4.11). Two of these genes, *NDRG1* and *ID2*, had correlated up-regulation of gene expression with DNA hypomethylation. Both genes encode proteins involved in DNA damage repair and transcription regulation in response to oxidative stress. Alternatively, *CDKN1A* was up-regulated in rotenone treated negative control cells but not in knockdown cells. We observed a decrease in DNA methylation at the hypoxic response element in this gene but it's conflicting role in both hypoxia and p53 mediated apoptosis is likely the reason for the observed transient gene expression.

We also saw significant changes in the one-carbon metabolism pathway when comparing rotenone treatment in α-Syn knockdown. The effect of rotenone and mitochondrial stress on one-carbon metabolism has been widely documented (Bao et al. 2016, Smirnova et al. 2016, Ron-Haril et a. 2018). It is well understood that the primary methyl donor to DNMT1 is S-adenosylmethionine (SAM), a co-substrate of the one-carbon metabolic process and a critical part of our understanding for how nutritional status and dietary exposures can determine phenotypes through the epigenome (Anderson et al. 2012). PD patients with α-Syn Lewy body inclusions have varying concentrations of SAM in their blood and patients with SAM concentrations indicative of higher DNA methylation levels had better cognitive prognosis than those with less methylation potential (Obeid et

al. 2009). Homocysteine is an amino acid produced after the methyl transfer from SAM to DNMT1. Homocysteine levels increase with age and elevated plasma homocysteine has been observed in PD patients (O'Suilleabhain et al. 2004). Increased homocysteine concentrations without further stimulation of the folate pathway to regenerate SAM reduces the methylation potential of neurons and has been shown to increase the susceptibility of dopaminergic neurons in a mouse model of MPTP induced mitochondrial dysfunction (Duan et al. 2002). Our data indicates that α-Syn may also mediate the DNA methylation response to rotenone and other mitochondrial toxicants through the availability of methyl donating groups and that combined with significant decreases in nuclear DNMT1 there will be widespread changes in DNA methylation and gene regulation.

Finally, we hypothesized that α-Syn effects on DNMT1 substrate availability and translocation would enhance the vulnerability of allele-specific methylated regions in the human genome. We analyzed transcriptomic data for DNMT1-dependent genes characterized in Chapter 3 and identified five of the genes in rotenone-treated negative control cells. Three genes were significantly increased in knockdown compared to the negative control (Table 4.5). The three genes (*IGF2*, *KCNQ101T*, *NNAT*) are all known imprinted genes with monoallelic expression patterns regulated by an ICR with a specific DNA methylation pattern. They are also all highly expressed in the brain and have biological relevance to PD pathology. We discussed the role of *IGF2* in neurogenesis above. Neuronatin, encoded by *NNAT*, is also associated with neuronal development and its regulation of calcium signaling in dendrites is critical in maintaining synaptic plasticity during aging (Oyang et al. 2011). Lastly the long, noncoding RNA encoded by *KCNQ101T* is the regulatory, antisense transcript of a potassium voltage gated channel required to propagate an action potential in neurotransmission. We investigated changes in DNA methylation patterns at DNMT1-dependent genes to determine if increased vulnerability

of allele-specific methylated regions and ICRs are correlated with α-Syn expression and aggregation.

We examined 132 CGs at DNMT1-dependent regions across 5 genes and identified three genes with differential methylation. We previously showed α-Syn decreases DNA methylation at two DNMT1-dependent genes (*HCN2* and NEFM) which are critical for synaptic plasticity. In this study, we identified two genes, *DLK1* and *GNAS*, were significantly hypermethylated in response to rotenone in α-Syn knockdown cells compared to the rotenone treated negative controls (Figure 4.12). This supports our hypothesis that rotenone-induced α-Syn mediates DNA methylation changes by interfering with DNMT1 translocation to the nucleus. While global DNA hypomethylation and regional hypomethylation at several DNMT1-dependent genes was observed in control cells exposed to rotenone; it is expected that other sites may experience hypermethylation due to the cooperative roles of DNA methyltransferases (DNMT3a/b) and the active demethylase TET enzymes. It should also be considered that our current methods measuring nuclear DNMT1 considers the soluble fraction of protein and not DNMT1 that may have remained attached to the chromatin. We investigated whether these patterns from existing DNMT enzymes may also be changed by α-Syn knockdown by examining the CGs within the *NNAT* gene which was significantly up-regulated in rotenone treated α-Syn knockdown cells. While we were not able to achieve adequate coverage of *NNAT* in all samples, we were able to compare methylation of CGs within the NNAT intron 1 in at least one biological replicate per treatment group. We observed a striking decrease in DNA methylation at 18 of the 21 CGs analyzed and an overall 11.6 decrease in methylation across the selected intron region. This change in methylation was associated with a 0.9 log2 fold change in mRNA expression. We conclude based on this evidence that α-Syn mediates regional increases and decreases in DNA methylation

levels and disrupts the expression of proteins such as *NNAT* which are critical in maintaining synaptic activity during aging.

It is widely accepted that DNA methylation regulation of gene expression is an important risk factor in PD particularly within idiopathic cases where environmental exposures and lifestyle factors drive disease etiology. The aggregation of α-syn protein has been recognized as a hallmark of PD and a root cause of neuronal dysfunction and death. It has also been established that α-Syn accumulation and DNA methylation are inversely correlated (Jowaed et al. 2010) either by activation of demethylation enzymes (Wu et al. 2020) or via inactivation of core DNA methyltransferases (Desplats et al. 2011). Few studies have investigated these mechanisms and even fewer studies have attempted to investigate these mechanisms in an environmental toxicant induced model of PD.

There is currently no cure for PD and treatment relies on dopamine replacement therapy. Targeting α-Syn has already been a focus of some clinical trials but directly targeting its expression with RNAi can be deleterious to neurons due to the endogenous role of α-Syn at the synapse (Savitt and Jankovic 2019). There has been success in early phase trials by targeting α-Syn oligomers rather than monomeric α-Syn at the synapse (Deeg et al. 2015). However, these drugs also face challenges in specifically targeting oligomers given the flexibility of α-Syn's conformational state (Lashuel et al. 2013). Other pharmaceutical targets include inducing degradation systems to break down aggregated α-Syn via inhibition of mammalian target of rapamycin (mTOR) but have also been largely unsuccessful due to off-target effects (Sardi et al. 2018). Interestingly, targeting the DNA methylation machinery may be a safer, more viable method to regulate α-Syn expression and aggregation in neurons. A recent study used a CRISPR deactivated Cas9 fused with the catalytic domain of the de novo methyltransferase (DNMT3b) to remethylate intron 1 of the *SNCA* gene which is tightly coupled to its expression (Kantor et al. 2018). They discovered that targeted re-methylation of the *SNCA* gene regulated α-Syn aggregation

and rescued disease-related cellular phenotypes in a human induced pluripotent stem cell model (iPSC) with triplication of the *SNCA* locus. Given our findings that targeting α-Syn in undifferentiated neurons stimulated neurogenesis, we believe that targeted DNA methylation should also be used on undifferentiated, dopaminergic precursor cells rather than solely mature, post-mitotic neurons to determine the efficacy of this intervention on adult neurogenesis in nigrostriatal tissues.

In summary, we conclude that α-Syn knockdown conferred both mitochondrial and genomic resilience to rotenone treatment. This resilience may be due to changes in DNA methylation at susceptible loci which is mediated by aggregated α-Syn through (1) DNMT1 sequestration in the cytoplasm, (2) inhibition of the hypoxic response, or (3) altered ratio of methyl-substrate in one-carbon metabolism. In the future, understanding the temporal association of α-Syn accumulation with the loss of TH+ neuronal cells will be critical in understanding the role of protein aggregation in mediated the oxidative stress signaling to the nucleus. It will also be critical to understand how neural activity both regulates and is changed by this process of α-Syn-induced loss of heterochromatin. These novel mechanisms for α-Syn's role on the epigenome have the potential to increase success in preventing the propagation of oxidative stress during aging in neuronal cell populations.

4.7 References

1. Abeliovich A, Schmitz Y, Fariñas I, Choi-Lundberg D, Ho W, Castillo PE et al. 2000. Mice lacking α-synuclein display functional deficits in the nigrostriatal dopamine system. Neuron 25(1):239-252.
2. Alerte TN, Akinfolarin AA, Friedrich EE, Mader SA, Hong C, Perez RG. 2008. α-Synuclein aggregation alters tyrosine hydroxylase phosphorylation and immunoreactivity: Lessons from viral transduction of knockout mice. Neurosci Lett 435(1):24-29.
3. Anderson OS, Sant KE, Dolinoy DC. 2012. Nutrition and epigenetics: An interplay of dietary methyl donors, one-carbon metabolism and DNA methylation. J Nutr Biochem 23(8):853-859; doi: 10.1016/j.jnutbio.2012.03.003 [doi].
4. Bao XR, Ong SE, Goldberger O, Peng J, Sharma R, Thompson DA et al. 2016. Mitochondrial dysfunction remodels one-carbon metabolism in human cells. Elife 5:10.7554/eLife.10575; doi: 10.7554/eLife.10575 [doi].
5. Baptista MJ, O'Farrell C, Daya S, Ahmad R, Miller DW, Hardy J et al. 2003. Co-ordinate transcriptional regulation of dopamine synthesis genes by α-synuclein in human neuroblastoma cell lines. J Neurochem 85(4):957-968.
6. Betarbet R, Sherer TB, MacKenzie G, Garcia-Osuna M, Panov AV, Greenamyre JT. 2000. Chronic systemic pesticide exposure reproduces features of parkinson's disease. Nat Neurosci 3(12):1301.
7. Braak H, Del Tredici K, Rüb U, De Vos RA, Steur ENJ, Braak E. 2003. Staging of brain pathology related to sporadic Parkinson's disease. Neurobiol Aging 24(2):197-211.
8. Braak H, Sastre M, Bohl JR, de Vos RA, Del Tredici K. 2007. Parkinson's disease: Lesions in dorsal horn layer I, involvement of parasympathetic and sympathetic pre- and postganglionic neurons. Acta Neuropathol 113(4):421-429.
9. Braak H, Braak E, Yilmazer D, Schultz C, de Vos RA, Jansen EN. 1995. Nigral and extranigral pathology in parkinson's disease. J Neural Transm Suppl 46:15-31.
10. Bracko O, Singer T, Aigner S, Knobloch M, Winner B, Ray J et al. 2012. Gene expression profiling of neural stem cells and their neuronal progeny reveals IGF2 as a regulator of adult hippocampal neurogenesis. J Neurosci 32(10):3376-3387; doi: 10.1523/JNEUROSCI.4248-11.2012 [doi].
11. Bui T, Sequeira J, Wen TC, Sola A, Higashi Y, Kondoh H et al. 2009. ZEB1 links p63 and p73 in a novel neuronal survival pathway rapidly induced in response to cortical ischemia. PLoS One 4(2):e4373; doi: 10.1371/journal.pone.0004373 [doi].
12. Chen EY, Tan CM, Kou Y, Duan Q, Wang Z, Meirelles GV et al. 2013. Enrichr: Interactive and collaborative HTML5 gene list enrichment analysis tool. BMC Bioinformatics 14(1):128.
13. Chorfa A, Bétemps D, Morignat E, Lazizzera C, Hogeveen K, Andrieu T et al. 2013. Specific pesticide-dependent increases in α-synuclein levels in human neuroblastoma (SH-SY5Y) and melanoma (SK-MEL-2) cell lines. toxicological sciences 133(2):289-297.
14. Collotta M, Bertazzi P, Bollati V. 2013. Epigenetics and pesticides. Toxicology 307:35-41.
15. de Boni L, Riedel L, Schmitt I, Kraus TF, Kaut O, Piston D et al. 2015. DNA methylation levels of α-synuclein intron 1 in the aging brain. Neurobiol Aging 36(12):3334. e7-3334. e11.
16. Deeg AA, Reiner AM, Schmidt F, Schueder F, Ryazanov S, Ruf VC et al. 2015. Anle138b and related compounds are aggregation specific fluorescence markers and

reveal high affinity binding to alpha-synuclein aggregates. Biochim Biophys Acta 1850(9):1884-1890; doi: 10.1016/j.bbagen.2015.05.021 [doi].
17. Desplats P, Spencer B, Coffee E, Patel P, Michael S, Patrick C et al. 2011. Alpha-synuclein sequesters Dnmt1 from the nucleus: A novel mechanism for epigenetic alterations in lewy body diseases. J Biol Chem 286(11):9031-9037; doi: 10.1074/jbc.C110.212589 [doi].
18. Dobin A, Davis CA, Schlesinger F, Drenkow J, Zaleski C, Jha S et al. 2013. STAR: Ultrafast universal RNA-seq aligner. Bioinformatics 29(1):15-21.
19. Duan W, Ladenheim B, Cutler RG, Kruman II, Cadet JL, Mattson MP. 2002. Dietary folate deficiency and elevated homocysteine levels endanger dopaminergic neurons in models of parkinson's disease. J Neurochem 80(1):101-110; doi: 10.1046/j.0022-3042.2001.00676.x [doi].
20. Eden E, Navon R, Steinfeld I, Lipson D, Yakhini Z. 2009. GOrilla: A tool for discovery and visualization of enriched GO terms in ranked gene lists. BMC Bioinformatics 10(1):48.
21. Fabregat A, Korninger F, Viteri G, Sidiropoulos K, Marin-Garcia P, Ping P et al. 2018. Reactome graph database: Efficient access to complex pathway data. PLoS computational biology 14(1):e1005968.
22. Feng G, Liu J, Wang Y, Wang Z, Hu Y, Xia Q et al. 2017. Effects of alpha-synuclein on primary spinal cord neurons associated with apoptosis and CNTF expression. Cell Mol Neurobiol 37(5):817-829.
23. Freeman DM, Lou D, Li Y, Martos SN, Wang Z. 2020. The conserved DNMT1 dependent methylation regions in human cells are vulnerable to environmental rotenone. Epigenetics & Chromatin, 13(1), 1-16.
24. Garcia-Reitboeck P, Anichtchik O, Dalley JW, Ninkina N, Tofaris GK, Buchman VL et al. 2013. Endogenous alpha-synuclein influences the number of dopaminergic neurons in mouse substantia nigra. Exp Neurol 248:541-545.
25. Ghiglieri V, Calabrese V, Calabresi P. 2018. Alpha-synuclein: From early synaptic dysfunction to neurodegeneration. Frontiers in neurology 9:295.
26. Grady JP, Murphy JL, Blakely EL, Haller RG, Taylor RW, Turnbull DM et al. 2014. Accurate measurement of mitochondrial DNA deletion level and copy number differences in human skeletal muscle. PLoS One 9(12):e114462; doi: 10.1371/journal.pone.0114462 [doi].
27. Häbig K, Walter M, Stappert H, Riess O, Bonin M. 2009. Microarray expression analysis of human dopaminergic neuroblastoma cells after RNA interference of SNCA—A key player in the pathogenesis of parkinson's disease. Brain Res 1256:19-33.
28. Hall H, Reyes S, Landeck N, Bye C, Leanza G, Double K et al. 2014. Hippocampal lewy pathology and cholinergic dysfunction are associated with dementia in Parkinson’s disease. Brain 137(9):2493-2508.
29. Henderson-Smith A, Fisch KM, Hua J, Liu G, Ricciardelli E, Jepsen K et al. 2019. DNA methylation changes associated with Parkinson’s disease progression: Outcomes from the first longitudinal genome-wide methylation analysis in blood. Epigenetics 14(4):365-382.
30. Jeong EY, Kim S, Jung S, Kim G, Son H, Lee DH et al. 2013. Enhancement of IGF-2-induced neurite outgrowth by IGF-binding protein-2 and osteoglycin in SH-SY5Y human neuroblastoma cells. Neurosci Lett 548:249-254.
31. Jowaed A, Schmitt I, Kaut O, Wullner U. 2010. Methylation regulates alpha-synuclein expression and is decreased in parkinson's disease patients' brains. J Neurosci 30(18):6355-6359; doi: 10.1523/JNEUROSCI.6119-09.2010 [doi].

32. Kandil EA, Sayed RH, Ahmed LA, Abd El Fattah, Mai A, El-Sayeh BM. 2019. Hypoxia-inducible factor 1 alpha and nuclear-related receptor 1 as targets for neuroprotection by albendazole in a rat rotenone model of parkinson's disease. Clinical and Experimental Pharmacology and Physiology 46(12):1141-1150.
33. Kanehisa M, Furumichi M, Tanabe M, Sato Y, Morishima K. 2017. KEGG: New perspectives on genomes, pathways, diseases and drugs. Nucleic Acids Res 45(D1):D353-D361.
34. Kantor B, Tagliafierro L, Gu J, Zamora ME, Ilich E, Grenier C et al. 2018. Downregulation of SNCA expression by targeted editing of DNA methylation: A potential strategy for precision therapy in PD. Molecular Therapy 26(11):2638-2649.
35. Labbé C, Lorenzo-Betancor O, Ross OA. 2016. Epigenetic regulation in Parkinson's disease. Acta Neuropathol 132(4):515-530.
36. Lashuel HA, Overk CR, Oueslati A, Masliah E. 2013. The many faces of α-synuclein: From structure and toxicity to therapeutic target. Nature Reviews Neuroscience 14(1):38-48.
37. Liao Y, Smyth GK, Shi W. 2013. The subread aligner: Fast, accurate and scalable read mapping by seed-and-vote. Nucleic Acids Res 41(10):e108-e108.
38. Lu H, Liu X, Deng Y, Qing H. 2013. DNA methylation, a hand behind neurodegenerative diseases. Frontiers in aging neuroscience 5:85.
39. Martin M. 2011. Cutadapt removes adapter sequences from high-throughput sequencing reads. EMBnet.journal 17(1):10-12.
40. Matsumoto L, Takuma H, Tamaoka A, Kurisaki H, Date H, Tsuji S et al. 2010. CpG demethylation enhances alpha-synuclein expression and affects the pathogenesis of parkinson's disease. PLoS One 5(11):e15522.
41. Miller DW, Hague SM, Clarimon J, Baptista M, Gwinn-Hardy K, Cookson MR et al. 2004. Alpha-synuclein in blood and brain from familial parkinson disease with SNCA locus triplication. Neurology 62(10):1835-1838; doi: 10.1212/01.wnl.0000127517.33208.f4 [doi].
42. Morrison BE. 2016. Discovery of nigral dopaminergic neurogenesis in adult mice. Neural Regen Res 11(6):878-881; doi: 10.4103/1673-5374.184449 [doi].
43. Motyl J, Wencel P, Cieślik M, Strosznajder R, Strosznajder J. 2018. Alpha-synuclein alters differently gene expression of sirts, PARPs and other stress response proteins: Implications for neurodegenerative disorders. Mol Neurobiol 55(1):727-740.
44. Obeid R, Schadt A, Dillmann U, Kostopoulos P, Fassbender K, Herrmann W. 2009. Methylation status and neurodegenerative markers in parkinson disease. Clin Chem 55(10):1852-1860; doi: 10.1373/clinchem.2009.125021 [doi].
45. O'Suilleabhain PE, Oberle R, Bartis C, Dewey RB,Jr, Bottiglieri T, Diaz-Arrastia R. 2006. Clinical course in parkinson's disease with elevated homocysteine. Parkinsonism Relat Disord 12(2):103-107; doi: S1353-8020(05)00199-9 [pii].
46. Oyang EL, Davidson BC, Lee W, Poon MM. 2011. Functional characterization of the dendritically localized mRNA neuronatin in hippocampal neurons. PLoS One 6(9):e24879; doi: 10.1371/journal.pone.0024879 [doi].
47. Pamies D, Block K, Lau P, Gribaldo L, Pardo CA, Barreras P et al. 2018. Rotenone exerts developmental neurotoxicity in a human brain spheroid model. Toxicol Appl Pharmacol 354:101-114.
48. Rao KR, Jayakumar A, Norenberg MD. 2005. Role of oxidative stress in the ammonia-induced mitochondrial permeability transition in cultured astrocytes. Neurochem Int 47(1-2):31-38.
49. Robinson MD, McCarthy DJ, Smyth GK. 2010. edgeR: A bioconductor package for differential expression analysis of digital gene expression data. Bioinformatics 26(1):139-140.

50. Ron-Harel N, Notarangelo G, Ghergurovich JM, Paulo JA, Sage PT, Santos D et al. 2018. Defective respiration and one-carbon metabolism contribute to impaired naive T cell activation in aged mice. Proc Natl Acad Sci U S A 115(52):13347-13352; doi: 10.1073/pnas.1804149115 [doi].
51. Sala G, Arosio A, Stefanoni G, Melchionda L, Riva C, Marinig D et al. 2013. Rotenone upregulates alpha-synuclein and myocyte enhancer factor 2D independently from lysosomal degradation inhibition. Biomed Res Int 2013:846725; doi: 10.1155/2013/846725 [doi].
52. Sardi SP, Cedarbaum JM, Brundin P. 2018. Targeted therapies for parkinson's disease: From genetics to the clinic. Mov Disord 33(5):684-696; doi: 10.1002/mds.27414 [doi].
53. Savitt D, Jankovic J. 2019. Targeting alpha-synuclein in parkinson's disease: Progress towards the development of disease-modifying therapeutics. Drugs 79(8):797-810; doi: 10.1007/s40265-019-01104-1 [doi].
54. Scott DA, Tabarean I, Tang Y, Cartier A, Masliah E, Roy S. 2010. A pathologic cascade leading to synaptic dysfunction in alpha-synuclein-induced neurodegeneration. J Neurosci 30(24):8083-8095; doi: 10.1523/JNEUROSCI.1091-10.2010 [doi].
55. Sermeus A, Michiels C. 2011. Reciprocal influence of the p53 and the hypoxic pathways. Cell death & disease 2(5):e164-e164.
56. Shah GN, Price TO, Banks WA, Morofuji Y, Kovac A, Ercal N et al. 2013. Pharmacological inhibition of mitochondrial carbonic anhydrases protects mouse cerebral pericytes from high glucose-induced oxidative stress and apoptosis. J Pharmacol Exp Ther 344(3):637-645; doi: 10.1124/jpet.112.201400 [doi].
57. Singleton A, Gwinn-Hardy K. 2004. Parkinson's disease and dementia with lewy bodies: A difference in dose? Lancet 364(9440):1105-1107; doi: 10.1016/S0140-6736(04)17117-1 [doi].
58. Singleton AB, Farrer M, Johnson J, Singleton A, Hague S, Kachergus J et al. 2003. Alpha-synuclein locus triplication causes parkinson's disease. Science 302(5646):841; doi: 10.1126/science.1090278 [doi].
59. Smirnova L, Harris G, Delp J, Valadares M, Pamies D, Hogberg HT et al. 2016. A LUHMES 3D dopaminergic neuronal model for neurotoxicity testing allowing long-term exposure and cellular resilience analysis. Arch Toxicol 90(11):2725-2743.
60. Sumikura H, Takao M, Hatsuta H, Ito S, Nakano Y, Uchino A et al. 2015. Distribution of α-synuclein in the spinal cord and dorsal root ganglia in an autopsy cohort of elderly persons. Acta neuropathologica communications 3(1):57.
61. Supek F, Bošnjak M, Škunca N, Šmuc T. 2011. REVIGO summarizes and visualizes long lists of gene ontology terms. PloS one 6(7):e21800.
62. Thomas B, Mandir AS, West N, Liu Y, Andrabi SA, Stirling W et al. 2011. Resistance to MPTP-neurotoxicity in alpha-synuclein knockout mice is complemented by human alpha-synuclein and associated with increased beta-synuclein and akt activation. PLoS One 6(1):e16706; doi: 10.1371/journal.pone.0016706 [doi].
63. Uversky VN, Li J, Fink AL. 2001. Pesticides directly accelerate the rate of α-synuclein fibril formation: A possible factor in parkinson's disease. FEBS Lett 500(3):105-108.
64. Vekrellis K, Stefanis L. 2012. Targeting intracellular and extracellular alpha-synuclein as a therapeutic strategy in parkinson's disease and other synucleinopathies. Expert opinion on therapeutic targets 16(4):421-432.
65. Wang Y, Wang X, Li R, Yang Z, Wang Y, Gong X et al. 2013. A DNA methyltransferase inhibitor, 5-Aza-2′-Deoxycytidine, exacerbates neurotoxicity and

upregulates P arkinson's Disease-Related genes in dopaminergic neurons. CNS neuroscience & therapeutics 19(3):183-190.
66. Wu F, Poon WS, Lu G, Wang A, Meng H, Feng L et al. 2009. α-Synuclein knockdown attenuates MPP induced mitochondrial dysfunction of SH-SY5Y cells. Brain Res 1292:173-179.
67. Wu TT, Liu T, Li X, Chen YJ, Chen TJ, Zhu XY et al. 2020. TET2-mediated Cdkn2A DNA hydroxymethylation in midbrain dopaminergic neurons injury of parkinson's disease. Hum Mol Genet; doi: ddaa022 [pii].
68. Ysselstein D, Joshi M, Mishra V, Griggs AM, Asiago JM, McCabe GP et al. 2015. Effects of impaired membrane interactions on α-synuclein aggregation and neurotoxicity. Neurobiol Dis 79:150-163.
69. Zagoura D, Canovas-Jorda D, Pistollato F, Bremer-Hoffmann S, Bal-Price A. 2017. Evaluation of the rotenone-induced activation of the Nrf2 pathway in a neuronal model derived from human induced pluripotent stem cells. Neurochem Int 106:62-73.
70. Zharikov AD, Cannon JR, Tapias V, Bai Q, Horowitz MP, Shah V et al. 2015. shRNA targeting α-synuclein prevents neurodegeneration in a Parkinson’s disease model. J Clin Invest 125(7):2721-2735.

4.8 Tables

Table 4.1 Treatment scheme for siRNA knockdown cells

DMSO (<0.002% v/v)	Rotenone (200 nM) in DMSO	
DMSO Ctrl	Rot Ctrl	Control- Lipofectamine vehicle control with no siRNA added
DMSO Neg Ctrl	Rot Neg Ctrl	Negative Control- Transfection control with scramble, non-target siRNA
DMSO siRNA	Rot siRNA	siRNA- Knockdown with siRNA targeting SNCA.

Table 4.2 qRT-PCR primers for RNA sequencing validation

Gene	Forward	Reverse
CDKN1A	TGTCCGTCAGAACCCATGC	AAAGTCGAAGTTCCATCGCTC
DLK1	CTTTCGGCCACAGCACCTAT	TGTCATCCTCGCAGAATCCAT
FBXO8	CCTACCTGAATGCAACTGACC	CATCCAGGATACCCTTGGACA
GNAS	TGCCTCGGGAACAGTAAGAC	GCCGCCCTCTCCATTAAAC
HERC3	TGTTGGGGATATTGGTCTCTGG	CCCTTGGTGTTCAAACCACAT
ID2	AGTCCCGTGAGGTCCGTTAG	AGTCGTTCATGTTGTATAGCAGG
IGF2	GTGGCATCGTTGAGGAGTG	CACGTCCCTCTCGGACTTG
KCNQ101T	TTGGTAGGATTTTGTTGAGG	CAACCTTCCCCTACTACC
TH	GGAAGGCCGTGCTAAACCT	GGATTTTGGCTTCAAACGTCTC
NDRG1	GTCCTTATCAACGTGAACCCTT	GCATTGGTCGCTCAATCTCCA
NNAT	ACTGGGTAGGATTCGCTTTTCG	ACACCTCACTTCTCGCAATGG
VEGFA	AGGGCAGAATCATCACGAAGT	AGGGTCTCGATTGGATGGCA

Table 4.3 BS-PCR primers

Gene chr:pos	Forward	Reverse
CDKN1A chr6:36683206-36684350	GTGGGAAGGAAGTAGGAAGATTAGT	ATAAAACTTAAACAAACCAAAACC
DLK1 chr14:100808189-100809386	TGGTAAAGTATTTTTGTGGAATGAG	AAAATTCAAAACCAACCTAAACAAC
GNAS_1 chr20:58851492-58852993	TGGGGGTTATGATTTAGAGTTTTAG	TCTTTCTTTTTACTCCAAACCAATC
GNAS_2 chr20:58854399-58855573	TTTGAGAGTTTTTAGTTTAAAGTT	AAAACAATTAAAATCCCTCCCTAAA
ID2 chr2:8679972-8681217	ATGAATTAAAATAGTGTTAAAATAAAATTT	CTAATAAAACCAACAATCTCTAA
IGF2 chr11:2148113-2148683	AGATAAGGAGGGGGTTTTAGTAAAAG	CTAACCACCAACAAAAAATTAAAC
KCNQ101T chr11:2697584-2698993	AGGGATTATAGTGGGGTATTGG	AAAACCTCATTAAAAACAAAAAA
NDRG1 chr8:133350022-133351154	GGGAGGGAAAGAATTAGTATTTGTT	TAAACCTCAATTTCCCCATCTATAA
NNAT_1 chr20:37520661-37521558	GTTAAAGTTTTTGAAAGGGGTATT	TTCCAAAAATAATAAATAAATAA
NNAT_2 chr20:37522243-37523130	TAAGTTGTGGGTTTAATTAGTTTG	CCCTCACTAACCTTACCAAATACTC

Table 4.4 HIF-1α target genes with hypoxia-response elements in RNA sequencing

HIF-1α hypoxia target genes		
DMSO x Rot Neg Ctrl	DMSO x Rot siRNA	Rot x Rot siRNA
↓*IGF2*	↓*IGF2*	↑*IGF2*
↓*NDRG1*	↓*NDRG1*	↑*NDRG1*
↓*ID2*	↓ *VEGFA*	↑*ID2*
↑*CDKN1A*	↓ *LOXL2*	↑*VEGFA*
↓ *VEGFA*		↑*ADM*
↓ *ADM*		↑*LDHA*
↓ *BNIP3*		
↓*LDHA*		

Neg Ctrl indicates SH-5YSY transfected with scramble siRNA and siRNA indicates SH-5YSY transfected with *SNCA* targeted DsiRNA.
red arrows indicate up-regulation or down-regulation of expression.
Underline indicates genes used for Bisulfite-amplicon sequencing.

Table 4.5 DNMT1-dependent regions in RNA sequencing

DNMT1-dependent genes		
DMSO x Rot Neg Ctrl	DMSO x Rot siRNA	Rot x Rot siRNA
↓*KCNQ1OT1*	↓*KCNQ1OT1*	↑*KCNQ1OT1*
↓*IGF2*	↓*IGF2*	↑*IGF2*
↓*DLK1*		↑*NNAT*
↓*GNAS*		
↑*HERC3*		
↓*FBXO8*		

Neg Ctrl indicates SH-5YSY transfected with scramble siRNA and siRNA indicates SH-5YSY transfected with *SNCA* targeted DsiRNA.
red arrows indicate up-regulation or down-regulation of expression.
Underline indicates genes used for Bisulfite-amplicon sequencing.

Table 4.6 Differentially Methylated CG sites at hypoxia response genes

Gene	CpG	delta
CDKN1A	36683981	-0.2
CDKN1A	36684008	14.9
CDKN1A	36684038	-10.2
CDKN1A	36684073	1.1
CDKN1A	36684087	-10.7
CDKN1A	36684101	-2.1
CDKN1A	36684115	-7.6
CDKN1A	36684131	-1.3
CDKN1A	36684134	3.4
CDKN1A	36684142	-6.1
CDKN1A	36684157	-2.5
CDKN1A	36684172	1.1
CDKN1A	36684183	0.3
CDKN1A	36684192	-10.8
CDKN1A	36684212	13.9
CDKN1A	36684218	-3.1
CDKN1A	36684229	-0.5
ID2	8680132	0.7
ID2	8680176	-2.1
ID2	8680193	-3.3
ID2	8680234	-4
ID2	8680246	-5.1
ID2	8680264	1.7
ID2	8680299	-0.7
ID2	8680414	1.6
ID2	8680437	0.9
ID2	8680442	-5
NDRG1	133350589	0.8
NDRG1	133350593	0.6
NDRG1	133350619	0.7
NDRG1	133350635	1.1
NDRG1	133350651	-0.5
NDRG1	133350689	-17.3
NDRG1	133350720	2.5
NDRG1	133350734	0.2
NDRG1	133350942	-1.1

Table 4.7 Differentially Methylated CG sites at DNMT1-dependent regions

Gene	CpG	delta
DLK1	100808288	2.3
DLK1	100808295	-0.4
DLK1	100808346	-1.2
DLK1	100808475	-3.9
DLK1	100808480	-1.6
DLK1	100808489	-2.8
DLK1	100808491	1.0
DLK1	100808498	0.2
DLK1	100808509	-0.5
DLK1	100808516	-0.3
DLK1	100808534	-0.4
DLK1	100808545	-1.8
DLK1	100808660	13.7
GNAS_1	5882612	0.5
GNAS_1	5882617	4.7
GNAS_1	5882626	2.4
GNAS_1	5882633	3.4
GNAS_1	5882638	4.5
GNAS_1	5882645	3.0
GNAS_1	5882650	6.7
GNAS_1	5882658	3.8
GNAS_1	5882674	4.4
GNAS_1	5882682	6.6
GNAS_1	5882733	-3.0
GNAS_1	5882741	3.2
GNAS_1	5882750	8.4
GNAS_1	5882778	6.1
GNAS_1	5882812	5.8
GNAS_1	5882823	-2.6
GNAS_1	5882835	5.5
GNAS_1	5882838	-6.4
GNAS_1	5882862	7.9
GNAS_1	5882871	-3.0
GNAS_1	5882878	-5.6
GNAS_1	5882883	-1.6
GNAS_1	5882888	1.0
GNAS_1	5882893	2.3

Gene	CpG	delta
GNAS_1	5882897	1.5
GNAS_2	588555134	-4.5
GNAS_2	588555136	-2.3
GNAS_2	588555167	4.6
GNAS_2	588555187	1.6
GNAS_2	588555208	-0.6
GNAS_2	588555220	0.3
GNAS_2	588555222	-4.8
GNAS_2	588555235	-7.8
GNAS_2	588555249	0.6
GNAS_2	588555267	-11.1
GNAS_2	588555290	1.7
GNAS_2	588555295	2.2
GNAS_2	588555317	0.5
GNAS_2	588555320	1.3
GNAS_2	588555333	0.2
GNAS_2	588555346	2.3
GNAS_2	588555349	5.7
NNAT_1	37520886	2.4
NNAT_1	37520931	-0.5
NNAT_1	37520962	-0.4
NNAT_1	37520984	-4.5
NNAT_1	37521026	-36.1
NNAT_1	37521029	3.1
NNAT_1	37521069	-20.8
NNAT_1	37521076	16.3
NNAT_1	37521118	-32.6
NNAT_1	37521129	-17.0
NNAT_1	37521167	-19.0
NNAT_1	37521169	-17.2
NNAT_1	37521175	-17.7
NNAT_1	37521188	-14.4
NNAT_1	37521192	-14.2
NNAT_1	37521205	-12.2
NNAT_1	37521207	-12.3
NNAT_1	37521214	-12.5
NNAT_1	37521216	-8.6
NNAT_1	37521222	-12.8
NNAT_1	37521230	-13.4

4.9 Figures

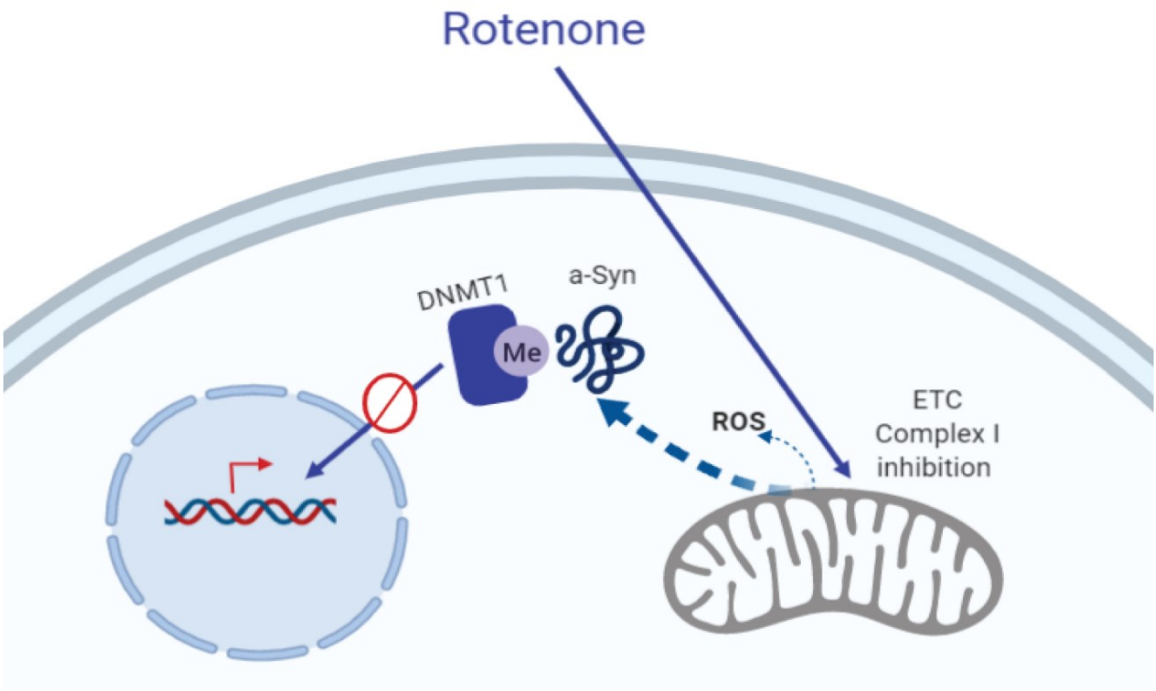

Figure 4.1 Illustration of rotenone-induced α-Syn sequestration of DNMT1.
Oxidative damage caused by rotenone exposure promotes α-Syn misfolding and aggregation. We hypothesize that accumulated α-Syn interacts with DNMT1 outside of the nucleus thereby contributing to global DNA hypomethylation.

.

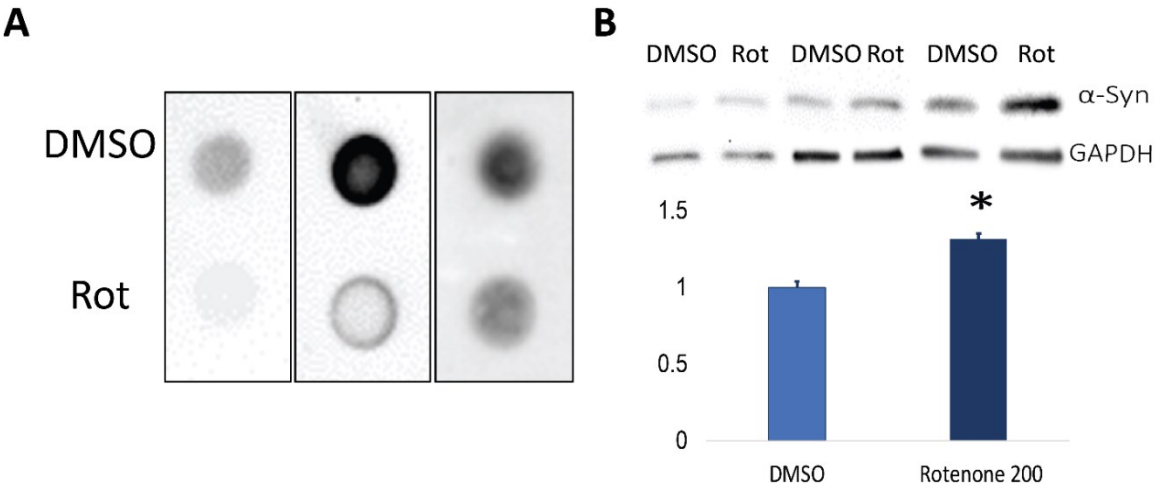

Figure 4.2 Rotenone-induced α-Syn accumulation is associated with DNA hypomethylation.

A) Global DNA hypomethylation from three biological replicates of SH-5YSY exposed to rotenone (200 nM, 24h) was observed using dot blot with anti-5methylCytosine (5mC) antibody. B) Protein was extracted from the same cells and α-Syn accumulation was measured with Western blot. Western was quantified with Image J and the relative ratio of α-Syn/ GAPDH (loading control) was used for significance testing with a paired Student's t-test (* $p<0.05$).

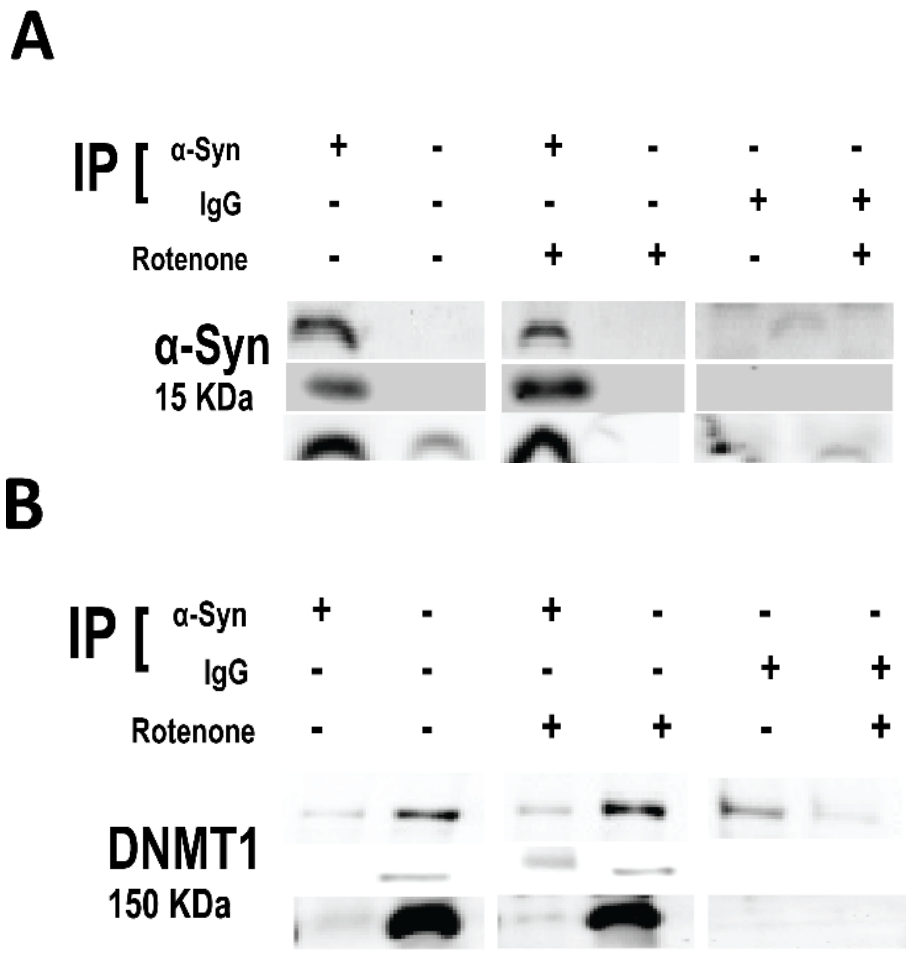

Figure 4.3 Rotenone-induced α-Syn interacts with DNMT1 within the whole cell. A) α-Syn was immunoprecipitated by magnetic bead from rotenone treated SH-5YSY. B) DNMT1 was immunoprecipitated with α-Syn only in cells exposed to rotenone. IgG was used as the negative control. IP = immunoprecipitated and indicates the antibody used in the experiment.

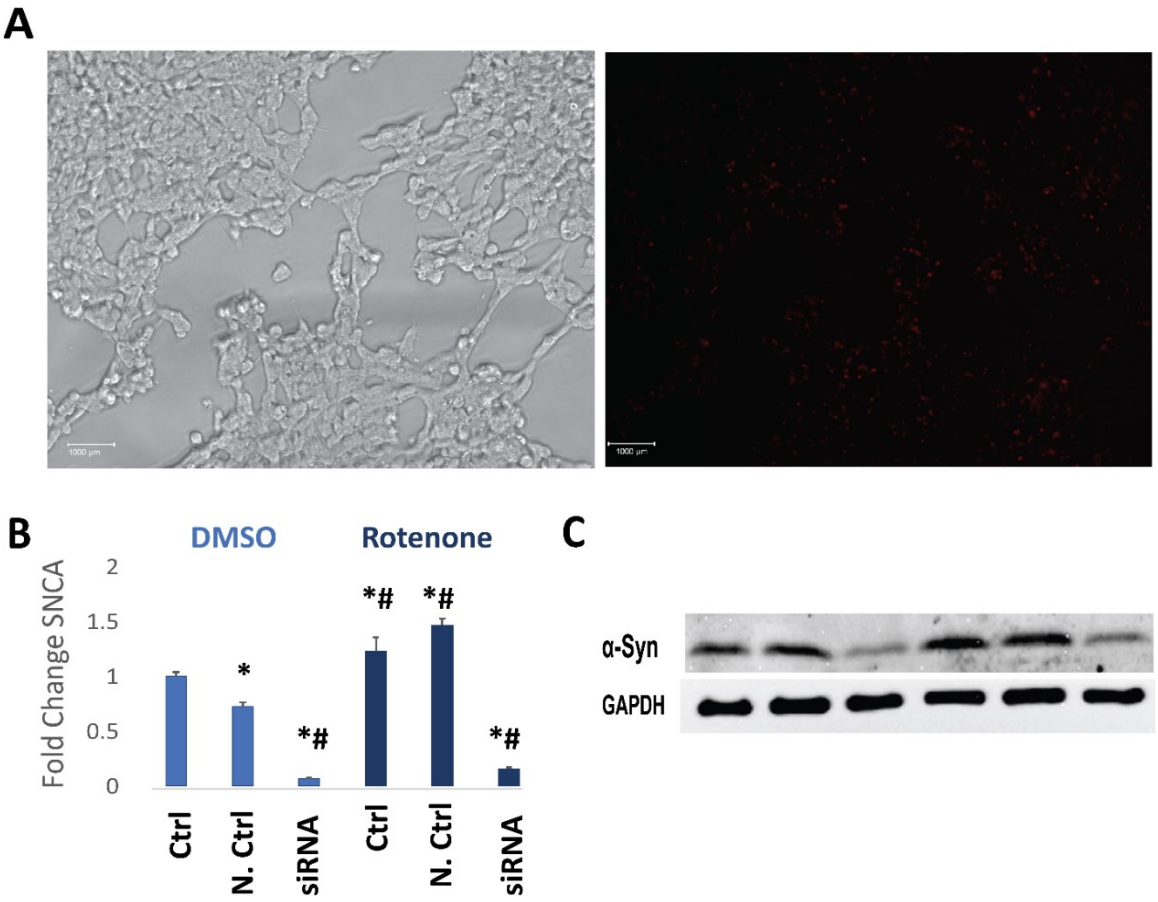

Figure 4.4 SH-5YSY siRNA transfection.
A) The efficiency of transfection conditions was tested with TYE-563 fluorescence control at 10 nM for 24h. B) TriFECTa kit DsiRNA hs.Ri.SNCA.13.2 at 10 nM was selected to knockdown *SNCA* transcript levels. The transcript expression of *SNCA* was measured after siRNA transfection and/or rotenone treatment (day 3) using qRT-PCR. * $p<0.05$ compared to non-treated control; # $p<0.05$ compared to non-treated negative control (scramble siRNA). C) Western blot of α-Syn was used to correlate changes in transcript expression with protein levels on day 3 post-transfection. SH-5YSY siRNA knockdown of α-Syn was successful and maintained knockdown during rotenone treatment.

-

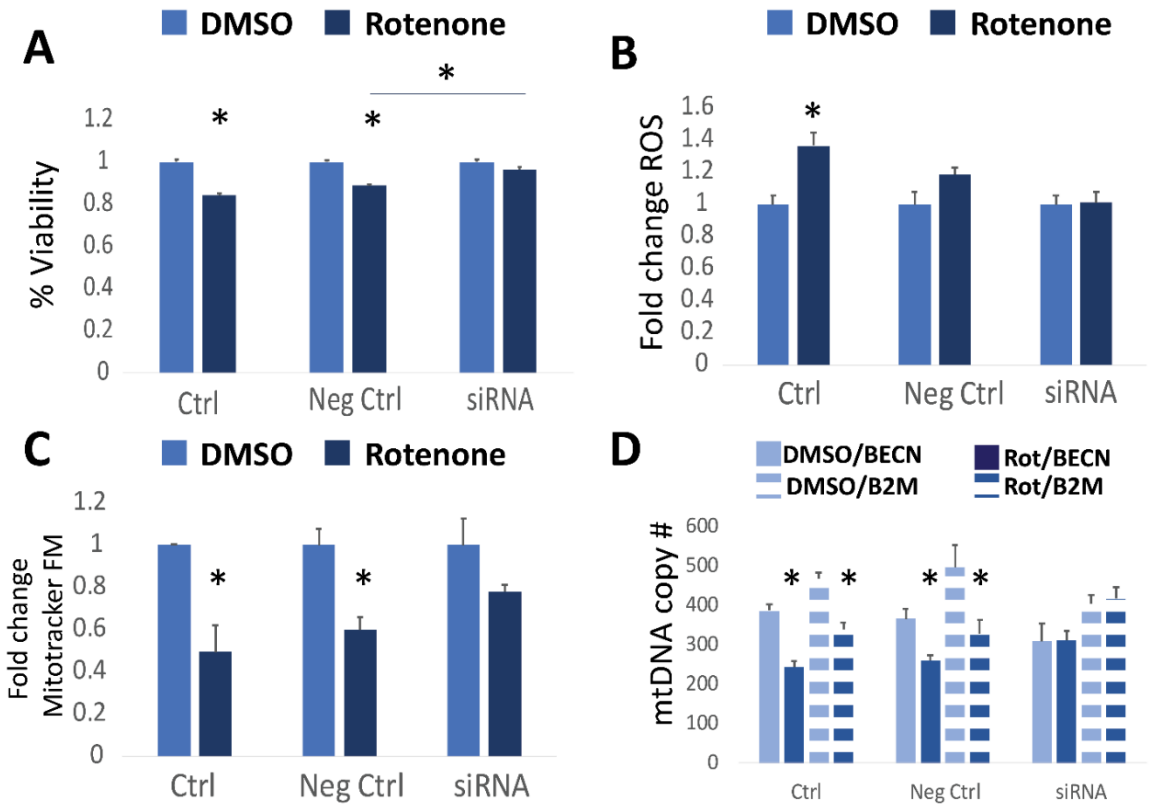

Figure 4.5 Mitochondrial resistance to rotenone treatment in α-Syn knockdown. A) The viability of mitochondria was estimated from cellular metabolic capacity using a resazurin based viability assay. The results are shown as the %viability compared to non-treated cells. B) Intracellular ROS was quantified using the DCFDA fluorescence assay and results are shown as the fold change in fluorescence compared to the non-treated cells. C) The number of mitochondria was measured with the Mitotracker FM Red fluorescence dye. The results are shown as the fold change in fluorescence compared to the non-treated cells. D) Mitochondrial DNA copy number is used to approximate mitochondrial function with higher copy numbers representing more robust mitochondria. The relative expression of two nuclear genes, *BECN1* and *B2M*, were compared to mitochondrial gene *ND1* using qPCR. Significance testing was done with a one-way ANOVA and a post-hoc multiple correction adjustment. (A-C) *p<0.05 (D) *false discovery rate (FDR)<0.05.

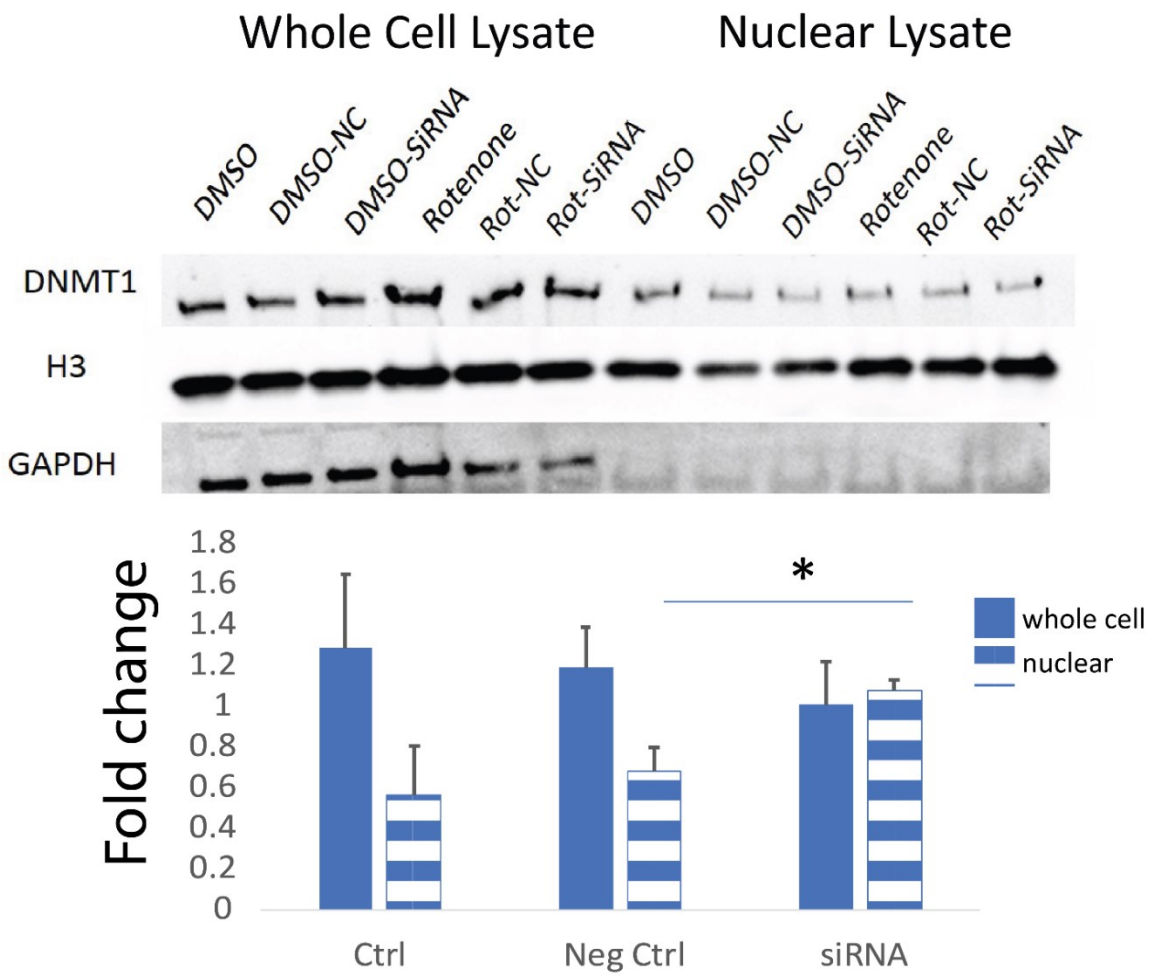

Figure 4.6 DNMT1 nuclear localization in response to rotenone treatment.
Nuclear proteins were isolated from rotenone treated SH-5YSY control and α-Syn knockdown cells. Input was collected prior to nuclear isolation for whole cell control. H3 was used as the nuclear marker and GAPDH as the non-nuclear/cytoplasmic marker to test nuclear fragment purity. DNMT1 was measured from both whole cell lysate and nuclear lysate using H3 as the loading control. Protein was quantified with Image J and the ratio of DNMT1/H3 was used for significance testing (*$p<0.05$).

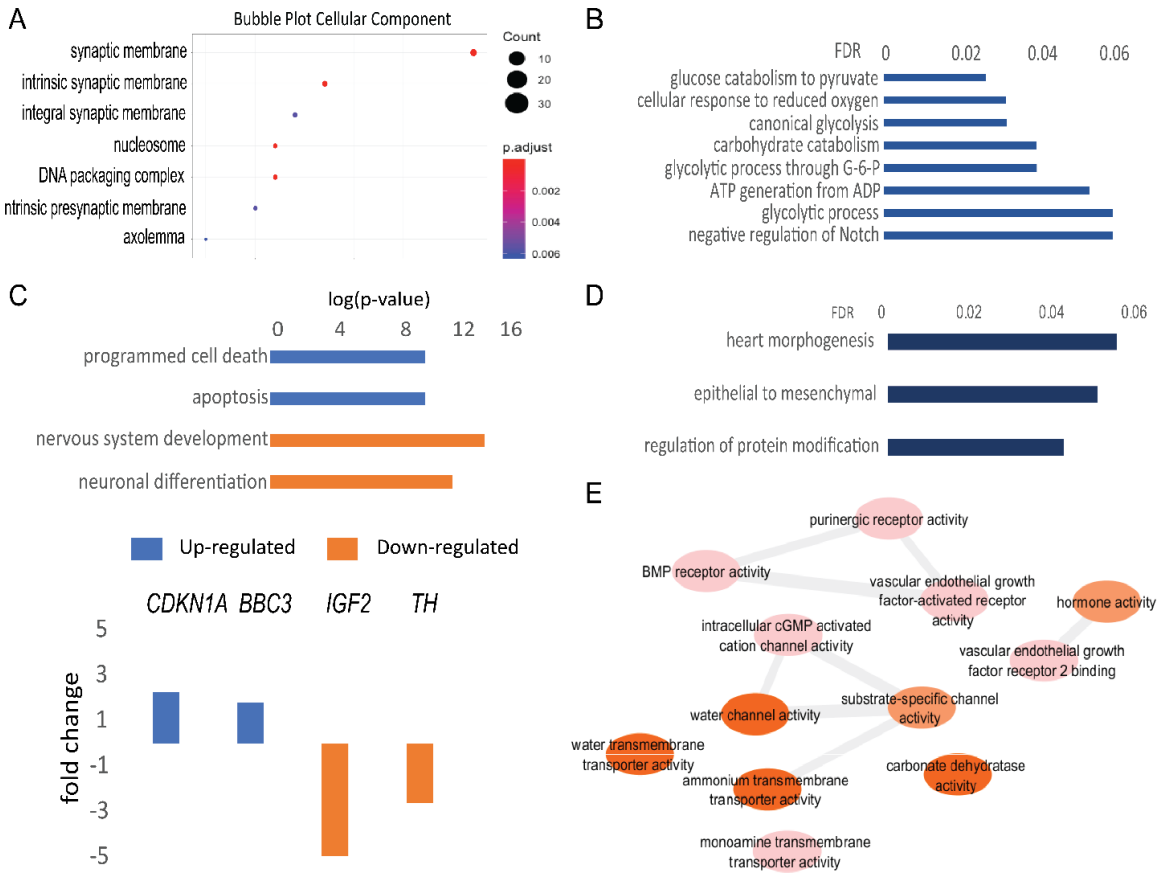

Figure 4.7 RNA sequencing of rotenone treated SH-5YSY control and α-Syn knockdown.

A) Gene Ontology cellular component annotation for DMSO versus rotenone treated negative control (scramble siRNA) SH-5YSY. Color indicates adjusted p-value and size of circle indicates the number of genes within that annotation represented in the dataset. B) Gene Ontology biological processes enriched in DMSO versus rotenone treated negative control cells. The x-axis represents the adjusted p-value using false discovery rate (FDR). C) The up-regulated and down-regulated biological processes in DMSO versus rotenone treated negative control cells are shown in the top graph with the x-value representing the Log2(p-value). The bottom graph shows the expression of key genes within these pathways. Blue is up- regulated and orange is down-regulated. D) Gene Ontology biological processes enriched in DMSO versus rotenone treated α-Syn knockdown cells. The x-axis represents the adjusted p-value using false discovery rate (FDR). E) Gene Ontology molecular functions represented in our dataset (not significant after p-value adjustment). Node color represents significance with dark orange being the most significant ($p<0.01$) and light orange ($p<0.05$). Edges represent interactions between molecular functions.

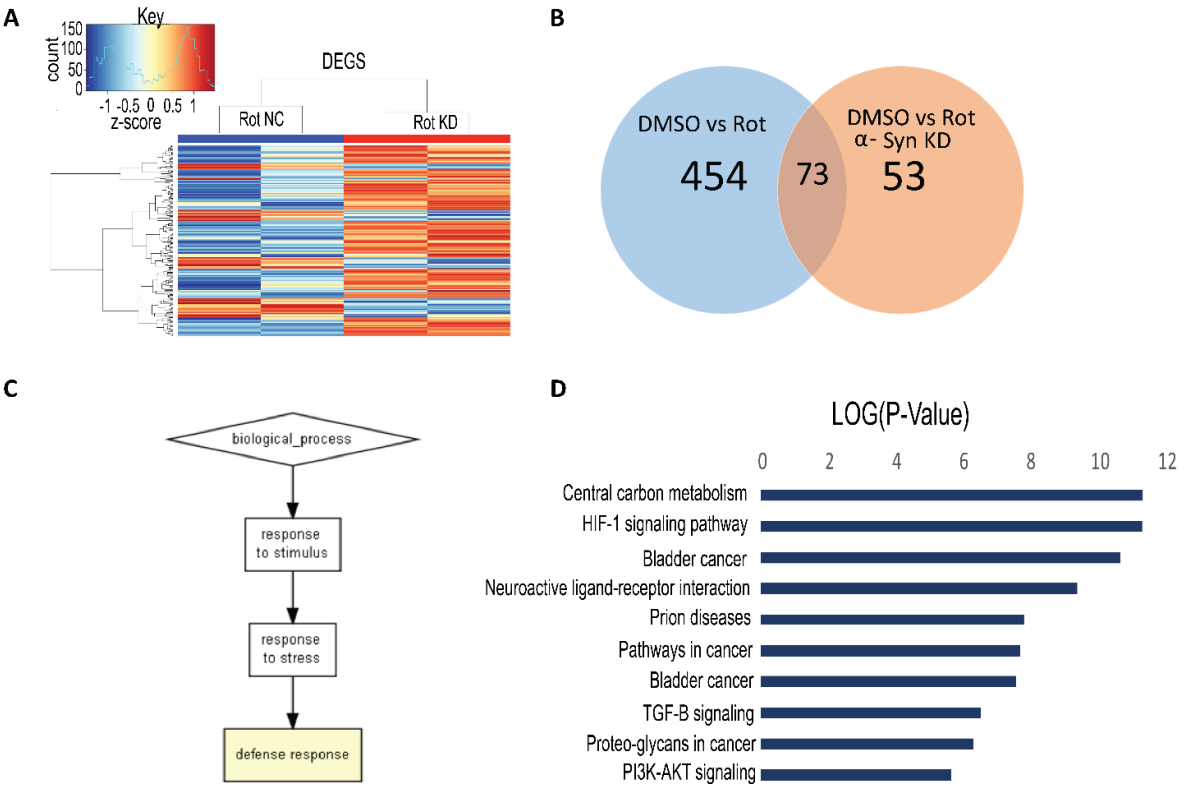

Figure 4.8 Comparison of transcriptomic changes in rotenone treated control versus α-Syn knockdown cells.

A) Heat map showing gene expression changes in rotenone treated negative control (Rot NC) and rotenone treated knockdown (Rot KD). B) Venn diagram of commonly shared differentially expressed genes (>1.5 fold change; FDR<0.05). There were 73 overlapping genes between datasets. C) Gene Ontology biological process enriched in genes differentially expressed between rotenone treated control and rotenone-treated knockdown. Yellow box indicates significance ($p<0.001$). D) The top pathways represented from the 2019 Kegg pathway database. The x-axis represents significance as the log2(p-value).

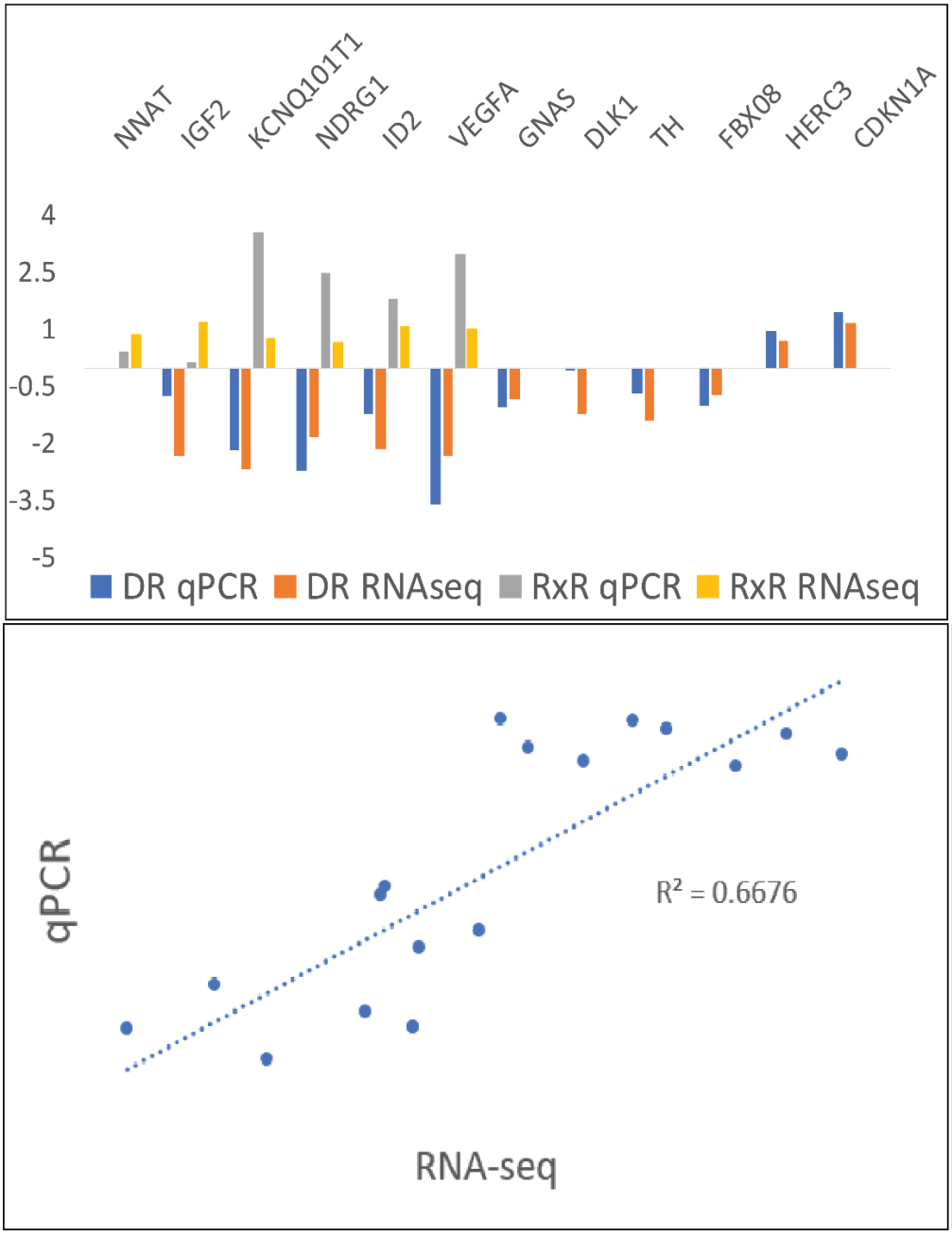

Figure 4.9 RNA sequencing validation with qRT-PCR.
Fold change comparison of RNA sequencing results versus qRT-PCR results in 12 selected genes and the linear calibration curve of RNA sequencing results with qRT-PCR results expressed as fold change in expression.

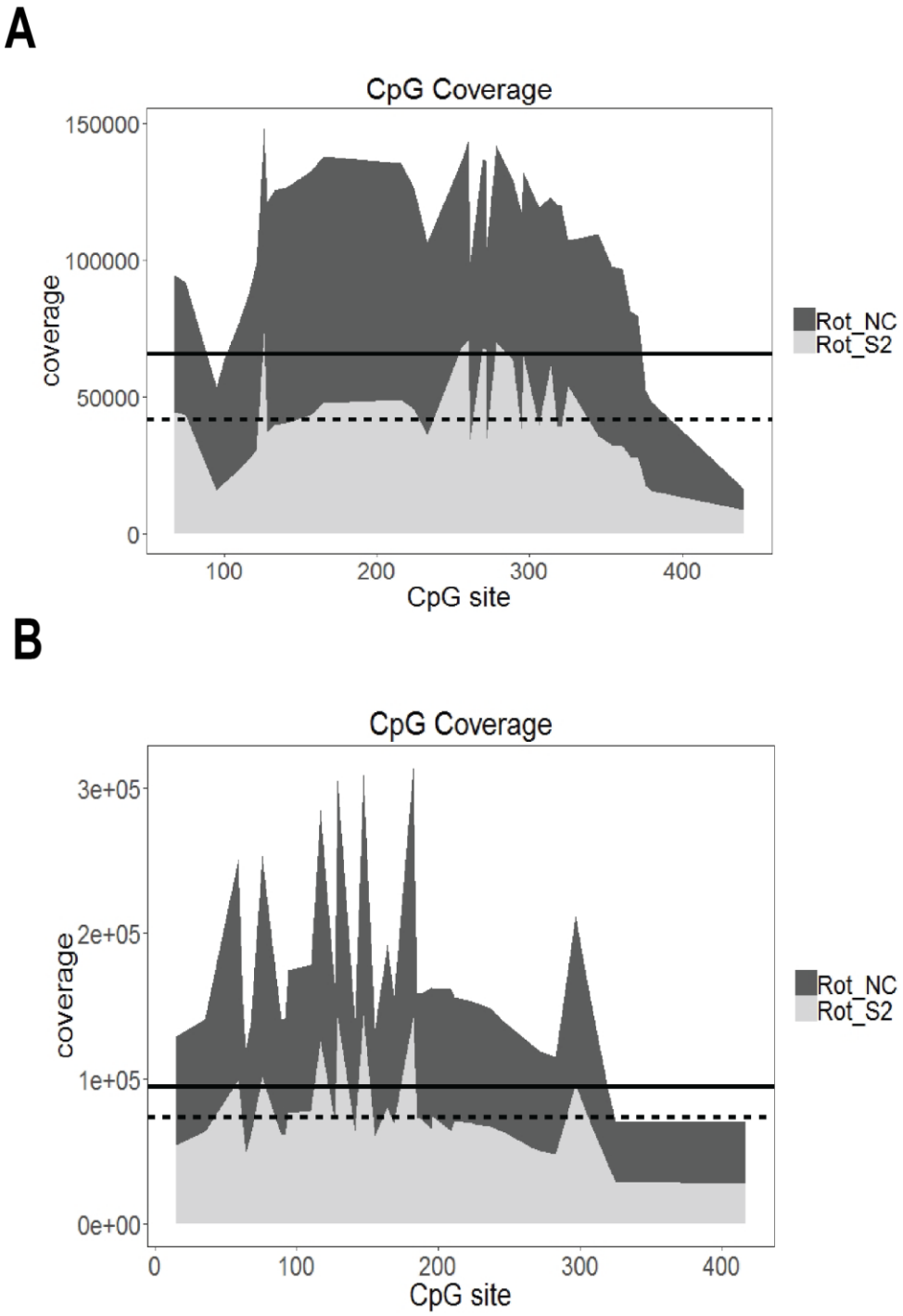

Figure 4.10 Bisulfite amplicon sequencing CpG coverage.
A) Coverage of CG nucleotides within hypoxia response elements at hypoxia target genes: *NDRG1, ID2, CDKN1A.* B) Coverage of CG nucleotides within DNMT1-dependent genes: *DLK1, GNAS, NNAT.* The average total coverage for all CpG sites within the amplified region is indicated by the straight line for negative control and the dash line for α-Syn knockdown cells.

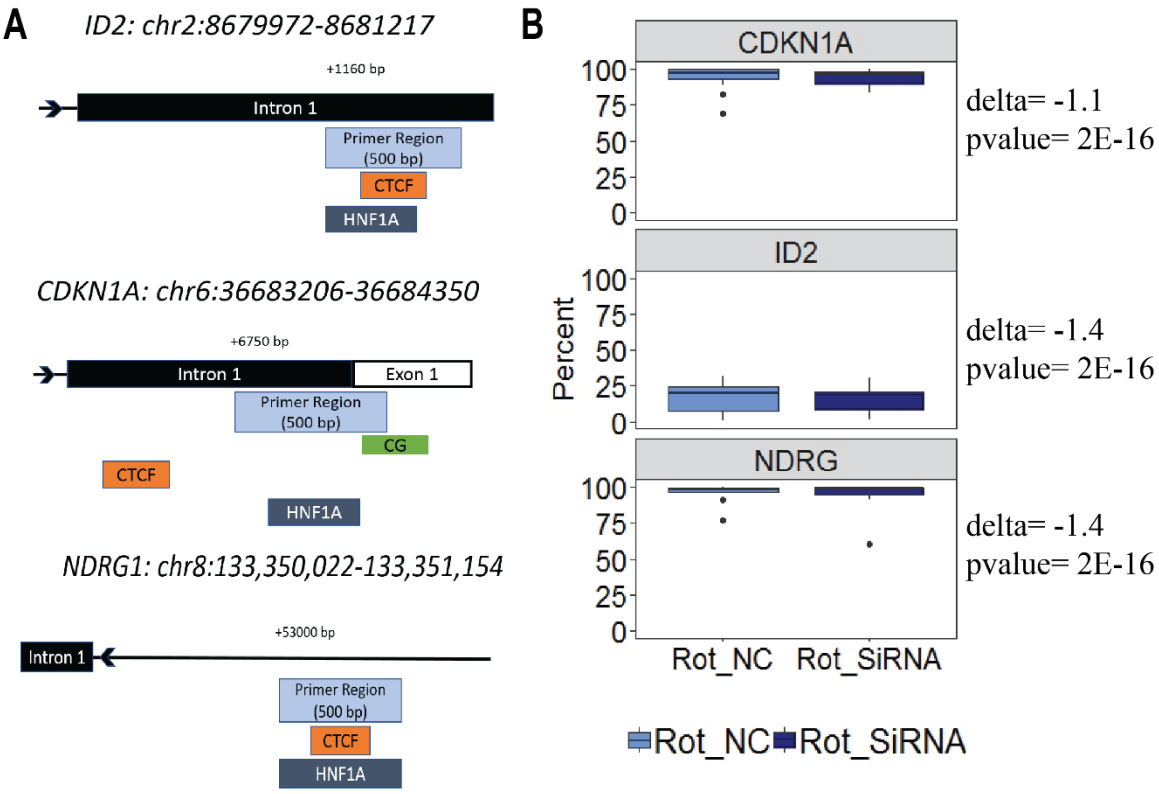

Figure 4.11 Altered CpG methylation at hypoxia response genes.
A) Genomic location of hypoxia response element at three HIF1α hypoxia target genes. The DNA element and distance from the transcription start site is annotated in black. The primer region box indicates the amplified region for Bisulfite-sequencing. The green CG box indicates CpG islands, if applicable. The orange box indicates a CTCF insulator binding motif. The dark blue box indicates the HIF1α (HNF1a) binding motif and the hypoxia response element. B) Significant differentially methylated cytosines are defined by Δ>0.1%; q-value<0.05. The percent methylation of all CpG sites within the amplified region shown. Delta indicates the change in the mean CpG methylation percentage and the associated p-value from Fisher's Exact test.

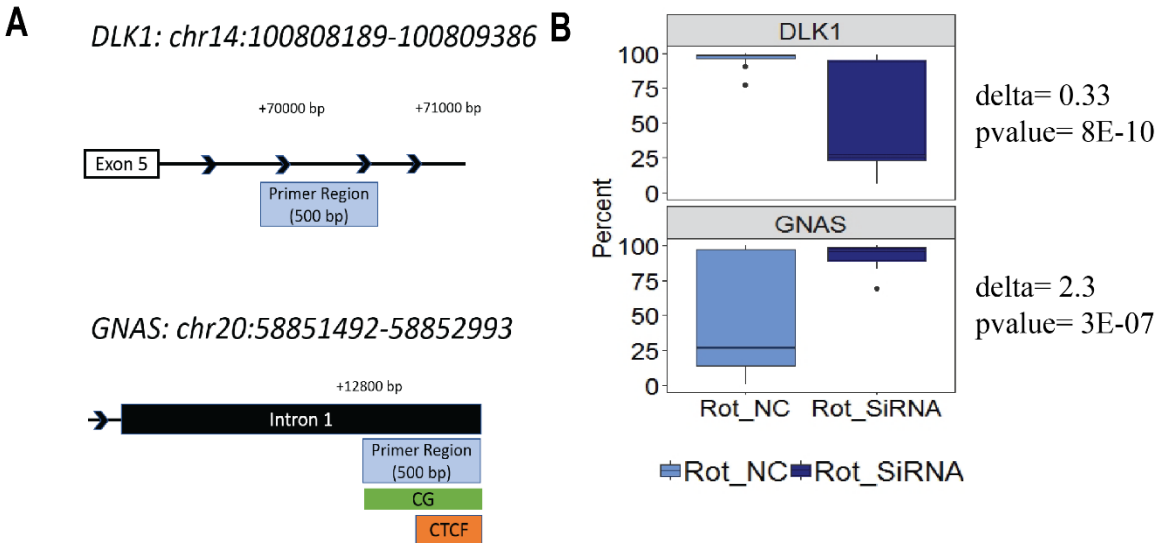

Figure 4.12 Altered CpG methylation at DNMT1-dependent genes.
A) Genomic location of DNMT1-dependent regions. The DNA element and distance from the transcription start site is annotated in black. The primer region box indicates the amplified region for Bisulfite-sequencing. The green CG box indicates CpG islands, if applicable. The orange box indicates a CTCF insulator binding motif. B) Significant differentially methylated cytosines are defined by Δ>0.1%; q-value<0.05. The percent methylation of all CpG sites within the amplified region shown. Delta indicates the change in the mean CpG methylation percentage and the associated p-value from Fisher's Exact test.

CHAPTER 5

THE INTEGRATED STRESS RESPONSE TO ROTENONE EXPOSURE INCREASES H3K27 ENHANCER ACTIVATION AND ALTERS METABOLIC REPROGRAMMING IN HUMAN NEURONAL CELLS.

5.1 Abstract

Mitochondrial dysfunction and oxidative stress are common pathological features of Parkinson's disease (PD). Our previous work demonstrates mitochondrial dysfunction altering enhancer activity. Intriguingly, PD-associated genetic variants also reside in enhancer regions. This evidence prompted us to link histone H3 acetylation, particularly H3 lysine 27 acetylation (H3K27ac), a maker of active enhancers, to the mitochondrial damage response. Herein, we investigated the role of the integrated stress response to rotenone in mediating H3K27ac enhancer activation by perturbing the balance of intracellular histone acetyltransferase PCAF with the nuclear histone deacetylase HDAC2. We used transcriptomics in combination with chromatin immunoprecipitation PCR (ChIP-PCR) to correlate the expression of genes involved in the integrated stress response with H3K27ac levels. We discovered that rotenone-induced mitochondrial damage significantly up-regulated the Activating Transcription Factor 4 (ATF4) signaling pathway and increased intracellular PCAF protein levels. We concluded that ATF4 recruitment of PCAF increased enhancer activation of pro-apoptotic genes, *CHOP and PUMA,* which are known targets of the integrated stress response. We determined that ATF4 activation was associated with increased enhancer activation of metabolic genes *PDP2* and *ACSL6,* which initiate metabolic reprogramming under oxidative stress and increase acetyl-CoA substrate availability. We also measured rotenone-induced intracellular reactive oxygen species and its inverse association with HDAC2 to facilitate pathological hyperacetylation. Our data demonstrate that the ATF4 mediated integrated stress response is an early

internal cue to regulate gene expression and propagate DNA damage induced by mitochondrial dysfunction.

5.2 Introduction

Rotenone inhibition of oxidative phosphorylation mimics cellular pathologies associated with Parkinson's disease (PD) including mitochondrial dysfunction, ATP depletion, cell cycle inhibition, oxidative stress, and the unfolded protein response (Kanthasamy et al. 2012, Xiong et al. 2011). Intracellular stress on the mitochondria and endoplasmic reticulum activates signaling cascades for secondary messengers and transcription factors to regulate the expression of genes involved in metabolic reprogramming, cell proliferation, and cell death. As a result, retrograde signaling from damaged organelles to the nucleus can shift the balance of chromatin modifying enzymes like histone acetyltransferases (HATs) and histone deacetylases (HDACs).

Histone acetylation refers to the post-translational modification of histone proteins that regulate the transcription of genes. Histone 3 (H3) is the most extensively modified of the histone proteins and histone mark H3K27ac is pursued in the scientific community because it is known to distinguish active enhancers from "poised" enhancers, which may become active after an external cue (Creyghton et al. 2010). The directional changes of H3 acetylation in PD pathology has been controversial and is dependent upon brain region and cell type (Gebremedhin and Rademacher 2016, Harrison et al. 2018). It has been suggested that H3 acetylation patterns in PD may also be dependent upon its etiology, with one study showing differences in basal acetylation levels between a patient with genetic (*LRRK2*- linked) disease and idiopathic (wild-type) disease (Sokhna et al. 2019, Yakhine-Diop et al. 2018). In addition, this study found varying levels of HDACs between genetic and idiopathic PD patients. There have even been discrepancies within PD models using complex I inhibitors. Rotenone and metformin have both been associated with hyperacetylation (Song et al. 2011, Feng et al. 2015, Fang et al. 2020) while MPTP has

been associated with both hyperacetylation and hypoacetylation (Gardian et al. 2004, Park et al. 2016).

Despite conflicting evidence, it is widely agreed upon that the homeostatic balance between HATs and HDACs in the nucleus is critical to maintain neuronal function and the tipping point of that balance is based on both genetic and environmental factors. Based on our previous report that mitochondrial dysfunction induced hyperacetylation in neurons (Huang et al. 2019), we hypothesized that rotenone-induced mitochondrial damage would initiate mitochondrial quality control signaling cascades that impairs genome-wide H3K27 enhancer activation. Herein, we focused on the role of the integrated stress response mediated by ATF4 in mediating histone acetylation of enhancers in our human neuronal cell line SH-5YSY. We investigated the mechanistic role of ATF4 in pathological hyperacetylation by examining its induction of histone acetyltransferase P300/CBP Associated Factor (PCAF), its regulation of pro-apoptotic gene expression, and its influence on acetyltransferase substrate availability. We also look at indirect effects of the integrated stress response and the inverse correlation mitochondrial reactive oxygen species (ROS) on nuclear HDAC2 depletion.

5.3 Materials and Methods

5.3.1 Cell culture and treatment of human cell line SH-5YSY

All media reagents and chemicals in cell culture were purchased from Sigma (St. Louis, MO). SH-5YSY were grown in Dulbecco's Modified Eagle Medium with high glucose, L-glutamine, and sodium pyruvate. Media was supplemented with 10% (v/v) heat inactivated fetal bovine serum and 1% (v/v) Penicillin-Streptomycin. SH-5YSY cells were confirmed by ATCC. Cells were treated at approximately 80% confluency with rotenone (200 nM) or DMSO vehicle control (<0.001%) for 24h.

5.3.2 Mitochondrial complex I inhibition

We estimated mitochondrial complex I inhibition based on a protocol by Diwakar et al. 2008. All reagents were purchased from Sigma (St. Louis, MO). We collected cells in homogenization buffer provided by the protocol at a cell density of approximately $1x10^6$ per 100 µL. We used a 22' syringe to homogenize cell lysate and incubated on ice for 20 minutes. Cells were centrifuged at 1000xg for 10 minutes at 4°C. The supernatant was collected and mitochondria were collected with centrifugation at 14,000xg for 30 minutes at 4°C. The supernatant was then removed from the mitochondria and the pellet was resuspended in 50-100 µL of fresh homogenization buffer. The mitochondria were sonicated in an Ultrasonic Bath Sonicator for 10 minutes at 4°C with 30 seconds on/ 60 seconds off. The lysate was then freeze/thawed at -80°C 3 times for 15 minutes each. The protein concentration after freeze/thaw cycles was measured using Qubit Protein Assay.

Fresh assay buffer was prepared using recipe by Diwakar et al. 2008 with 3 mM potassium cyanide (instead of sodium cyanide) and 2 µg/mL of antimycin was added immediately before use. In a 24-well plate, 25-50 µg of mitochondrial lysate was added to each well with 10 µL of 2.5 mM ubiquinone and assay buffer to a total volume of 500 µL. For negative control wells, 25-50 µg of mitochondrial lysate was added to assay buffer with no ubiquinone to a total of 500 µL. Wells were pre-incubated for 2 minutes at room temperature and then 20 µL of 5 mM β-NADH was added to each well. The absorbance at 340 nm was measured every 30 seconds for 2 minutes. The ΔA_{340}/min is equal to the slope of the line for β-NADH oxidation with ubiquinone subtracted by the slope of the line for β-NADH spontaneous oxidation (no ubiquinone). Complex I activity was calculated as:

$$\frac{\frac{\Delta A340}{\min} \text{ x } 1000 \text{ x} 2}{\frac{0.00622}{nM * cm} \text{ x protein(mg)}}$$

5.3.3 Mitotracker FM Red and mtDNA copy number quantification

Mitochondrial number was estimated with Mitotracker Red FM (Invitrogen, M22425). Following rotenone treatment, cells were incubated with Mitotracker (500 nM) for 1h at 37 °C. Cells were fixed with 1.5% formaldehyde for 10 mins at room temperature before fluorescence was measured at 580/640 nm. Mitochondrial DNA (mtDNA) copy number was estimated from 5 ng total DNA using a qPCR method published by Grady et al. 2014. We compared the mitochondrial gene ND1 (F: ATGGCCAACCTCCTACTCCT; R:GCGGTGATGTAGAGGGTGAT) to genomic genes *BECN1* (F:CGAGGCTCAAGTGTTTAGGC; R: ATGTACTGGAAACGCCTTGG) and *B2M* (F:CCAGCAGAGAATGGAAAGTCAA, R: TCTCTCTCCATTCTTCAGTAAGTCAACT).

5.3.4 Western blot for global H3K27ac

SH-5YSY cells were collected after 24 hours treatment and histones were extracted using the Abcam Histone Extraction kit according to kit instructions (Cambridge, UK). Histone protein concentration was measured by Qubit Protein Assay from ThermoFisher (Waltham, MA). Protein (5 µg) was loaded onto 4-15% Bio-Rad Page Gels and transferred to 0.45 um nitrocellulose (Bio-Rad, Hercules, CA). The blots were incubated with H3K27ac primary antibody (1:1000; Abcam ab4729) overnight at 4°C and anti-rabbit IgG conjugated secondary antibody (1:5000, Santa Cruz Biotechnology Sc-2357) for 1h at room temperature. The histone protein was normalized to total histone 3 (H3; Abcam ab1791) and quantified with Image J software. We tested significance by comparing the ratio of H3K27ac/H3 with a two-tailed Student's paired t-test.

5.3.5 RNA extraction and RNA sequencing library construction

Total RNA was extracted from two replicates of SH-5YSY using the Trizol method (Invitrogen, Carlsbad, CA). A total of 2ug per sample was used for library construction using the TruSeq Sample Preparation kit from Illumina (San Diego, CA). Poly-A containing mRNA molecules were isolated from total RNA using oligo-dT attached magnetic beads.

Isolated mRNA was then fragmented and synthesized into double stranded cDNA according to kit instructions. Ligation of unique Illumina adapter indices was completed for each sample before bead purification. Libraries were loaded onto a 2% agarose gel and library products between 200-800 bp were purified using the mini-Elute gel extraction kit from Qiagen (Hilden, Germany). Approximately 150 ng was sent for sequencing on a HiSeq-X platform with 100 bp paired-end reads.

5.3.6 RNA sequencing analysis

The raw BCL files were converted into FastQ files using CASAVA 1.8.2 (CASAVA). Raw sequencing reads were processed using TaRGETII RNA-seq pipeline which was prepared for large size RNA-seq sample processing (https://github.com/ShaopengLiu1/RNA-seq_QC_analysis). Cutadapt (V2.8) (Martin 2011) was used to remove any remaining adapter sequences from the high throughput sequencing reads. Sequencing reads were aligned to the human genome (hg38) with STAR aligner (v2.5.4b) (Dobin et al. 2013). For mRNA analyses, the Gencode database (Gencode version 27) was chosen as the annotation reference. Read counts of annotated genes were counted using featureCount from the SubRead package (Liao et al. 2013). The raw read counts of each transcript were normalized by library size, then further normalized based on empirical controls using RUVg from the RUVseq package (REF-PMID: 25150836). Differentially expressed genes were defined as those with a 1.5-fold change in expression using an adjust p-value (false discovery rate) <0.05 from the edgeR package (Robinson et al. 2010). Gene Ontology annotation was done with GOrila and visualized with Revigo (Eden et al. 2009; Supek et al. 2011). Biological pathway analysis was done with reactome pathway analysis (Fabregat et al. 2018).

5.3.7 qRT-PCR validation

Total RNA was extracted from an additional replicate of control and α-Syn knockdown SH-5YSY treated with DMSO or rotenone using the same procedures as

stated above. A total of 500ng RNA was converted to cDNA with the PrimeScript RT reagent kit with gDNA eraser from Takara (Kusatsu, Japan). We selected six genes for quantitative PCR (qRT-PCR) analysis using primers listed in Table 5.1. All qRT-PCR reactions were performed on a 7500 Real-Time PCR system from Applied Biosystems (Foster City, CA) using the iTaq Universal SYBR Green Supermix from Bio-Rad (Hercules, CA). The change in expression was normalized to the GAPDH housekeeping gene and expressed as fold change ($2^{-\Delta\Delta CT}$).

5.3.8 SH-5YSY chromatin immunoprecipitation

All chemicals were purchased from Sigma unless otherwise noted (St. Louis, MO). *SH-5YSY* were harvested after 24 hours treatment and resuspended in fresh media at $10x10^6$ cells/ mL in a conical tube. Cells were fixed with 1% formaldehyde for 10 minutes at room temperature. The reaction was stopped with 0.2 M glycine and incubation at room temperature for 5 minutes. Fixed cells were centrifuged for 5 minutes at 300xg 4°C and washed with 1 mL cold PBS. The cell pellet was stored at -80°C until chromatin immunoprecipitation (CHIP).

Cell pellets were resuspended at approximately $1x10^6$ -cells/ 0.1 mL with PBS + 0.5 % Triton-X + 1% protease inhibitor cocktail and incubated on ice for 10 minutes prior to centrifugation for 5 minutes at 400xg 4°C. The pellet was resuspended in TE buffer pH 8.0 with protease inhibitor and PMSF. Cells were sonicated at high intensity for 30s on/ 60s off until DNA fragments were within 200-800 bp as checked by 2% agarose gel. After sonication, samples were centrifuged for 15 minutes at 14,000xg 4°C to pellet insoluble material. Sheared chromatin was transferred to RIPA buffer and approximately 10% was saved for input DNA extraction.

ChIP was done with Dynabeads Protein A (Invitrogen, Carlsbad, CA) and 4 µg of primary ChIP grade antibody (H3K27ac Abcam ab4729 or Rabbit IgG Santa Cruz Biotechnology sc-2025). Beads were washed with lithium chloride (LiCl 0.25M) buffer and

immunoprecipitated DNA was extracted from beads using phenol: chloroform method. DNA was quantified using Qubit dsDNA high sensitivity assay (Thermo Fisher, Waltham, MA).

5.3.9 SH-5YSY ChIP PCR analysis

We selected eight genes for quantitative PCR (qPCR) analysis using primers listed in Table 5.2. All qPCR reactions were performed on a 7500 Real-Time PCR system from Applied Biosystems (Foster City, CA) using the iTaq Universal SYBR Green Supermix from Bio-Rad (Hercules, CA). H3K27ac enrichment was calculated from the Ct threshold value as a percent of the total input DNA. Rabbit IgG samples were used as a negative control.

5.3.10 Western Blot for PCAF and HDAC2

Cells were lysed with PBS lysis buffer (from *4.3.4*) with 0.05% Triton-X. Cells were syringe homogenized and incubated on ice for 20 minutes. Approximately 50% cell volume was saved for whole cell lysate. Cells were centrifuged at 600 x g for 6 minutes at 4°C and the supernatant was removed from the nuclei. Nuclei were washed in lysis buffer without supplementation and then resuspended in fresh PBS lysis buffer with 0.5% Triton-X. Whole cell lysate and nuclear lysate was sonicated in an Ultrasonic Bath Sonicator 3 times for 10 seconds each. We ran 15 µg of the whole cell lysate versus the nuclear lysate on Western blot with nuclear marker H3 (1:1000, Abcam ab1791), cytoplasmic marker GAPDH (1:1000, Sigma G9549), HDAC2 (1:500, Millipore 05-814), and PCAF (1:500, Bethyl A301-666). We quantified PCAF in whole cell lysate normalized to GAPDH. We quantified HDAC2 in the nucleus normalized to H3. We tested significance by comparing the ratio of antibody/loading control with a two-tailed Student's paired t-test.

5.3.11 Acetyl-CoA Assay

SH-5YSY cells were scraped from plates after treatment (no trypsin) using the assay buffer from the Abcam acetyl-CoA assay kit (ab87546). Cells were homogenized

by syringe and centrifuged at 10,000xg for 10 mins 4°C. The supernatant was deproteinated with ice cold perchloric acid (1M) from Sigma (St. Louis, MO). The deproteinated sample was centrifuged for 2 min at 13,000xg 4°C and transferred to a new tube. The sample was neutralized with 2M KOH (Sigma) and centrifuged again at 13,000xg for 15 minutes at 4°C. The supernatant was used for acetyl-CoA according to kit instructions using 50 uL of sample per well. Samples were compared to a standard curve ranging from 0-60 pmol and calculated as pmol/ul. Significance testing was done with a two-tailed paired Student's t-test.

5.4 Results

5.3.1 Rotenone complex I inhibition hinders mitochondrial function.

To characterize mitochondrial complex I inhibition, we examined the changes in absorbance from βNADH oxidation outlined in the protocol by Diwakar et al. 2008. Control mitochondrial complex I activity was 1157±396 nM/min per mg protein. Rotenone reduced activity by 0.55-fold (643±295 nM/min per mg protein) (Figure 5.1) To measure mitochondrial potential, we used the DCFDA fluorescence assay and the intensity decreased by 0.74-fold ±0.07 ($p<0.05$) with rotenone exposure (Figure 5.1). Next, we used mtDNA copy number as another determinant of mitochondrial function by analyzing the number of copies of the mitochondrial gene *ND1*, which encodes complex I, against two separate genomic genes *BECN* and *B2M*. The number of *ND1* copies remained consistent in both tests with 385 ± 17 (vs *BECN*) and 467± 14 (vs *B2M*). There was significant depletion of mitochondrial DNA copy number using both genes (Figure 5.1). The number of *ND1* copies decreased to 243±14 and 337±19, respectively.

5.3.2 Rotenone H3K27 enhancer activation is associated with global transcriptome changes.

Histones were extracted from DMSO and rotenone treated SH-5YSY and the global level of enhancer mark H3K27ac was estimated with Western blot. We observed a

significant 1.2-fold increase in H3K27ac levels with rotenone treatment ($p<0.01$) (Figure 5.2). This increase was similar in scale to the observed increase in HEK293 cells from Chapter 2 Figure 2.3 and in rat dopaminergic neurons in Huang et al. 2019. Because H3K27ac is tightly correlated with gene expression, we analyzed global changes in gene expression with RNA-seq from two biological replicates. We discovered 1897 genes were differentially expressed in response to rotenone treatment (>1.5-fold change, FDR<0.05). The majority (73%) were down-regulated and 121 genes were changed more than 9-fold. The top genes (by Log2FC) were *RSPO* (-12 LOG2FC, FDR<10^{-60}); *HNF1A* (-8.4 LOG2FC, FDR<10^{-10}); *ASNS* (3.3 LOG2FC, FDR<10^{-20}); and *GD15* (3.6 Log2FC, FDR<10^{-20}). These genes are involved in TGFβ, HIF-1α, ATF4, and WNT transcription factor signaling (Figure 5.2). To validate our RNA-seq results, we completed qRT-PCR validation on six selected genes involved in the ATF4 signaling response (Figure 5.2).

To determine what transcriptional target genes were enriched in our dataset, we used the TRUUST transcription factor database which uses a sentence-based text mining approach from over 20 million PubMed articles to determine regulatory networks (Han et al. 2018). This network analysis gave us four transcription factors with target genes enriched in our dataset that were significant after p-value adjustment (FDR<0.05) (Table 5.3). We also looked at pathway enrichment with reactome pathways (Figure 5.2) (Fabregat et al. 2018). Only two pathways were significantly enriched from down-regulated genes and both involved chromatin-opening. The up-regulated genes were enriched with pathways involving the unfolded protein response (*ATF4*), amino acid deprivation (*ASNS*) and oxidative stress induced senescence (*p21*). These pathways and transcription factors are further described in the Discussion section.

5.3.3 Rotenone-induced ATF4 signaling increases intracellular acetyltransferase.

The transcription factors ATF4 (Figure 5.2) and ATF3 were significantly up-regulated in our RNA-seq dataset (0.8 LOG2FC, FDR<0.01) as was the EIF2α kinase

responsible for its activation (1 LOG2FC, FDR<0.01). Additionally, their target genes were enriched in our differentially expressed genes including those targets involved in neuronal apoptosis (*PUMA, TRIB3, p21,* and CHOP). ATF4 is a prominent stress factor and mediates the integrated stress response. It is a basic region/leucine zipper (bZIP) transcription factor and regularly forms heterodimers with CAAT/enhancer-binding protein (C/EBP) for DNA binding (Gachon et al. 2001). ATF4 and C/EBP then recruit histone acetyltransferases to enhancer sites to promote opening of chromatin for transcription. ATF4 is responsible for the recruitment of P300-CBP Associated Factor (PCAF) which acts as a cofactor for the transcriptional regulation of the pro-apoptotic *CHOP* (*DDIT3)* gene (Cherasse et al. 2007). We examined PCAF in rotenone-treated cells with up-regulated ATF4 gene expression. Indeed, a significant increase in intracellular PCAF protein (7.5-fold change, p<0.05) was detected from four biological replicates. Next, we characterized the H3K27ac enrichment at enhancers of ATF4 pro-apoptotic target genes (*CHOP, PUMA, TRIB3,* and *p21)* that were all significantly up-regulated in our RNA-seq data. Two of these genes, *PUMA* and *CHOP*, had significantly increased acetylation at enhancers (Figure 5.3). Both genes increased by approximately 6% compared to the vehicle control (FDR<0.05).

5.3.4 Rotenone increases acetylation of metabolic genes involved in acetyl-CoA synthesis.

Intracellular PCAF is associated with increased acetylation at enhancers of ATF4 target genes *PUMA* and *CHOP*. PCAF has acetyltransferase activity independent of P300/CBP and is known to regulate cell cycle arrest in cancer cells (Love et al. 2012). PCAF preferentially acetylates H3 lysine 9 and lysine 14 residues. However, the activity and specificity of acetyltransferases can be modulated by the availability of their substrate (Ronowske et al. 2018). In our RNA-seq dataset, we noticed a down-regulation of glycolytic genes and up-regulation of genes involved in the tricarboxylic acid (TCA) cycle

(Figure 5.4). Acetyl-CoA is the primary substrate for histone acetyltransferase enzymes and its concentration in neuronal tissues is important for neuronal function (Mews et al. 2017). Therefore, the metabolic shift caused by the integrated stress response may be responsible for increasing acetyl-CoA substrate levels and global acetylation patterns. We revealed increased H3K27ac at enhancers of 2 acetyl-CoA genes (*ACSL6* and *PDP2*) (Figure 5.4). The level of H3K27 enhancer activation was increased by 8% and 3%, respectively (FDR<0.05). To explore potential responsibility, we measured the acetyl-CoA metabolite concentration using the acetyl-CoA Pico-Probe Fluorometric assay from three separate experiments. Unexpectedly, we discovered a decrease in total acetyl-coA from 2 pmol/μl to 1.6 pmol/μl ($p<0.05$).

5.3.4 Rotenone-induced oxidative stress reduces nuclear histone deacetylase.

We investigated the role of histone deacetylase enzymes rather than histone acetyltransferase activity on the acetylation patterns of enhancers exposed to rotenone. We measured intracellular oxidative stress in response to rotenone treatment and observed a significant 1.4-fold change increase in ROS ($p<0.05$) (Figure 5.5). HDAC2 is a ubiquitously expressed nuclear enzyme with global histone deacetylase activity (Grozinger et al. 1999). We observed a significant decrease in HDAC2 in the nucleus of rotenone treated neurons (0.55-fold, $p<0.05$) that was inversely correlated with the increase in intracellular ROS (Figure 5.5).

5.5 Discussion

The role of histone acetylation in PD remains to be elucidated. However, multiple reports show that pesticide-induced models of PD have pathological hyperacetylation (Song et al. 2010, Song et al. 2011, Feng et al. 2015, Huang et al. 2019). We measured global levels of H3K27ac because of its role in marking active enhancers and its tight coupling to the transcriptome (Creyghton et al. 2010). We saw a significant increase in global H3K27ac after treatment with rotenone agreeing with our previous report in rat

dopaminergic neurons treated with rotenone (Huang et al. 2019). We used RNA-sequencing to correlate changes in gene expression with observed enhancer activation. We analyzed differentially expressed genes (DEGs) for target genes of known transcription factors using the TRUUST text mining database (Han et al. 2018). We discovered four transcription factors with targets significantly enriched in our dataset (Table 5.3).

The most significant transcription factor, *HIF1α,* and its cofactor, *VHL*, are both associated with the hypoxia response. Most of the target genes were down-regulated which agrees with our previous finding that the hypoxic response was reduced in response to rotenone (Chapter 4 Figure 4.8). This is supported by other studies that show increasing *HIF1α* activity is neuroprotective and can improve the redox environment of dopaminergic neurons (Zhang et al. 2011). The activity of HIF1α can be modified by post-translational modifications including ubiquitination by VHL. The induction of p53 can also have a negative effect on HIF1α activity through competitive inhibition of P300 histone acetyltransferase (Schmid et al. 2004). We observed an increase in H3K27ac at genes associated with p53-mediated intrinsic apoptosis (Figure 5.3) and this may indicate that the reduced activity of HIF1α may be mediated by p53 recruitment of histone acetyltransferases.

The transcription factor ASCL1, or MASH1, was also enriched among our DEGs. This protein regulates the transcription of genes involved in neurogenesis and neuronal differentiation. ASCL1 is of importance in PD literature for its capacity to convert human fibroblasts into induced neurons without transitioning first into pluripotent stem cells (Xu et al. 2017). This is critical because adult cells may maintain age-related changes in their epigenome and prevent errors stemming for a force state of high proliferation potential before re-differentiation. ASCL1 is also responsible for the transcription of genes involved in metabolic shift during dopaminergic maturation (Zheng et al. 2016). Post-mitotic

neurons rely more heavily on ATP production from oxidative phosphorylation and regulate the expression of glycolytic genes. The appropriate shut down of aerobic glycolysis is critical for neuronal differentiation and survival.

The final enriched transcription factor and the focus of our study was ATF4. We also checked the pathway enrichment of up-regulated genes and discovered that ATF4-mediated integrated stress response was the primary signaling pathway triggered in response to rotenone. The integrated stress response is stimulated by protein aggregation, glucose deprivation, and hypoxia (Pitale et al. 2017). ATF4 is the primary regulator of the mitochondrial stress response and is activated upon mtDNA depletion and complex I inhibition as seen in Figure 5.1 (Quiros et al. 2017, Kasai et al. 2019, Kim et al. 2013).

ATF4 is ubiquitously expressed in low levels but chronic cellular stress causes sustained overexpression and induces intrinsic apoptotic pathways. In the rat substantia nigra, lentiviral overexpression of ATF4 transcripts by 3.2-fold significantly decreased the number of dopaminergic neurons (Gully et al. 2016). In our rotenone-treated neurons, we observed a significant up-regulation of ATF4 and activator EIF2 kinase by 1.7-fold and 2-fold, respectively (Figure 5.2). We also measured increased H3K27ac at enhancers of pro-apoptotic genes in Figure 5.3. There was increased enhancer activation at genes *CHOP* and *PUMA* in response to ATF4 up-regulation. This agrees with reports that ATF4 pro-apoptotic pathways up-regulate *CHOP* to activate *PUMA* to increase mitochondrial membrane permeability and facilitate the release of cytochrome C (Huang et al. 2015). The N-terminus of ATF4 binds to histone acetyltransferases and this interaction stabilizes the transcription factor (Cherasse et al. 2007). The recruitment of histone acetyltransferase PCAF is responsible for the transcriptional regulation of *CHOP*. We saw an increase in intracellular PCAF protein with rotenone treatment (Figure 5.3). While ATF4 mediated integrated stress is responsible for the enhancer acetylation in pro-apoptotic

genes after rotenone treatment, the ability for recruited PCAF to explain global hyperacetylation remains dependent upon the availability of substrate.

Histone acetyltransferase activity requires optimal acetyl-CoA concentrations from oxidative metabolism and their specificity also varies with acetyl-CoA availability (Pietrocola et al. 2015). Therefore, rates of acetyl-CoA conversion and its compartmentalization have a role in diverse neurological pathologies (Ronowska et al. 2018). This has been demonstrated in hippocampal neurons in which reductions in acetyl-CoA synthetase (ACSS2) resulted in decreased histone acetylation and impaired expression of memory-related genes (Mews et al. 2017). Rotenone exposure and ATF4 signaling impairs glucose metabolism and metabolically reprograms cells to utilize fatty acids (Han and Kaufman et al. 2016, Seo et al. 2009, Worth et al. 2014). In one study by Worth et al. 2014 in SH-5YSY neurons, rotenone treatment decreased glycolytic acetyl-CoA production but maintained intracellular acetyl-CoA levels through increased fatty acid mitochondrial import and β-oxidation. ATF4 signaling has a similar response and results in the accumulation of short chain fatty acids via enhanced import (Han and Kaufman et al. 2016). We observed a down-regulation of genes encoding glycolytic metabolites including *PGK1* (-0.9 log2FC, FDR<0.001) which has been shown to protect against complex I inhibition in mice by supporting glycolytic ATP production (Cai et al. 2019). We discovered an increase in *ACSL6*, a long-chain acyl-CoA synthetase which supports β-oxidation in the mitochondria (Figure 5.4) (Soupene and Kupyers et al. 2008). This gene was also actively enhanced by H3K27ac suggesting a possible mechanism for ATF4 transcription factor activity to cause global hyperacetylation.

Pyruvate dehydrogenase is the enzyme responsible for the conversion of acetyl-CoA from pyruvate, the primary metabolite of glycolysis. The pyruvate dehydrogenase complex has a critical role in neuronal oxidative metabolism and its activity is sensitive to changes in metabolic programming (Park et al. 2018). Pyruvate dehydrogenase activity is

regulated by post-translational phosphorylation in which the pyruvate dehydrogenase kinase (PDK1) inactivates the enzyme and the pyruvate dehydrogenase phosphatase (PDP2) re-activates it. Mitochondrial dysfunction and complex I inhibition results in sustained activation of the pyruvate dehydrogenase complex and increases global acetyl-CoA levels and reduces lactic acid needed for anaerobic ATP production (Park et al. 2018). These changes in cellular metabolite concentrations are associated with neurological disease. We discovered both a decrease in the gene encoding PDK1 (-1.5 log2FC, FDR<$5x10^{-9}$) and an increase in the gene encoding PDP2 (1.0 log2FC, FDR<$5x10^{-5}$) (Figure 5.4). We also saw increases in the genes encoding enzymes ME1 and PCK2 which take metabolites of the TCA cycle and convert them back to pyruvate (Figure 5.4). We discovered increased H3K27ac at the enhancer of the *PDP2* gene further supporting our hypothesis that mitochondrial dysfunction can promote histone hyperacetylation through increased substrate availability of acetyl-CoA. However, we were not able to see increases in intracellular acetyl-CoA in rotenone treated cells (Figure 5.4). Acetyl-CoA levels fluctuate rapidly and can be difficult to measure within whole cell extracts (Pietrocola et al. 2015). Thus, our inability to see increases in acetyl-CoA in the nucleus may have been due to varying concentrations of acetyl-CoA within subcellular compartments that was not detectable with our assay. This is supported by another study that shows rotenone-induced mitochondrial damage can promote the translocation of the pyruvate dehydrogenase complex from the mitochondria to the nucleus (Sutendra et al. 2014). Nuclear pyruvate dehydrogenase remains active by blocking PDK1 inhibition and its sustained activity in the nucleus facilitates pathological hyperacetylation despite decreases in cytosolic acetyl-CoA.

Finally, rotenone-induced complex I inhibition, oxidative stress, ATF4 activation, and metabolic shift does not only affect the activity of histone acetyltransferase enzymes but can also directly influence histone deacetylases. HDAC2 is a class I histone

deacetylase that is ubiquitously expressed in the nucleus (Seto et al. 2014). It is well established that intracellular ROS and nitrosative stress can be potent inhibitors of HDAC2 activity (Kreuz and Fischle 2016). It has also been reported that metabolic reprogramming as a result of mitochondria dysfunction can increase the synthesis of HDAC2 inhibitor β-hydroxybutyrate (βHOB) from fatty acid catabolism. Rotenone increases in βHOB in multiple human cell lines including SH-5YSY has already been reported by Basu and Blair (2011). We observed an increase in both intracellular ROS induced by rotenone exposure and the reduction of nuclear HDAC2 protein levels (Figure 5.5). We examined metabolic shift in response to rotenone exposure and discovered the up-regulation of genes involved in lipid metabolism. Of these genes, *HMGCS1*, which encodes the HMG CoA synthase was significantly increased by 2-fold (FDR<10^{-3}). This enzyme is involved in the production of ketones from fatty acids and is a rate-limiting enzyme in the production of βHOB. Furthermore, it has been shown in murine hippocampal neurons that HDAC2 regulates the apoptotic factor FOXO3a from binding *p21* cell cycle kinase inhibitor (Peng et al. 2015). However, increased intracellular ROS can inhibit HDAC2 regulation of FOXO3a and increases histone 4 lysine 16 (H4K16) acetylation at the transcription start site of *p21*. We observed an increase in *p21* expression but not an increase in H3K27ac (Figure 5.4). This supports the role of the integrated stress response induced HDAC inhibition in causing non-specific global hyperacetylation across all histone proteins. We recommend further studies using metabolomic approaches investigate the nuclear concentrations of acetyl-CoA and βHOB in response to mitochondrial dysfunction.

In summary, rotenone-induced mitochondrial dysfunction and mtDNA depletion in human neuronal cell line SH-5YSY activated the integrated stress response mediated by ATF4 and was associated with global increases in H3K27ac. Enhancer activation was observed at pro-apoptotic genes, *CHOP* and *PUMA*, which are regulated by ATF4 transcription factor activity through the induction and recruitment of PCAF. The role of the

integrated stress response in metabolic reprogramming also increased acetylation at enhancers of genes involved in mitochondrial lipolysis (*ACSL6*) and pyruvate dehydrogenase activation (*PDP2)* which provides a pathway for increased acetyl-CoA substrate availability and non-specific histone acetyltransferase activity. Furthermore, intracellular ROS and the production of ketones strengthens rotenone-induced pathological hyperacetylation by degrading nuclear HDAC2. This pathway gives additional insights into the intersection of multiple pathways that provide feedback to the nucleus from mitochondria. It supports the critical role of the integrated stress response and ATF4 signaling in maintaining the delicate balance between histone acetyltransferase and histone deacetylase enzymes. It also provides evidence that ATF4 mediated changes in histone acetylation patterns at metabolic genes could provide early cues for metabolic shift and the dysregulated production of primary metabolites in chromatin regulation. Epigenetic cues that occur prior to motor pathology can aid in earlier diagnosis and improve therapeutic interventions by stimulating ATF4 regulation through the antioxidant response.

5.6 References

1. Basu SS, Blair IA. 2011. Rotenone-mediated changes in intracellular coenzyme A thioester levels: Implications for mitochondrial dysfunction. Chem Res Toxicol 24(10):1630-1632.
2. Cai R, Zhang Y, Simmering JE, Schultz JL, Li Y, Fernandez-Carasa I et al. 2019. Enhancing glycolysis attenuates Parkinson's disease progression in models and clinical databases. J Clin Invest 129(10).
3. Cherasse Y, Maurin A, Chaveroux C, Jousse C, Carraro V, Parry L et al. 2007. The p300/CBP-associated factor (PCAF) is a cofactor of ATF4 for amino acid-regulated transcription of CHOP. Nucleic Acids Res 35(17):5954-5965.
4. Creyghton MP, Cheng AW, Welstead GG, Kooistra T, Carey BW, Steine EJ et al. 2010. Histone H3K27ac separates active from poised enhancers and predicts developmental state. Proc Natl Acad Sci U S A 107(50):21931-21936; doi: 10.1073/pnas.1016071107 [doi].
5. Diwakar L, Ray A, Ravindranath V. 2008. Complex I assay in mitochondrial preparations from CNS. Current protocols in toxicology 38(1):17.10. 1-17.10. 7.
6. Dobin A, Davis CA, Schlesinger F, Drenkow J, Zaleski C, Jha S et al. 2013. STAR: Ultrafast universal RNA-seq aligner. Bioinformatics 29(1):15-21.
7. Eden E, Navon R, Steinfeld I, Lipson D, Yakhini Z. 2009. GOrilla: A tool for discovery and visualization of enriched GO terms in ranked gene lists. BMC Bioinformatics 10(1):48.
8. Fabregat A, Korninger F, Viteri G, Sidiropoulos K, Marin-Garcia P, Ping P et al. 2018. Reactome graph database: Efficient access to complex pathway data. PLoS computational biology 14(1):e1005968.
9. Fang W, Zhang J, Hong L, Huang W, Dai X, Ye Q et al. 2020. Metformin ameliorates stress-induced depression-like behaviors via enhancing the expression of BDNF by activating AMPK/CREB-mediated histone acetylation. J Affect Disord 260:302-313.
10. Feng Y, Liu T, Dong S, Guo Y, Jankovic J, Xu H et al. 2015. Rotenone affects p53 transcriptional activity and apoptosis via targeting SIRT 1 and H3K9 acetylation in SH-SY 5Y cells. J Neurochem 134(4):668-676.
11. Gachon F, Gaudray G, Thébault S, Basbous J, Koffi JA, Devaux C et al. 2001. The cAMP response element binding protein-2 (CREB-2) can interact with the C/EBP-homologous protein (CHOP). FEBS Lett 502(1-2):57-62.
12. Gardian G, Yang L, Cleren C, Calingasan NY, Klivenyi P, Beal MF. 2004. Neuroprotective effects of phenylbutyrate against MPTP neurotoxicity. Neuromolecular medicine 5(3):235-241.
13. Gebremedhin KG, Rademacher DJ. 2016. Histone H3 acetylation in the postmortem Parkinson's disease primary motor cortex. Neurosci Lett 627:121-125.
14. Grozinger CM, Hassig CA, Schreiber SL. 1999. Three proteins define a class of human histone deacetylases related to yeast Hda1p. Proc Natl Acad Sci U S A 96(9):4868-4873; doi: 10.1073/pnas.96.9.4868.
15. Gully JC, Sergeyev VG, Bhootada Y, Mendez-Gomez H, Meyers CA, Zolotukhin S et al. 2016. Up-regulation of activating transcription factor 4 induces severe loss of dopamine nigral neurons in a rat model of Parkinson's disease. Neurosci Lett 627:36-41.
16. Han H, Cho J, Lee S, Yun A, Kim H, Bae D et al. 2018. TRRUST v2: An expanded reference database of human and mouse transcriptional regulatory interactions. Nucleic Acids Res 46(D1):D380-D386.

17. Han J, Kaufman RJ. 2016. The role of ER stress in lipid metabolism and lipotoxicity. J Lipid Res 57(8):1329-1338; doi: 10.1194/jlr.R067595.
18. Harrison IF, Smith AD, Dexter DT. 2018. Pathological histone acetylation in Parkinson's disease: Neuroprotection and inhibition of microglial activation through SIRT 2 inhibition. Neurosci Lett 666:48-57.
19. Huang M, Lou D, Charli A, Kong D, Jin H, Anantharam V et al. 2019. Mitochondrial dysfunction induces epigenetic dysregulation by H3K27 hyperacetylation to perturb active enhancers in Parkinson's disease models. bioRxiv:808246.
20. Kanthasamy A, Jin H, Anantharam V, Sondarva G, Rangasamy V, Rana A et al. 2012. Emerging neurotoxic mechanisms in environmental factors-induced neurodegeneration. Neurotoxicology 33(4):833-837.
21. Kasai S, Yamazaki H, Tanji K, Engler MJ, Matsumiya T, Itoh K. 2018. Role of the ISR-ATF4 pathway and its cross talk with Nrf2 in mitochondrial quality control. Journal of clinical biochemistry and nutrition:18-37.
22. Kim KH, Jeong YT, Kim SH, Jung HS, Park KS, Lee H et al. 2013. Metformin-induced inhibition of the mitochondrial respiratory chain increases FGF21 expression via ATF4 activation. Biochem Biophys Res Commun 440(1):76-81.
23. Kreuz S, Fischle W. 2016. Oxidative stress signaling to chromatin in health and disease. Epigenomics 8(6):843-862.
24. Liao Y, Smyth GK, Shi W. 2013. The subread aligner: Fast, accurate and scalable read mapping by seed-and-vote. Nucleic Acids Res 41(10):e108-e108.
25. Love IM, Sekaric P, Shi D, Grossman SR, Androphy EJ. 2012. The histone acetyltransferase PCAF regulates p21 transcription through stress-induced acetylation of histone H3. Cell cycle (Georgetown, Tex.) 11(13):2458-2466; doi: 10.4161/cc.20864.
26. Martin M. 2011. Cutadapt removes adapter sequences from high-throughput sequencing reads. EMBnet.journal 17(1):10-12.
27. Mews P, Donahue G, Drake AM, Luczak V, Abel T, Berger SL. 2017. Acetyl-CoA synthetase regulates histone acetylation and hippocampal memory. Nature 546(7658):381-386.
28. Park S, Jeon J, Min B, Ha C, Thoudam T, Park B et al. 2018. Role of the pyruvate dehydrogenase complex in metabolic remodeling: Differential pyruvate dehydrogenase complex functions in metabolism. Diabetes & metabolism journal 42(4):270-281.
29. Peng S, Zhao S, Yan F, Cheng J, Huang L, Chen H et al. 2015. HDAC2 selectively regulates FOXO3a-mediated gene transcription during oxidative stress-induced neuronal cell death. J Neurosci 35(3):1250-1259; doi: 10.1523/JNEUROSCI.2444-14.2015.
30. Pietrocola F, Galluzzi L, Bravo-San Pedro JM, Madeo F, Kroemer G. 2015. Acetyl coenzyme A: A central metabolite and second messenger. Cell metabolism 21(6):805-821.
31. Pitale PM, Gorbatyuk O, Gorbatyuk M. 2017. Neurodegeneration: Keeping ATF4 on a tight leash. Frontiers in cellular neuroscience 11:410.
32. Quirós PM, Prado MA, Zamboni N, D'Amico D, Williams RW, Finley D et al. 2017. Multi-omics analysis identifies ATF4 as a key regulator of the mitochondrial stress response in mammals. J Cell Biol 216(7):2027-2045.
33. Robinson MD, McCarthy DJ, Smyth GK. 2010. edgeR: A bioconductor package for differential expression analysis of digital gene expression data. Bioinformatics 26(1):139-140.

34. Ronowska A, Szutowicz A, Bielarczyk H, Gul-Hinc S, Klimaszewska-Łata J, Dyś A et al. 2018. The regulatory effects of acetyl-CoA distribution in the healthy and diseased brain. Frontiers in Cellular Neuroscience 12:169.
35. Schmid T, Zhou J, Brüne B. 2004. HIF-1 and p53: Communication of transcription factors under hypoxia. J Cell Mol Med 8(4):423-431.
36. Seo J, Fortuno ES,3rd, Suh JM, Stenesen D, Tang W, Parks EJ et al. 2009. Atf4 regulates obesity, glucose homeostasis, and energy expenditure. Diabetes 58(11):2565-2573; doi: 10.2337/db09-0335.
37. Seto E, Yoshida M. 2014. Erasers of histone acetylation: The histone deacetylase enzymes. Cold Spring Harb Perspect Biol 6(4):a018713; doi: 10.1101/cshperspect.a018713.
38. Shimazu T, Hirschey MD, Newman J, He W, Shirakawa K, Le Moan N et al. 2013. Suppression of oxidative stress by beta-hydroxybutyrate, an endogenous histone deacetylase inhibitor. Science 339(6116):211-214; doi: 10.1126/science.1227166.
39. Song C. 2011. Role of hyperacetylation of histones and non-histone proteins in environmental neurotoxicants-induced dopaminergic neuronal cell death.
40. Song C, Kanthasamy A, Anantharam V, Sun F, Kanthasamy AG. 2010. Environmental neurotoxic pesticide increases histone acetylation to promote apoptosis in dopaminergic neuronal cells: Relevance to epigenetic mechanisms of neurodegeneration. Mol Pharmacol 77(4):621-632; doi: 10.1124/mol.109.062174.
41. Soupene E, Kuypers FA. 2008. Mammalian long-chain acyl-CoA synthetases. Exp Biol Med 233(5):507-521.
42. Supek F, Bošnjak M, Škunca N, Šmuc T. 2011. REVIGO summarizes and visualizes long lists of gene ontology terms. PloS one 6(7):e21800.
43. Sutendra G, Kinnaird A, Dromparis P, Paulin R, Stenson TH, Haromy A et al. 2014. A nuclear pyruvate dehydrogenase complex is important for the generation of acetyl-CoA and histone acetylation. Cell 158(1):84-97.
44. Wortel IM, van der Meer, Laurens T, Kilberg MS, van Leeuwen FN. 2017. Surviving stress: Modulation of ATF4-mediated stress responses in normal and malignant cells. Trends in Endocrinology & Metabolism 28(11):794-806.
45. Worth AJ, Basu SS, Snyder NW, Mesaros C, Blair IA. 2014. Inhibition of neuronal cell mitochondrial complex I with rotenone increases lipid beta-oxidation, supporting acetyl-coenzyme A levels. J Biol Chem 289(39):26895-26903; doi: 10.1074/jbc.M114.591354.
46. Xiong N, Long X, Xiong J, Jia M, Chen C, Huang J et al. 2012. Mitochondrial complex I inhibitor rotenone-induced toxicity and its potential mechanisms in Parkinson's disease models. Crit Rev Toxicol 42(7):613-632.
47. Xu Z, Chu X, Jiang H, Schilling H, Chen S, Feng J. 2017. Induced dopaminergic neurons: A new promise for Parkinson's disease. Redox biology 11:606-612.
48. Yakhine-Diop S, Rodriguez-Arribas M, Martanez-Chacon G, Uribe-Carretero E, Gomez-Sanchez R, Aiastui A et al. 2018. Acetylome in human fibroblasts from Parkinson's disease patients. Frontiers in Cellular Neuroscience 12:97.
49. Yakhine-Diop SMS, Martinez-Chacon G, Uribe-Carretero E, Niso-Santano M, Gonzalez-Polo RA, Fuentes JM. 2019. The paradigm of protein acetylation in Parkinson's disease. Neural Regen Res 14(6):975-976; doi: 10.4103/1673-5374.250575 [doi].
50. Zhang Z, Yan J, Chang Y, ShiDu Yan S, Shi H. 2011. Hypoxia inducible factor-1 as a target for neurodegenerative diseases. Curr Med Chem 18(28):4335-4343.

51. Zheng X, Boyer L, Jin M, Mertens J, Kim Y, Ma L et al. 2016. Metabolic reprogramming during neuronal differentiation from aerobic glycolysis to neuronal oxidative phosphorylation. Elife 5:e13374.

5.7 Tables

Table 5.1 qRT-PCR primers for RNA-seq validation

ATF4	CTCCGGGACAGATTGGATGTT	GGCTGCTTATTAGTCTCCTGGA
EIF2	AAGGGGATACCCAAACAGAGG	TTCATCAGCTTCCAAATCCTTGT
CEBPB	CTTCAGCCCGTACCTGGAG	GGAGAGGAAGTCGTGGTGC
JUN	TCCAAGTGCCGAAAAAGGAAG	CGAGTTCTGAGCTTTCAAGGT
DDIT3	GGAAACAGAGTGGTCATTCCC	CTGCTTGAGCCGTTCATTCTC
CDKN1A	TGTCCGTCAGAACCCATGC	AAAGTCGAAGTTCCATCGCTC

Table 5.2 ChIP-PCR primers for H3K27ac

ATF4	cttccgggacagattggatgtt	ggctgcttattagtctcctggac
EIF2	aaggggatacccaaacagagg	ttcatcagcttccaaatccttgt
CEBPB	cttcagcccgtacctggag	ggagaggaagtcgtggtgc
JUN	tccaagtgccgaaaaaggaag	cgagttctgagctttcaaggt
DDIT3	ggaaacagagtggtcattccc	ctgcttgagccgttcattctc
CDKN1A	tgtccgtcagaacccatgc	aagtcgaagttccatcgctc

Table 5.3 TRUUST 2019 analysis

TF	p-value	FDR
ATF4	2.50E-05	0.014
ACSL1	2.94E-05	0.017
VHL	3.06E-05	0.009
HIF1A	4.46E-05	0.008

5.8 Figures

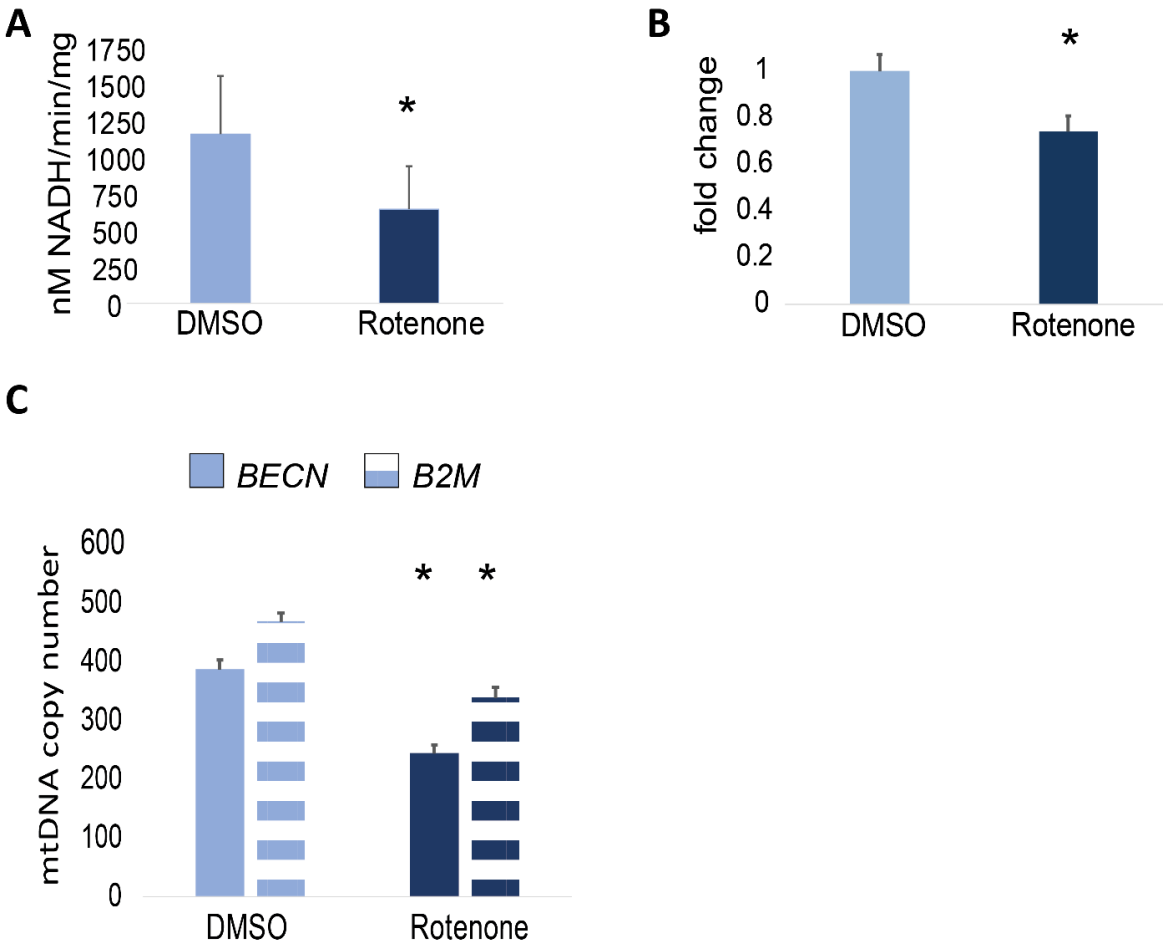

Figure 5.1 Rotenone exposure causes mitochondrial dysfunction.
A) Rotenone-induced complex I inhibition was measured by *in-vitro* assay using the absorbance reduction of oxidized βNADH with or without the presence of the electron donator, ubiquinone. The complex I activity is expressed as nM βNADH oxidized/ assay duration(min) * protein concentration (mg). B) Mitotracker FM Red was used to quantify intracellular mitochondria using the intensity of their fluorescence at 580/640 nm. The results are shown in fold change in fluorescence intensity. C) Mitochondrial DNA depletion was estimated using qPCR to measure copy number of mitochondrial gene (*ND1)* relative to two genomic genes, *BECN* (solid color) and *B2M* (striped). Mitochondrial DNA depletion was observed using either genomic gene.

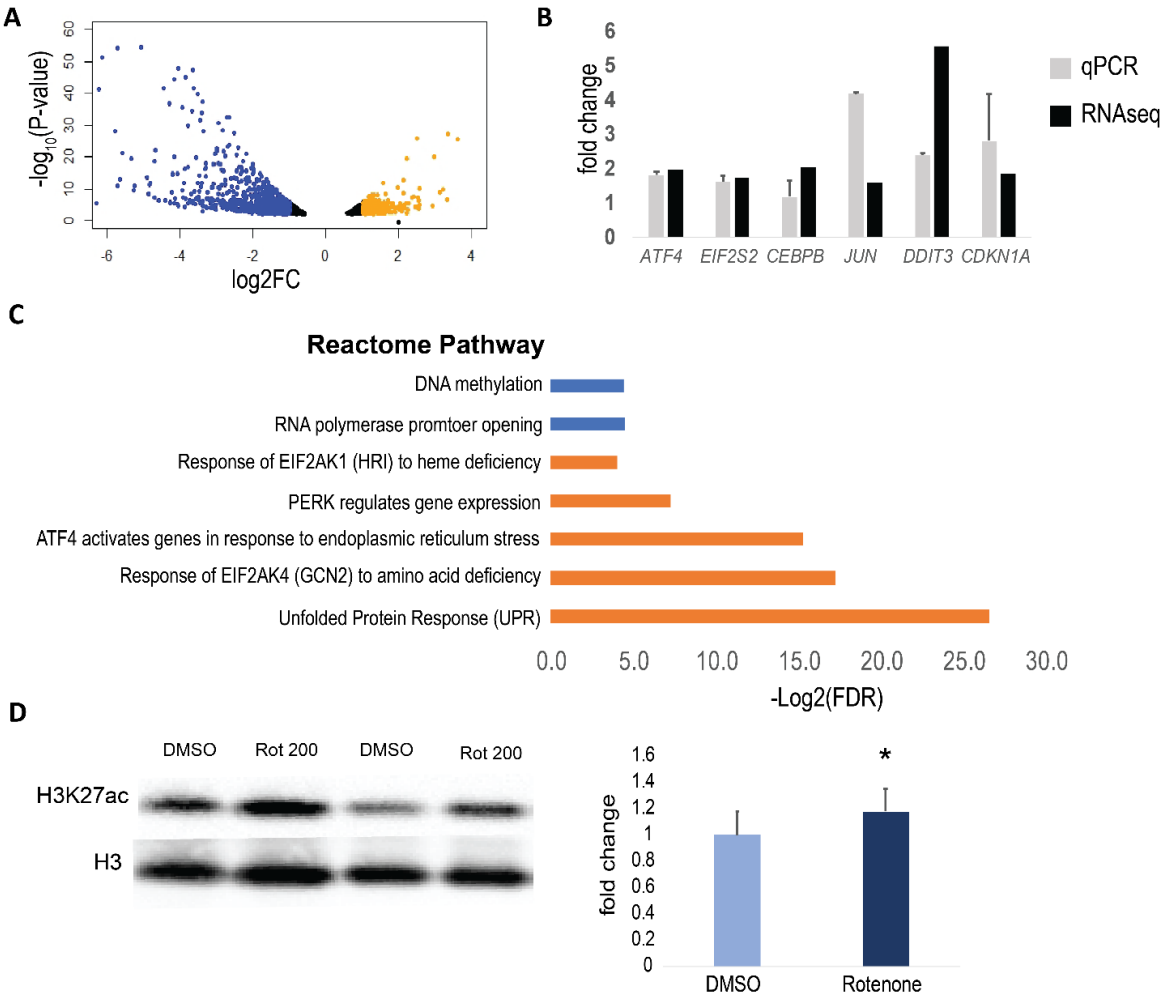

Figure 5.2 Rotenone enhancer activation causes global changes in gene expression.

A) The volcano plot of differentially expressed genes (DEGs) with the x-axis representing their change in expression (log2FC) and the y-axis representing the significance of that change (-log(P-value)). Down-regulated genes (log2FC<-1) were highlighted in blue and up-regulated genes (log2FC>1) were highlighted in orange. B) qRT-PCR validation for six genes selected from RNA sequencing data shows similar changes in gene expression in an additional replicate. C) Reactome pathway enrichment analysis with adjusted p-value (FDR<0.05) was used to determine pathways enriched in down-regulated versus up-regulated genes. Down-regulated pathways are in blue and up-regulated pathways are in orange. The x-axis represents the significance expressed as the -log2(FDR). D) Histone enhancer mark H3K27ac was observed by Western from extracted histones after rotenone treatment. H3K27ac was significantly increased in rotenone treated neurons after normalizing to histone 3 (H3) nuclear loading control protein. The quantification is shown below the Western and is expressed as fold change in chemiluminescence of DMSO. All significance testing was done with a two-tailed t-test and * represents a significant result ($p<0.05$).

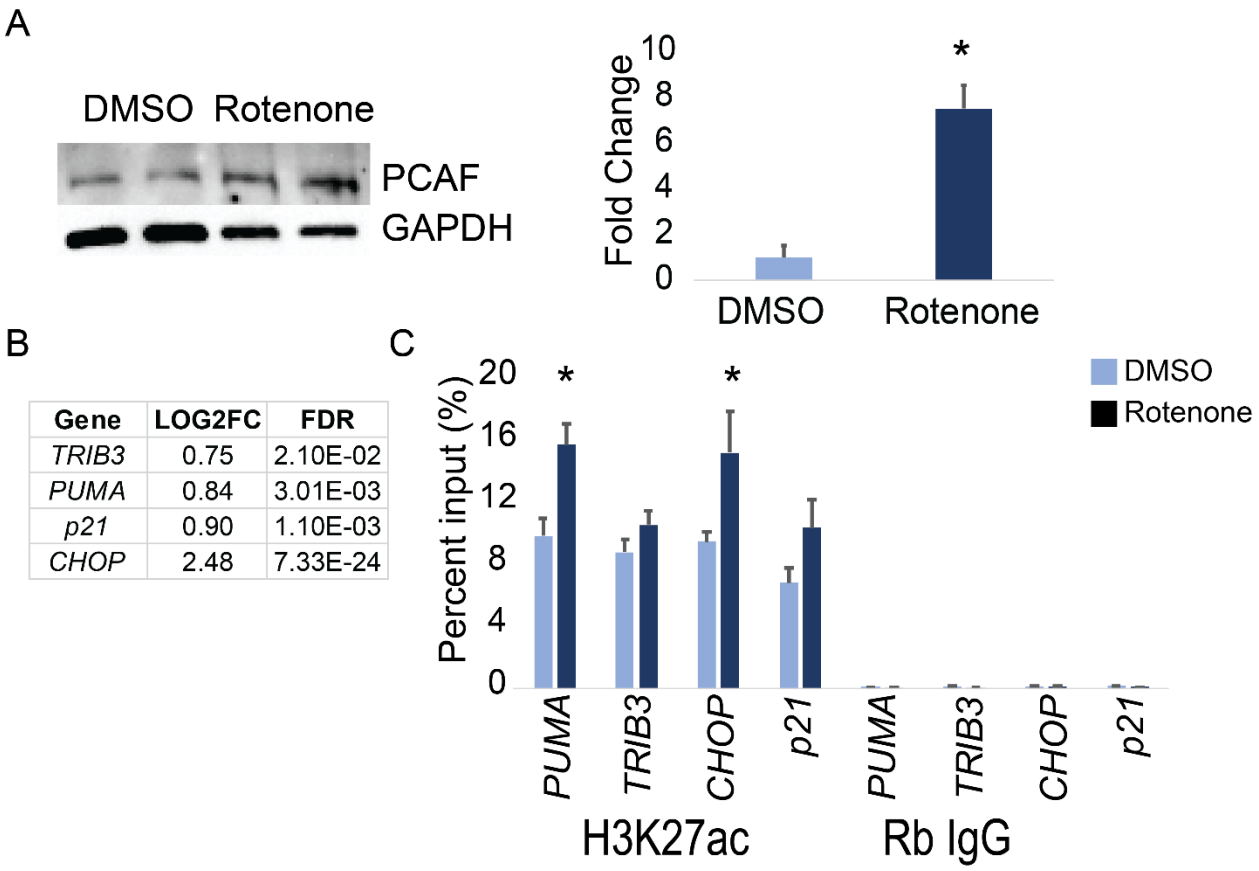

Gene	LOG2FC	FDR
TRIB3	0.75	2.10E-02
PUMA	0.84	3.01E-03
p21	0.90	1.10E-03
CHOP	2.48	7.33E-24

Figure 5.3 Rotenone-induced ATF4 signaling increases histone acetyltransferase PCAF and acetylates genes involved in apoptosis.
A) We measured the intracellular protein level of P300-CBP Associated Factor (PCAF) from four biological replicates. PCAF acts a cofactor to ATF4 in rotenone treated cells. We saw a significant up-regulation after quantification (right of Western) by normalizing PCAF to the intracellular loading control GAPDH. The results are expressed as fold change in antibody chemiluminescence relative to vehicle control (DMSO) after normalization. Significance testing was done with a two-tailed Student's t-test (* $p<0.05$). B) Pro-apoptotic genes under transcriptional control of ATF4 were observed in our differentially expressed genes from RNA sequencing. Their changes in expression (log2FC) and the significance of that change in expression (adjusted p-value FDR) are shown in the table. C) The H3K27ac enrichment of enhancers at ATF4 pro-apoptotic target genes are shown by ChIP-PCR. Rabbit IgG was used as the negative control for immunoprecipitation. Significance was tested with a two-tailed Student's t-test and multiple hypotheses were corrected using the false discovery rate method (* FDR<0.05).

A

Gene	LOG2FC	FDR
PDP2	1.09	5.6E-05
ACSL6	0.98	2.6E-02
PCK2	0.83	1.7E-03
ME1	0.59	4.6E-02

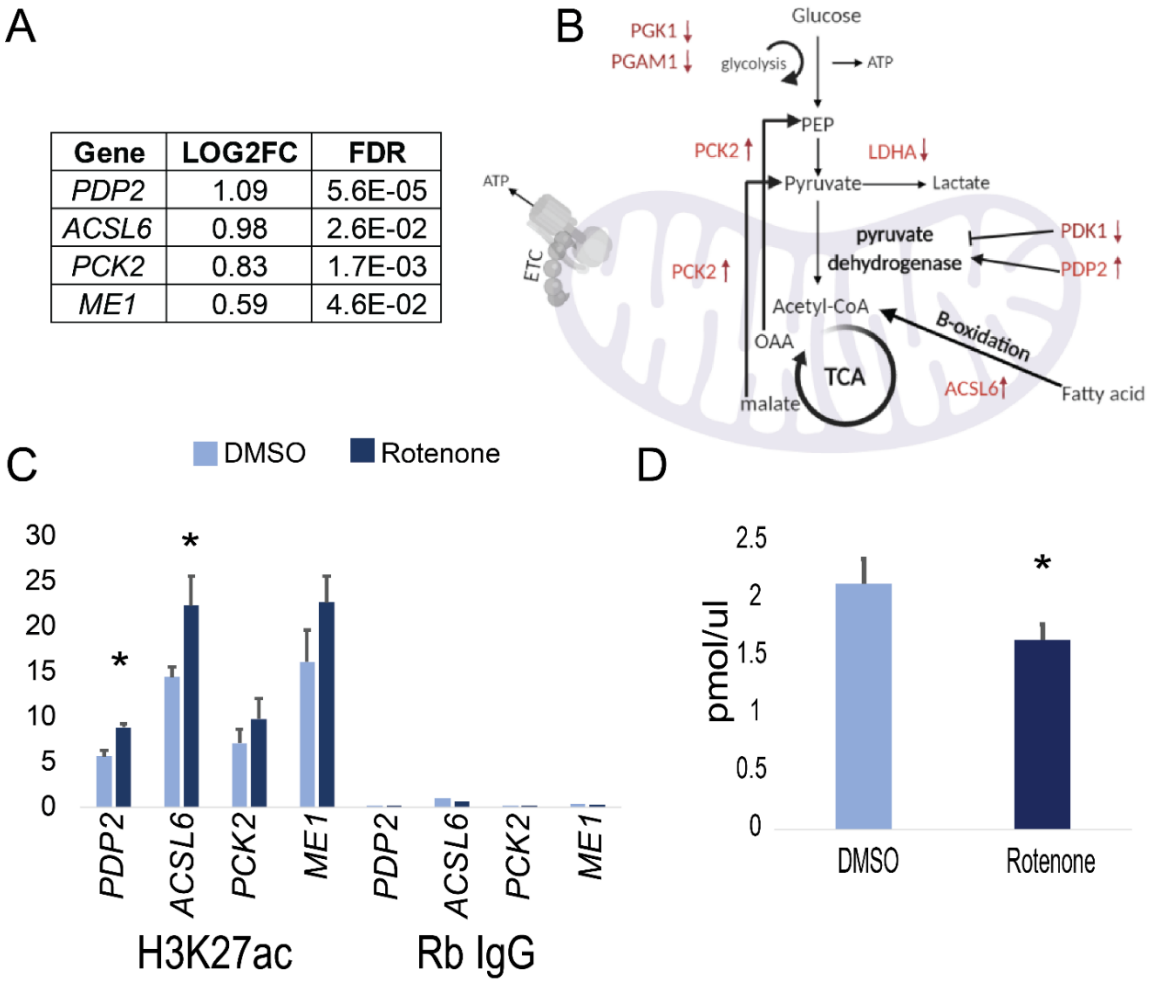

Figure 5.4 Rotenone exposure increases acetylation of enhancers at metabolic genes.

A) Metabolic genes used for H3K27ac enrichment with CHIP-PCR are shown in the table. These genes were all significantly up-regulated in our RNA sequencing data. Their expression (log2FC) and the significance of their change in expression (adjusted p-value FDR) are also shown. B) The image shows more metabolic genes differentially expressed in our RNA sequencing data and their role in synthesizing acetyl-CoA, the substrate for histone acetyltransferase enzymes. Genes in red are differentially expressed and their arrow represents the direction of their change in expression. C) The H3K27ac enrichment of enhancers at up-regulated metabolic genes involved in acetyl-CoA synthesis are shown by CHIP-PCR. Rabbit IgG was used as the negative control for immunoprecipitation. Significance was tested with a two-tailed Student's t-test and multiple hypotheses were corrected using the false discovery rate method (* FDR<0.05). D) The amount of intracellular acetyl-CoA substrate was measured after rotenone treatment using the Abcam PicoProbe Fluorometric assay. The results are shown in pmol/ul of deproteinized sample and significance was done with a two-tailed Student's t-test (* p<0.05).

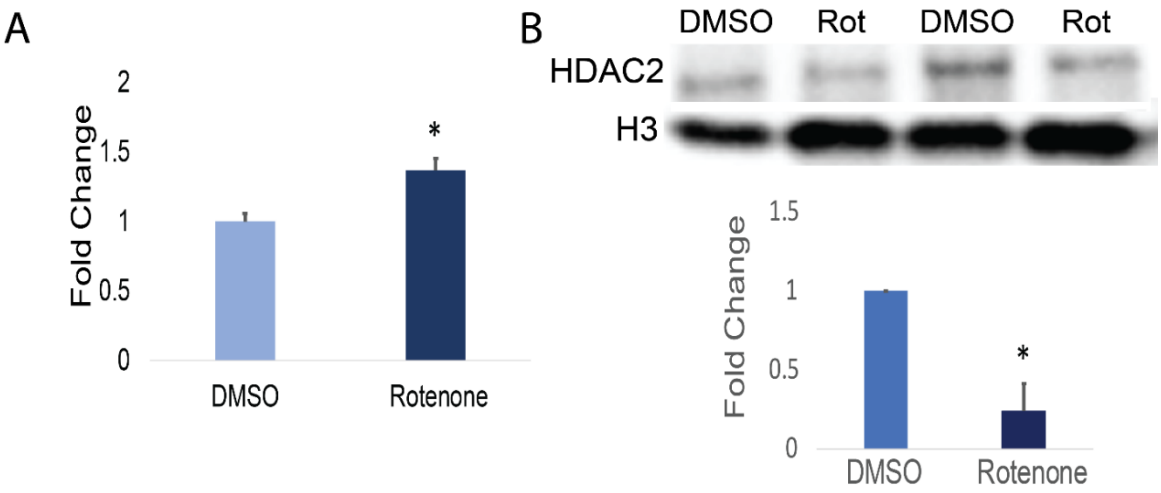

Figure 5.5 Rotenone-induced oxidative stress is associated with decreased nuclear histone deacetylase enzyme HDAC2.
A) We measured intracellular reactive oxygen species within rotenone treated neurons using the DCFDA fluorometric assay. The results are shown as the fold change in fluorescence intensity in rotenone treated cells relative to the vehicle control (DMSO). B) We extracted nuclear proteins from three biological replicates of rotenone treated neurons and measured concentrations of global histone deacetylase HDAC2. The quantification for the Western is shown below and expressed as the fold change in chemiluminescence relative to the nuclear loading control H3. Significance testing for all results was done with a Student's t-test (*$p<0.05$).

CHAPTER 6

SUMMARY OF MECHANISTIC INSIGHTS AND TRANSLATABILITY TO DOPAMINERGIC NEURONS

6.1 Summary of rotenone effects on the neuronal epigenome

Rotenone is an organic pesticide with epidemiological evidence connecting its use to increased risks of neurodegeneration and Parkinsonism in agricultural workers and their families. It is a potent mitochondrial complex I inhibitor and has been shown to impair motor function in rodents at concentrations as low as 20 nM in the brain (Greenamyre et al. 2001). Though the deleterious effect of rotenone on cellular respiration is well-established, it is not required for rotenone to deplete the number of dopaminergic cells *in-vitro* (Choi et al. 2008). In cell models, rotenone exposure recapitulates pathological hallmarks of neuronal dysfunction and aging including oxidative stress, protein aggregation, metabolic reprogramming, and p53 mediated apoptosis. We used two human cell lines (*HEK293* and *SH-5YSY*) to model rotenone toxicity and to study the mechanisms involved in gene-environment interacts relevant to Parkinson's disease (PD). The goal of this dissertation was to characterize global changes in epigenetic patterns in response to rotenone and to discern the molecular mechanisms involved in early stages of pathogenesis. We also aimed to identify vulnerable regions of the genome and to interpret the role of their dysregulated expression on neuronal function.

We began our exploration into rotenone mediated changes in chromatin regulation by focusing on DNA methylation. Global decreases in DNA methylation have been reported in patients with PD and Lewy body dementia, a neurodegenerative disorder with distinct aggregation of α-Synuclein (α-Syn) protein (Matsumoto et al. 2010). We discovered that 200 nM rotenone exposure for 24h caused striking reductions in total 5-

methylcytosine (5mC) in genomic DNA from both cell lines. Allele-specific CTCF transcription factor binding was altered in response to rotenone and modified the expression of PD genetic risk factors. We also identified regions with allele-specific methylation (ASM) and predicted genes with monoallelic expression were among those vulnerable to rotenone exposure. These regions which we previously determined were dependent on the DNA methyltransferase I (DNMT1) enzyme, included both germline imprinted regions and non-germline regions with a novel, switchable ASM phenotype. Both regions are of interest for understanding the patterning and persistence of DNA methylation as a result of exposure because they are hypothesized to be largely resistant to global demethylation events during development (Martos et al. 2017, Freeman and Wang 2019). The vulnerability of these regions to rotenone supports the hypothesis that early life exposures can cause a rewiring of neuronal activity that promotes pathology over time (Braak et al. 2003).

Rotenone induced hypomethylation was associated with the accumulation of α-Syn. We revealed that accumulated α-Syn interacts with DNMT1 after rotenone treatment and sequesters it from the nucleus (Figure 6.1). This was supported by the resilience of DNMT1-depedent regions to rotenone in α-Syn knockdown neurons. Furthermore, targeting α-Syn increased cellular resistance to rotenone and improved mitochondrial function. We analyzed HIF1α signaling and reported the novel finding that α-Syn accumulation diminishes the hypoxic response and sensitizes cells to mitochondrial damage.

Histone acetylation is the other most studied epigenetic mark in PD pathogenesis. While there are conflicting results based on brain region, disease etiology, and neuronal cell type, it is broadly agreed upon that rotenone exposure causes hyperacetylation of Histone 3 (H3) proteins (Song et al. 2011, Park et al. 2016, Huang et al. 2019).

Additionally, acetylation of H3 lysine 27 (H3K27) is tightly coupled to open chromatin and active enhancers (Creyghton et al. 2010). We explored the role of the cellular integrated stress response to mitochondrial damage on the recruitment of histone acetyltransferase (HAT) and deacetylase enzymes (HDAC). We found that ATF4 signaling not only increased enhancer activation mark H3K27ac at pro-apoptotic genes but also increased metabolic expression toward the generation of acetyl-CoA (Figure 6.1). The distribution of acetyl-CoA is critical for neuronal function and its availability determines the activity of HATs (Ronowska et al. 2018). Rotenone-induced oxidative stress was also associated with reduced histone deacetylase 2 (HDAC2) protein in the nucleus thereby supporting pathological hyperacetylation (Feng et al. 2015).

In conclusion, rotenone inhibition of mitochondrial complex I generates a redox environment that facilitates α-Syn misfolding and aggregation. The accumulation of α-Syn inhibits DNMT1 maintenance of the methylome and prevents the HIF1α mediated response to hypoxia. The propagation of oxidative stress and mitochondrial damage activates the integrated stress response and disrupts the balance of histone modifying enzymes in the nucleus. These two independent but complementary mechanisms cause global changes in gene expression profiles that destabilize neuronal activity and weaken the aging brain.

6.2 The *LUHMES* Dopaminergic Model

While Braak's hypothesis describes a spatial and temporal progression of neuronal death from the periphery to the cortex, the clinical definition of Parkinson's disease is defined by death of dopaminergic neurons in the midbrain (Braak et al. 2003, Braak et al. 2007). A limitation of our current data is that neither *HEK293* or *SH-5YSY* are specific for a mature dopaminergic neuron. In contrast, the *LUHMES* (lund human mesencephalic) cell line is derived from a healthy, mesencephalic tissue and is conditionally immortalized

with a tetracycline-controlled v-*myc* transgene. These cells can be differentiated into mature dopaminergic neurons in 2D and 3D models of disease (Krug et al. 2013, Harris et al. 2017). Unlike induced pluripotent stem cell (iPSC) models, these genes are predetermined for the dopaminergic lineage and therefore do not present challenges with multi-cellular phenotype effects (Harris et al. 2017). They also lack epigenetic memory remaining from the tissue of origin (Kim et al. 2010).

Complex I inhibition with MPP+ and rotenone have been tested in *LUHMES* models (Krug et al. 2013, Krug et al. 2014, Smirnova et al. 2016, Harris et al. 2018). Differentiated neurons were able to form tissue-like interactions *in-vitro* and complex I inhibition significantly reduced neurite outgrowth (Smirnova et al. 2016). While 100 nM was the lowest observed adverse effect level for mitochondria function and morphology, doses as low as 50 nM had large effects on the transcriptome (Harris et al. 2018). From these experiments, rotenone (100 nM) for 48h resulted in similar decreases in mitochondrial viability and membrane potential as our cellular models. Furthermore, complex I inhibition by rotenone exposure (Smirnova et al. 2016) and MPP+ (Krug et al. 2014, Smirnova et al. 2016) shifted cellular metabolism. One-carbon metabolism was altered to increase the production of glutathione in the oxidative stress response. This led to an overall increase in homocysteine levels which is associated with reduced DNA methylation patterns in the blood of PD patients (Obeid et al. 2009). We discovered that rotenone changes in one-carbon metabolism were associated with α-Syn accumulation and that aggregation may contribute to the sensitivity of cells to complex I inhibition (Duan et al. 2002). These studies also identified ATF4 as a superordinate regulator of early changes in gene expression in *LUHMES* (Krug et al. 2014, Smirnova et al. 2016). ATF4 signaling reduced glucose flux and increased non-glycolytic pyruvate production similar to our findings in Chapter 5.

Based on the concurring evidence found in our analysis of early transcriptomic changes to complex I inhibition, we hypothesized that rotenone treatment at 200 nM for 24 or 48h would produce similar trends in the epigenome of *LUHMES* cells as in the *SH-5YSY* non-dopaminergic neuronal cell line. We also hypothesized that dopaminergic neurons would be more vulnerable to rotenone exposure because of their selective vulnerability to stress (Hirsch et al. 1988). This increased susceptibility is predicted to be a result of their high energy demand and the innate reactive oxygen species (ROS) generated in dopamine synthesis (Chan et al. 2010). Additionally, experiments in SH-5YSY were done in a proliferating immortalized cell with enhanced PI3K/Akt signaling activity to promote survival in response to mitochondrial complex I inhibition (Santo et al. 2012, Zhu et al. 2012).

6.3 Cell culture and treatment of *LUHMES* cells

Cell culture of *LUHMES* was done based on methods by Krug et al. 2014 and Harris et al. 2017. We chose to culture cells in 2D versus 3D to reduce variability between cell lines. The timeline used in cell culture and treatment is presented in Figure 6.2. Flasks and 6-well plates were coated with poly-L-ornithine and fibronectin at least 24h prior to attachment with *LUHMES* (recipe Table 6.1). We cultured proliferating, undifferentiated *LUHMES* cells attached to a 75cm^2 flask to a confluency of approximately 80% in proliferating media (recipe Table 6.2). We pre-differentiated *LUHMES* in a large 175cm^2 flaks with approximately 6x10^6 cells for 24h in proliferation medium and then changed the media to differentiation medium supplemented with tetracycline to turn off expression of *v-myc*. The cells were then grown in differentiation medium for an additional 48h. Cells were seeded into 6-well plates at 1x10^6 cells per 2 mL wells for treatment with rotenone. Cells were fully differentiated after 72 h on day 5 (d5) and treated with rotenone on d6 or d7. Rotenone (200 nM) was diluted into differentiation medium with DMSO as a vehicle control (<0.002% v/v). After treatment, Presto Blue reagent was added at 10% (v/v) and

incubated for 1h at 37°C before measuring fluorescence (excitation 530 nm/ emission 590 nm). Cells were then washed and collected for additional experiments.

6.4 *LUHMES* cells were not more susceptible to rotenone exposure.

We quantified mitochondrial viability as a measure of its metabolic capacity to reduce resazurin to resorufin. We did not see a decrease in viability at either timepoint in response to rotenone (Figure 6.2). Although, *LUHMES* cells treated with rotenone (100 nM) for 48h in 3D decreased mitochondrial viability by 20%, the same dose in 2D did not decrease viability in a study by Krug et al. 2013. While no effects on the mitochondria were observed, both Smirnova et al. 2016 and Krug et al. 2013 observed diminished neurite outgrowth and transcriptomic changes in response to rotenone before other molecular endpoints.

6.5 *LUHMES* cells had increased α-Syn expression but not DNA methylation.

All methods for *LUHMES* used the same protocols as *SH-5YSY* in Chapter 4.3. We used qRT-PCR for *SNCA* gene expression analysis and observed significant up-regulation of transcripts after 24h exposure (Figure 6.3). We did not observe the increased expression of *SNCA* after 48h exposure. This may be due to the up-regulation of post-transcriptional controls for protein aggregation. We observed a significant increase in mir-34 after rotenone treatment in *SH-5YSY* but not in *SNCA* knockdown neurons. This miRNA is up-regulated in response to rotenone in rat striatal dopaminergic neurons (Horst et al. 2018) and has been shown to target *SNCA* specifically *in-vitro* (Kabaria et al. 2014).

We decided to focus on DNA methylation from *LUHMES* after 24h rotenone treatment using the dot blot analysis of 5mC. We did not observe any change in DNA methylation after rotenone treatment (Figure 6.3). We concluded that α-Syn accumulation wasn't associated with DNA hypomethylation in this model because of the lack of cell cycle progression and neuronal activity in *LUHMES* cell culture.

Active DNA demethylation in post-mitotic cells is still controversial (Ooi et al. 2008, Gavin et al. 2013) but evidence does suggest a role of active demethylation in reactivating silenced genes in mature neuronal cells (Chen et al. 2003, Martinowich et al. 2003). DNMT inhibitors can decrease DNA methylation in post-mitotic neurons *in-vitro* and up-regulate the expression of neurotropic genes to stress (Feng et al. 2010, Levenson et al. 2006, Ravindran et al. 2005). However, this change in DNA methylation may be activity dependent and thus their demethylation relies on neural electrical signals from adjacent neurons (Nelson et al. 2008). While *LUHMES* cells are electrically active in culture, heterogeneity in activity may cause a loss of effect seen with a low sensitivity method (Harris et al. 2018). Furthermore, other studies have shown that while DNMT1 is a critical factor in adult neurogenesis and the survival of proliferating cells in the cortex, the requirement for DNMT1 expression is extinguished after maturation (Noguchi et al. 2015).

6.6 *Global H3K27ac enhancer enrichment was maintained in LUHMES* cells.

Global H3K27ac enrichment in *LUHMES* was detected using the same protocols as *SH-5YSY* in Chapter 5.3. We extracted histones from *LUHMES* cells treated with rotenone for 24h and quantified changes in enhancer activation mark H3K27ac (Figure 6.4). We discovered a significant 1.8-fold increase in H3K27ac ($p<0.05$) which was stronger than the increase observed in rotenone treated *HEK293* (1.3-fold) and *SH-5YSY* (1.2-fold). We concluded that the integrated stress response was activated early upon rotenone exposure and led to the significant up-regulation in pro-apoptotic genes and those involved in metabolic reprogramming (Chapter 5). This was replicated by experiments in *LUHMES* where significant increases in the integrated stress response to complex I inhibition was observed by Smirnova et al. 2016 and Krug et al. 2014. Krug et al. 2014 also reported similar changes in glycolytic flux and pyruvate production indicating possible increases in acetyl-CoA concentrations.

Histone modifications are critical during neurogenesis for the stage and site dependent regulation of gene expression in different populations of neuronal cells (Gray et al. 2015, Mo et al. 2015). It has long been established that neuronal activity and synaptic plasticity requires remodeling of the chromatin landscape to control the expression of genes involved in cognition and behavior (Guan et al. 2002). Critical periods that begin immediately after learning require strict temporal regulation of gene expression for long-term potentiation and memory formation (Peixoto and Abel 2013). These mechanisms are directed by transcription factors and the recruitment of histone modifying enzymes to the chromatin. For example, in sensory neurons, the immediate activation of CREB proteins including ATF4 control the ratio of HATs/HDACs at plasticity genes to strengthen or prune the affected synapse (Feng et al. 2007). Chromatin modifying enzymes at enhancers can even oscillate rhythmically with external stimuli which is seen with HAT/HDACs at the regulatory regions of circadian genes (Etchegaray et al. 2003). With modern advancements in next generation sequencing, we are gaining insights into the shaping of nuclear architecture at single-cell resolution to understand how chromatin accessibility is manipulated by neural activity (Gallegos et al. 2018, Su et al. 2017).

Chromatin accessibility changes driven by neural electrical impulses were enriched at enhancers (Su et al. 2017). This can have a significant impact on the function of dopaminergic neurons which have a specific patterning of open chromatin regions that are intrinsic to their cellular subtype (Gendron et al. 2019). A recent study in *LUHMES* cells also reports the significance of enriched H3K27ac and chromatin accessibility to the molecular signature of differentiated dopaminergic neurons versus undifferentiated precursors (Pierce et al. 2018). These open chromatin regions control the expression of transcription factors involved in neurogenesis and importantly were enriched for regions with PD-risk associated single nucleotide polymorphisms (SNPs). The enrichment of PD associated SNPs at active enhancers has been reported in multiple cell lines across

various tissues (Coetzee et al. 2016). Genetic variants at active enhancers can alter transcription factor binding as we reported in Chapter 2B where PD associated SNPs at active H3K27ac marked enhancers altered the binding of the CTCF insulator. Altered transcription factor binding has also been shown in mouse *ex-vivo* dopaminergic neurons that had disease associated SNPs at activated enhancers surrounding the *SNCA* gene (McClymont et al. 2018).

6.7 Histone 3 variant H3.3 dynamics in rotenone treated *LUHMES*

H3K27ac is linked to a non-canonical H3 variant (H3.3). Non-canonical variant H3.3 only differs from canonical variants of H3 (H3.1/H3.2) by 4-5 amino acid residues but has many functional differences. For example, H3.3 is the only H3 variant that is expressed independent of cellular replication (Chen and Jin, 2017). H3.3 is localized to active regions of the genome and controls activity-dependent gene expression (Maze et al. 2015). Thus, it is essential for regulating chromatin in post-mitotic neurons (Jin and Felsenfeld, 2007). H3.3 accumulates with age in the human brain and is associated with maintaining neuronal plasticity. Historically, it was accepted that histone variants were stable leaving post-translational modifications of nucleosomes as the primary mechanisms for regulating gene expression. However, recent studies have shown that histones are dynamic, and incorporation of newly synthesized histone variants throughout life is important for marking active genes in neuronal plasticity (Maze et al. 2015). Histone turnover affects the intrinsic stability of H3 variants and makes them vulnerable to environmental exposure (Chen and Jin, 2017). The overexpression of H3.3 and its incorporation into the chromatin can impair neuronal function in the aging brain thereby contributing to disease. To explore the connection of increased H3K27ac with H3.3, we measured H3.3 in rotenone treated *LUHMES* cells (Figure 6.4). As expected, we saw correlated increases in H3.3 variant (1.8-fold change) with H3K27 enhancer activation. It is important to mention that we discovered rotenone treatment significantly down-

regulated multiple genes including H3 genes at the H1 cluster in our SH-5YSY cells. The H1 cluster encodes repetitive histones proteins that form the nucleosome and the expression of these genes can affect the deposition of newly synthesized histone variants (Dunleavy et al. 2011).

6.8 Future directions in *LUHMES* dopaminergic models

6.8.1 Rotenone effects on dopaminergic neurogenesis

We observed DNA hypomethylation in rotenone treated proliferating neurons (*SH-5YSY*) (Chapter 4). We did not see a change in DNA methylation in response to rotenone treatment in fully, differentiated dopaminergic neurons in culture (Figure 6.3). The role of DNA methyltransferases in the survival of post-mitotic neurons is not well understood. For instance, Feng et al. 2010 found that DNMTs regulate synaptic activity and survival of mature forebrain cortical neurons while Noguchi et al. 2015 found that DNMT1 expression was no longer required for the activity of mature hippocampal neurons. It is widely accepted, however, that DNMT expression is critical for the survival and maturation of neural progenitor cells (Fan et al. 2001, Hutnick et al. 2009). Hypomethylation of proliferating cells altered the expression of genes involved in apoptosis and differentiation. The expression of DNMT1 was also critical for the survival and migration of cortical interneurons which play an essential role in the circuitry between brain regions (Pensold et al. 2016).

We hypothesize that rotenone-induced hypomethylation alters the proliferation and differentiation of neural progenitor cells in the developing and adult brain. We propose treating *LUHMES* cells with rotenone at different timepoints during pre-differentiation and during the 72h maturation period between d3-d5 (Figure 6.2). The expression and methylation of genes involved in neurogenesis, axonal transport, and neuronal morphology would be correlated to the detected number of mature TH+ dopaminergic neurons with immunofluorescence. Disruption of dopaminergic maturation and the

connectivity of the striatum to the motor cortex could explain the long latency between exposure and extensive dopaminergic cell death. For instance, it was shown that agricultural workers exposed to rotenone had a similar increase in PD risk regardless of the time of exposure cessation (Tanner et al. 2011). Thought it has been previously thought that neurogenesis in the adult brain is extremely limited, it has more recently been proven that the differentiation of proliferating cells into functional dopaminergic neurons in the adult substantia nigra Is feasible (Zhao et al. 2002, Arzate et al. 2019).

6.8.2 Rotenone changes in DNA methylation in stimulated dopaminergic neurons

DNA methylation in somatic cells has traditionally been viewed as stable and that active demethylation was rare (Ooi et al. 2008). This implied that DNA was only passively demethylated with replication and that changes in DNA methylation would be propagated in dividing cells well after the removal of the stressor (Suzuki and Bird, 2008). More recently, it is understood that DNA methylation enzymatic activity persists outside of replication including during transcription (Metivier et al. 2008) and during DNA repair (Yamagata et al. 2012). The role of oxidative damage and DNA repair mechanisms in regulating DNA methylation is supported in hippocampal neurons in which DNA damage inducible gene *GADD45b* acts as a negative regulator of memory formation (Sultan et al. 2012). This indicates that DNA methylation patterns in post-mitotic neurons rely on the balance of DNA methyltransferases and DNA demethylase enzymes (TET) much like with histone modifying enzymes (Gavin et al. 2013).

The activities of these enzymes are activity dependent (Nelson et al. 2008). DNA methylation stabilizes neuronal interactions in the hippocampus and that hippocampal electrical activity sustained the expression of de novo DNA methyltransferase 3a (Levenson et al. 2006, Oliveira et al. 2012). Similarly, neural activity stimulates TET1 enzymes in cortical neurons and reactivated the expression of the neural growth factor encoded by *BDNF* (Martinowich et al. 2003). Intriguingly, we discovered that our human

DNMT1-dependent regions with sensitivity to rotenone exposure encoded proto-cadherins, voltage-gated ion channels, synaptic proteoglycans, and microtubules involved in facilitating neurotransmission (Chapter 3). We hypothesize that while *LUHMES* cells *in-vitro* are capable of electrical activity, the effect of rotenone on neural activity in culture overwhelms the ability of the cell to facilitate active demethylation. We propose that mature dopaminergic neurons are first depolarized with treatment of potassium chloride (KCl) before rotenone treatment (Martinowich et al. 2003). Alternatively, a novel tool may be used to deliver direct current electrical stimulation to cultured neurons before treatment (Mobini et al. 2018).

6.8.3 Rotenone effects on dopaminergic neural activity related enhancer activation.

We observed global increases in the acetylation of enhancers in *LUHMES* cells treated with rotenone for 24h (Figure 6.4). Chromatin accessibility and enhancer activation is critical to maintain synaptic plasticity during aging (Su et al. 2019, Pierce et al. 2018). Similar to DNA methylation enzymes, the activity of histone modifying enzymes are also related to neural activity (Feng et al. 2007). Rotenone injection into the peritoneal cavity reduces electric neuronal activity in adult rats (Darbinyan et al. 2017). It can also interfere with neuronal polarity, inhibit axogenesis, and destabilize microtubules (reviewed in Bisbal and Sanchez, 2019).

We propose that rotenone restricted neural activity in dopaminergic neurons is mediated by changes in histone acetylation of enhancers. The location of active enhancers may be correlated with genes involved in synaptic plasticity using chromatin immunoprecipitation (ChIP)- sequencing. Lastly, the role of chromatin accessibility in controlling electrical impulses should be investigated with ATAC-seq and patch-clamp electrophysiology in *LUHMES.* In a previous experiment, rotenone-induced changes in *LUHMES* neural activity were ameliorated after rotenone wash-out (Harris et al. 2018). It

would be interesting to see if H3K27ac and chromatin organization was amended after recovery from rotenone treatment.

6.8.4 Rotenone effects on histone variant turnover dynamics

Histone 3 non-canonical variant H3.3 is tightly coupled to gene expression and active enhancers. We revealed rotenone increased H3.3 levels with elevated H3K27ac. H3.3 accumulates in neurons with aging and we hypothesize that this accumulation is associated with pathological hyperacetylation in response to rotenone. Furthermore, H3.3 turnover in chromatin is dependent on proteasome degradation which is known to be obstructed in PD (Kanthasamy et al. 2012). We have found no prior studies that examine the involvement of histone variant H3.3 in PD pathogenesis. However, it seems likely that the deposition of histone H3.3 and its incorporation into the nucleosome is critical for maintaining longevity in post-mitotic dopaminergic neurons in the midbrain. The acetylation of H3.3 histone versus the canonical H3 histones should be investigated with mass spectrometry. For example, the relationship of age accumulated H3.3 was determined to be a causal factor in the histone methylation landscape in mouse hepatocytes (Tvardovskiy et al. 2017). Targeting H3.3 may also provide a novel target to regulate pathological hyperacetylation and improve cellular toxicity to rotenone *in-vitro*.

6.9 References

1. Arzate DM, Guerra-Crespo M, Covarrubias L. 2019. Induction of typical and atypical neurogenesis in the adult substantia nigra after mouse embryonic stem cells transplantation. Neuroscience 408:308-326.
2. Bisbal M, Sanchez M. 2019. Neurotoxicity of the pesticide rotenone on neuronal polarization: A mechanistic approach. Neural regeneration research 14(5):762-766; doi: 10.4103/1673-5374.249847.
3. Braak H, Del Tredici K, Rüb U, De Vos RA, Steur ENJ, Braak E. 2003. Staging of brain pathology related to sporadic Parkinson's disease. Neurobiol Aging 24(2):197-211.
4. Braak H, Sastre M, Bohl JR, de Vos RA, Del Tredici K. 2007. Parkinson's disease: Lesions in dorsal horn layer I, involvement of parasympathetic and sympathetic pre- and postganglionic neurons. Acta Neuropathol 113(4):421-429.
5. Chan CS, Gertler TS, Surmeier DJ. 2010. A molecular basis for the increased vulnerability of substantia nigra dopamine neurons in aging and parkinson's disease. Movement disorders 25(S1):S63-S70.
6. Chen D, Jin C. 2019. Histone variants in environmental-stress-induced DNA damage repair. Mutation Research/Reviews in Mutation Research 780:55-60.
7. Chen WG, Chang Q, Lin Y, Meissner A, West AE, Griffith EC et al. 2003. Derepression of BDNF transcription involves calcium-dependent phosphorylation of MeCP2. Science 302(5646):885-889; doi: 10.1126/science.1086446 [doi].
8. Choi WS, Kruse SE, Palmiter RD, Xia Z. 2008. Mitochondrial complex I inhibition is not required for dopaminergic neuron death induced by rotenone, MPP+, or paraquat. Proc Natl Acad Sci U S A 105(39):15136-15141; doi: 10.1073/pnas.0807581105 [doi].
9. Coetzee SG, Pierce S, Brundin P, Brundin L, Hazelett DJ, Coetzee GA. 2016. Enrichment of risk SNPs in regulatory regions implicate diverse tissues in Parkinson's disease etiology. Scientific reports 6:30509.
10. Creyghton MP, Cheng AW, Welstead GG, Kooistra T, Carey BW, Steine EJ et al. 2010. Histone H3K27ac separates active from poised enhancers and predicts developmental state. Proc Natl Acad Sci U S A 107(50):21931-21936; doi: 10.1073/pnas.1016071107 [doi].
11. Darbinyan LV, Hambardzumyan LE, Simonyan KV, Chavushyan VA, Manukyan LP, Sarkisian VH. 2017. Rotenone Impairs Hippocampal Neuronal Activity in a Rat Model of Parkinson's Disease. .
12. Duan W, Ladenheim B, Cutler RG, Kruman II, Cadet JL, Mattson MP. 2002. Dietary folate deficiency and elevated homocysteine levels endanger dopaminergic neurons in models of parkinson's disease. J Neurochem 80(1):101-110; doi: 10.1046/j.0022-3042.2001.00676.x [doi].
13. Dunleavy EM, Almouzni G, Karpen GH. 2011. H3. 3 is deposited at centromeres in S phase as a placeholder for newly assembled CENP-A in G1 phase. Nucleus 2(2):146-157.
14. Etchegaray J, Lee C, Wade PA, Reppert SM. 2003. Rhythmic histone acetylation underlies transcription in the mammalian circadian clock. Nature 421(6919):177-182.
15. Fan G, Beard C, Chen RZ, Csankovszki G, Sun Y, Siniaia M et al. 2001. DNA hypomethylation perturbs the function and survival of CNS neurons in postnatal animals. J Neurosci 21(3):788-797; doi: 21/3/788 [pii].
16. Feng J, Fouse S, Fan G. 2007. Epigenetic regulation of neural gene expression and neuronal function. Pediatr Res 61(7):58-63.

17. Feng J, Zhou Y, Campbell SL, Le T, Li E, Sweatt JD et al. 2010. Dnmt1 and Dnmt3a maintain DNA methylation and regulate synaptic function in adult forebrain neurons. Nat Neurosci 13(4):423.
18. Feng Y, Liu T, Dong S, Guo Y, Jankovic J, Xu H et al. 2015. Rotenone affects p53 transcriptional activity and apoptosis via targeting SIRT 1 and H3K9 acetylation in SH-SY 5Y cells. J Neurochem 134(4):668-676.
19. Gallegos DA, Chan U, Chen L, West AE. 2018. Chromatin regulation of neuronal maturation and plasticity. Trends Neurosci 41(5):311-324.
20. Gavin DP, Chase KA, Sharma RP. 2013. Active DNA demethylation in post-mitotic neurons: A reason for optimism. Neuropharmacology 75:233-245.
21. Gendron J, Colace-Sauty C, Beaume N, Cartonnet H, Guegan J, Ulveling D et al. 2019. Long non-coding RNA repertoire and open chromatin regions constitute midbrain dopaminergic neuron-specific molecular signatures. Scientific reports 9(1):1-16.
22. Gray JM, Kim TK, West AE, Nord AS, Markenscoff-Papadimitriou E, Lomvardas S. 2015. Genomic views of transcriptional enhancers: Essential determinants of cellular identity and activity-dependent responses in the CNS. J Neurosci 35(41):13819-13826; doi: 10.1523/JNEUROSCI.2622-15.2015 [doi].
23. Greenamyre JT, Sherer TB, Betarbet R, Panov AV. 2001. Complex I and parkinson's disease. IUBMB Life 52(3-5):135-141.
24. Guan Z, Giustetto M, Lomvardas S, Kim J, Miniaci MC, Schwartz JH et al. 2002. Integration of long-term-memory-related synaptic plasticity involves bidirectional regulation of gene expression and chromatin structure. Cell 111(4):483-493.
25. Harris G, Eschment M, Orozco SP, McCaffery JM, Maclennan R, Severin D et al. 2018. Toxicity, recovery, and resilience in a 3D dopaminergic neuronal in vitro model exposed to rotenone. Arch Toxicol 92(8):2587-2606.
26. Harris G, Hogberg H, Hartung T, Smirnova L. 2017. 3D differentiation of LUHMES cell line to study recovery and delayed neurotoxic effects. Current protocols in toxicology 73(1):11.23. 1-11.23. 28.
27. Hirsch E, Graybiel AM, Agid YA. 1988. Melanized dopaminergic neurons are differentially susceptible to degeneration in parkinson's disease. Nature 334(6180):345-348; doi: 10.1038/334345a0.
28. Horst CH, Schlemmer F, de Aguiar Montenegro N, Domingues ACM, Ferreira GG, da Silva Ribeiro, Cínthia Yara et al. 2018. Signature of aberrantly expressed microRNAs in the striatum of rotenone-induced parkinsonian rats. Neurochem Res 43(11):2132-2140.
29. Huang M, Lou D, Charli A, Kong D, Jin H, Anantharam V et al. 2019. Mitochondrial dysfunction induces epigenetic dysregulation by H3K27 hyperacetylation to perturb active enhancers in Parkinson’s disease models. bioRxiv:808246.
30. Hutnick LK, Golshani P, Namihira M, Xue Z, Matynia A, Yang XW et al. 2009. DNA hypomethylation restricted to the murine forebrain induces cortical degeneration and impairs postnatal neuronal maturation. Hum Mol Genet 18(15):2875-2888.
31. Jin C, Felsenfeld G. 2007. Nucleosome stability mediated by histone variants H3.3 and H2A.Z. Genes Dev 21(12):1519-1529; doi: 21/12/1519 [pii].
32. Kabaria S, Choi DC, Chaudhuri AD, Mouradian MM, Junn E. 2015. Inhibition of miR-34b and miR-34c enhances α-synuclein expression in parkinson's disease. FEBS Lett 589(3):319-325.
33. Kanthasamy A, Jin H, Anantharam V, Sondarva G, Rangasamy V, Rana A et al. 2012. Emerging neurotoxic mechanisms in environmental factors-induced neurodegeneration. Neurotoxicology 33(4):833-837.

34. Krug AK, Balmer NV, Matt F, Schönenberger F, Merhof D, Leist M. 2013. Evaluation of a human neurite growth assay as specific screen for developmental neurotoxicants. Arch Toxicol 87(12):2215-2231.
35. Krug AK, Gutbier S, Zhao L, Pöltl D, Kullmann C, Ivanova V et al. 2014. Transcriptional and metabolic adaptation of human neurons to the mitochondrial toxicant MPP. Cell death & disease 5(5):e1222-e1222.
36. Levenson JM, Roth TL, Lubin FD, Miller CA, Huang IC, Desai P et al. 2006. Evidence that DNA (cytosine-5) methyltransferase regulates synaptic plasticity in the hippocampus. J Biol Chem 281(23):15763-15773; doi: M511767200 [pii].
37. MÃ©tivier R, Gallais R, Tiffoche C, Le PÃ©ron C, Jurkowska RZ, Carmouche RP et al. 2008. Cyclical DNA methylation of a transcriptionally active promoter. Nature 452(7183):45-50; doi: 10.1038/nature06544.
38. Martinowich K, Hattori D, Wu H, Fouse S, He F, Hu Y et al. 2003. DNA methylation-related chromatin remodeling in activity-dependent BDNF gene regulation. Science 302(5646):890-893; doi: 10.1126/science.1090842 [doi].
39. Martos SN, Li T, Ramos RB, Lou D, Dai H, Xu J et al. 2017. Two approaches reveal a new paradigm of 'switchable or genetics-influenced allele-specific DNA methylation'with potential in human disease. Cell Discovery 3:17038.
40. Matsumoto L, Takuma H, Tamaoka A, Kurisaki H, Date H, Tsuji S et al. 2010. CpG demethylation enhances alpha-synuclein expression and affects the pathogenesis of parkinson's disease. PLoS One 5(11):e15522.
41. Maze I, Wenderski W, Noh K, Bagot RC, Tzavaras N, Purushothaman I et al. 2015. Critical role of histone turnover in neuronal transcription and plasticity. Neuron 87(1):77-94.
42. McClymont SA, Hook PW, Soto AI, Reed X, Law WD, Kerans SJ et al. 2018. Parkinson-associated SNCA enhancer variants revealed by open chromatin in mouse dopamine neurons. The American Journal of Human Genetics 103(6):874-892.
43. Mo A, Mukamel EA, Davis FP, Luo C, Henry GL, Picard S et al. 2015. Epigenomic signatures of neuronal diversity in the mammalian brain. Neuron 86(6):1369-1384.
44. Mobini S, Leppik L, Barker JH. 2016. Direct current electrical stimulation chamber for treating cells in vitro. BioTechniques 60(2):95-98; doi: 10.2144/000114382.
45. Nelson ED, Kavalali ET, Monteggia LM. 2008. Activity-dependent suppression of miniature neurotransmission through the regulation of DNA methylation. J Neurosci 28(2):395-406; doi: 10.1523/JNEUROSCI.3796-07.2008 [doi].
46. Noguchi H, Kimura A, Murao N, Matsuda T, Namihira M, Nakashima K. 2015. Expression of DNMT1 in neural stem/precursor cells is critical for survival of newly generated neurons in the adult hippocampus. Neurosci Res 95:1-11.
47. Obeid R, Schadt A, Dillmann U, Kostopoulos P, Fassbender K, Herrmann W. 2009. Methylation status and neurodegenerative markers in parkinson disease. Clin Chem 55(10):1852-1860; doi: 10.1373/clinchem.2009.125021 [doi].
48. Oliveira AMM, Hemstedt TJ, Bading H. 2012. Rescue of aging-associated decline in Dnmt3a2 expression restores cognitive abilities. Nat Neurosci 15(8):1111-1113; doi: 10.1038/nn.3151.
49. Ooi SK, Bestor TH. 2008. The colorful history of active DNA demethylation. Cell 133(7):1145-1148.
50. Park G, Tan J, Garcia G, Kang Y, Salvesen G, Zhang Z. 2016. Regulation of histone acetylation by autophagy in parkinson disease. J Biol Chem 291(7):3531-3540; doi: 10.1074/jbc.M115.675488 [doi].
51. Peixoto L, Abel T. 2013. The role of histone acetylation in memory formation and cognitive impairments. Neuropsychopharmacology 38(1):62-76.

52. Pensold D, Symmank J, Hahn A, Lingner T, Salinas-Riester G, Downie BR et al. 2017. The DNA methyltransferase 1 (DNMT1) controls the shape and dynamics of migrating POA-derived interneurons fated for the murine cerebral cortex. Cerebral Cortex 27(12):5696-5714.
53. Pierce SE, Tyson T, Booms A, Prahl J, Coetzee GA. 2018. Parkinson's disease genetic risk in a midbrain neuronal cell line. Neurobiol Dis 114:53-64.
54. Ravindran CM, Ticku MK. 2005. Role of CpG islands in the up-regulation of NMDA receptor NR2B gene expression following chronic ethanol treatment of cultured cortical neurons of mice. Neurochem Int 46(4):313-327.
55. Ronowska A, Szutowicz A, Bielarczyk H, Gul-Hinc S, Klimaszewska-Łata J, Dyś A et al. 2018. The regulatory effects of acetyl-CoA distribution in the healthy and diseased brain. Frontiers in Cellular Neuroscience 12:169.
56. Santo EE, Stroeken P, Sluis PV, Koster J, Versteeg R, Westerhout EM. 2013. FOXO3a is a major target of inactivation by PI3K/AKT signaling in aggressive neuroblastoma. Cancer Res 73(7):2189-2198; doi: 10.1158/0008-5472.CAN-12-3767 [doi].
57. Smirnova L, Harris G, Delp J, Valadares M, Pamies D, Hogberg HT et al. 2016. A LUHMES 3D dopaminergic neuronal model for neurotoxicity testing allowing long-term exposure and cellular resilience analysis. Arch Toxicol 90(11):2725-2743.
58. Song C, Kanthasamy A, Anantharam V, Sun F, Kanthasamy AG. 2010. Environmental neurotoxic pesticide increases histone acetylation to promote apoptosis in dopaminergic neuronal cells: Relevance to epigenetic mechanisms of neurodegeneration. Mol Pharmacol 77(4):621-632; doi: 10.1124/mol.109.062174 [doi].
59. Su Y, Shin J, Zhong C, Wang S, Roychowdhury P, Lim J et al. 2017. Neuronal activity modifies the chromatin accessibility landscape in the adult brain. Nat Neurosci 20(3):476.
60. Sultan FA, Wang J, Tront J, Liebermann DA, Sweatt JD. 2012. Genetic deletion of *gadd45b*, a regulator of active DNA demethylation, enhances long-term memory and synaptic plasticity. J Neurosci 32(48):17059; doi: 10.1523/JNEUROSCI.1747-12.2012.
61. Suzuki MM, Bird A. 2008. DNA methylation landscapes: Provocative insights from epigenomics. Nature Reviews Genetics 9(6):465-476.
62. Tanner CM, Kamel F, Ross GW, Hoppin JA, Goldman SM, Korell M et al. 2011. Rotenone, paraquat, and parkinson's disease. Environ Health Perspect 119(6):866-872; doi: 10.1289/ehp.1002839 [doi].
63. Tvardovskiy A, SchwÃ¤mmle V, Kempf SJ, Rogowska-Wrzesinska A, Jensen ON. 2017. Accumulation of histone variant H3.3 with age is associated with profound changes in the histone methylation landscape. Nucleic Acids Res 45(16):9272-9289; doi: 10.1093/nar/gkx696.
64. Yamagata Y, SzabÃ³ P, SzÃ¼ts D, Bacquet C, ArÃ nyi T, Paldi A. 2012. Rapid turnover of DNA methylation in human cells. Epigenetics 7(2):141-145; doi: 10.4161/epi.7.2.18906.
65. Zhao M, Momma S, Delfani K, Carlen M, Cassidy RM, Johansson CB et al. 2003. Evidence for neurogenesis in the adult mammalian substantia nigra. Proc Natl Acad Sci U S A 100(13):7925-7930; doi: 10.1073/pnas.1131955100 [doi].
66. Zhu G, Wang X, Wu S, Li Q. 2012. Involvement of activation of PI3K/Akt pathway in the protective effects of puerarin against MPP -induced human neuroblastoma SH-SY5Y cell death. Neurochem Int 60(4):400-408.

6.10 Tables

Table 6.1 Coating recipe for *LUHMES* culture

Components	Coating (20 mL)
Milli Q H2O	19 mL
PLO (1 mg/ml)	1 mL
Fibronectin (1 mg/ml)	20 µL

Table 6.2 Proliferation medium recipe for *LUHMES* culture

Proliferation Medium (20 mL)	
Advanced DMEM/F12 Medium	19.6 mL
N2 Supplement (100×)	200 µL
Glutamine (1 mg/mL)	200 µL
FGF (160 µg/mL)	5 µL

Table 6.3 Differentiation medium recipe for *LUHMES* culture

Differentiation Medium (100 mL)	
Advanced DMEM/F12 Medium	97 mL
N2 Supplement (100×)	1 mL
Glutamine (1 mg/mL)	1 mL
cAMP (100 mM)	1 mL
Tetracycline (2 mg/mL)	100 µL
GDNF (20 µg/mL)	10 µL

6.11 Figures

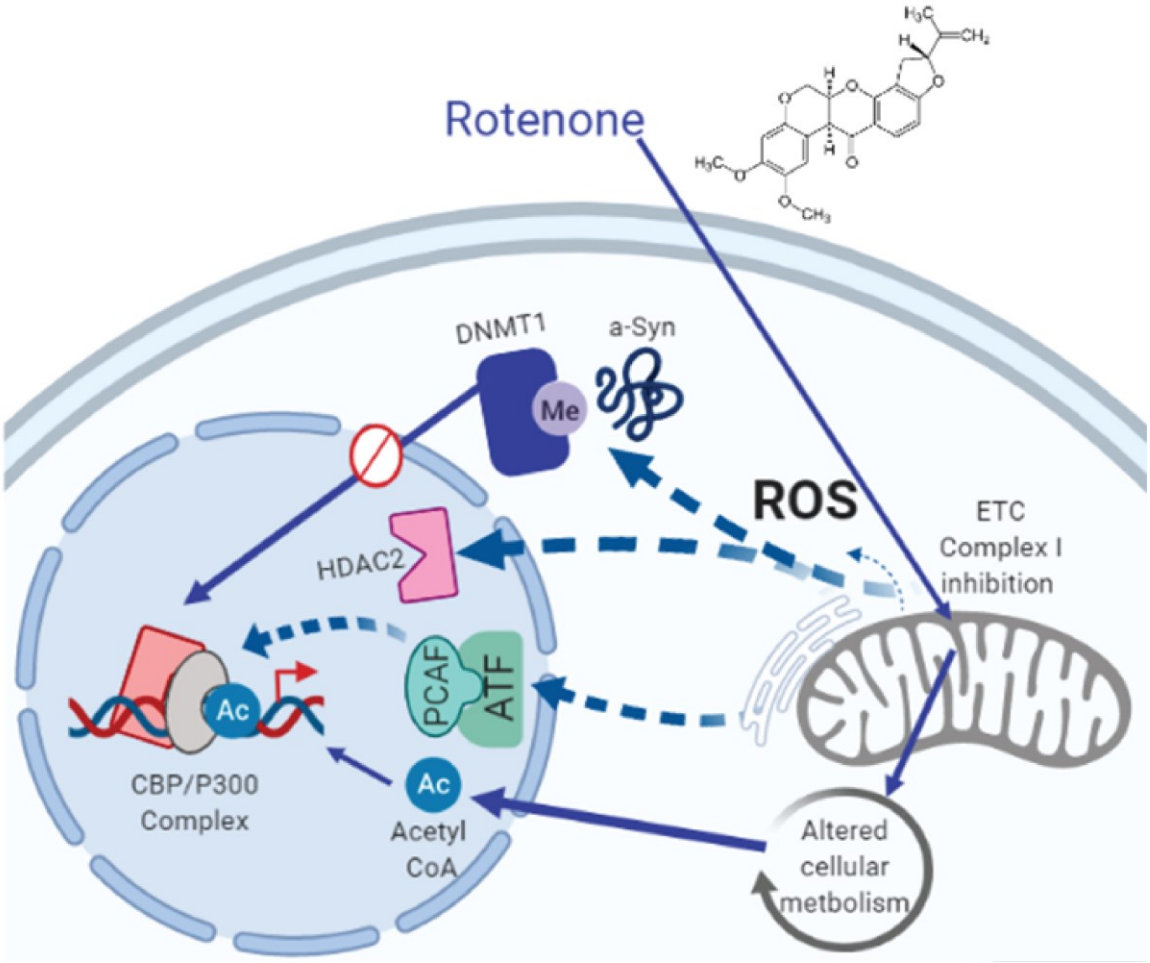

Figure 6.1 Mechanistic insights into rotenone mediated epigenetic alterations. We used rotenone to induce mitochondrial complex I inhibition and oxidative stress in *HEK293* and *SH-5YSY* immortalized cell lines. Oxidative stress promotes accumulation of α-Syn which interferes with DNMT1 translocation into the nucleus to maintain global DNA methylation patterns. Mitochondrial stress and the unfolding protein response also activate the integrated stress response via ATF4 transcription factor signaling. ATF4 induced histone acetyltransferase recruitment to the chromatin and the up-regulated expression of metabolic genes increases the pyruvate dehydrogenase complex production of acetyl-CoA. The generation of reactive oxygen species and activation of post-translational modifying proteins degrades HDAC2 nuclear protein and prevents global deacetylase activity.

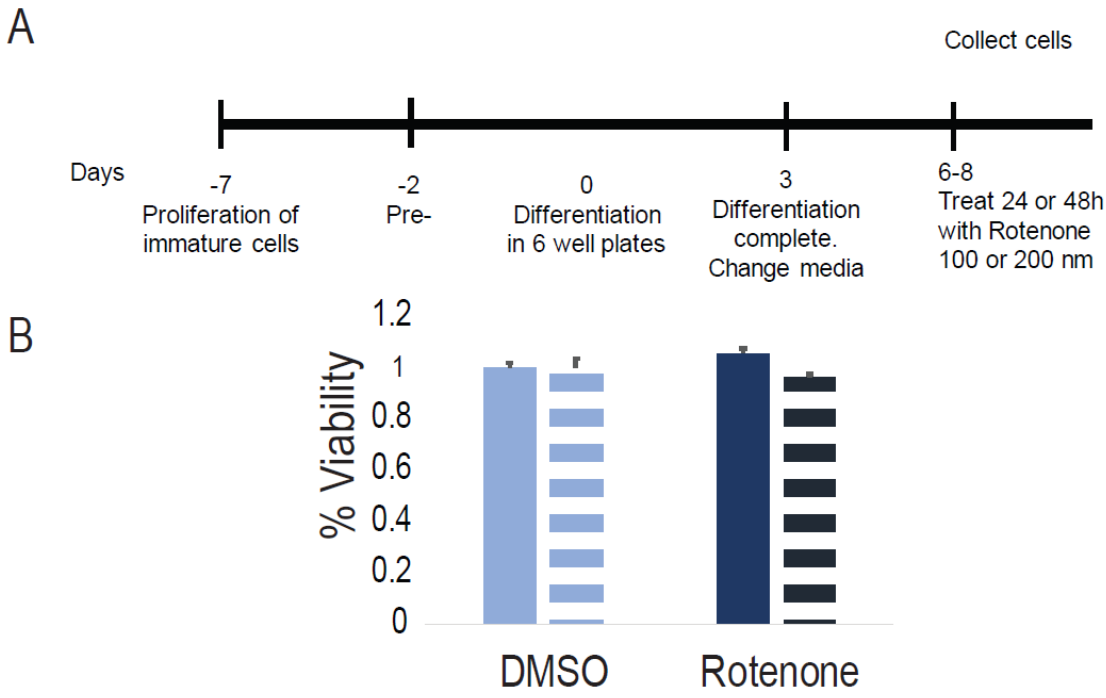

Figure 6.2 Cell culture timeline and *LUHMES* mitochondrial viability
A) *LUHMES* cells were grown *in-vitro* in proliferation medium before pre-differentiation. Differentiation was started in a 175cm^2 flask in media supplemented with tetracycline to turn off the *v-myc* proto-oncogene. The cells were seeded into 6 well plates for treatment and differentiation was complete after d3. The cells were treated with rotenone (200 nM) for 24 or 48h.

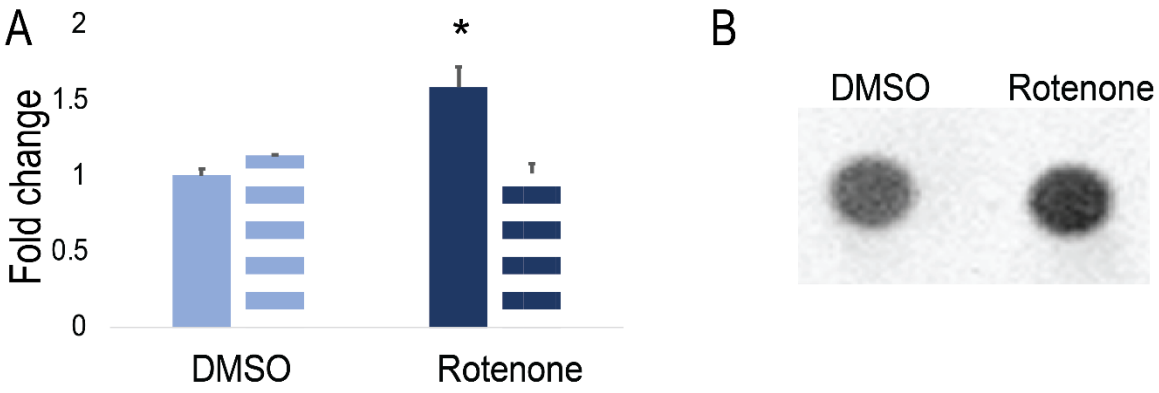

Figure 6.3 *LUHMES SNCA* accumulation and DNA methylation
A) Rotenone treatment in *LUHMES* cells increased the expression of α-Syn encoding gene *SNCA* transcripts after 24h (solid bar) but not 48h (striped bar). The y-axis is expressed in fold change relative to the housekeeping gene, *GAPDH*. * $p<0.05$.
B) Global DNA methylation was qualitatively assessed with dot blot using an antibody for 5-methylcytosine (5mC). DNA methylation was not changed by rotenone treatment.

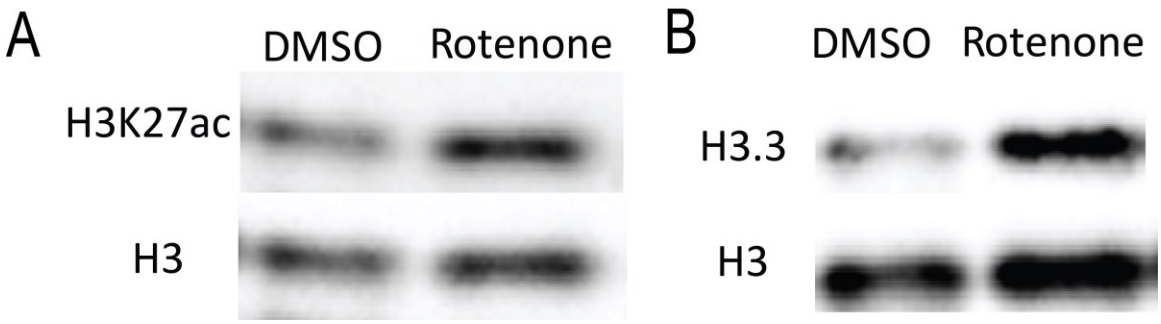

Figure 6.4 Global enhancer activation mark H3K27ac and H3 variant H3.3
A) Rotenone treatment in *LUHMES* cells increased the acetylation of enhancer regions assessed with Western of H3K27ac levels in extracted histones. Rotenone treatment significantly increased H3K27ac relative to total H3 by 1.8-fold (p-value =0.03).
B) We measured non-canonical histone variant (H3.3) in rotenone treated *LUHMES*. H3.3 was correlated with H3K27ac and increased by 1.8-fold relative to total H3.

CHAPTER 7

POTENTIAL FOR CROSSTALK BETWEEN METHYLATION AND ACETYLATION

7.1 Introduction

In this dissertation, we focused on two primary epigenetic mechanisms, DNA methylation and histone acetylation, that have been studied in experimental models of rotenone neurotoxicity. Additionally, these mechanisms have been examined in the blood and post-mortem tissues of Parkinson's disease (PD) patients.

DNA methylation is widely agreed to be reduced in PD patients but the extent of this hypomethylation is variable by region and cell type (Matsumoto et al. 2010). We examined two cellular models of rotenone neurotoxicity and discovered rotenone treatment reduces global DNA methylation patterns. Areas of vulnerability include imprinted control regions, non-germline ASMs, allele-specific transcription factor binding sites, and stress response elements. This response was not observed in the post-mitotic dopaminergic neurons and we hypothesized that it was the lack of replication or neural activity that explained the variability in methylation (Chapter 6).

Histone acetylation is controversial, and studies have suggested that hyperacetylation versus hypoacetylation depends on the region and other etiological factors (Yakhine-Drop et al. 2018). Our rotenone treated cells agreed with most reports that mitochondrial complex I inhibition is associated with pathological hyperacetylation (Song et al. 2010, Feng et al. 2015, Huang et al. 2019). This phenotype was replicated in post-mitotic dopaminergic neurons. We focused on the acetylation of histone 3 lysine 27 (H3K27ac) because of its role in marking active enhancers from poised enhancers (Creyghton et al. 2010). Enhancer activation and chromatin opening are molecular signatures of maturation and neural activity (Pierce et al. 2018, Su et al. 2019). However,

histone acetylation at other lysine residues is also likely. For example, H3 lysine 56 (H3K56) acetylation may be a site of interest due to its role in regulating nucleosome assembly and histone variant turnover (Matsumoto et al. 2005, Li et al. 2008). There is also interest in the role of histone methylation. While, this paper focuses on histone acetylation, H3 lysine 4 (H3K4) methylation plays a significant role in marking active enhancers. This histone modification is also associated with neural activity and is required for most cognitive functions within the hippocampus (Collins et al. 2019). In fact, dysregulated expression and function of histone lysine methyltransferases are often found in neurodevelopmental disorders. Like H3 acetylation patterns, H3 methylation is often correlated with histone variant H3.3 and one study showed that H3.3 accumulation may explain open-chromatin modification, H3 lysine 36 di-methylation ($H3K36me^2$), increases with age (Maze et al. 2018).

Synaptic plasticity is maintained during aging by the active homeostatic balance between epigenetic enzymes. Intriguingly, our investigation into the mechanisms behind DNA methylation and histone acetylation changes in response to rotenone intersected at multiple points in the mitochondrial signaling pathway to the chromatin. For instance, the hypoxic response was significantly reduced in response to rotenone treatment in *SH-5Y*SY that was recovered after α-Synuclein knockdown (Chapter 4). The integrated stress response mediated by ATF4 regulates cellular apoptosis and activation of p53 (Pitale et al. 2017). The interaction of ATF4, hypoxic transcription factor HIF1α, and TP53 within the cytoplasm plays a crucial role in the balance of epigenetic modifying enzymes recruited to the chromatin. We hypothesize that mitochondrial dysfunction activates early response transcription factors to regulate the balance and activity of DNA modifying enzymes in the nucleus and that α.-Synuclein toxicity drives the direction of this response.

7.2 Mitochondrial stress response and α-Syn in mediating the epigenome.

Neurons are metabolically active cells with high energy demands required to propagate action potentials long distances via myelinated axons to facilitate neurotransmitter release from the post-synaptic membrane. This energy requirement is estimated to account for as much as 20% of the body's total energy consumption (Alle et al. 2009). The cellular capacity to adapt its metabolic response in response to external stimuli to meet its energy demands requires widespread modifications to chromatin structure that causes long-term changes to organismal function (Jimenez-Chillaron et al. 2012). This has been proven in the famed Dutch Famine cohort where nutrient deprived babies born to mothers with low caloric intake during the third trimester suffered from higher morbidity risk in adulthood that extended into future generations (Stein et al. 2000). Metabolic disruption and mitochondrial dysfunction are common features among almost all neurological disorders with distinct importance in neurodegeneration (Sebastian et al. 2017). In PD, the generation of reactive oxygen species from mitochondrial dysfunction is a hallmark of disease pathogenesis and results in the crosstalk of multiple pathways that promote oxidative damage induced loss of heterochromatin (Kreuz and Fischle et al. 2016). In our cellular models of rotenone neurotoxicity, we confirmed two immediate transcription factor responses to mitochondrial complex I inhibition was the hypoxia response by HIF1α and the unfolded protein response by ATF4.

Mitochondrial damage sensing proteins upregulate the activity of the mitochondrial unfolded protein response in *C. elegans* (Tian et al. 2016). The communication between mitochondrial sensors and the endoplasmic reticulum unfolded protein response has also been reported in mammals and is regulated by both the activating kinase (PERK) and the ubiquitin ligase (PARK2) (Bouman et al. 2011, Ivanova et al. 2018). PARK2 is responsive to changes in mitochondrial membrane potential and is the most common genetic mutation in familial PD (Bekris et al. 2010). We previously determined that the CTCF binding motif at the PARK2 enhancer was vulnerable to rotenone induced changes in DNA methylation

and resulted in altered CTCF insulator binding activity (Chapter 2B). Ubiquitin ligases, PARK2 and pVHL, regulate the hypoxic response by marking HIF1α for degradation and can strengthen the interaction of ATF4 and TP53 with histone acetyltransferase p300 (Sermeus and Michels et al. 2011, Tothova et al. 2018).

The lack of HIF-1α is associated with reductions in dopaminergic neurons in culture and in the substantia nigra of knockout mice (Milosevic et al. 2007). Interestingly, HIF1α is expressed in hypoxia (low oxygen) and normoxia (normal oxygen) and its expression increases DNA methylation via reduced activity of demethylases (Cimmino et al. 2019). The hypoxic response also depletes intracellular acetyl-CoA concentrations and thus alters the activity of histone acetyltransferases (Golovko et al. 2006, Tothova et al. 2018). Inhibition of the hypoxic response by the unfolded protein response can therefore promote histone acetylation. The integrated stress response to mitochondrial complex I inhibition and oxidative stress stimulates the opening of chromatin via histone acetyltransferases and promotes DNA demethylation via the enhanced expression of transcription and DNA repair genes (*PPAR* and *GADD45*b) (Golovko et al. 2006). Furthermore, ATF4 is a key regulator of the mitochondrial one-carbon metabolism pathway as evidenced by our RNA-sequencing data in rotenone induced hyperacetylated neurons (Chapter 5) (Kasai et al. 2018). One-carbon metabolism is significantly altered in complex I inhibited *SH-5YSY* as well as in *LUHMES* (Krug et al. 2014). This pathway regulates the antioxidant stress response via the transsulfuration pathway which directly alters the metabolite concentrations of homocysteine. Increases in neuronal homocysteine has been observed in PD patients and is associated with reduced DNA methylation and reduced recruitment of histone deacetylases (HDAC) (O'Suilleabhain et al. 2004, Tothova et al. 2018). The lack of nuclear HDACs caused by oxidative stress can diffuse disruptions in DNA methylation patterns. For instance, the nuclear interaction of HDAC2 with DNMT3a2 is

reported to be important for maintaining DNA methylation of imprinted control regions during development (Ma et al. 2015).

Mitochondrial damage sensing proteins and molecular chaperones mediating the endoplasmic reticulum stress response are all sensitive to the accumulation of α-Synuclein. We discovered recovery in the expression of hypoxia response genes with the knockdown of α-Synuclein expression (Chapter 4). In addition, α-Synuclein knockout mice had reductions in acyl-CoA synthetase expression that was rescued by the overexpression of wild-type but not mutant *SNCA* gene (Golovko et al. 2006). We concluded that fatty acid metabolism was critical for maintaining histone acetylation in response to rotenone and reported increased H3K27ac at enhancers of fatty acid beta-oxidation gene *ACSL6* (Chapter 5). We do not know whether α-Synuclein accumulation directly interferes with HIF1α signaling directly through protein-protein interactions or indirectly through the activation of the integrated stress response. However, it seems that α-Synuclein toxicity plays a critical role in the regulation of the epigenome.

7.3 Lysine methylation of histones in rotenone treated cells

Histone lysine methylation is less studied in terms of rotenone-induced neurotoxicity or PD. Injection of complex I inhibitor is associated with changes in lysine methylation at enhancers and is responsive to treatment with Levodopa (Nicholas et a. 2008). Lysine methylation can indicate both repressed and open chromatin. Active enhancers are flagged by lysine methylation specifically H3 lysine 4 di-or-tri-methylation ($H3K4me^2$ or $H3K4me^3$). Alternatively, H3K4 mono-methylation or $H3K4me^1$ are considered primed enhancers when not associated with increased H3K27ac and have lower levels of transcription that can be activated in response to an external stimulus. $H3K4me^1$ still has an important role in chromatin organization as it facilitates the recruitment of the cohesion complex responsible for promoting chromatin looping during

transcription (Creyghton et al. 2010). Di-methylation of H3 lysine 36 ($H3K36me^2$) is also associated with open chromatin to facilitate DNA damage repair and is tightly coupled to age-related levels of H3.3 similar to H3K27ac (Maze et al. 2018). Finally, repressed chromatin is associated with the methylation status of H3 lysine 9 (H3K9) and $H3K9me^2$ has been reported to have an important role in regulating synaptic activity through the expression of post-synaptic SNARE complexes (Sugeno et al. 2016). The overexpression of α-Synuclein has been shown to negatively regulate the expression of these synaptic proteins via increased histone methylation of H3K9.

Like with other histone modifying enzymes, the balance of histone methyltransferases and histone demethylases regulate gene expression and genomic stability. Increased oxidative stress and high levels of homocysteine restrict histone methylation via alterations in one-carbon metabolism. Interestingly, we revealed that rotenone-induced DNA hypomethylation may also increase the expression of the lysine demethylase, *KDM7A*, which is encoded at a vulnerable DNMT1-dependent region (Chapter 3 Table 3.5). The demethylation activity of *KDM7A* is known to reduce methylation at H3K9 and upregulate expression of synaptic proteins.

The lysine demethylases (KDMs) encoded by the *JmjC* gene family are also regulated by mitochondrial metabolism. Rotenone-induced production of the TCA cycle metabolite fumarate inhibits KDMs and increases H3K4 enhancer activation via methylation (Kreuz and Fischle et al. 2016). ATF4 is activated by disruptions in mitochondrial metabolic activity and can also stimulate the expression of *JMJD3* (or KDM6B) which demethylates $H3K27me^3$, an enhancer repressor mark, to promote global histone acetylation (Shan et al. 2012).

7.4 Conclusions

Post-mitotic neurons were once considered to have stable chromatin. However, recent advancements have provided evidence that neuron depolarization reshapes nuclear organization and thus chromatin regulation is essential for the plasticity of aging neurons. Early mitochondrial dysfunction causes epigenetic reprogramming that can lead to persistent alterations of neural activity and behavior throughout life. Metabolic changes can vary in the brain in accordance with the energy demands of the cell. For example, dopaminergic neurons require more energy and therefore may be more sensitive to mitochondrial dysfunction than other neuronal subtypes (Chan et al. 2010). Chromatin regulation is also variable and depends on the activation of immediate transcription factors involved in the cellular stress response. For instance, we observed an increase in ATF4 activation and a decrease in HIF1α response in rotenone treated neurons. This selective activation of the early stress response was associated with the accumulation of α-Synuclein and therefore may explain some differences in the pathology between Lewy body-associated PD and atypical PD (Kasten et al. 2013). The observed effects at chromatin can also be variable because of the distinct sensitivities of chromatin modifying enzymes to oxidative stress, metabolic disturbances, and protein unfolding. While pathological hyperacetylation was observed in all cell models treated with rotenone, DNA methylation patterns were not consistent between proliferating cells and post-mitotic neurons. This may be due to increased passive demethylation during replication in proliferative cells or lack of electrically activated demethylation.

In summary, our data investigate a novel mechanism demonstrating how mitochondrial dysfunction and protein aggregation can change global chromatin architecture. We explore the importance of early response transcription factors and the presence of accumulated α-Synuclein in mediating the crosstalk between chromatin modifying enzymes. Targeting mitochondrial quality control proteins and α-Synuclein

aggregates have had little success in clinical trials. We propose that targeting down-stream transcription factor complexes with chromatin modifying enzymes may improve pharmaceutical strategies in PD. We hypothesize that metabolites generated from the early stress response pathways and their epigenetic signature could be useful for creating early diagnostic biomarkers. This is supported by the presence of α-Synuclein protein in the blood (Matsumoto et al. 2017), enriched PD-associated genetic variants in active enhancers of non-neuronal cell types (Coetzee et al. 2016), and the concordance of DNA methylation patterns between blood and brain tissues (Masilah et al. 2013). Though mapping epigenetic responses to mitochondrial dysfunction in neurons is complex, we predict a unique molecular signature exists that is specific to a class of toxicant (i.e. complex I inhibitor) and/or underlying etiological factor (i.e. Lewy body formation).

7.5 References

1. Alle H, Roth A, Geiger J. 2009. Energy-efficient action potentials in hippocampal mossy fibers. Science 325(5946):1405; doi: 10.1126/science.1174331.
2. Bekris LM, Mata IF, Zabetian CP. 2010. The genetics of parkinson disease. J Geriatr Psychiatry Neurol 23(4):228-242.
3. Bouman L, Schlierf A, Lutz AK, Shan J, Deinlein A, Kast J et al. 2011. Parkin is transcriptionally regulated by ATF4: Evidence for an interconnection between mitochondrial stress and ER stress. Cell Death & Differentiation 18(5):769-782; doi: 10.1038/cdd.2010.142.
4. Chan CS, Gertler TS, Surmeier DJ. 2010. A molecular basis for the increased vulnerability of substantia nigra dopamine neurons in aging and Parkinson's disease. Movement disorders 25(S1):S63-S70.
5. Cimmino F, Avitabile M, Lasorsa VA, Montella A, Pezone L, Cantalupo S et al. 2019. HIF-1 transcription activity: HIF1A driven response in normoxia and in hypoxia. BMC Medical Genetics 20(1):37; doi: 10.1186/s12881-019-0767-1.
6. Coetzee SG, Pierce S, Brundin P, Brundin L, Hazelett DJ, Coetzee GA. 2016. Enrichment of risk SNPs in regulatory regions implicate diverse tissues in Parkinson's disease etiology. Scientific reports 6:30509.
7. Collins BE, Greer CB, Coleman BC, Sweatt JD. 2019. Histone H3 lysine K4 methylation and its role in learning and memory. Epigenetics & Chromatin 12(1):7; doi: 10.1186/s13072-018-0251-8.
8. Creyghton MP, Cheng AW, Welstead GG, Kooistra T, Carey BW, Steine EJ et al. 2010. Histone H3K27ac separates active from poised enhancers and predicts developmental state. Proc Natl Acad Sci U S A 107(50):21931-21936; doi: 10.1073/pnas.1016071107.
9. Feng Y, Liu T, Dong S, Guo Y, Jankovic J, Xu H et al. 2015. Rotenone affects p53 transcriptional activity and apoptosis via targeting SIRT 1 and H3K9 acetylation in SH-SY 5Y cells. J Neurochem 134(4):668-676.

10. Golovko MY, Rosenberger TA, Faergeman NJ, Feddersen S, Cole NB, Pribill I et al. 2006. Acyl-CoA synthetase activity links wild-type but not mutant alpha-synuclein to brain arachidonate metabolism. Biochemistry (NY) 45(22):6956-6966; doi: 10.1021/bi0600289.
11. Huang M, Lou D, Charli A, Kong D, Jin H, Anantharam V et al. 2019. Mitochondrial dysfunction induces epigenetic dysregulation by H3K27 hyperacetylation to perturb active enhancers in Parkinson's disease models. bioRxiv:808246.
12. Ivanova IG, Park CV, Yemm AI, Kenneth NS. 2018. PERK/eIF2Î± signaling inhibits HIF-induced gene expression during the unfolded protein response via YB1-dependent regulation of HIF1 translation. Nucleic Acids Res 46(8):3878-3890; doi: 10.1093/nar/gky127.
13. Jiménez-Chillarón JC, Díaz R, Martínez D, Pentinat T, Ramón-Krauel M, Ribó S et al. 2012. The Role of Nutrition on Epigenetic Modifications and their Implications on Health. Biochimi 94(11):2242-63; doi: 10.1016/j.biochi.2012.06.012.
14. Kasai S, Yamazaki H, Tanji K, Engler MJ, Matsumiya T, Itoh K. 2018. Role of the ISR-ATF4 pathway and its cross talk with Nrf2 in mitochondrial quality control. Journal of clinical biochemistry and nutrition:18-37.
15. Kasten M, Klein C. 2013. The many faces of alpha-synuclein mutations. Movement Disorders 28(6):697-701.
16. Kreuz S, Fischle W. 2016. Oxidative stress signaling to chromatin in health and disease. Epigenomics 8(6):843-862.
17. Krug AK, Gutbier S, Zhao L, Pöltl D, Kullmann C, Ivanova V et al. 2014. Transcriptional and metabolic adaptation of human neurons to the mitochondrial toxicant MPP. Cell death & disease 5(5):e1222-e1222.
18. Li Q, Zhou H, Wurtele H, Davies B, Horazdovsky B, Verreault A et al. 2008. Acetylation of Histone H3 Lysine 56 Regulates Replication-Coupled Nucleosome Assembly. Cell 134(2):244-55; doi: 10.1016/j.cell.2008.06.018.
19. Ma P, de Waal E, Weaver JR, Bartolomei MS, Schultz RM. 2015. A DNMT3A2-HDAC2 complex is essential for genomic imprinting and genome integrity in mouse oocytes. Cell Rep 13(8):1552-1560.
20. Masliah E, Dumaop W, Galasko D, Desplats P. 2013. Distinctive patterns of DNA methylation associated with parkinson disease: Identification of concordant epigenetic changes in brain and peripheral blood leukocytes. Epigenetics 8(10):1030-1038.
21. Masumoto H, Hawke D, Kobayashi R, Verreault A. 2005. A role for cell-cycle-regulated histone H3 lysine 56 acetylation in the DNA damage response. Nature 436(7048):294-298; doi: 10.1038/nature03714.
22. Matsumoto J, Stewart T, Sheng L, Li N, Bullock K, Song N et al. 2017. Transmission of a-synuclein-containing erythrocyte-derived extracellular vesicles across the blood-brain barrier via adsorptive mediated transcytosis: Another mechanism for initiation and progression of Parkinson's disease? Acta neuropathologica communications 5(1):71-71; doi: 10.1186/s40478-017-0470-4.
23. Matsumoto L, Takuma H, Tamaoka A, Kurisaki H, Date H, Tsuji S et al. 2010. CpG demethylation enhances alpha-synuclein expression and affects the pathogenesis of Parkinson's disease. PLoS One 5(11):e15522; doi: 10.1371/journal.pone.0015522.
24. Maze I, Wenderski W, Noh K, Bagot RC, Tzavaras N, Purushothaman I et al. 2015. Critical role of histone turnover in neuronal transcription and plasticity. Neuron 87(1):77-94.
25. Milosevic J, Maisel M, Wegner F, Leuchtenberger J, Wenger RH, Gerlach M et al. 2007. Lack of hypoxia-inducible factor-1 alpha impairs midbrain neural precursor

cells involving vascular endothelial growth factor signaling. J Neurosci 27(2):412-421.
26. Nicholas AP, Lubin FD, Hallett PJ, Vattem P, Ravenscroft P, Bezard E et al. 2008. Striatal histone modifications in models of levodopa-induced dyskinesia. J Neurochem 106(1):486-494; doi: 10.1111/j.1471-4159.2008.05417.x.
27. O'Suilleabhain PE, Oberle R, Bartis C, Dewey RB,Jr, Bottiglieri T, Diaz-Arrastia R. 2006. Clinical course in Parkinson's disease with elevated homocysteine. Parkinsonism Relat Disord 12(2):103-107; doi: S1353-8020(05)00199-9.
28. Pierce SE, Tyson T, Booms A, Prahl J, Coetzee GA. 2018. Parkinson's disease genetic risk in a midbrain neuronal cell line. Neurobiol Dis 114:53-64.
29. Pitale PM, Gorbatyuk O, Gorbatyuk M. 2017. Neurodegeneration: Keeping ATF4 on a tight leash. Frontiers in cellular neuroscience 11:410.
30. Sebastian D, PalacÃn M, Zorzano A. 2017. Mitochondrial dynamics: Coupling mitochondrial fitness with healthy aging. Trends Mol Med 23(3):201-215; doi: 10.1016/j.molmed.2017.01.003.
31. Sermeus A, Michiels C. 2011. Reciprocal influence of the p53 and the hypoxic pathways. Cell death & disease 2(5):e164-e164.
32. Shan J, Fu L, Balasubramanian MN, Anthony T, Kilberg MS. 2012. ATF4-dependent regulation of the JMJD3 gene during amino acid deprivation can be rescued in Atf4-deficient cells by inhibition of deacetylation. J Biol Chem 287(43):36393-36403; doi: 10.1074/jbc.M112.399600.
33. Song C, Kanthasamy A, Anantharam V, Sun F, Kanthasamy AG. 2010. Environmental neurotoxic pesticide increases histone acetylation to promote apoptosis in dopaminergic neuronal cells: Relevance to epigenetic mechanisms of neurodegeneration. Mol Pharmacol 77(4):621-632; doi: 10.1124/mol.109.062174.
34. Stein AD, Lumey LH. 2000. The relationship between maternal and offspring birth weights after maternal prenatal famine exposure: The dutch famine birth cohort study. Human biology:641-654.
35. Su Y, Shin J, Zhong C, Wang S, Roychowdhury P, Lim J et al. 2017. Neuronal activity modifies the chromatin accessibility landscape in the adult brain. Nat Neurosci 20(3):476.
36. Sugeno N, Jackel S, Voigt A, Wassouf Z, Schulze-Hentrich J, Kahle PJ. 2016. A-Synuclein enhances histone H3 lysine-9 dimethylation and H3K9me2-dependent transcriptional responses. Scientific reports 6:36328-36328; doi: 10.1038/srep36328.
37. Tathova B, Kovalska¡ M, Kalenska¡ D, TomaÅ¡cova¡ A, Lehotska J. 2018. Histone hyperacetylation as a response to global brain ischemia associated with hyperhomocysteinemia in rats. International journal of molecular sciences 19(10):3147; doi: 10.3390/ijms19103147.
38. Tian Y, Garcia G, Bian Q, Steffen K, Joe L, Wolff S et al. 2016. Mitochondrial Stress Induces Chromatin Reorganization to Promote Longevity and UPR(mt). Cell 165(5):1197-1208; doi: 10.1016/j.cell.2016.04.011.
39. Yakhine-Diop S, Rodriguez-Arribas M, Martanez-Chac G, Uribe-Carretero E, Gomez-Sanchez R, Aiastui A et al. 2018. Acetylome in human fibroblasts from Parkinson's disease patients. Frontiers in Cellular Neuroscience 12:97.
40. Ysselstein D, Joshi M, Mishra V, Griggs AM, Asiago JM, McCabe GP et al. 2015. Effects of impaired membrane interactions on α-synuclein aggregation and neurotoxicity. Neurobiol Dis 79:150-163.

APPENDIX

Supplemental File 1: Chapter 2 differentially expressed genes from rotenone treated HEK293

Genename	logFC	FDR
STC1	-3.87	2.3E-50
PPP1R10	-1.88	4.1E-40
RN7SL1	-2.15	9.5E-37
ADAMTS1	1.76	1.7E-35
SH3BP5-AS1	-2.06	3.7E-34
NCOA5	-2.01	1.2E-31
ZNF37A	-1.71	2.1E-30
MT-TQ	2.97	1.8E-29
CYR61	1.88	7.4E-26
PCF11	-1.54	1.6E-25
ZNF605	-1.60	4.4E-25
KRCC1	-2.00	7.2E-25
MT-TP	2.82	7.6E-25
SAT1	1.79	5.3E-24
RN7SL2	-1.88	5.8E-24
HIST2H2BE	2.91	5.8E-24
ZSWIM5	-1.67	3.6E-23
TSC22D3	1.47	2.4E-22
FOSB	1.86	1.3E-21
ALMS1-IT1	2.54	3.2E-21
RIPK1	-1.93	7.0E-21
MEX3B	1.65	7.8E-21
THAP9-AS1	1.53	5.7E-20
ILF3-AS1	1.65	2.4E-19
PFKFB4	-1.85	3.6E-19
BRD2	1.35	4.7E-19
SOX4	1.19	7.9E-19
C1QTNF6	-1.68	1.0E-18
JUN	1.42	1.6E-18
PIM1	1.35	1.7E-18
ZNF280C	1.25	2.4E-18
RN7SK	-4.17	4.1E-18
ZNF587B	-1.78	9.9E-18
ARC	1.87	1.8E-17
HSPA5	1.17	2.4E-17
MSMO1	1.58	3.5E-17
TGIF1	1.41	6.2E-17
DOK3	-2.57	1.1E-16
PAQR6	-1.56	1.6E-16
MT-TA	2.80	2.1E-16
WDR52	-1.87	7.4E-16
B3GALT6	-1.47	9.3E-16

PPP1R18	1.20	1.0E-15
GAB2	1.67	1.7E-15
LRRC37A9P	-1.84	3.0E-15
CAPN12	1.78	1.7E-14
IQCE	-1.12	2.2E-14
SAMD9	-1.83	2.3E-14
CYP2U1	-1.61	2.4E-14
FZD6	-1.29	3.0E-14
ZBED3	-1.12	4.3E-14
PER1	1.37	6.7E-14
LGR5	-1.14	1.0E-13
C15orf38	-1.17	1.1E-13
ZC3H4	-1.48	1.3E-13
MYB	1.53	1.8E-13
INSIG1	1.24	2.0E-13
TUFM	1.05	2.0E-13
TSC22D2	1.10	2.0E-13
PPFIA4	-1.37	2.6E-13
PPP1R32	1.95	3.1E-13
TAF1D	1.14	3.9E-13
PRKACB	-1.19	4.3E-13
MID1IP1	1.29	4.6E-13
SDHAP3	-1.33	6.0E-13
LINC00680	-1.59	1.4E-12
NUTM2D	-1.90	1.6E-12
AK4	-1.04	2.8E-12
LOX	-1.87	3.8E-12
SLC39A3	1.57	4.1E-12
KCNAB3	-2.35	4.2E-12
BBC3	1.50	4.4E-12
FAM46B	2.42	4.4E-12
CNN2	1.15	5.1E-12
WNK4	-1.62	5.1E-12
PGK1	-1.08	5.1E-12
LRRC37A4P	-1.19	6.3E-12
RBM15	1.00	7.6E-12
FKRP	-1.19	1.1E-11
MT-ND2	-0.97	1.1E-11
HYAL3	-2.19	1.2E-11
C12orf4	-1.12	1.3E-11
LCMT2	-1.39	1.5E-11
SULF1	-1.18	1.5E-11
DNAJA1	-1.01	1.7E-11
HMGCS1	1.01	2.2E-11
GPR75	-1.54	2.2E-11
SQLE	0.94	2.6E-11
ATF3	1.24	3.9E-11

RPL18A	0.95	4.6E-11
FOXD2-AS1	1.28	4.6E-11
RHOB	1.14	4.8E-11
MAX	-0.98	4.9E-11
H1F0	1.07	5.4E-11
C11orf95	-1.03	5.6E-11
P2RY11	-1.70	5.7E-11
CSRNP1	1.44	6.2E-11
MYC	1.03	6.3E-11
P4HA1	-1.32	7.5E-11
EXO5	-1.22	1.0E-10
ADAM1A	-1.86	1.1E-10
SCRN3	-1.05	1.2E-10
LDLR	0.97	1.2E-10
FAM212B	-1.27	1.5E-10
ZNF302	-0.95	1.5E-10
PRNP	-0.91	1.7E-10
SLC16A13	-1.32	1.8E-10
GRB7	1.29	1.8E-10
CHAMP1	-0.96	1.9E-10
MT-CYB	-0.85	2.0E-10
ANKRD29	-1.25	2.1E-10
ZNF37BP	-0.91	2.1E-10
LRIF1	-1.14	2.2E-10
FAM178A	-1.02	2.2E-10
JUNB	1.63	2.3E-10
GNRHR2	2.62	2.4E-10
LINC00863	-1.47	2.5E-10
SFPQ	-0.88	2.5E-10
SERTAD3	1.19	2.6E-10
RNF168	1.01	2.8E-10
IKBIP	-1.25	2.8E-10
SLC16A9	-1.43	2.8E-10
ZNF449	0.97	3.0E-10
ID3	1.32	3.2E-10
TUFT1	1.00	3.7E-10
PSKH1	-1.27	4.8E-10
GBE1	-1.21	4.8E-10
ZNF526	1.01	4.8E-10
PARP9	-1.39	5.5E-10
PRIMPOL	-1.22	5.8E-10
BNIP3	-1.22	5.8E-10
RBM12	-0.94	6.3E-10
DUSP1	1.08	6.3E-10
ZNF252P	-1.45	6.7E-10
TMEM45A	-1.20	6.7E-10
ZNF333	1.03	6.9E-10

RPL13AP5	2.61	7.4E-10
ACTG1	0.88	7.5E-10
EMILIN3	-1.18	8.3E-10
ZNF467	1.71	8.8E-10
SRD5A3	-1.08	9.6E-10
PDE3B	-1.21	9.7E-10
SACS	-0.93	1.1E-09
KLF9	0.92	1.1E-09
CTGF	1.35	1.1E-09
OVGP1	1.26	1.2E-09
PLOD2	-1.19	1.2E-09
C22orf46	-1.07	1.3E-09
IER2	0.97	1.4E-09
TINCR	1.82	1.5E-09
PDP2	0.97	1.5E-09
HFM1	-1.46	1.7E-09
SRR	-1.20	1.7E-09
NREP	-0.94	1.8E-09
LPAR1	-1.12	1.8E-09
ZFX	-0.90	1.9E-09
MIR210HG	-3.61	2.1E-09
EPC2	-0.99	2.1E-09
MTND2P28	-0.93	2.3E-09
BRPF3	-0.91	2.4E-09
METTL7B	-1.55	2.7E-09
HELB	1.35	2.9E-09
C1orf63	0.91	3.1E-09
NR4A2	1.68	3.1E-09
ASMTL	1.18	3.3E-09
MYH3	-1.62	3.3E-09
JAG1	0.90	3.4E-09
SLC25A29	0.93	3.5E-09
HNRNPL	0.80	3.8E-09
NIPAL2	-1.61	4.5E-09
NEK9	-0.83	4.7E-09
QRICH2	-2.31	4.8E-09
FANCE	1.02	4.8E-09
GFOD2	1.02	5.0E-09
FAM131A	1.18	5.2E-09
METTL22	0.91	5.2E-09
MNX1	1.05	5.7E-09
DPY19L2P2	-1.48	5.7E-09
FLNA	0.85	7.0E-09
ARHGAP8	1.54	7.2E-09
CHTF8	-0.93	7.2E-09
FAM134B	-1.58	7.7E-09
MAST3	0.99	8.2E-09

HGSNAT	-0.92	9.1E-09
ZC3H12C	-1.41	9.2E-09
GLUL	0.78	9.7E-09
SRSF6	-0.80	9.9E-09
MMP15	1.10	1.1E-08
ZNF555	1.19	1.1E-08
MUC19	-1.32	1.2E-08
ZNF74	0.97	1.3E-08
ZNF75A	-0.95	1.3E-08
TRPM4	1.11	1.3E-08
ZNF883	-1.22	1.3E-08
KIAA1683	-2.92	1.4E-08
STAT4	-1.45	1.5E-08
SH3D21	-1.25	1.5E-08
CDKN2B	1.27	1.5E-08
SLC29A2	0.88	1.6E-08
WNT3	-1.06	1.6E-08
ZNF551	-1.27	1.7E-08
AMPD3	-1.92	1.8E-08
CDT1	1.01	1.9E-08
ZBTB43	0.95	2.0E-08
KCTD15	-0.84	2.3E-08
CDK13	-0.86	2.5E-08
CSPG4P12	-1.06	2.6E-08
SLC1A4	-1.36	2.7E-08
TBX19	1.53	2.8E-08
HOTAIRM1	0.97	2.8E-08
ZNF497	-2.32	3.0E-08
MFAP3	-0.96	3.0E-08
NAA10	1.00	3.0E-08
IGSF10	-1.21	3.7E-08
DGCR5	-1.12	4.3E-08
EXOC8	0.86	4.3E-08
SH2D3A	1.04	4.3E-08
TEX15	-0.98	4.3E-08
RPL17	1.03	4.3E-08
AGPAT3	-0.83	4.7E-08
SPOCK2	-1.72	4.7E-08
EIF3I	0.78	4.7E-08
MIER2	0.87	4.9E-08
MVP	1.29	5.0E-08
DDIT3	1.05	5.0E-08
RPPH1	-3.28	5.1E-08
YJEFN3	-1.12	5.3E-08
MCM3AP-AS1	-1.08	5.4E-08
DCP1B	-1.05	5.4E-08
ZBTB1	-1.02	5.7E-08

PSPC1	-0.80	6.1E-08
AURKC	1.45	6.1E-08
RNF122	1.09	6.2E-08
SALL4	1.82	6.2E-08
EIF5A	0.98	6.3E-08
ZNF235	-1.24	6.4E-08
JAK3	1.68	6.4E-08
RBBP6	-0.91	6.4E-08
KIAA1161	0.94	6.6E-08
RP1L1	1.83	7.0E-08
DDB2	-0.81	7.1E-08
GCAT	1.09	7.1E-08
FAM84B	0.76	7.4E-08
BNIP3L	-1.08	7.4E-08
PIEZO2	-1.13	7.5E-08
IL12A	1.27	7.5E-08
DRAP1	0.93	8.1E-08
SRSF3	-0.76	8.4E-08
ICAM5	1.00	8.4E-08
LDHA	-0.74	8.5E-08
NR1D1	1.24	8.5E-08
TRAK2	-0.86	8.6E-08
ZDHHC22	1.05	8.6E-08
ZNF585B	-0.89	8.6E-08
CCDC124	0.82	8.9E-08
ZNF594	-1.34	8.9E-08
ALX4	-1.01	9.2E-08
ZNF239	-1.02	9.6E-08
ANKRD9	1.04	9.7E-08
FASTKD5	-1.00	1.0E-07
RAB3A	1.28	1.0E-07
MR1	-1.09	1.1E-07
PPP1R15A	0.96	1.1E-07
ZNF41	-1.09	1.2E-07
CARD6	-1.43	1.2E-07
TRIP11	-0.82	1.4E-07
MT-ND6	0.78	1.4E-07
HES1	0.99	1.4E-07
GFOD1	0.95	1.4E-07
UCP3	-2.38	1.4E-07
EGLN1	-0.86	1.4E-07
ZNF559	-1.22	1.5E-07
ZNF559	-1.22	1.5E-07
PSMG3-AS1	-1.64	1.5E-07
MEIS1	0.83	1.5E-07
NAB2	1.01	1.6E-07
FLVCR2	-2.16	1.6E-07

POLR1E	0.84	1.7E-07
PPAPDC1B	1.07	1.8E-07
SNHG1	0.80	1.8E-07
GNB3	-1.08	1.8E-07
HMCN1	-0.89	1.8E-07
CENPC	0.91	1.8E-07
SEMA3B	-1.52	1.8E-07
ZNF736	-0.89	1.8E-07
GAD1	1.21	1.9E-07
IGHMBP2	0.82	1.9E-07
ZSCAN5A	-1.40	2.0E-07
LYSMD1	0.81	2.0E-07
ZMYND8	-0.78	2.3E-07
MESDC2	-0.76	2.3E-07
SIRT5	-0.93	2.4E-07
TET1	0.80	2.4E-07
PLXNA4	-1.11	2.4E-07
SNX27	0.76	2.5E-07
ACTB	1.02	2.6E-07
ATF5	-1.06	2.6E-07
PLEKHH3	1.06	2.6E-07
MANSC1	-1.21	2.7E-07
FLRT2	-0.87	2.8E-07
LMBR1L	0.80	2.8E-07
AHNAK2	-0.85	2.8E-07
NSL1	-0.81	2.8E-07
CLK3	0.91	2.8E-07
TTC9C	0.88	2.9E-07
ZBTB12	-0.91	3.0E-07
FAM46C	0.99	3.3E-07
ZNF330	0.80	3.4E-07
HES7	1.77	3.6E-07
KLHL11	0.96	3.7E-07
TRNP1	-1.00	4.2E-07
AMMECR1	-0.77	4.2E-07
SAMD8	0.86	4.2E-07
NEFM	0.80	4.3E-07
DLX5	1.07	4.6E-07
CCDC162P	-1.23	4.7E-07
CCNB1IP1	0.79	4.8E-07
GADD45A	0.90	4.8E-07
IQCH-AS1	-1.21	5.0E-07
NUPL2	-0.82	5.3E-07
SF1	-0.75	5.4E-07
ZNF117	-1.15	5.5E-07
BRMS1L	-0.91	5.5E-07
MAN2B1	0.88	5.6E-07

SEC13	0.73	5.7E-07
SLC22A23	-0.87	5.9E-07
COL17A1	-0.99	6.1E-07
HECA	0.84	6.1E-07
FER	-0.86	6.2E-07
SPRY3	1.14	6.3E-07
TMEM209	-0.74	6.4E-07
HSD17B10	0.76	6.6E-07
SLC2A11	-1.18	6.6E-07
HOXD13	0.73	6.9E-07
KLHL42	-0.81	7.0E-07
LRP11	-0.75	7.1E-07
PDIA5	0.89	7.1E-07
C17orf97	-2.15	7.6E-07
BRCC3	-0.81	7.6E-07
ARRDC3	0.94	7.7E-07
POLR3D	0.73	8.0E-07
C2orf43	-1.00	8.2E-07
ADAM8	-1.90	8.2E-07
MPST	0.80	8.4E-07
MFSD5	-1.05	8.4E-07
ECSIT	0.85	8.5E-07
TMEM64	-0.93	8.6E-07
DDT	0.90	9.3E-07
FAM162A	-0.72	9.4E-07
LENG8-AS1	1.27	9.6E-07
LINC00115	1.50	9.9E-07
NSD1	-0.72	1.0E-06
HBP1	0.87	1.0E-06
RIPK4	0.96	1.0E-06
ANXA2R	1.83	1.0E-06
ANKRD34B	-1.11	1.0E-06
ZNF780B	-0.90	1.0E-06
DUSP6	1.34	1.0E-06
PPP1R15B	0.70	1.1E-06
PHKG1	1.86	1.1E-06
MEF2A	-0.73	1.1E-06
HSP90B1	0.72	1.2E-06
TADA2A	-0.76	1.2E-06
FBXL21	-0.98	1.2E-06
APPBP2	-0.74	1.2E-06
MPZ	1.38	1.3E-06
METTL21B	1.15	1.4E-06
RFX7	-0.84	1.4E-06
ZBTB3	1.35	1.4E-06
CCNO	1.02	1.4E-06
RAB7L1	0.79	1.4E-06

ICK	-0.79	1.4E-06
GATAD1	0.79	1.5E-06
IRGQ	0.76	1.5E-06
SOGA1	-0.84	1.5E-06
MT-ND1	-0.80	1.6E-06
ZMYND11	-0.73	1.6E-06
PPIL6	-1.41	1.7E-06
HMMR	-0.78	1.7E-06
LINC00174	-0.93	1.7E-06
FDFT1	0.68	1.7E-06
YAE1D1	-0.83	1.8E-06
ZNFX1	0.75	1.9E-06
HOXA11	0.88	1.9E-06
PTCHD4	-1.64	1.9E-06
ASH1L-AS1	1.65	2.0E-06
C1GALT1C1	-1.06	2.0E-06
C10orf12	0.77	2.0E-06
SUN2	0.77	2.0E-06
CHP1	0.70	2.1E-06
BCAS2	-0.72	2.1E-06
ZNF777	-0.76	2.1E-06
PSD4	-1.43	2.1E-06
VCPIP1	0.80	2.1E-06
ERN1	0.81	2.1E-06
UMPS	-0.79	2.3E-06
MTMR3	0.69	2.3E-06
NDUFA4L2	-2.13	2.3E-06
TBC1D3F	-1.01	2.3E-06
JRKL	0.82	2.3E-06
PPP1R26	0.76	2.3E-06
ANKEF1	-0.92	2.4E-06
ZDHHC11	-1.04	2.5E-06
CREBRF	0.87	2.5E-06
FEM1C	0.84	2.5E-06
RPAP2	-0.85	2.5E-06
OLIG2	1.48	2.5E-06
ZNF697	0.78	2.6E-06
RN7SL3	-2.08	2.7E-06
GTF3A	0.74	2.7E-06
LINC00858	-1.48	2.8E-06
RER1	-0.77	2.8E-06
SLC26A10	-0.90	2.8E-06
GATAD2B	0.69	2.8E-06
C9orf156	-1.14	2.9E-06
ZNF655	-0.79	2.9E-06
C17orf59	1.31	3.1E-06
PAPOLA	-0.66	3.1E-06

HECTD2	-0.88	3.2E-06
LINC01125	-1.27	3.2E-06
CD83	-0.91	3.2E-06
TEX261	-0.71	3.2E-06
ZNF644	-0.83	3.3E-06
F8	-1.20	3.3E-06
CPSF6	-0.66	3.4E-06
PROX1	0.99	3.4E-06
GAL	0.88	3.6E-06
NDUFA13	-1.41	3.6E-06
STK38	-0.73	3.7E-06
ZNF829	-0.73	3.7E-06
ZNF470	-0.99	3.7E-06
ANKRD27	0.69	3.7E-06
CHSY3	-1.12	3.8E-06
ST6GALNAC4	1.00	3.8E-06
USP40	-0.79	3.8E-06
ZNF292	-0.85	3.9E-06
ZEB1	0.90	4.0E-06
POU3F2	0.78	4.2E-06
TMEM159	1.19	4.2E-06
SCARA3	-0.84	4.3E-06
TOE1	-0.75	4.3E-06
TMEM80	-0.96	4.3E-06
GAS5	0.74	4.3E-06
ELOVL2	-0.70	4.5E-06
SNRPA	0.70	4.5E-06
MRPL55	0.72	4.6E-06
SLC25A25	0.86	4.7E-06
NDUFS8	0.83	4.8E-06
RBM26-AS1	-1.89	4.8E-06
NRN1	-0.87	4.8E-06
B4GALT6	-0.87	4.8E-06
RNF207	-0.98	4.9E-06
LINC00965	-1.61	4.9E-06
KBTBD6	0.75	4.9E-06
ZEB1-AS1	0.97	4.9E-06
DNAH6	-1.15	4.9E-06
GABARAPL1	0.75	4.9E-06
GRIN2C	-3.06	4.9E-06
GADD45B	0.90	4.9E-06
DNAH1	-0.95	5.2E-06
CABLES1	-0.79	5.3E-06
RBM4B	-0.97	5.5E-06
CAMLG	0.75	5.7E-06
C1R	-1.14	5.7E-06
MFAP3L	-0.81	5.9E-06

SAP30L	-0.87	6.2E-06
SYNE3	1.21	6.3E-06
ZNF418	-2.63	6.4E-06
POLR2J4	-1.62	6.4E-06
DNAJC19P5	2.46	6.5E-06
EPHA6	0.79	6.7E-06
C6orf211	-0.75	6.7E-06
FAM214B	0.94	6.7E-06
LINC00649	-0.85	6.8E-06
PLXDC1	-1.19	6.9E-06
ZFP36	0.87	6.9E-06
RABAC1	0.71	7.0E-06
TMEM127	-0.76	7.1E-06
ZNF66	-1.82	7.1E-06
KLF4	0.95	7.1E-06
MVB12A	0.82	7.1E-06
ITGA8	-0.78	7.2E-06
EPDR1	-0.87	7.3E-06
TEF	0.83	7.3E-06
EIF3C	0.79	7.8E-06
VAX1	-1.85	7.9E-06
ZNF542	-1.31	7.9E-06
PNP	0.84	8.0E-06
HMBOX1	0.74	8.0E-06
ZFAND2B	0.97	8.2E-06
PHF20L1	-0.72	8.2E-06
ZUFSP	0.78	8.2E-06
FAM66C	-1.37	8.3E-06
CCP110	0.72	8.3E-06
TICRR	0.68	8.4E-06
PAIP2B	0.69	8.4E-06
PRRT4	-0.81	8.4E-06
PPM1J	1.21	8.5E-06
APCDD1	-0.93	8.5E-06
TUBE1	0.78	8.7E-06
CLDND2	1.57	8.8E-06
HTRA1	-0.72	9.0E-06
WHAMM	0.75	9.0E-06
BRICD5	-1.47	9.0E-06
SMYD5	0.73	9.1E-06
STON2	0.76	9.1E-06
FLT1	-0.79	9.2E-06
MLH3	-0.72	9.2E-06
RAB33B	0.86	9.3E-06
DACT3	1.11	9.4E-06
C6orf136	0.81	1.0E-05
TIGD1	0.84	1.0E-05

ZBTB38	-0.87	1.0E-05
ALG6	-0.83	1.0E-05
NDUFS6	0.68	1.0E-05
OGT	-0.66	1.0E-05
LCA5L	-2.68	1.0E-05
DCBLD2	-0.69	1.0E-05
CHRNA10	-3.00	1.0E-05
ZFHX2	-1.09	1.1E-05
GAN	0.70	1.1E-05
DNAH10OS	0.98	1.2E-05
CLN5	-1.02	1.2E-05
JOSD1	-0.72	1.2E-05
C22orf39	0.83	1.2E-05
LXN	-0.84	1.2E-05
FKBP14	0.79	1.2E-05
HSD17B7P2	1.50	1.2E-05
FBXO4	-1.45	1.3E-05
ANTXR1	-0.66	1.3E-05
YPEL3	1.01	1.3E-05
NTMT1	0.77	1.3E-05
WASH7P	0.96	1.3E-05
SLC25A5	0.66	1.3E-05
ZDHHC24	0.93	1.3E-05
RGS16	0.96	1.3E-05
RPLP2	0.69	1.3E-05
RAB23	-0.74	1.3E-05
KLHL24	0.85	1.3E-05
ABI3BP	-1.43	1.3E-05
LINC00641	-0.68	1.4E-05
IQCC	0.86	1.4E-05
TMEM198B	-0.70	1.4E-05
PYGO1	-0.89	1.4E-05
MTERF	-0.96	1.4E-05
SLC38A10	-0.72	1.4E-05
MSTO2P	0.98	1.4E-05
SLC29A3	-1.11	1.4E-05
PMEPA1	-0.99	1.5E-05
FASN	0.69	1.5E-05
BEND3	-0.80	1.6E-05
H2AFY2	-0.65	1.6E-05
LYPD6	-0.94	1.6E-05
TTC12	-0.79	1.6E-05
SNHG3	0.90	1.6E-05
CCDC138	-0.73	1.6E-05
NETO2	-0.65	1.6E-05
HCG18	-0.71	1.7E-05
PTK2B	-0.93	1.7E-05

MYO15B	-0.95	1.7E-05
SDF2L1	1.35	1.7E-05
MUM1L1	-0.95	1.7E-05
CD99	0.71	1.7E-05
RAG1	-2.33	1.7E-05
MYOM2	-1.17	1.7E-05
KPNA6	0.64	1.7E-05
TIPARP	0.74	1.8E-05
MRPL52	0.75	1.8E-05
NDUFB8	1.41	1.8E-05
HIST1H4E	-2.47	1.8E-05
HDX	-1.28	1.8E-05
SSH1	-0.64	1.8E-05
BOLA3-AS1	0.72	1.9E-05
SOX9	0.88	1.9E-05
IER3	0.85	1.9E-05
CCER2	-2.00	1.9E-05
ALDH1L2	-0.63	1.9E-05
ADAM21	-2.37	2.0E-05
KATNAL2	-1.10	2.0E-05
ENO3	-0.88	2.0E-05
C7orf49	-0.72	2.0E-05
TSPYL1	0.68	2.0E-05
RDM1	0.88	2.0E-05
PDK1	-0.74	2.0E-05
THNSL1	-0.84	2.1E-05
TMSB4X	0.69	2.1E-05
CYP26A1	1.14	2.1E-05
ACLY	0.65	2.1E-05
EDARADD	-0.95	2.1E-05
EEF1A2	0.90	2.2E-05
PDP1	0.74	2.2E-05
RPS15	0.70	2.2E-05
RPUSD3	0.69	2.3E-05
ZIK1	-1.20	2.3E-05
ARHGAP31	-0.82	2.3E-05
RPLP1	1.01	2.3E-05
LHX9	-0.99	2.3E-05
SAMD11	-0.70	2.3E-05
MANF	0.70	2.3E-05
HOXC13	0.78	2.3E-05
COX18	0.83	2.4E-05
MOCOS	-1.24	2.4E-05
SPDL1	-0.67	2.4E-05
YOD1	0.75	2.4E-05
CSRP2BP	-0.78	2.4E-05
CNKSR3	0.65	2.4E-05

LRP8	0.67	2.4E-05
ASF1A	-0.74	2.5E-05
FZD8	0.81	2.5E-05
CYB5D2	-0.92	2.5E-05
ORAOV1	-0.70	2.5E-05
HOXA-AS2	0.86	2.5E-05
DUSP8P5	1.11	2.5E-05
ZNF75D	-0.70	2.5E-05
PLAGL2	-0.63	2.5E-05
CXorf38	0.84	2.6E-05
AGGF1	-0.65	2.6E-05
PPP6R3	-0.61	2.6E-05
DOCK8	-0.91	2.6E-05
YPEL2	0.71	2.6E-05
OGFR	0.72	2.6E-05
SRBD1	-0.78	2.7E-05
TAF1A	0.91	2.7E-05
RBM47	-0.97	2.8E-05
HLCS	-0.78	2.8E-05
APH1B	-0.80	2.8E-05
ASF1B	-0.67	2.8E-05
CSF1	-0.78	3.0E-05
GPC4	0.63	3.0E-05
NFKB1	-0.82	3.0E-05
HYLS1	-0.93	3.0E-05
ZNF554	-0.81	3.0E-05
TPPP	0.80	3.1E-05
SHISA4	-1.96	3.1E-05
SLTM	-0.61	3.1E-05
GTF2H2	0.85	3.1E-05
FNTB	-1.12	3.2E-05
PTMA	0.62	3.2E-05
PTRH2	-0.65	3.2E-05
NMRK1	-0.99	3.2E-05
IL18R1	-1.00	3.3E-05
AIFM2	-2.10	3.3E-05
GOLGA8A	-0.62	3.3E-05
BABAM1	1.07	3.3E-05
CROCCP2	0.72	3.4E-05
TRIM52-AS1	0.75	3.5E-05
SNHG10	0.82	3.5E-05
WDR33	-0.60	3.7E-05
HUNK	-0.78	3.7E-05
ARL16	0.74	3.8E-05
ULBP2	0.87	3.8E-05
ZSCAN25	-0.73	3.8E-05
LONRF2	-0.66	3.9E-05

ZNF112	-1.05	3.9E-05
SYNM	-0.66	3.9E-05
SLC31A1	0.64	3.9E-05
ARHGDIA	0.79	4.1E-05
NDE1	0.63	4.1E-05
USP31	0.71	4.1E-05
RRM2	0.60	4.1E-05
SNRPB	0.94	4.1E-05
ZNF852	-1.30	4.1E-05
SSH3	-1.89	4.2E-05
ZNF780A	-0.82	4.3E-05
HOXA9	0.75	4.3E-05
ZNF549	-0.83	4.3E-05
HLA-E	0.61	4.4E-05
ZNF140	-0.85	4.6E-05
PAFAH2	-0.88	4.6E-05
ZDBF2	-0.77	4.7E-05
SLC30A6	-0.72	4.7E-05
SMAD7	0.72	4.8E-05
SLC9A2	-1.64	4.8E-05
ZNF274	-0.62	4.9E-05
PPIC	0.78	5.0E-05
GOLGA2	0.66	5.0E-05
GPRASP1	-1.60	5.1E-05
RSRC2	0.78	5.1E-05
AKAP17A	0.67	5.1E-05
C8orf31	-1.31	5.1E-05
RPGRIP1L	-0.71	5.1E-05
GBAP1	-0.95	5.2E-05
GTPBP1	0.70	5.3E-05
SMIM19	-0.81	5.4E-05
PIK3CA	4.25	5.4E-05
TTC30A	-0.90	5.4E-05
FAXC	-0.68	5.5E-05
SMARCAD1	-0.61	5.6E-05
WBSCR22	0.64	5.6E-05
ERVK3-1	-0.65	5.7E-05
ELK4	0.84	5.8E-05
RNF6	-0.61	5.8E-05
KMT2E-AS1	1.35	5.9E-05
LHFPL4	-0.86	6.0E-05
EML2	0.62	6.0E-05
ZNF804A	-1.66	6.0E-05
ASNSD1	-0.65	6.1E-05
PANK1	-0.76	6.1E-05
DZIP3	-0.66	6.1E-05
ALKBH6	0.76	6.1E-05

SP8	1.19	6.4E-05
DDIT4	0.67	6.4E-05
F3	1.07	6.4E-05
LHX4	0.82	6.5E-05
BRCA1	-0.66	6.5E-05
DPH7	0.68	6.5E-05
ADAT2	0.67	6.5E-05
ZNF577	-0.87	6.6E-05
NUDT22	0.92	6.6E-05
E2F2	0.70	6.7E-05
ZNF480	-0.76	6.8E-05
AP3B2	-0.92	6.9E-05
C17orf80	-0.74	7.0E-05
LINC00202-1	-0.80	7.2E-05
ERLIN1	0.60	7.2E-05
HN1	0.63	7.3E-05
ANKRD11	-0.59	7.4E-05
FAM114A2	-0.66	7.5E-05
JAGN1	-0.80	7.5E-05
SHISA2	0.78	7.5E-05
NPM3	0.61	7.5E-05
HABP4	0.78	7.5E-05
SERTAD2	0.73	7.5E-05
RRP15	-0.64	7.6E-05
DTX3L	-1.21	7.6E-05
CLDN15	-0.73	7.7E-05
ZNF649	-0.76	7.8E-05
FAM124A	-1.52	7.9E-05
IL11RA	-0.80	7.9E-05
HNRNPU-AS1	0.64	7.9E-05
LINC00632	0.93	7.9E-05
ALPK2	-1.78	7.9E-05
EID2B	0.97	8.0E-05
HCG11	-0.80	8.1E-05
ZWINT	-0.59	8.1E-05
ZBTB16	1.03	8.1E-05
SLC1A1	-0.75	8.2E-05
AAR2	-0.66	8.2E-05
LRRC8D	-0.78	8.4E-05
VARS	0.61	8.6E-05
RBM11	0.75	8.6E-05
TMEM62	-1.01	8.8E-05
LAMP1	0.63	8.8E-05
USP49	0.64	8.8E-05
NHP2	0.62	8.8E-05
TRMT11	0.65	8.8E-05
DDX6	-0.62	8.8E-05

TTC18	-1.08	8.8E-05
NRIP1	-0.63	8.9E-05
CCDC61	0.98	8.9E-05
CCDC81	2.28	9.0E-05
CD101	-1.14	9.0E-05
KDELR1	0.58	9.0E-05
UBAP1L	-1.02	9.0E-05
MBLAC2	-0.72	9.0E-05
ANKMY1	-0.80	9.1E-05
ZNF85	-0.75	9.1E-05
ANGPT1	-0.97	9.2E-05
TBC1D22A	-0.68	9.2E-05
LINC00638	-1.76	9.3E-05
SIGMAR1	0.59	9.4E-05
PSMG4	0.77	9.5E-05
ANTXR2	-0.67	9.5E-05
CIRBP-AS1	-1.14	9.7E-05
GTF2H1	-0.65	9.7E-05
ISCA1	-0.69	9.8E-05
XYLB	-0.71	9.9E-05
DPP7	-1.07	1.0E-04
C10orf118	0.73	1.0E-04
SLC35A5	-0.76	1.0E-04
ITGA2	-0.69	1.0E-04
DHFRL1	-1.04	1.0E-04
CCRN4L	0.86	1.0E-04
DENND6B	-1.13	1.0E-04
SCGB2B2	-1.39	1.0E-04
NEU3	0.64	1.0E-04
EPC1	-0.63	1.1E-04
RAPGEF5	0.64	1.1E-04
GUCY1A3	-0.76	1.1E-04
BASP1	0.79	1.1E-04
KIAA1211L	-1.63	1.1E-04
SNHG15	0.59	1.1E-04
TRPC1	-0.74	1.1E-04
AEN	-0.61	1.1E-04
CXorf40A	-0.73	1.1E-04
ATAD5	0.59	1.1E-04
AP5B1	-0.82	1.1E-04
PALMD	-0.95	1.1E-04
HCFC2	0.69	1.1E-04
SYNC	-1.76	1.1E-04
NUAK2	1.17	1.1E-04
PHC3	0.64	1.1E-04
IER5	0.74	1.1E-04
RNF128	-0.71	1.1E-04

KDM7A	0.67	1.2E-04
TMPO-AS1	-0.81	1.2E-04
BARHL2	1.38	1.2E-04
TRMT10A	-0.81	1.2E-04
OLFML2A	-1.08	1.2E-04
KLF6	0.65	1.2E-04
PHACTR1	0.70	1.2E-04
PUSL1	0.84	1.2E-04
ST6GALNAC3	-0.79	1.2E-04
KIAA1875	-1.58	1.3E-04
NYNRIN	-0.70	1.3E-04
HMGB3	0.58	1.3E-04
SMOC2	-2.11	1.3E-04
CCDC9	0.73	1.3E-04
BTRC	-0.63	1.3E-04
LIAS	0.91	1.3E-04
BEND5	-1.62	1.3E-04
HIVEP3	-0.72	1.4E-04
RPL18	0.64	1.4E-04
CTU2	0.83	1.4E-04
ZNF229	-0.83	1.4E-04
AARSD1	1.20	1.4E-04
CDK17	0.65	1.4E-04
COL7A1	-0.82	1.4E-04
PPP1R26-AS1	-1.24	1.4E-04
RIMKLA	-0.98	1.4E-04
ZNF583	-0.87	1.4E-04
LINC00839	-0.94	1.5E-04
COTL1	0.72	1.5E-04
AK9	-1.05	1.5E-04
ZNRD1	0.78	1.5E-04
ZNF484	0.99	1.5E-04
NUP214	-0.58	1.5E-04
NAT6	0.85	1.5E-04
HEY2	1.06	1.5E-04
ZNF217	0.74	1.5E-04
ZNF793	-0.69	1.5E-04
AMER1	-0.67	1.5E-04
LPCAT4	0.74	1.5E-04
TFRC	-0.61	1.5E-04
SNCAIP	-0.85	1.5E-04
LYPLAL1	-0.71	1.5E-04
CDKN1B	0.58	1.5E-04
RAD52	0.63	1.5E-04
COL9A2	-0.79	1.5E-04
FOXC2	1.18	1.5E-04
SLC25A24	-0.65	1.6E-04

BCL9L	0.74	1.6E-04
HS3ST3A1	0.78	1.6E-04
PPHLN1	-0.59	1.6E-04
IBA57	-0.69	1.6E-04
KCNB1	-1.32	1.7E-04
SUSD2	-2.18	1.7E-04
DPY19L2	-1.05	1.7E-04
MIR34A	-1.60	1.7E-04
EP400NL	-0.66	1.7E-04
RIC8B	-0.68	1.7E-04
MTMR1	-0.59	1.7E-04
N6AMT2	-1.07	1.7E-04
ZNF688	-1.13	1.7E-04
C5	-1.89	1.8E-04
GJA5	-1.40	1.8E-04
C5orf28	-0.95	1.8E-04
KIAA1407	-0.97	1.8E-04
SLC38A9	-0.66	1.8E-04
PRPSAP1	0.59	1.8E-04
IFIT5	-0.61	1.9E-04
HSPA2	-0.72	1.9E-04
LIG4	-0.69	1.9E-04
GPR27	-0.70	1.9E-04
ASIC3	-0.97	1.9E-04
VAPB	-0.65	1.9E-04
PAWR	0.63	1.9E-04
PARD6B	0.97	2.0E-04
UFSP1	-1.76	2.0E-04
ZNF708	-0.81	2.0E-04
CEACAM19	-0.73	2.0E-04
DUSP7	0.69	2.0E-04
CHCHD2	0.90	2.0E-04
LYRM7	-0.69	2.0E-04
PIGC	-0.68	2.0E-04
SENP5	0.63	2.1E-04
PRX	0.79	2.1E-04
AGER	-1.04	2.1E-04
FHL3	0.93	2.1E-04
FBXO46	0.75	2.1E-04
ANK3	-0.59	2.1E-04
SEMA7A	0.84	2.1E-04
DTYMK	0.71	2.1E-04
MXD1	0.68	2.2E-04
KIAA0232	-0.64	2.2E-04
TMEM254-AS1	-1.34	2.2E-04
KIAA1549L	-0.63	2.2E-04
RICTOR	0.69	2.2E-04

ZC3H12A	0.74	2.2E-04
ZNF790	-0.74	2.2E-04
TLR3	-1.37	2.3E-04
SIK2	-0.63	2.3E-04
N4BP2	-0.66	2.3E-04
CDC27	-0.59	2.3E-04
ADAMTS10	-0.70	2.3E-04
ATP1A3	0.68	2.3E-04
BCHE	-0.74	2.3E-04
CHURC1	-0.96	2.3E-04
ZNF121	0.59	2.3E-04
ZCWPW1	-1.00	2.3E-04
ID4	0.66	2.4E-04
KBTBD11	-0.83	2.4E-04
UBXN8	-0.70	2.4E-04
TUBB2B	0.61	2.4E-04
C9orf37	0.79	2.4E-04
DDAH2	0.74	2.5E-04
SIRPA	-0.65	2.5E-04
SGK3	0.98	2.5E-04
GCDH	0.66	2.6E-04
INPP5D	-0.73	2.6E-04
IGSF8	0.73	2.6E-04
DNM1P35	-1.82	2.6E-04
NRP2	0.63	2.6E-04
SLC26A7	-0.94	2.6E-04
GTPBP3	0.64	2.6E-04
CENPF	-0.58	2.6E-04
TMEM194B	-0.99	2.6E-04
IGDCC4	-0.69	2.6E-04
HIST3H2A	1.22	2.6E-04
SNED1	-0.86	2.7E-04
TDRD6	-1.38	2.7E-04
BNIP1	0.70	2.7E-04
MROH6	-1.08	2.7E-04
ITPKC	0.66	2.7E-04
CCDC85B	1.55	2.7E-04
LIPT2	-1.01	2.7E-04
ALDH1A3	-0.70	2.7E-04
AKAP8L	0.59	2.7E-04
NDUFS7	0.66	2.7E-04
MAF	0.64	2.7E-04
ZNF765	-0.78	2.8E-04
ZNF827	-0.78	2.8E-04
HSPA1B	0.65	2.8E-04
SLC19A2	0.69	2.8E-04
TTN-AS1	-0.73	2.8E-04

PGBD2	-1.33	2.9E-04
STARD5	0.84	2.9E-04
RHOQP1	1.40	2.9E-04
VSTM4	-0.78	2.9E-04
CSPG5	-0.76	2.9E-04
FAM69A	-0.64	3.0E-04
DACT1	0.68	3.0E-04
UBE2S	0.75	3.0E-04
CISH	0.95	3.0E-04
RPRD2	-0.60	3.0E-04
CRELD1	0.64	3.0E-04
ZNF354C	-0.93	3.0E-04
TMEM165	-0.62	3.0E-04
C12orf65	0.66	3.0E-04
PIM3	0.66	3.1E-04
TRPT1	0.84	3.1E-04
DPYSL4	-1.01	3.1E-04
BUD13	0.60	3.1E-04
C2CD2	-0.63	3.1E-04
NAALADL1	1.78	3.2E-04
TIRAP	-0.77	3.2E-04
STRADA	0.79	3.2E-04
STAG1	-0.63	3.2E-04
CFI	-0.99	3.2E-04
KIF24	-0.70	3.2E-04
ARHGAP28	-0.73	3.3E-04
GPRIN3	0.60	3.3E-04
PHF3	0.61	3.3E-04
THRB	-0.61	3.3E-04
TMEM18	-0.61	3.3E-04
MSRB3	-0.61	3.3E-04
DRAM1	-0.99	3.3E-04
SCAMP5	-0.65	3.3E-04
ZNF124	-1.33	3.4E-04
SLC37A2	1.06	3.4E-04
MED17	-0.66	3.4E-04
RASA4CP	-1.98	3.5E-04
USB1	0.62	3.6E-04
MBNL1-AS1	0.91	3.6E-04
TRPA1	-1.22	3.6E-04
PRICKLE4	-0.81	3.6E-04
SNAPC2	1.01	3.6E-04
PIH1D2	-1.83	3.7E-04
PCGF1	0.62	3.7E-04
SNX18P7	-1.72	3.7E-04
PHLDB3	0.76	3.7E-04
WDR63	-0.81	3.8E-04

STOX1	-0.97	3.8E-04
POLR3B	-0.62	3.9E-04
TMEM79	0.80	3.9E-04
GPER1	-1.43	3.9E-04
TROVE2	0.59	3.9E-04
ADSSL1	1.00	3.9E-04
GLRX5	0.59	4.0E-04
FZD5	0.62	4.0E-04
MEF2C	-0.61	4.0E-04
NKX2-8	1.49	4.0E-04
TBC1D8	0.60	4.1E-04
DYNLL1-AS1	-1.03	4.1E-04
SNORA75	1.69	4.1E-04
CD55	0.61	4.2E-04
EMP1	0.86	4.2E-04
CMBL	0.58	4.2E-04
RGMB	0.64	4.3E-04
ZNF615	0.66	4.4E-04
CCNJL	-1.19	4.4E-04
DISP1	-0.68	4.4E-04
SLC25A1	0.62	4.5E-04
MYH15	-1.36	4.5E-04
ETNK1	-0.62	4.5E-04
GDNF-AS1	-0.85	4.5E-04
ZNF581	0.90	4.5E-04
PEX3	-0.60	4.6E-04
SRGAP2C	0.83	4.6E-04
CCDC89	-1.64	4.6E-04
PPDPF	0.87	4.6E-04
C2orf72	-0.74	4.6E-04
CREG2	1.42	4.7E-04
ANKRD31	-1.62	4.7E-04
ITPRIP	0.65	4.7E-04
NECAP2	-0.61	4.7E-04
C2CD2L	0.78	4.8E-04
ZNF202	-0.65	4.9E-04
RGPD5	1.65	4.9E-04
DLX2	0.63	5.0E-04
ATL1	-0.93	5.0E-04
COLGALT1	0.61	5.0E-04
NKX2-4	-0.77	5.0E-04
RND1	1.00	5.0E-04
TXLNB	-0.95	5.1E-04
MAFK	0.90	5.1E-04
FBLN2	1.77	5.2E-04
NPC1L1	-1.20	5.2E-04
FAM86HP	-1.73	5.2E-04

RUVBL2	0.62	5.3E-04
RLTPR	0.95	5.3E-04
ZNF519	-0.70	5.3E-04
C22orf26	-1.63	5.4E-04
AKIP1	0.67	5.5E-04
ZFP36L1	0.76	5.5E-04
ZNF782	-1.01	5.6E-04
LYPD3	1.13	5.7E-04
ADM	0.65	5.7E-04
FGFR3	0.59	5.8E-04
ZNF32	-0.70	5.8E-04
SIX4	0.61	5.8E-04
DLX6	0.60	5.9E-04
AMH	-1.02	5.9E-04
TEX264	-0.61	5.9E-04
EIF4A1	0.62	5.9E-04
FOS	0.92	5.9E-04
HIST1H1E	-2.09	5.9E-04
CDK5R1	0.69	5.9E-04
DDTL	-0.97	5.9E-04
CBX7	-0.77	5.9E-04
PIGP	-0.62	6.0E-04
ARNT2	-0.60	6.0E-04
C19orf82	-1.39	6.1E-04
TOR1A	-0.63	6.2E-04
CCDC110	-1.32	6.2E-04
DHRS7B	-0.71	6.2E-04
CCDC102A	-1.10	6.3E-04
URGCP	-0.60	6.3E-04
USP4	0.58	6.4E-04
UBOX5	0.65	6.5E-04
GUCY1B2	-1.16	6.6E-04
PKD1P6	0.69	6.6E-04
C21orf67	-1.31	6.6E-04
RAD51C	-0.68	6.7E-04
C3orf62	-1.15	6.7E-04
KLHL3	-0.62	6.7E-04
IRAK1BP1	-0.62	6.7E-04
GCNT1	0.70	6.8E-04
OR2A1-AS1	-0.98	6.8E-04
ZNF574	0.70	6.8E-04
WASH6P	0.80	6.8E-04
CASP8	-0.59	6.9E-04
CCDC19	1.41	7.0E-04
TMEM254	-0.67	7.0E-04
HOTTIP	-1.05	7.0E-04
HOXA7	-0.71	7.2E-04

ZNF394	0.74	7.3E-04
ZNF404	-0.94	7.3E-04
DGKZ	0.65	7.3E-04
AKIRIN2	0.65	7.3E-04
ARID3A	0.64	7.4E-04
C16orf52	-0.74	7.4E-04
TMEM5	-0.69	7.5E-04
CNEP1R1	0.77	7.5E-04
CTBP1-AS2	-0.59	7.5E-04
TP53RK	-0.73	7.6E-04
MRPL43	0.59	7.6E-04
STAC3	-1.02	7.7E-04
HOMEZ	-0.60	7.8E-04
BCDIN3D	-0.86	7.9E-04
RLIM	0.59	7.9E-04
CTSO	-0.91	8.0E-04
GPX1	0.67	8.0E-04
TMEM132B	-0.84	8.1E-04
CCDC47	-0.63	8.1E-04
TNS3	-0.60	8.1E-04
PDRG1	0.72	8.1E-04
ENPP5	0.73	8.1E-04
LRRC66	-1.85	8.1E-04
IRS2	0.63	8.2E-04
C15orf57	0.67	8.2E-04
ZNF699	0.86	8.2E-04
CARF	-0.84	8.3E-04
DHRSX	-0.82	8.3E-04
MALAT1	0.71	8.4E-04
TRAM2-AS1	-0.88	8.5E-04
SLC16A14	-0.64	8.5E-04
MESP2	1.72	8.6E-04
TK2	-0.86	8.7E-04
CCDC14	-0.59	8.9E-04
RBM3	0.64	8.9E-04
EEF1A1P19	1.74	9.0E-04
TMEM39B	-0.71	9.2E-04
ARG2	0.62	9.2E-04
ZNF107	-0.64	9.2E-04
PTER	-0.63	9.2E-04
LINC01002	0.90	9.2E-04
PRIMA1	-0.78	9.3E-04
RMND1	0.61	9.3E-04
TENC1	-0.65	9.4E-04
KDM4D	-0.87	9.5E-04
BCL7B	-0.73	9.5E-04
POLN	-0.76	9.8E-04

ZWILCH	-0.62	9.8E-04
PAX1	-0.88	9.8E-04
NKX6-1	0.79	9.9E-04
XRCC4	-0.79	9.9E-04
CACNG8	-0.93	1.0E-03
PTPRZ1	-0.77	1.0E-03
SLC6A8	0.61	1.0E-03
TMEM98	-0.60	1.0E-03
TLE3	0.58	1.0E-03
PGM2L1	0.64	1.0E-03
ZNF681	-1.23	1.0E-03
RIPK2	0.60	1.0E-03
THSD7A	-1.06	1.0E-03
EIF4A2	0.60	1.0E-03
RMRP	-3.25	1.0E-03
ZNF724P	0.75	1.0E-03
IFIT1	-0.71	1.0E-03
NUPR1	-1.05	1.1E-03
FBXO27	0.76	1.1E-03
SSPO	-0.88	1.1E-03
NACC2	-0.62	1.1E-03
LRRIQ1	-1.10	1.1E-03
FAM193B	0.71	1.1E-03
ERV3-1	-0.74	1.1E-03
FTX	-1.69	1.1E-03
HCN2	0.66	1.1E-03
NXPH3	0.92	1.1E-03
C14orf28	1.01	1.1E-03
THAP3	0.70	1.1E-03
WDR31	-1.07	1.1E-03
FANCM	0.61	1.1E-03
FBXL2	0.71	1.1E-03
SNORD117	1.07	1.1E-03
SLC16A6	-1.12	1.1E-03
PHF1	0.62	1.1E-03
DEPTOR	0.63	1.1E-03
ZNF570	0.60	1.1E-03
BAMBI	0.63	1.2E-03
TNFRSF12A	1.16	1.2E-03
HERC6	-0.68	1.2E-03
OXTR	0.87	1.2E-03
DLL1	0.62	1.2E-03
CDC37L1	0.67	1.2E-03
ZNF296	0.87	1.2E-03
SCN5A	-0.94	1.2E-03
ZNF783	-0.65	1.2E-03
TTPAL	-0.72	1.2E-03

FAM118B	-0.75	1.2E-03
ANKDD1A	1.30	1.2E-03
VPS18	-0.72	1.2E-03
ING3	-0.65	1.3E-03
ELOF1	0.62	1.3E-03
ZNF853	-0.61	1.3E-03
TTLL11	-0.79	1.3E-03
VCPKMT	0.77	1.3E-03
DUSP10	0.68	1.3E-03
C15orf61	0.83	1.3E-03
SDCBP2	1.13	1.3E-03
MORN1	-0.76	1.3E-03
PYROXD1	-0.73	1.3E-03
SLC9A8	-0.63	1.3E-03
KIAA1045	-1.27	1.3E-03
ATG4D	0.66	1.3E-03
RBAK	-0.62	1.3E-03
PHF21B	0.76	1.3E-03
SRP14-AS1	-0.91	1.3E-03
ZNF471	-0.74	1.3E-03
MAP2K7	0.62	1.4E-03
TLR5	-1.59	1.4E-03
TMEM67	-0.60	1.4E-03
NAT9	0.61	1.4E-03
MAD2L2	0.61	1.4E-03
ZNF627	0.76	1.4E-03
LINC00176	-1.32	1.4E-03
ITPRIPL2	-0.61	1.4E-03
PEX11A	-0.66	1.4E-03
TRAM1	-0.64	1.4E-03
ISL2	0.64	1.4E-03
DGCR11	1.25	1.4E-03
CALHM2	0.61	1.4E-03
PDE4B	-0.87	1.5E-03
SBNO2	0.70	1.5E-03
C12orf5	-0.66	1.5E-03
NAT1	-0.89	1.5E-03
CALCB	0.72	1.5E-03
AP4S1	-1.44	1.5E-03
RASSF4	-0.75	1.5E-03
TXNDC5	0.97	1.5E-03
MIEF2	0.64	1.5E-03
SPPL2A	-0.65	1.5E-03
ZNF268	-0.62	1.5E-03
TBX2	0.66	1.5E-03
MAMDC4	-0.90	1.5E-03
PPARGC1A	0.76	1.5E-03

TBC1D17	0.68	1.6E-03
NEK11	-1.31	1.6E-03
LINC-PINT	1.10	1.6E-03
HOXC8	-0.59	1.6E-03
NEXN	-0.59	1.6E-03
CLGN	-0.83	1.6E-03
TNFAIP8L3	1.55	1.6E-03
ARMCX4	-1.37	1.6E-03
RAB36	-0.76	1.6E-03
CEP97	0.59	1.6E-03
RGS7BP	-0.92	1.6E-03
DHDH	1.13	1.6E-03
LINC01023	1.66	1.6E-03
ACSS3	0.73	1.7E-03
DOLK	-0.71	1.7E-03
XKR5	-1.14	1.7E-03
PDCD7	0.59	1.7E-03
MAFF	1.45	1.7E-03
f	0.62	1.7E-03
EDA2R	-0.70	1.7E-03
GEM	0.71	1.7E-03
CUZD1	-1.12	1.7E-03
SCN2A	-1.59	1.7E-03
WNK3	0.62	1.7E-03
SDAD1P1	-1.15	1.7E-03
MAPKAPK5-AS1	0.78	1.7E-03
SHROOM1	-0.69	1.7E-03
ACTRT3	-1.53	1.8E-03
METTL25	-1.01	1.8E-03
KLF16	0.69	1.8E-03
HIST1H2BJ	1.06	1.8E-03
PTHLH	1.15	1.8E-03
TAGLN	-1.09	1.8E-03
SPSB2	0.86	1.8E-03
LIMK1	0.71	1.8E-03
COX5A	0.72	1.8E-03
RPS6KB2	0.60	1.8E-03
PAXIP1-AS2	-0.95	1.8E-03
MURC	-1.03	1.9E-03
GDNF	-0.85	1.9E-03
AOC2	0.64	1.9E-03
CYP4X1	-0.62	1.9E-03
TPH1	-1.71	1.9E-03
IQCH	-1.00	1.9E-03
SHC2	-0.79	1.9E-03
DHRS1	0.68	1.9E-03
PTPMT1	-0.80	2.0E-03

FIGN	0.63	2.0E-03
S1PR2	0.84	2.0E-03
KRAS	1.02	2.0E-03
ANKHD1-EIF4EBP3	-1.63	2.1E-03
TDRD12	-1.17	2.1E-03
SKIL	0.67	2.1E-03
TMEM134	0.74	2.1E-03
MGMT	0.65	2.1E-03
FAM86B3P	0.58	2.1E-03
TRIM36	0.62	2.1E-03
ZNF695	1.16	2.1E-03
ALG11	-0.86	2.1E-03
UBALD2	0.83	2.1E-03
P2RY1	0.67	2.1E-03
HSF4	-0.93	2.1E-03
STK17B	0.69	2.1E-03
MYLIP	0.67	2.2E-03
ZNF528	-0.80	2.2E-03
TEAD4	0.61	2.2E-03
PEX6	-0.58	2.2E-03
CHCHD5	0.76	2.2E-03
MAEA	-0.66	2.2E-03
KCNMB3	-1.35	2.2E-03
ZNF425	-1.28	2.2E-03
SLC7A11	-0.70	2.2E-03
TMEM117	-0.62	2.2E-03
PKIA	-0.60	2.2E-03
GNG5	0.63	2.2E-03
MSTN	-1.33	2.2E-03
TRAF1	-0.99	2.2E-03
GRB14	0.72	2.2E-03
HELQ	-0.72	2.2E-03
SCAND2P	0.62	2.2E-03
PRSS27	-1.12	2.3E-03
MDH1B	-1.75	2.3E-03
RHBDF1	0.60	2.3E-03
TNFAIP8L1	0.71	2.3E-03
C9orf89	0.85	2.3E-03
DCHS1	-0.94	2.3E-03
CDKN2D	0.83	2.3E-03
TMEM168	-0.65	2.3E-03
OPHN1	0.58	2.3E-03
ARFRP1	0.66	2.3E-03
PPP4R1L	0.67	2.3E-03
WDR4	0.58	2.3E-03
SLC25A19	0.63	2.3E-03

TUSC1	-0.71	2.3E-03
VWDE	0.61	2.3E-03
BEAN1	-1.21	2.3E-03
NFIL3	0.64	2.4E-03
AMY2B	-1.12	2.4E-03
LPAR3	0.61	2.4E-03
CASC2	-0.99	2.5E-03
NFKBIB	0.74	2.5E-03
SHPK	1.21	2.5E-03
FBXL19-AS1	-0.74	2.5E-03
SAMD1	0.61	2.6E-03
ZNF836	-1.44	2.6E-03
ZNF502	-0.96	2.6E-03
TPST1	-0.59	2.6E-03
IL6R	0.60	2.6E-03
MRPL1	-0.77	2.6E-03
SCN1B	0.92	2.6E-03
SDCBP2-AS1	-1.31	2.6E-03
NFATC4	-0.61	2.6E-03
PAM16	1.05	2.6E-03
ZNF862	-0.61	2.6E-03
FZD10-AS1	-1.46	2.6E-03
NHLH2	-1.82	2.7E-03
RHBDL3	-0.59	2.7E-03
C1RL	-0.83	2.7E-03
PLEKHG4B	-0.65	2.7E-03
XRCC6BP1	0.69	2.8E-03
THEM4	-0.60	2.8E-03
DTX4	-0.61	2.8E-03
SH2B3	0.58	2.8E-03
LDOC1	0.62	2.8E-03
ITGB1BP2	-1.17	2.8E-03
LRRC17	-1.19	2.9E-03
AP4E1	-0.66	2.9E-03
TEAD3	0.61	2.9E-03
SREBF1	-0.61	2.9E-03
DLL4	1.03	2.9E-03
NHSL2	-0.84	2.9E-03
GRK4	-0.73	3.0E-03
RNF19B	0.58	3.0E-03
FN3K	-1.24	3.0E-03
SOCS3	1.25	3.0E-03
ANPEP	1.58	3.0E-03
PRR22	-1.14	3.0E-03
RASL11B	0.73	3.1E-03
WDR45	-0.61	3.1E-03
TMEM41B	0.58	3.1E-03

CCDC53	-0.62	3.1E-03
TTC3P1	-1.09	3.1E-03
QPCTL	0.62	3.2E-03
KCTD21	-0.89	3.2E-03
CHST2	0.90	3.2E-03
HAPLN3	0.58	3.2E-03
NR0B1	1.18	3.3E-03
APOLD1	-0.67	3.3E-03
ROMO1	0.60	3.3E-03
LINC00648	-1.21	3.3E-03
C1orf145	-1.17	3.4E-03
BSCL2	-0.90	3.4E-03
RGMA	0.60	3.4E-03
CABLES2	-0.59	3.4E-03
ZNF385C	-1.01	3.4E-03
MCF2L	-0.61	3.4E-03
PDXP	1.63	3.4E-03
ZNF337-AS1	-0.87	3.4E-03
PDK4	0.76	3.4E-03
CCDC28B	0.65	3.4E-03
RUSC1-AS1	-1.08	3.4E-03
ALPK1	-0.59	3.5E-03
FAM86EP	-0.99	3.5E-03
PARK2	-0.82	3.5E-03
MC1R	-1.06	3.6E-03
ALG5	-0.67	3.6E-03
CDH10	-0.72	3.6E-03
DENND2C	0.59	3.6E-03
PRKAR1B	-0.63	3.6E-03
CLHC1	-0.76	3.6E-03
FHOD1	0.60	3.7E-03
DNAJB9	0.68	3.7E-03
NXT2	-0.61	3.7E-03
SLC35B3	-0.58	3.7E-03
LRRC57	0.62	3.8E-03
ZNF34	0.74	3.8E-03
KIAA1456	-1.08	3.8E-03
MARVELD3	0.70	3.9E-03
PKD2	-0.64	3.9E-03
CACNA2D3	0.80	3.9E-03
SLC6A16	-0.73	3.9E-03
ZSCAN30	-0.58	3.9E-03
EPN1	0.58	3.9E-03
TCIRG1	-1.18	4.0E-03
KIAA1024	-0.58	4.0E-03
SPATA18	-0.64	4.0E-03
NPPC	1.04	4.0E-03

CCDC176	-1.10	4.0E-03
IRX3	0.68	4.0E-03
SOS1-IT1	0.81	4.0E-03
LINC00467	-0.73	4.1E-03
ZNF485	-0.77	4.1E-03
FRY	0.59	4.2E-03
SNHG17	0.60	4.2E-03
EXTL3-AS1	0.93	4.3E-03
NPTX1	-0.61	4.3E-03
H1FX	0.59	4.3E-03
FAM83H-AS1	-0.80	4.3E-03
NPL	-0.64	4.3E-03
CRY2	0.62	4.4E-03
RNASET2	0.64	4.4E-03
GKAP1	0.63	4.5E-03
B3GAT2	-0.78	4.5E-03
C8orf48	-1.45	4.5E-03
TFEB	0.82	4.5E-03
GNB2	0.70	4.6E-03
MTG1	-0.70	4.6E-03
METAP1D	-0.63	4.6E-03
ZNF284	0.70	4.6E-03
MBD3	-0.59	4.6E-03
CLEC11A	1.07	4.6E-03
FOXD3	0.97	4.8E-03
ADRB1	1.10	4.8E-03
RNF170	-0.61	4.8E-03
FAM226A	1.15	4.9E-03
FAM226B	1.15	4.9E-03
RHBDL1	-1.00	4.9E-03
SSR4P1	-1.64	4.9E-03
RAB27B	-0.82	5.0E-03
NELFB	0.59	5.1E-03
PTMS	0.61	5.1E-03
HSCB	0.77	5.1E-03
PRR4	-1.03	5.1E-03
C6orf183	-0.59	5.2E-03
ZNF10	-0.65	5.2E-03
KRTCAP2	0.66	5.2E-03
KCTD18	-0.59	5.2E-03
WDR96	-1.46	5.2E-03
KCNJ4	0.96	5.2E-03
FILIP1L	-1.46	5.2E-03
ZNF382	-0.70	5.2E-03
PLAG1	0.68	5.3E-03
PILRA	-1.09	5.4E-03
RHPN1	-0.98	5.4E-03

OMA1	-0.61	5.4E-03
FOXN4	-0.74	5.4E-03
PITX1	0.61	5.4E-03
ABCC8	-0.72	5.5E-03
ZBED3-AS1	-0.90	5.5E-03
SNORD94	1.01	5.5E-03
PTGES2	0.74	5.6E-03
SLC23A3	-1.63	5.7E-03
EPM2A	-0.65	5.7E-03
PHLDA1	0.66	5.7E-03
IFT88	-0.59	5.8E-03
GOLGA2P5	-0.74	5.8E-03
SNORD101	1.46	5.9E-03
CCDC180	-1.71	5.9E-03
C19orf52	0.61	6.0E-03
SLC25A34	-1.55	6.0E-03
PAXIP1-AS1	0.76	6.0E-03
ABCG1	0.99	6.1E-03
LSMEM1	1.25	6.1E-03
SNORD83A	0.90	6.1E-03
TGM2	-0.85	6.1E-03
HOXA10-AS	-0.66	6.2E-03
ZSCAN12P1	-1.27	6.2E-03
WEE2-AS1	-1.25	6.2E-03
C1orf50	0.62	6.2E-03
FAM50B	-0.71	6.2E-03
CDO1	-0.64	6.3E-03
GLIPR1	-0.73	6.4E-03
ZNF611	-0.65	6.4E-03
OSGEPL1	-0.59	6.4E-03
MAP2K6	-0.61	6.4E-03
MID1IP1-AS1	-1.15	6.4E-03
DMTN	-0.93	6.5E-03
SEMA3G	-0.79	6.6E-03
TEX35	-1.41	6.6E-03
RERG	-1.18	6.7E-03
PRR13	0.59	6.7E-03
NKX2-5	0.81	6.7E-03
PCBD2	-0.76	6.8E-03
HSD17B7	0.76	6.8E-03
WDR81	-0.67	6.8E-03
EMC9	0.64	6.9E-03
EFCAB6	-1.10	6.9E-03
C6orf165	0.92	6.9E-03
C6orf163	-1.21	6.9E-03
SPINK5	-1.04	6.9E-03
LINC00526	1.27	7.0E-03

SCARNA10	-1.32	7.2E-03
GTPBP10	-0.66	7.2E-03
REPS2	-0.69	7.4E-03
ST3GAL2	0.58	7.4E-03
IQCG	-0.69	7.4E-03
FAM195A	0.84	7.4E-03
EIF3J-AS1	0.70	7.4E-03
ARL6IP6	-0.61	7.5E-03
MGLL	0.81	7.5E-03
SCUBE1	-0.59	7.5E-03
LINC01123	1.11	7.5E-03
ORAI2	0.58	7.5E-03
C11orf70	-0.79	7.5E-03
SRSF8	-0.71	7.6E-03
STEAP1	-0.62	7.7E-03
TPI1P2	-1.60	7.7E-03
TTC32	-0.59	7.7E-03
HIST1H1C	0.74	7.7E-03
FAM86C2P	-0.65	7.8E-03
PNPLA3	0.64	7.8E-03
BEST1	-1.00	7.8E-03
TRIM59	0.82	7.8E-03
ZDHHC1	-0.74	7.9E-03
C19orf10	0.68	7.9E-03
IFT80	-0.60	7.9E-03
QDPR	0.64	7.9E-03
TSPAN2	-0.69	7.9E-03
BHLHB9	-0.73	8.0E-03
PALM2	0.73	8.2E-03
BCL7C	0.61	8.3E-03
SNORD69	0.85	8.3E-03
PTGER2	-1.17	8.6E-03
JAKMIP1	-1.09	8.7E-03
CLDN4	0.92	8.7E-03
CARD9	-1.39	8.8E-03
BCL10	0.58	8.8E-03
EMILIN2	0.60	8.8E-03
FAM149A	-0.68	8.9E-03
MAP6	-1.04	8.9E-03
NME5	-0.93	9.0E-03
REG1A	1.01	9.0E-03
MBOAT1	0.63	9.1E-03
BIN3	-0.58	9.1E-03
HSD3B7	-1.25	9.2E-03
NRG4	-0.60	9.2E-03
PRR7	1.09	9.3E-03
SNORD20	1.45	9.3E-03

IFI27	-0.82	9.3E-03
ELMO3	-1.11	9.3E-03
C16orf46	1.34	9.4E-03
FAM96B	0.58	9.4E-03
CYP2D6	-1.24	9.4E-03
BRAF	0.67	9.5E-03
RGS9	-0.87	9.6E-03
CACTIN-AS1	-1.17	9.6E-03
ZBED5-AS1	-1.16	9.6E-03
GABRA5	-0.59	9.6E-03
FAM174B	-0.78	9.6E-03
NDUFC2	-0.78	9.7E-03
SYNPO2	-1.49	9.8E-03
LOH12CR1	0.58	9.9E-03
ICA1L	-0.65	9.9E-03
SMIM4	0.87	9.9E-03
FOLR1	-0.91	9.9E-03
DLK2	1.22	9.9E-03
TMEM99	-0.59	1.0E-02
TCHH	-0.83	1.0E-02
CCT6P3	0.67	1.0E-02
CCDC147-AS1	1.11	1.0E-02
MED31	-0.59	1.0E-02
ZBTB11-AS1	-1.02	1.0E-02
CNR1	-1.24	1.0E-02
RELL2	0.62	1.0E-02
C10orf10	0.72	1.0E-02
KCTD17	0.58	1.1E-02
DNAJC5G	-1.36	1.1E-02
HILPDA	-0.69	1.1E-02
C1orf116	1.01	1.1E-02
RPL18AP3	1.44	1.1E-02
MT2A	0.70	1.1E-02
FERMT1	-1.36	1.1E-02
STK31	-1.19	1.1E-02
EHBP1L1	-0.60	1.1E-02
UBE2V1	0.83	1.1E-02
INE1	0.81	1.1E-02
TMEM17	-0.89	1.1E-02
SYTL4	0.63	1.1E-02
KIAA0391	0.97	1.1E-02
C7orf63	0.72	1.1E-02
SNORA33	1.30	1.1E-02
KCNC1	-0.65	1.1E-02
BMP8B	-0.63	1.1E-02
FAM132B	-0.58	1.1E-02
ZBTB7C	-0.63	1.1E-02

BMP4	0.59	1.2E-02
EXOSC4	0.76	1.2E-02
ZNF32-AS2	0.98	1.2E-02
NAT14	0.60	1.2E-02
CHL1	-0.95	1.2E-02
CXXC4	-0.60	1.2E-02
TMEM51-AS1	-1.20	1.2E-02
IER5L	1.19	1.2E-02
SPSB1	-0.68	1.2E-02
STYK1	0.75	1.2E-02
PPAN	-0.89	1.2E-02
CDH7	-0.58	1.2E-02
INCA1	-1.31	1.3E-02
MRPS31P5	0.98	1.3E-02
LRRTM4	-0.74	1.3E-02
PLEKHF1	0.76	1.3E-02
DMPK	-0.62	1.3E-02
SPAG17	-1.43	1.3E-02
CCDC7	-0.99	1.3E-02
HRSP12	-0.61	1.3E-02
CCDC178	-1.32	1.3E-02
ANKRD24	-0.79	1.3E-02
WAS	-1.21	1.3E-02
PLEKHN1	1.03	1.3E-02
ZNF707	0.61	1.3E-02
TMEM27	-1.14	1.3E-02
PDE7B	-1.22	1.3E-02
HCG15	-0.85	1.3E-02
SMN2	-0.67	1.4E-02
CDK15	-0.84	1.4E-02
SNORD17	0.72	1.4E-02
PLIN1	-0.88	1.4E-02
LY6G5B	-0.75	1.4E-02
PABPC1P3	1.12	1.4E-02
DUOX2	-1.33	1.4E-02
SNRNP25	0.65	1.4E-02
FGF5	-0.80	1.4E-02
FLVCR1-AS1	0.90	1.4E-02
ANKLE1	-1.07	1.4E-02
IL12RB2	-0.63	1.4E-02
ZBTB8B	0.66	1.4E-02
CYP27B1	-0.65	1.5E-02
NDST4	-1.23	1.5E-02
TMEM54	0.92	1.5E-02
CAMK2B	-1.17	1.5E-02
PTPRB	-0.82	1.5E-02
LURAP1	0.74	1.5E-02

POF1B	-1.26	1.5E-02
DRP2	0.73	1.5E-02
PPP1R3F	-0.82	1.5E-02
PINK1-AS	-0.67	1.5E-02
SNX18P3	-0.83	1.5E-02
HSPB1	0.59	1.5E-02
CCDC183-AS1	-0.69	1.5E-02
HBQ1	1.25	1.5E-02
SPSB3	0.60	1.5E-02
APLF	-0.83	1.5E-02
MIR4519	0.97	1.5E-02
BTBD19	-0.71	1.5E-02
HYPK	0.63	1.5E-02
FAM131B	0.77	1.6E-02
NACAD	-0.91	1.6E-02
PSMD6-AS2	-0.99	1.6E-02
TMEM169	-1.37	1.6E-02
HNRNPA3P6	1.06	1.6E-02
ARMC12	-1.28	1.6E-02
KLF15	0.66	1.6E-02
LINC00909	-0.77	1.6E-02
ANKRD20A4	0.93	1.7E-02
SAMD15	-1.02	1.7E-02
CAPN10-AS1	0.85	1.7E-02
ID1	0.88	1.7E-02
GOLGA8R	-0.79	1.7E-02
LINC01021	-0.75	1.7E-02
PPAPDC1A	-0.87	1.7E-02
AMIGO1	-0.73	1.7E-02
XK	-0.69	1.7E-02
CYBRD1	-0.64	1.7E-02
HES4	0.68	1.7E-02
WDR72	-0.71	1.7E-02
C15orf59	-0.66	1.7E-02
COL24A1	-0.67	1.7E-02
EPPK1	-0.81	1.7E-02
CHRNB1	0.79	1.7E-02
RPS15A	0.63	1.8E-02
CTNNA3	-0.84	1.8E-02
ZNF628	0.80	1.8E-02
ZNF28	-0.61	1.8E-02
CYP3A5	-0.75	1.8E-02
OTUD1	0.64	1.8E-02
CCDC122	-0.61	1.8E-02
RRAS	0.78	1.9E-02
CLYBL	-0.62	1.9E-02
CYP2J2	-0.69	1.9E-02

LINC01003	1.27	1.9E-02
NEUROG2	1.16	1.9E-02
TMEM155	-1.05	1.9E-02
GLIS1	0.69	1.9E-02
MTUS2	1.21	1.9E-02
TECTA	-0.85	1.9E-02
SLC8A3	-0.82	1.9E-02
CEP44	0.67	1.9E-02
IFITM3	0.84	2.0E-02
TMEM44-AS1	-0.98	2.0E-02
RNF180	-0.86	2.0E-02
T	-1.26	2.0E-02
CYP4F26P	-0.73	2.0E-02
TGFB1	0.72	2.0E-02
CCDC181	0.69	2.0E-02
BCL3	0.78	2.0E-02
C9orf16	0.63	2.0E-02
SLC26A4	-1.24	2.0E-02
NOTCH2NL	-0.59	2.1E-02
USP2-AS1	1.02	2.1E-02
TBC1D10A	0.68	2.1E-02
TNS1	-0.63	2.1E-02
DDX47	0.77	2.1E-02
NRAS	1.16	2.1E-02
ABCA8	-0.68	2.1E-02
SLC46A3	-0.70	2.1E-02
OCEL1	0.68	2.1E-02
MKX	-0.62	2.1E-02
GJB7	-0.63	2.1E-02
SLC52A2	0.59	2.2E-02
MAPK13	0.77	2.2E-02
ARHGEF37	-0.66	2.2E-02
ZNF805	0.62	2.2E-02
RDH14	-0.65	2.2E-02
PDE3A	-0.80	2.2E-02
BFSP1	-0.98	2.2E-02
IFIT2	-1.13	2.2E-02
RAB4B	0.84	2.2E-02
BHLHE41	-0.62	2.3E-02
KLRAP1	-0.67	2.3E-02
PLA2G7	-0.61	2.3E-02
C2CD4C	-1.09	2.3E-02
LINC01116	-1.03	2.3E-02
KCNE4	-0.98	2.3E-02
BBS5	0.66	2.3E-02
CEL	-1.02	2.4E-02
KRT8P12	0.65	2.4E-02

SLC17A7	1.09	2.4E-02
GIPR	0.76	2.4E-02
ZNF17	-0.58	2.4E-02
GPR137C	-0.58	2.4E-02
RGS5	-0.61	2.4E-02
LIN7B	0.59	2.4E-02
TTC25	-0.93	2.4E-02
B3GALT5	-0.68	2.4E-02
HSPB6	-1.19	2.4E-02
UNC5A	-0.91	2.4E-02
STEAP1B	-0.65	2.4E-02
CCDC107	0.66	2.4E-02
RIBC2	-0.67	2.4E-02
MAFB	0.65	2.5E-02
MSRA	0.92	2.5E-02
SPRY2	0.59	2.5E-02
TMEM126A	0.66	2.5E-02
NDNF	-0.66	2.5E-02
CRIP3	0.91	2.5E-02
TSACC	-0.75	2.6E-02
LRRIQ3	-1.21	2.6E-02
CCDC144CP	-0.70	2.6E-02
RFTN2	-1.13	2.6E-02
U2AF1L4	0.68	2.6E-02
FAM66D	-1.25	2.7E-02
SBF2-AS1	-0.76	2.7E-02
SYNGR4	-0.99	2.7E-02
SUV420H2	0.64	2.7E-02
KNDC1	-0.77	2.7E-02
CXorf24	1.06	2.8E-02
CUBN	-0.85	2.8E-02
MIR1254-1	0.83	2.8E-02
ZNF582	-0.64	2.8E-02
CELSR3	-0.59	2.8E-02
FAM157A	0.62	2.8E-02
DIO2	-0.97	2.9E-02
LRRN2	-1.09	2.9E-02
LINC00893	-0.75	2.9E-02
ADRA2C	0.59	2.9E-02
ZCCHC18	0.95	2.9E-02
RDH16	0.89	2.9E-02
LRRTM2	-0.78	2.9E-02
GLDN	-0.61	2.9E-02
NEB	-1.06	3.0E-02
LAMTOR5-AS1	-0.84	3.0E-02
GLUD1P3	0.70	3.0E-02
TMCC1-AS1	-0.92	3.0E-02

TRPM3	-0.93	3.0E-02
PIK3IP1	0.71	3.0E-02
KCNJ11	1.01	3.0E-02
HLX	0.61	3.1E-02
CCDC144A	-1.03	3.1E-02
OVOL2	0.95	3.1E-02
EOMES	-0.61	3.1E-02
WDR78	-0.92	3.1E-02
MUC20	-1.11	3.2E-02
ARIH2OS	1.13	3.2E-02
CDHR3	-0.67	3.2E-02
GATA6-AS1	0.73	3.2E-02
PTH1R	-1.19	3.2E-02
SH2D4A	-1.19	3.2E-02
SCARNA17	-1.28	3.2E-02
PCSK1N	0.90	3.2E-02
DDX60	-0.59	3.2E-02
RPL28	0.59	3.2E-02
FOXP3	-1.18	3.2E-02
FAM203A	-0.66	3.2E-02
DNAJC22	-0.58	3.3E-02
ZNF846	-0.77	3.3E-02
DNAJC30	-0.62	3.4E-02
FER1L4	-0.75	3.4E-02
MRPS17	-0.72	3.5E-02
ATP5D	0.60	3.5E-02
LRRC69	-1.07	3.5E-02
URAHP	0.81	3.6E-02
SMCO4	0.69	3.6E-02
MIF	0.59	3.6E-02
DNAAF3	-0.78	3.6E-02
LINC00461	-0.84	3.6E-02
INA	-0.68	3.6E-02
TMEM184A	-1.20	3.6E-02
ZC3H6	0.58	3.7E-02
zfhx2-as1	-0.87	3.7E-02
CYP4F32P	-0.73	3.7E-02
SNORA66	1.02	3.8E-02
FRMD3	-1.03	3.8E-02
TMEM145	-0.59	3.8E-02
SPIN3	-0.63	3.9E-02
MLKL	-0.88	4.0E-02
ZNF429	-0.60	4.0E-02
SENP8	-0.59	4.1E-02
EFCAB4B	-0.66	4.1E-02
SRRM5	-0.81	4.1E-02
ZNF571-AS1	-0.80	4.1E-02

COL9A1	-0.61	4.2E-02
C1orf213	0.72	4.2E-02
SRRM2-AS1	-0.62	4.3E-02
RMDN2	-1.00	4.3E-02
AKAP3	-0.92	4.3E-02
SLC2A4	0.69	4.3E-02
SNX18P16	-1.08	4.4E-02
GPR3	0.85	4.4E-02
CCNT2-AS1	-0.86	4.4E-02
PCDH1	0.61	4.4E-02
ADPRHL1	-0.62	4.5E-02
CPLX1	0.66	4.5E-02
RXRG	-0.94	4.5E-02
ZMYND10	-0.86	4.5E-02
NAIP	-0.82	4.5E-02
EMR2	-0.66	4.6E-02
GPC2	0.61	4.7E-02
CDK5R2	1.07	4.7E-02
C12orf60	-0.79	4.7E-02
SNORA50	0.92	4.7E-02
NIPSNAP3B	0.73	4.7E-02
COL4A4	-0.69	4.8E-02
ZNF23	0.75	4.9E-02
ACRC	-0.64	5.0E-02
CAPS2	-1.22	5.0E-02

Supplemental File 2: Chapter 4 differentially expressed genes from rotenone treated SH-5YSY negative control.

Genename	logFC	FDR
RSPO1	-5.81	5.13E-60
TFAMP1	-4.17	1.05E-54
AC104129.1	-5.55	4.82E-42
AL136529.1	-4.31	2.23E-39
TMEM51-AS1	-3.05	8.19E-39
BHLHE40	-3.21	1.22E-38
NEDD9	-4.31	1.63E-37
C20orf166-AS1	-3.43	2.85E-36
CA12	-4.55	1.98E-33
AC138028.2	-3.60	1.06E-30
CXCR4	-3.95	2.74E-30
AC134312.1	-3.18	3.68E-28
CARTPT	-3.96	3.68E-28
AC135782.1	-3.33	5.43E-27
AC138028.1	-3.93	9.53E-27
GPER1	-4.27	2.20E-26
TRIM29	-3.36	3.96E-25
TSPEAR-AS1	-2.44	1.54E-24
SOBP	-2.40	3.11E-24
KCNQ1OT1	-2.68	1.57E-23
CFAP43	-2.85	1.59E-23
TSPEAR-AS2	-2.57	4.77E-23
AL109615.3	-3.45	1.02E-21
ELFN1	-2.78	2.94E-21
GDF10	-2.66	7.91E-21
CABP7	-2.26	1.12E-20
VEGFA	-2.31	1.31E-20
TLX1	-2.91	1.13E-19
CARMN	-2.91	6.25E-19
AQP1	-2.39	1.75E-18
HSPB7	-2.66	2.01E-18
AC134312.4	-3.14	3.09E-18
HTR1E	-2.21	4.73E-18
NXPH4	-3.16	1.69E-16
AQP10	-3.33	1.89E-16
ADM	-2.29	2.76E-16

AC074389.2	-3.80	3.22E-16
NRP1	-2.12	3.39E-16
DARS-AS1	-3.17	2.03E-15
NTNG2	-2.44	2.29E-15
MCHR1	-3.14	2.65E-15
AP001065.1	-2.15	2.73E-15
LINC00304	-3.06	3.67E-15
OLFM1	-2.14	3.80E-15
DUSP7	-2.38	4.37E-15
RTL1	-1.70	4.65E-15
ID2	-2.14	1.17E-14
LINC02348	-2.71	3.39E-14
SLC2A1	-1.76	3.98E-14
NDUFA4L2	-2.83	7.89E-14
PTK6	-2.89	3.06E-13
CERK	-1.73	3.22E-13
HEY1	-2.02	3.35E-13
N4BP3	-1.86	3.61E-13
SOX9	-1.82	5.42E-13
CU639417.2	-2.35	6.28E-13
EPB41L4B	-1.91	7.67E-13
ZMAT4	-2.07	1.17E-12
NDRG1	-1.82	3.89E-12
LRRC4	-2.20	5.22E-12
DIO3	-2.14	5.93E-12
ANGPTL4	-2.17	9.19E-12
HK2	-1.59	1.22E-11
SSUH2	-1.73	1.58E-11
PPP1R3C	-2.12	3.39E-11
LINC01679	-2.23	3.65E-11
AC027228.2	-1.60	5.01E-11
FAM43A	-2.21	8.76E-11
CYB561	-1.49	1.32E-10
ZNF469	-1.53	2.38E-10
SLC18A1	-2.11	3.02E-10
STARD13	-1.60	3.47E-10
PFKFB4	-1.53	3.71E-10
TMEM51	-1.65	4.94E-10
APLN	-1.96	6.64E-10
OLFML2A	-1.78	8.10E-10

GDF15	1.87	1.19E-09
PDK1	-1.41	1.78E-09
SLC35D3	-1.72	1.78E-09
RGS4	-1.64	2.43E-09
QRICH2	-1.72	2.68E-09
FOSL2	-1.65	3.19E-09
CDKN1C	-3.21	4.67E-09
PRCD	-1.69	5.23E-09
SYT8	-2.21	5.26E-09
TNNI2	-2.57	6.49E-09
KCNMA1	-1.52	9.21E-09
DOK3	-1.75	9.43E-09
KIAA1614	-1.36	1.24E-08
C2CD4B	-2.77	1.32E-08
EGLN3	-1.85	1.66E-08
ASNS	1.81	1.88E-08
GABRP	-1.73	2.06E-08
AC015802.5	-2.02	2.17E-08
FOS	-1.58	2.55E-08
PDZD7	-1.37	2.63E-08
CABP1	-1.87	2.80E-08
IGF2-AS	-2.01	2.90E-08
SH2D5	1.70	4.16E-08
PPP1R3B	-1.30	5.03E-08
PIEZO1	-1.84	5.33E-08
DIO3OS	-1.66	8.51E-08
GPRC5B	-1.49	8.62E-08
LINC01963	-1.44	8.79E-08
HIST1H2AC	-1.67	9.51E-08
LDHA	-1.50	1.02E-07
ADORA2A	-1.49	1.30E-07
TBX2-AS1	1.39	1.45E-07
FAM167A	-1.39	1.63E-07
PFKFB3	-1.33	1.77E-07
DDC	-1.66	2.46E-07
CYGB	-1.52	2.79E-07
EPAS1	-1.26	3.36E-07
HSPA5	-1.16	3.81E-07
CDKN1A	1.19	4.34E-07
LSP1	-1.64	4.96E-07

IGF2	-2.31	5.88E-07
AL513477.1	-1.61	6.81E-07
SSR4P1	-1.65	8.11E-07
EML1	-1.21	8.48E-07
CDH23	-1.34	8.79E-07
AK4	-1.15	1.51E-06
AASS	1.29	1.73E-06
CHRND	-1.43	1.74E-06
AL021368.2	1.56	1.94E-06
NCOA5	-1.15	2.51E-06
MIR210HG	-2.38	2.64E-06
SLC16A12	-1.47	2.88E-06
DGCR9	-1.40	3.13E-06
HIST1H2BD	-1.45	5.05E-06
C8orf58	-1.38	5.59E-06
SCML4	-1.39	5.59E-06
AP001062.1	-1.54	8.01E-06
COX4I2	-1.92	9.61E-06
PRODH	-1.61	1.06E-05
DRGX	-1.15	1.34E-05
KCNC1	-1.09	1.79E-05
AC026688.2	-1.14	2.04E-05
ST3GAL6	-1.09	2.16E-05
CCND1	-1.09	2.28E-05
LINC02151	-1.32	2.52E-05
LOXL2	-1.20	2.64E-05
CACNG8	-1.15	2.72E-05
HMCN2	-1.15	3.47E-05
P4HA1	-1.05	3.50E-05
SFXN3	-1.07	4.64E-05
BDKRB2	-1.29	5.08E-05
GPR146	-1.64	5.15E-05
SGMS1-AS1	-1.16	5.36E-05
AC015802.3	-1.49	6.73E-05
STS	-1.21	7.78E-05
SLC37A2	1.52	7.84E-05
TBC1D30	-1.17	8.02E-05
PDE4C	-1.04	8.11E-05
KCNC4	1.14	8.12E-05
DNAH10	-1.18	9.21E-05

ADPRHL1	-1.49	9.68E-05
AC010680.2	-1.40	9.94E-05
AC011700.1	-1.32	1.06E-04
CFAP44	-0.99	1.09E-04
PIPOX	-1.30	1.11E-04
DDB2	0.97	1.13E-04
TSNAXIP1	-1.23	1.20E-04
ARHGEF4	0.99	1.68E-04
KLF10	-0.98	1.77E-04
INHBE	1.57	1.80E-04
ZMAT3	0.99	1.80E-04
HNRNPM	-0.96	1.81E-04
HIST1H2BK	-1.33	2.03E-04
C17orf97	-1.43	2.03E-04
GGT5	-1.18	2.15E-04
ZNF425	-1.11	2.17E-04
ADARB1	-0.95	2.18E-04
XYLT1	-0.94	2.83E-04
ETS2	-0.93	3.05E-04
MZF1-AS1	-1.22	3.14E-04
DIRAS2	1.14	3.23E-04
EGR1	-1.04	3.23E-04
KDM3A	-0.90	3.41E-04
PLXNA2	-0.90	3.80E-04
CEBPB	1.43	3.95E-04
ARHGAP45	-1.22	4.53E-04
BNIP3	-1.15	4.67E-04
ZNF804A	-0.91	4.68E-04
HSPA8	-0.88	4.68E-04
FOXR2	-1.09	5.03E-04
PEAR1	-0.94	5.05E-04
MYO15B	0.97	5.24E-04
ARHGEF37	-0.94	5.28E-04
CYR61	1.17	5.50E-04
KLF15	0.98	5.50E-04
CLCNKA	-0.98	5.53E-04
DLK1	-1.20	5.64E-04
PLIN5	1.15	5.69E-04
SH3BP5-AS1	-0.97	5.83E-04
TNFRSF19	-1.22	5.94E-04

HIST1H2BE	-1.12	6.06E-04
LPCAT4	0.87	6.17E-04
FUT11	-0.99	6.59E-04
AC007388.1	1.09	7.48E-04
PCSK6	-0.91	7.68E-04
DDIT4	-1.17	8.00E-04
PPP1R32	1.14	8.28E-04
LINC00511	-1.36	8.28E-04
EDA2R	1.04	1.02E-03
COL23A1	-1.15	1.10E-03
PAX7	-1.35	1.11E-03
NTNG1	1.24	1.13E-03
SLC25A25-AS1	-0.89	1.13E-03
SYT5	-1.00	1.20E-03
C4orf47	-1.21	1.21E-03
ARRDC4	-0.88	1.25E-03
ALS2CL	0.96	1.31E-03
AC022239.3	-1.11	1.34E-03
AL392083.1	-0.88	1.55E-03
EGLN1	-0.86	1.63E-03
LINC01250	-0.92	1.69E-03
GPR75	-1.14	1.76E-03
FAM163B	-0.96	1.77E-03
SLC16A14	0.90	1.80E-03
KCNJ11	1.03	1.90E-03
PINK1-AS	-0.93	1.93E-03
PSMG3-AS1	-0.84	1.96E-03
ADAMTS2	-0.91	2.03E-03
AC021074.1	1.23	2.08E-03
AL136964.1	0.91	2.13E-03
RD3	-0.90	2.13E-03
RIMKLA	-0.84	2.14E-03
AC022239.1	-1.21	2.36E-03
ZNF547	-1.08	2.37E-03
MIR34AHG	0.94	2.38E-03
DGCR5	-0.99	2.43E-03
SCART1	0.94	2.46E-03
DCST2	1.15	2.53E-03
CCBE1	-0.95	2.62E-03
CHTF18	0.82	2.67E-03

KIAA1683	-0.89	2.70E-03
AC012513.3	-1.09	2.78E-03
CTH	0.89	2.81E-03
TCTA	-0.90	2.81E-03
AC011498.7	-1.20	2.81E-03
AC092198.1	-0.98	2.86E-03
AFF1	-0.80	2.90E-03
PGAM1	-1.00	2.92E-03
THEGL	1.12	2.95E-03
PCDH9	1.01	2.97E-03
ZMIZ1	-0.78	3.00E-03
SCARB1	-0.87	3.00E-03
ADSSL1	0.84	3.01E-03
ZNF395	-0.81	3.13E-03
AL591848.4	-1.14	3.15E-03
CEP44	0.78	3.20E-03
RERG	-0.87	3.42E-03
NECTIN1	-0.80	3.56E-03
PKM	-0.86	3.57E-03
MT-RNR2	0.85	3.81E-03
RYR2	-1.16	3.86E-03
TH	-1.38	3.89E-03
ZNF781	-0.92	3.92E-03
ENO1	-0.84	3.94E-03
LMO1	-1.03	3.94E-03
FAM162A	-1.05	4.04E-03
EIPR1-IT1	-1.14	4.09E-03
EXD3	0.98	4.14E-03
DUSP4	0.76	4.14E-03
ZNF596	-0.86	4.16E-03
HIC2	-0.81	4.19E-03
AC009533.1	0.90	4.29E-03
HILPDA	-0.78	4.43E-03
GATA2	-0.84	4.65E-03
SDCBP2-AS1	-0.97	4.76E-03
TPRG1L	-0.79	4.83E-03
FAM72B	0.79	4.90E-03
AL021068.1	1.18	4.98E-03
PIK3IP1	-0.93	5.17E-03
TMEM178A	1.14	5.33E-03

BBC3	0.86	5.45E-03
AC105383.1	1.00	5.61E-03
ATXN7L2	0.81	5.61E-03
AP4S1	-0.90	5.65E-03
CNTNAP2	1.17	5.66E-03
AC144652.1	0.85	5.69E-03
SLC8A3	-0.77	5.69E-03
AP000866.1	-1.07	5.72E-03
AL596202.1	-0.85	5.84E-03
AC024940.1	1.01	5.84E-03
SPATA18	0.94	6.22E-03
ZFHX2	-0.78	6.32E-03
Z84485.1	1.15	6.37E-03
AC022748.2	-1.01	6.37E-03
LINC00926	-1.15	6.53E-03
OSGIN1	1.12	6.61E-03
NRIP3	0.84	6.74E-03
AC021092.1	-0.86	6.82E-03
ATG16L2	0.79	7.21E-03
TNIP1	-0.78	7.22E-03
FASTKD5	-0.77	7.24E-03
DPY19L1P1	0.96	7.33E-03
LRRC37A3	-0.79	7.41E-03
LMO7	0.80	7.47E-03
ISL2	0.94	7.69E-03
NR1D2	0.81	7.69E-03
PWAR6	-0.84	7.70E-03
GLS2	0.95	7.84E-03
PGK1	-0.81	7.89E-03
PLD1	0.83	7.99E-03
AC017048.3	0.91	8.19E-03
POLR3H	-0.77	8.19E-03
AP003356.1	-1.08	8.19E-03
SLC1A2	-1.05	8.68E-03
CHGA	-0.91	8.73E-03
CYP4V2	-0.76	8.78E-03
PAQR5	0.82	9.11E-03
MDH1B	-0.99	9.19E-03
AC010931.2	-0.92	9.31E-03
PCDH10	0.86	9.46E-03

DNAJA1	-0.71	9.51E-03
SAMD15	-0.96	9.59E-03
GPR63	0.77	9.70E-03
DDX50P1	1.01	9.75E-03
SPTBN5	-0.87	9.75E-03
AC006058.3	0.97	9.87E-03
GNAS	-0.81	9.87E-03
MTFP1	-1.16	1.01E-02
TEX261	-0.74	1.03E-02
ITGB5	-0.73	1.04E-02
RAB36	-0.84	1.05E-02
GAS6-AS2	0.97	1.05E-02
PDGFC	1.05	1.07E-02
MYCBPAP	0.80	1.08E-02
BCOR	-0.72	1.09E-02
ICAM5	1.11	1.09E-02
UTP14A	-0.71	1.10E-02
AP000911.1	-0.96	1.12E-02
AMPD3	-0.80	1.12E-02
SLITRK5	0.81	1.16E-02
TPI1P2	-1.10	1.16E-02
RBM44	1.09	1.17E-02
GRIP2	0.77	1.21E-02
GAS6	0.71	1.21E-02
HIST1H2BG	-0.98	1.21E-02
HOXD10	0.86	1.24E-02
AC021945.1	1.21	1.26E-02
AC022239.4	-1.14	1.30E-02
ZDHHC19	0.96	1.34E-02
AC022239.2	-0.95	1.34E-02
KIF26B	-0.82	1.35E-02
P2RY6	-1.05	1.36E-02
ST3GAL6-AS1	-1.02	1.36E-02
NR1D1	0.93	1.37E-02
GFOD1	0.86	1.39E-02
ENDOD1	0.81	1.40E-02
NGFR	0.79	1.40E-02
PIH1D2	-1.09	1.43E-02
HERC2P5	1.02	1.43E-02
FPGT-TNNI3K	0.96	1.43E-02

RRP7BP	0.81	1.43E-02
CNN2	0.71	1.43E-02
LZTS1	-0.72	1.44E-02
UACA	0.70	1.45E-02
METTL22	0.71	1.46E-02
SRSF3	-0.69	1.47E-02
PTOV1-AS1	-1.04	1.47E-02
POP1	-0.77	1.47E-02
ZNF571-AS1	-0.94	1.50E-02
CDHR1	0.83	1.51E-02
PLOD1	-0.77	1.51E-02
HS6ST3	1.10	1.51E-02
SYNPO	-0.69	1.51E-02
FMN1	1.03	1.54E-02
TRIM24	-0.69	1.54E-02
SCN5A	-0.74	1.56E-02
SH3D21	-0.72	1.71E-02
ANKS1B	0.99	1.72E-02
KIF17	0.79	1.72E-02
AF131215.5	-0.77	1.77E-02
SLC25A35	0.76	1.79E-02
SDAD1P1	-0.80	1.81E-02
SPNS2	-0.96	1.81E-02
LINC02268	-0.73	1.85E-02
CARD9	0.70	1.90E-02
CD9	-0.88	1.90E-02
GRB14	0.75	1.93E-02
RIPOR3	-0.81	1.94E-02
LINC00632	0.74	1.95E-02
CLYBL	0.75	1.95E-02
NTN4	0.89	2.00E-02
SLC4A11	0.75	2.00E-02
SLC43A1	0.80	2.01E-02
SEMA3D	0.99	2.02E-02
C3orf62	-0.74	2.03E-02
RAD52	0.70	2.04E-02
SLC12A4	0.68	2.06E-02
LINC00342	-0.77	2.06E-02
ARID3A	-0.77	2.10E-02
FER1L4	-0.75	2.10E-02

HIST2H2BE	-0.81	2.13E-02
FUT9	0.93	2.15E-02
EDIL3	0.92	2.15E-02
TNNT3	-1.05	2.16E-02
SNHG14	-0.72	2.17E-02
FBXO8	-0.70	2.18E-02
MTRNR2L8	0.90	2.19E-02
PROX1	-0.68	2.19E-02
SEMA5B	-0.82	2.20E-02
AP001160.3	-0.93	2.22E-02
DNAJC30	-0.82	2.25E-02
HERC3	0.72	2.26E-02
NELL1	0.69	2.26E-02
MAN2C1	0.66	2.33E-02
DHRS3	0.86	2.36E-02
ERMP1	0.69	2.36E-02
P2RY11	-0.80	2.37E-02
AC037459.3	-0.77	2.38E-02
DHX9	-0.66	2.44E-02
AC106895.2	-0.74	2.45E-02
DOK4	-0.69	2.47E-02
MAGEA12	-0.67	2.47E-02
DIRC3	-1.10	2.48E-02
ERO1B	0.71	2.53E-02
GALNT18	-0.75	2.54E-02
ARHGEF28	0.70	2.54E-02
EIF4BP3	0.78	2.58E-02
CHAC1	0.85	2.60E-02
CCNA1	0.83	2.65E-02
ISLR2	-0.68	2.66E-02
ZNF789	-0.67	2.68E-02
HSPG2	0.69	2.68E-02
GTF2IP13	-0.69	2.71E-02
AC044797.1	-0.98	2.72E-02
COMMD9	-0.68	2.77E-02
AC007996.1	-0.96	2.78E-02
FGF11	-0.93	2.84E-02
AC097468.1	-1.14	2.88E-02
VPS33A	-0.69	2.89E-02
ATL1	-0.70	2.90E-02

TPI1	-0.76	2.95E-02
LRP4	0.69	2.97E-02
GLCCI1	-0.73	3.05E-02
GPM6A	0.86	3.08E-02
AL513534.1	-0.83	3.16E-02
AC120114.1	0.82	3.16E-02
SCNN1D	0.82	3.17E-02
AP001922.6	-1.18	3.17E-02
MSTO2P	0.69	3.19E-02
SEMA3C	0.68	3.19E-02
C9orf3	-0.66	3.20E-02
BLVRB	0.78	3.22E-02
TMEFF2	0.73	3.32E-02
AC018521.5	-0.81	3.37E-02
GRIA2	0.66	3.38E-02
AC007541.1	0.93	3.38E-02
PCDH18	0.72	3.38E-02
LRRC75A	-0.73	3.38E-02
CMTM8	0.90	3.39E-02
MXD3	0.78	3.39E-02
LFNG	-0.70	3.40E-02
SOX6	-0.80	3.41E-02
RHOB	-0.79	3.48E-02
MIRLET7BHG	-0.83	3.58E-02
RNF32	-0.96	3.59E-02
PCK2	0.63	3.59E-02
ZNF849P	0.90	3.63E-02
BNIP3L	-0.63	3.65E-02
TMEM45A	-0.72	3.67E-02
CYB5A	-0.74	3.68E-02
ZNF333	0.66	3.68E-02
FTX	-0.64	3.68E-02
ITPK1	-0.63	3.68E-02
TNC	-0.79	3.74E-02
AC048341.2	-0.89	3.74E-02
AC239868.2	-0.71	3.74E-02
HIST1H1C	-0.75	3.74E-02
PDP2	0.64	3.76E-02
ZNF75A	-0.66	3.80E-02
INHA	-0.99	3.81E-02

ST20-AS1	-0.94	3.82E-02
TTC39B	0.67	3.88E-02
AP006623.1	-0.85	3.89E-02
FBXL2	0.66	3.91E-02
MYH15	-0.66	3.91E-02
AC092329.4	-0.80	3.91E-02
SHMT2	-0.65	3.92E-02
MANF	-0.70	3.95E-02
ACSL6	0.94	3.98E-02
HSD17B14	0.73	3.98E-02
XKR5	0.71	4.00E-02
AC110285.2	0.80	4.04E-02
AL358472.2	0.80	4.04E-02
PPIF	-0.64	4.10E-02
CAMK2A	-0.84	4.10E-02
PGBD2	-0.74	4.14E-02
ID3	0.79	4.15E-02
TBX2	0.64	4.17E-02
KCTD19	0.71	4.18E-02
PLK2	0.87	4.18E-02
AC131212.2	0.95	4.22E-02
EML6	0.73	4.23E-02
SARDH	0.71	4.23E-02
ERVMER34-1	0.81	4.25E-02
PIDD1	0.69	4.33E-02
HMX2	0.99	4.36E-02
AC004893.2	-0.73	4.36E-02
ZEB1-AS1	0.66	4.37E-02
IRF6	-0.89	4.37E-02
AC006538.1	-0.90	4.38E-02
GNRHR2	0.80	4.40E-02
MALAT1	0.60	4.40E-02
AL365199.1	-0.88	4.41E-02
MT-CYB	-0.60	4.44E-02
AC099778.1	-0.91	4.47E-02
FAM86B3P	0.67	4.47E-02
HES7	0.86	4.50E-02
ARID3B	-0.63	4.54E-02
VWA5B2	0.81	4.56E-02
RIPK1	-0.64	4.56E-02

ERBB4	0.68	4.62E-02
PPP1R26-AS1	-0.97	4.62E-02
MAGED1	-0.65	4.65E-02
ADORA2B	-0.88	4.68E-02
MOCS3	-0.66	4.75E-02
DDX60L	0.67	4.85E-02
SOX7	-0.75	4.87E-02
SPECC1L	-0.66	4.93E-02
IPO5P1	-0.72	4.93E-02
AC020659.1	-0.84	4.96E-02

Supplemental File 3: Chapter 4 differentially expressed genes from rotenone treated SH-5YSY α-Synuclein knockdown cells.

Genename	logFC	FDR
CABP7	-1.64	1.40E-08
TFAMP1	-1.99	1.97E-08
NDUFA4L2	-1.65	3.08E-08
C20orf166-AS1	-1.69	7.84E-08
AC104129.1	-2.22	9.97E-08
AC135782.1	-2.36	3.05E-07
AC138028.2	-1.89	8.47E-07
CARTPT	-1.89	2.14E-06
TNNI2	-2.02	2.96E-06
CFAP43	-1.55	3.69E-06
STC1	-3.71	5.00E-06
CXCR4	-1.86	6.94E-06
AL136529.1	-1.72	1.07E-05
AC138028.1	-1.91	1.10E-05
CA9	-2.57	1.10E-05
HIST1H1D	-3.32	1.36E-05
MT-TQ	1.35	4.19E-05
NEDD9	-1.75	5.25E-05
DARS-AS1	-2.19	5.25E-05
GPER1	-1.91	5.85E-05
AC134312.4	-1.38	6.00E-05
KCNQ1OT1	-2.23	6.00E-05
CDKN1C	-1.28	6.55E-05
TBX1	-2.42	1.41E-04
PDE4C	-1.22	1.81E-04
C20orf24	1.40	1.87E-04
CA12	-1.84	1.93E-04
AC134312.1	-1.45	2.63E-04
GRIK3	-2.28	2.63E-04
CLCNKA	-1.22	3.00E-04
AC074389.2	-1.86	3.00E-04
BHLHE40	-1.20	4.30E-04
TSPEAR-AS1	-1.35	7.41E-04
MT-TA	1.43	1.08E-03
CARMN	-1.56	1.08E-03
PIEZO1	-1.13	1.20E-03

RSPO1	-1.81	1.28E-03
NTNG2	-1.21	1.30E-03
MCHR1	-1.63	1.30E-03
SNORD69	-2.82	1.31E-03
NXPH4	-1.33	1.57E-03
AC022239.3	-1.24	1.65E-03
CU639417.2	-1.22	1.75E-03
AP001065.3	-1.59	1.86E-03
GATA5	-2.85	1.86E-03
TSPEAR-AS2	-1.32	1.91E-03
AQP1	-1.12	1.97E-03
ARHGAP45	-1.37	2.42E-03
HNF1A	-1.79	2.45E-03
COL23A1	-1.13	2.72E-03
OLFM1	-1.07	2.99E-03
AC025279.1	-3.35	2.99E-03
CDH23	-1.13	3.24E-03
CEP295NL	-2.22	3.65E-03
PCBP2-OT1	-2.73	3.99E-03
CABP1	-1.48	5.07E-03
AL591845.1	-1.08	5.39E-03
NRP1	-1.27	5.62E-03
AQP10	-1.35	5.62E-03
AL109615.3	-1.32	5.66E-03
TMEM105	-1.37	5.66E-03
AC008895.1	-2.92	5.66E-03
ANGPTL4	-1.23	5.75E-03
IGF2	-0.95	6.29E-03
AC006042.3	-1.51	6.29E-03
ACTL8	-1.86	6.29E-03
CDRT4	-1.67	6.40E-03
FER1L4	-0.92	6.65E-03
TLX1	-1.48	6.65E-03
CAPN8	-1.52	6.86E-03
NDRG1	-0.96	6.97E-03
HIST1H2AC	-1.05	6.97E-03
AC004584.3	-2.46	7.39E-03
FAM43A	-1.20	8.07E-03
ZNF460	-1.39	8.45E-03
SOX9	-0.96	8.53E-03

FOSB	-2.13	8.89E-03
VEGFA	-0.99	9.06E-03
AC138028.5	-1.67	9.43E-03
N4BP3	-1.02	9.52E-03
SYT8	-1.32	9.80E-03
HEY1	-0.94	9.82E-03
HIST2H2BE	-1.14	1.09E-02
AC007663.1	-1.61	1.11E-02
AP006284.1	-1.31	1.21E-02
CROCC2	-2.00	1.22E-02
SRXN1	2.68	1.31E-02
PPP1R3C	-1.05	1.35E-02
AC013472.3	-2.53	1.35E-02
WNT11	-1.98	1.37E-02
HSPB7	-1.03	1.39E-02
C2CD4B	-1.32	1.68E-02
SLC18A1	-1.04	1.73E-02
CU459211.1	-1.96	1.75E-02
SNURF	-2.49	1.78E-02
HIST1H1E	-2.35	1.95E-02
C6orf99	1.69	1.98E-02
LOXL2	-0.84	1.99E-02
MIR616	-1.87	2.12E-02
TMEM51-AS1	-1.20	2.21E-02
ADORA2A	-0.94	2.23E-02
AC124283.3	-2.06	2.28E-02
STARD13	-0.90	2.30E-02
RSPH9	-1.30	2.44E-02
SH3D21	-0.83	2.46E-02
HMCN2	-0.87	2.69E-02
AP001065.1	-0.97	2.97E-02
PDZD7	-0.87	3.00E-02
ZMAT4	-0.96	3.00E-02
ANGPTL6	-1.69	3.03E-02
CBLN1	0.92	3.16E-02
AL138724.1	2.40	3.21E-02
CARD11	-2.25	3.34E-02
SOBP	-1.07	3.60E-02
FAM129A	0.84	3.65E-02
FAM86EP	1.16	3.94E-02

HIST1H2BG	-1.04	3.99E-02
TMEFF1	1.09	4.11E-02
SOSTDC1	1.71	4.39E-02
AC007336.1	-1.52	4.39E-02
AC019257.1	-1.93	4.39E-02
AC013394.1	-2.23	4.39E-02
AC092447.7	-1.21	4.47E-02
MT-TS1	1.35	4.53E-02
DIO3	-0.91	4.57E-02
TCERG1L	-2.26	4.60E-02
C1QTNF12	-1.56	4.60E-02
AL096816.1	-1.71	4.99E-02

Supplemental File 4: Chapter 5 differentially expressed genes from rotenone treated SH-5YSY.

Genename	logFC	FDR
RSPO1	3.70	3.0E-20
TFAMP1	2.07	1.4E-18
CDKN1C	1.55	9.9E-16
ELFN1	1.63	2.7E-15
AC104129.1	3.13	1.1E-14
TMEM51-AS1	1.54	7.9E-14
AC134312.1	1.63	9.2E-14
BHLHE40	1.72	1.6E-13
AC134312.4	1.62	7.5E-13
TRIM29	1.88	9.0E-13
C20orf166-AS1	1.61	1.7E-12
NEDD9	2.26	1.0E-11
AL136529.1	2.16	7.1E-11
AC010931.2	1.61	1.3E-10
IGF2	1.24	1.3E-10
CXCR4	1.63	4.8E-10
HSPB7	1.26	5.0E-10
VEGFA	1.04	2.0E-08
ECEL1	1.14	5.7E-08
DUSP7	1.19	1.2E-07
GABRP	1.80	1.3E-07
RTL1	0.95	1.3E-07
ISLR2	1.08	9.6E-07
AC138028.2	1.58	1.2E-06
HTR1E	1.29	1.4E-06
ASS1	1.92	1.4E-06
KIAA1614	1.09	2.1E-06
AP001065.1	1.10	2.4E-06
IL6	3.95	3.0E-06
RUNX1	1.37	3.5E-06
NTNG2	1.07	3.7E-06
SOBP	0.98	1.2E-05
TSPEAR-AS1	0.99	2.5E-05
CA12	2.36	2.9E-05
PRSS56	2.13	2.9E-05
AC002480.2	4.63	6.4E-05

TSPEAR-AS2	0.95	7.1E-05
NPY	0.92	7.8E-05
OLFM1	0.84	8.6E-05
CFAP43	1.09	9.4E-05
NDUFA4L2	0.95	9.4E-05
COL17A1	3.84	1.1E-04
LINC00304	2.02	1.4E-04
AQP1	0.80	1.5E-04
SNCA	-0.84	1.5E-04
ISLR	1.47	2.0E-04
SSUH2	1.04	2.3E-04
RET	0.74	3.2E-04
HEY1	0.82	3.3E-04
CYB561	0.88	3.7E-04
IGF2-AS	1.30	7.3E-04
AL136964.1	-1.02	8.6E-04
AP001065.3	2.39	1.0E-03
GDF10	1.06	1.0E-03
NCAM2	-1.13	1.1E-03
AL365199.1	1.25	1.1E-03
CARTPT	1.58	1.1E-03
CAPN8	2.67	1.2E-03
AC027228.2	1.22	1.4E-03
TFPI2	0.79	1.4E-03
MYO15B	-1.31	1.4E-03
AL138963.3	1.75	1.4E-03
ALDH8A1	3.59	1.5E-03
SLC2A1	0.73	1.5E-03
NXPH4	1.41	1.6E-03
ID2	1.11	1.6E-03
CRH	3.00	1.9E-03
HS3ST2	1.50	1.9E-03
DIO3	1.08	2.2E-03
TBX4	-1.28	2.2E-03
NNAT	0.88	2.3E-03
PRCD	0.77	2.9E-03
MALAT1	-0.66	2.9E-03
DIRAS2	-1.08	2.9E-03
HS6ST3	-1.35	2.9E-03
AC053503.5	-1.53	2.9E-03

LINC01679	1.26	2.9E-03
PTGIR	0.87	3.4E-03
TMEM51	0.81	3.6E-03
LINC00473	0.81	3.9E-03
TEX261	0.78	3.9E-03
GADD45G	0.97	4.0E-03
MIR186	-1.58	4.1E-03
AC092198.1	0.96	4.3E-03
AL390961.2	-1.18	4.5E-03
AC090897.1	1.04	5.0E-03
ANO9	-0.74	5.1E-03
CERK	0.68	5.2E-03
ERBB4	-0.82	5.3E-03
KCNQ1OT1	0.76	5.6E-03
AC107214.2	2.04	6.2E-03
NDRG1	0.66	6.2E-03
PGAM1	0.84	6.5E-03
AQP10	1.57	6.6E-03
SLC18A1	0.71	6.9E-03
FAM163B	0.68	6.9E-03
DOK3	1.10	7.2E-03
AL513477.1	1.14	7.9E-03
GATA2-AS1	0.93	8.0E-03
LDHA	0.78	8.2E-03
MYOM2	2.37	8.4E-03
SLC12A3	2.34	8.4E-03
AC022748.1	1.71	8.4E-03
GAL	0.85	8.4E-03
SLC22A18	-0.88	8.4E-03
PPP1R32	-1.07	8.5E-03
CCDC81	-1.39	9.5E-03
NCOA5	0.71	9.7E-03
AL138724.1	2.77	9.7E-03
PPM1J	-1.44	1.0E-02
QRICH2	1.00	1.1E-02
TMEM158	1.40	1.1E-02
C20orf24	0.90	1.1E-02
AC138028.5	2.93	1.1E-02
TLX1	1.28	1.1E-02
PFKFB3	0.66	1.1E-02

AL109615.3	1.55	1.2E-02
AL161729.1	1.13	1.2E-02
RGS4	0.62	1.2E-02
CABP7	0.63	1.2E-02
AC008443.4	-1.91	1.2E-02
CYP4V2	0.66	1.2E-02
SNX30	-0.67	1.2E-02
LMO7	-0.76	1.2E-02
AC245060.5	-1.02	1.3E-02
APLN	0.95	1.3E-02
ADAM12	0.66	1.4E-02
AC087276.2	-1.65	1.4E-02
AC091230.1	2.92	1.4E-02
LYPD3	-1.59	1.4E-02
FAM167A	0.62	1.5E-02
ZNF596	0.75	1.6E-02
GPER1	1.88	1.6E-02
PTK6	1.58	1.6E-02
C17orf97	1.20	1.6E-02
TMEM200B	-1.43	1.6E-02
SCRG1	-1.65	1.6E-02
DNM1P47	2.06	1.7E-02
AC010680.2	1.12	1.7E-02
CEP44	-0.85	1.7E-02
NTNG1	-1.12	1.7E-02
FSTL5	-0.77	1.7E-02
CARMN	1.31	1.7E-02
CCND1	0.70	1.7E-02
THBS1	1.75	1.8E-02
LINC01547	1.07	1.8E-02
TBX2-AS1	-0.70	1.8E-02
CDR1	1.24	1.9E-02
HSPA5	0.84	1.9E-02
LINC02348	1.28	2.0E-02
RPL13AP5	-0.60	2.0E-02
AC024361.1	-1.47	2.0E-02
HSPA9P1	1.45	2.1E-02
LIMA1	0.61	2.1E-02
DDX60	-1.92	2.1E-02
AC092139.4	2.85	2.1E-02

FGFR3	-0.91	2.2E-02
TNFRSF19	0.96	2.2E-02
ITGB5	0.62	2.5E-02
AC138028.1	1.60	2.5E-02
ALS2CL	-0.78	2.5E-02
AL354836.1	1.43	2.7E-02
DIO3OS	0.86	2.9E-02
CAVIN1	-2.04	3.0E-02
AC010809.1	2.16	3.0E-02
ADM	0.82	3.0E-02
C14orf144	0.79	3.0E-02
CFAP44	0.64	3.1E-02
STEAP2	-0.62	3.1E-02
AVEN	0.84	3.2E-02
SCNN1D	-0.74	3.2E-02
GLUD1P2	-0.98	3.2E-02
AL021368.2	-1.07	3.2E-02
GRIA2	-0.65	3.2E-02
BBS5	-0.76	3.3E-02
FLRT1	0.69	3.6E-02
AC074389.2	1.83	3.6E-02
EGLN3	0.80	3.7E-02
PDZK1	0.80	3.7E-02
TRIM7	-1.21	3.7E-02
NOXA1	-1.33	3.7E-02
VWDE	-0.64	3.9E-02
SNCA-AS1	-1.62	3.9E-02
FBXO6	-1.23	4.1E-02
AC008280.3	-1.88	4.3E-02
HSPA8P5	1.79	4.3E-02
P2RY1	-1.11	4.7E-02
ACVR1C	-1.40	4.8E-02
GDF5	-1.66	5.0E-02

APPENDIX CHAPTER ONE:

Manganese-induced Parkinsonism in mice is reduced using a novel contaminated water sediment exposure model[5]

Abstract

Heavy metals enter the aquatic environment and accumulate within water sediments, but these metal-sediment interactions remain to be explored within toxicity studies. We developed an exposure model in mice that encapsulates the aquatic microenvironment of metals before exposure. Male and female *C57/BL6* mice were exposed via their drinking water to manganese contaminated sediment (Sed_Mn) or to manganese without sediment interaction (Mn) for six weeks. Sediment interaction did not alter weekly manganese ingestion from water in males or females. We analyzed motor impairment, a common feature in manganese-induced Parkinsonism, using the beam traversal, cylinder, and accelerating rotarod tests. Sed_Mn mice performed better overall compared to Mn mice and males were more sensitive to manganese than females in both Sed_Mn and Mn treatment groups. Our study indicates that metal-sediment interactions may alter metal toxicity in mammals and introduces a new exposure model to test the toxicity of metal contaminants of drinking water.

[5] This data has been accepted for publication in *Environmental Toxicology and Pharmacology* on March 13, 2020. Authors: Dana M. Freeman, Rachel O'Neal, Qiang Zhang, Edward J. Bouwer, Zhibin Wang. doi:10.1016/j.etap.2020.103399

1. Introduction

Heavy metal contamination of drinking water poses a significant public health risk across the globe (EPA 2015). Exposure to heavy metals such as lead, arsenic, and manganese are associated with increased risks of various cancers, declined cognitive ability, and altered thyroid function (EPA 2015). The World Health Organization (WHO) has sought to mitigate health effects resulting from excess metal exposure via drinking water by setting global maximum contaminant levels (MCLs) (WHO 2011). Unfortunately, due to the challenges associated with climate change, aging infrastructures, and the lack of a comprehensive removal technique, many populations are exposed to levels of metals much higher than WHO guidelines (Chowdhury 2016).

Toxicology studies regularly use mouse models to gain mechanistic insights into heavy metal exposure and chronic illnesses. These studies model exposures by using invasive techniques such as oral gavage or by repeatedly dosing large concentrations of heavy metal salts directly into the water supply. A limitation of this method is the omission of complex metal-sediment interactions within water systems that may alter metal toxicity. Heavy metals accumulate within sediments and concentrations can exceed those in the water by three to five orders of magnitude (Bryan & Langston 1992). Metals can be transformed within these sediments into compounds with altered bioavailability and behavior (Nicolau 2006). While metal speciation and bioavailability in water is well understood; it remains challenging to study these reactions within complex microenvironments such as sediments (Bryan & Langston 1992, Islam 2015). The goal of this study was to develop an *in-vivo* exposure model that includes the effects of metal-sediment interactions to test the toxicity of heavy metals in water.

To our goal, we used manganese, a common water contaminant with well-studied toxic effects in animal studies. Manganese toxicity is associated with neurological

dysfunction and manganese-induced Parkinsonism, a neurodegenerative disorder with clinical similarities to Parkinson's disease (Chartlet 2012, Guilarte & Gonzales 2015, O'Neal & Zhang 2015, Bouabid 2016, Sarkar 2018). Excess manganese exposures in animals have been shown to disrupt mitochondrial function, induce neuroinflammation, obstruct neurotransmission, and damage the basal ganglia of the midbrain (Guilarte & Gonzales 2015, Bouabid 2016, Sarkar 2018). Extensive neuronal death and tissue damage in the midbrain impairs motor function control and can be reliably measured in animals using various motor behavioral tests (Brooks & Dunnett 2009). Despite a robust animal phenotype, there is a lack of human data on the risks of Parkinson's disease from the ingestion of manganese from drinking water (Chartlet 2012). Therefore, further understanding of the mechanisms occurring in the brain following manganese ingestion is needed. A recent study in plants observed reduced toxicity of manganese in water with the presence of silicates in the soil by reducing uptake into the cytoplasm (Blamey 2018). We hypothesized a similar mechanism may occur in mammalian systems. We exposed wild-type *C57/BL6* mice to manganese contaminated drinking water for six weeks by either putting manganese directly into the water (see methods- Mn) or by first incubating water with manganese contaminated sediment (see methods- Sed_Mn). The effects of different treatments on Parkinsonism in mice were determined by measuring altered motor function in three behavioral tests: the beam traversal test, the cylinder test, and the rotarod test. The aims of this study were (1) to determine if mice could be exposed to metals via contaminated sediment (2) to determine if incubating water with contaminated sediment changes the behavioral phenotype over time (3) to determine if there were sex dependent effects. Herein we report our mice exposed to manganese contaminated sediment produced a Parkinsonian phenotype in males but not females. We observed altered manganese toxicity in both males and females exposed to manganese contaminated sediment despite having been exposed to the same amount of total manganese (mg) as

mice given manganese directly in water (Mn). We observed a trend of increased sensitivity of males to manganese treatment in both manganese treated groups (Sed_Mn and Mn) in 9at least two behavioral tests.

2. Methods

2.1 Chemicals and Manganese Water Preparation:

Ottawa Sand from Restek (Bellefont, PA) was purchased as the sediment. The sediment control contained 1 kg of sand per 2L of Nestle Pure Life water in an autoclaved glass bottle. The contaminated sediment was spiked with manganese chloride (Sigma, St. Louis, MO) at 1 g $MnCl_2 \cdot 4H_2O$ per 1 kg of sediment. The concentration of manganese in sediment was selected based on our previous work analyzing heavy metal contamination of Baltimore harbor sediments using inductively coupled plasma mass spectrometry (ICP-MS) (Graham 2009; Wadhawan 2013). Water and spiked sediment were incubated out of light at room temperature two weeks before treatment began. The water was filtered from the sediment every three days before being given to the mice. The pH of the filtered water was monitored during the study and remained between 6-7 which is suitable for groundwater. The manganese chloride water solution was prepared fresh every three days at a concentration of 0.5 g/L.

2.2 Animals and Treatment:

Forty wild-type male and female *C57/BL6* mice ages 8-10 weeks were purchased from Jackson Laboratory (Bar Harbor, ME). Mice were housed 5 mice per cage on a 14-10 hour light-dark cycle in a AAALAC accredited facility. Mice were given food and water *ad libitum*. Food with the minimum required manganese content was purchased from Research Diets Inc. (New Brunswick, NJ). Mice were held for 10 days to acclimate before treatment. All procedures involving animals were performed under the guidance of the

National Research Council's *Guide for the Care of Laboratory Animals* (NRC 2010) and approved by the Johns Hopkins University Animal Care and Use Committee. Mice were exposed via their drinking water for six weeks. Treatment groups included water incubated with manganese contaminated sediment (Sed_Mn) and water contaminated with manganese with no sediment (Mn). They were given freshly prepared water every three days. Food and water intake were recorded bi-weekly. Body weights were recorded weekly.

2.3 Manganese Detection Assay and Estimated Daily Exposure:

Water filtered from the manganese sediment reaction was collected at the beginning and the end of the study and stored at -20°C. The detection of manganese in water sediment samples was completed using the sodium periodate oxidation method with instructions and reagents provided by the manganese test kit model MN-5 purchased from HACH (Loveland, CO). A standard curve was generated using three freshly prepared manganese standards at 100, 500, and 1000 mg/L. Three technical replicates for each standard and sample were measured by UV Vis absorbance at 525 nm in a 96 well clear bottom plate. The estimated daily exposure of manganese contaminated sediment water was calculated using the average concentration of the two unknown samples and the weekly water intake rate of each cage divided by the average body weight (kg) of each cage.

2.4 Behavioral Tests:

Rotarod Test

The accelerating rotarod test was used to assess motor coordination on the first and last day of treatment. The automated accelerating rotarod from Harvard Apparatus (Cambridge, MA) was generously loaned to us by the Jiou Wang laboratory at Johns

Hopkins Bloomberg School of Public Health. Each mouse was trained one day prior to testing for both timepoints and given as many trials as needed to successfully balance on the moving rotarod for three runs with one minute of rest between runs. On test days, the mice were given three trials on the rotarod accelerating linearly from 4 rpm to 40 rpm for a maximum of five minutes. The latency to fall (seconds) was recorded for each mouse.

Cylinder Test

The cylinder test was used to assess balance and exploratory rearing behavior every two weeks. Mice were placed in a clear glass cylinder (diameter = 10 cm) under minimal light at the end of their dark cycle for a total of two minutes. Rears were defined as the lifting of one or both forelimbs above shoulder level and contacting the wall of the glass cylinder (Cannon 2009). The mouse must bring all forelimbs back to the ground before another rear was counted. Rears were counted by the handler at the time of testing and by a blind observer using a video recording of each test.

Beam Traversal Test

The beam test was used to assess balance and motor coordination every week. Mice were placed on the far end of a wooden rod (diameter = 1.6 cm) approximately 60 cm from a dark cardboard box containing the home cage bedding. In the first week before exposure, mice were trained one day prior to testing for baseline abilities. Training consisted of acclimating the mouse to the box and giving the mouse as many trials as necessary until it was consistently moving forward across the beam into the box. On testing days, if a mouse turned around on the beam or fell off the beam then that trial would be discarded. The mouse was video recorded, and the time for the mouse to cross the beam across three successful trials was reported by a blind observer.

2.5 Biostatistics:

One-way analysis of variance (ANOVA) was used to analyze differences in behavior between the four mouse treatment groups within each time period for both males and females. Two-way ANOVA was conducted to analyze the effect of time and sediment incubation on behavioral phenotypes expressed as the fold change compared to the water (Ctrl) or sediment water control (Sed). Post hoc analysis was performed with both one-way and two-way ANOVA using the Tukey Honest Significance Difference test. The Student's t-test was used to compare sex dependent effects on behavioral phenotypes expressed as the fold change compared to the water (Ctrl) or sediment water control (Sed). Post hoc Bonferroni correction was used for significance of the Student's t-test. For all analyses, $p<0.05$ was considered significant.

3. Results

3.1 Manganese exposure does not alter food/water intake or weight.

Food and water intake were monitored during the 10-day acclimation period and bi-weekly during the six weeks of exposure. The amount of food and water consumed by male and female mice remain unchanged during the study regardless of treatment group (Figure 1). Intriguingly, the control female cage had a significantly higher water intake rate compared to the other female cages that began before treatment and continued throughout the study (Figure 1d). We do not believe reduced water intake in the other cages was due to manganese exposure. The weight of each mouse was recorded weekly. No mouse lost more than 20% of their body weight during the exposure period and the change in weight of each mouse was not different among treatment groups (Figure 2). Overall male mice gained an average of 0.8 g over the six-week period while female mice gained 1.47 g ($p\leq0.01$, *Student's t-test*).

3.2 Manganese sediment interaction does not alter total manganese in drinking water and males consume more total manganese than females.

The effect of sediment incubation on manganese content was determined from filtered water collected at the beginning and end of the six-week exposure period. The abundance of manganese in the water was 446 and 473 mg/L, respectively. There was no significant difference in the total amount of manganese consumed from water by the manganese water (Mn) and the manganese sediment (Sed_Mn) cage for males or females (Figure 3a). However, female treatment groups (Mn and Sed_Mn) did consume less total manganese than males. We used the average body weight for each group to determine if the estimated daily exposure (mg/kg*day) was significantly different for males and females. Male Sed_Mn treated mice had a lower estimated daily exposure than female Sed_Mn treated mice (54 mg/kg*day and 62 mg/kg*day, respectively). Mice treated with manganese directly in the water received the same estimated daily dose of approximately 61 mg/kg*day regardless of sex (Figure 3b).

3.3 Sediment interaction reduces the effect of manganese on beam test performance in males.

We examined the effect of sediment interaction on the development of Parkinsonism by using the beam traversal test to examine motor coordination and balance weekly during the six weeks of exposure. We recorded the average time over three trials for each mouse to cross the beam to the box containing the home cage bedding. No significant changes were detected in males or females until week six of exposure (Figure 4). At week six, only males exposed to manganese directly in water (Mn) took longer to cross the beam than the control mice (Figure 4a). The effect of both length of exposure and manganese sediment interaction on beam test performance was observed in males. Manganese sediment interaction significantly reduced the time to cross the beam in week

four and six of exposure (Figure 4b) (*two-way ANOVA, p≤0.05*). The exposure time between week four and week six did not significantly increase the observed effect of sediment interaction. Neither female treatment group had reduced performance on the beam test during the study and there was no observed effect of sediment incubation on the average time to cross the beam (Figure 4c, 4d). Therefore, our results indicate a possible gender-dependent behavioral phenotype in response to manganese.

3.4 Sediment interaction reduces the effect of manganese on cylinder test performance in males and females.

We examined rearing behavior every other week using the cylinder test. Rearing describes the lifting of the forelimbs onto the walls of the glass cylinder and allows us to analyze motor coordination using natural exploratory behavior without prior training. We observed a decrease in rearing behavior in male and female Mn groups at week four and six (Figure 5a, 5c). We observed a decrease in rearing behavior in only male Sed_Mn mice after six weeks (Figure 5a). The effect of both length of exposure and manganese sediment interaction on rearing behavior was observed. Manganese sediment interaction significantly reduced the number of rears counted in males and females at week four and six (Figure 5b, 5d) (*two-way ANOVA, p≤0.05*). The length of exposure had a significant effect on the rearing behavior in males indicating an increased effect of sediment interaction with time (*two-way ANOVA, p<0.01*). This was not observed in females.

3.5 Sediment interaction reduces the effect of manganese on rotarod test performance in males and females.

We examined balance and motor coordination at the end of the study using the accelerating rotarod test. This test measures the amount of time a mouse can balance on a rotating rod and is one of the most common tests used to quantify neurological deficits

in rodents (Brooks & Dunnett 2009). We observed a decrease in time on the rotarod in the male Mn mice when compared to the control mice (ANOVA, $p<0.05$) and a slight decrease in male Sed_Mn mice (NS, ANOVA, $p=0.065$) (Figure 6a). Manganese treatment did not significantly decrease the time on the rotarod in females (Figure 6c). Manganese sediment interaction reduced the fold change in time on the rotarod in both males and females but was only significant in females (Student's t-test, $p<0.05$) (Figure 6b, 6d).

3.6 Males performed worse than females in at least one of the three behavioral tests in both manganese treated groups.

We observed differences in behavioral outcomes for males and females exposed to manganese during the study. We analyzed motor deficits at week six using the fold change in performance compared to the treatment group's respective controls (Mn/Ctrl; Sed_Mn/Sed) (Figure 7). In the beam test, males took a significantly longer time to cross the beam than females in the Mn exposure group (Student's t-test, $p<0.05$). However, in the Sed_Mn exposure group, males and females performed the same and were not different than controls. In the cylinder test, males had reduced rearing behavior than females exposed to manganese in both groups (Student's t-test, corrected $p<0.05$). In the rotarod test, males spent slightly less time on the rotarod than females in both exposure groups, but these were not found to be significant. Significance was reported with raw non-adjusted p-values for each of these hypothesis tests. **Discussion**

In this study we used manganese to test our proposed exposure model because of its well-studied mechanisms in the brain and its reproducible motor phenotype in mice. We chose a commercial sediment for this pilot test to avoid convoluting the end behavioral outcome. The commercial sediment was made predominately of silica which is a major constituent of watershed and marine sediments. Manganese is known to leach to minerals such as silicates in the watershed and mineral content in water sediments has been of

interest to study increased risks of neurodegeneration (Choi 2006; Chartlet 2012). The sediment used in this model was sterile and had a consistent pH but potential changes in these factors on metal toxicity will still need to be studied in the future by using more complex sediments in the exposure model.

We selected an environmentally relevant sediment concentration of manganese of 1000 mg/kg sediment based on our previous work in the Baltimore City harbor (Graham 2009; Wadhawan 2013) and expected 0.5g/L as the maximum concentration of total manganese in the water after incubation. This concentration was also used for the Mn treatment group in which manganese water was prepared fresh every three days. We predicted that 0.5 g/L would be sufficient for this model based on another study that used the same dose in the drinking water of *C57/BL6* males and found significant deposition of manganese in the brain and a measurable motor phenotype (Krishna 2014). The concentration was not expected to be lethal given numerous studies using concentrations ≥ 1g/L to study neurotoxic effects in rodents (Chandra 1981; Anderson 2008; Avila 2008; Alsulimani 2015). We closely monitored food intake and weight during the study to verify that behavioral changes were due to neurotoxic mechanisms and not acute systemic failure. We observed no significant reductions in food intake or weight among mice in the study (Figure 1 and 2).

It was unclear whether water incubation with sediment would affect the taste of the water and alter the mouse rate of ingestion. We recorded weekly water intake and found that mouse drinking behavior was not significantly altered from the pre-exposure acclimation period suggesting that mice did not seem to experience any taste aversions (Figure 1). We used the sodium periodate oxidation method and UV absorbance to detect total manganese content in water after filtration of contaminated sediment. The average total manganese was 0.46 g/L indicating that manganese was not simply degraded or

being filtered out of the drinking water. We used the manganese concentration and water intake to compare manganese ingestion between treatment groups. We found no differences in the amount of manganese consumed weekly within male or female manganese treated mice (Figure 3). To determine if males and females received a similar dose of manganese we calculated the estimated daily exposure using the weekly manganese ingested divided by number of mice per group (n=5) and the average weight per group. We did not observe any change in the estimated daily exposure between male and female Mn treatment but did observe a reduction in the daily exposure of Sed_Mn males compared to Sed_Mn females (Figure 3).

We successfully exposed mice to manganese via contaminated sediment and produced a Parkinsonian phenotype in males as early as four weeks of exposure. Male Sed_Mn mice performed significantly worse than male controls in the cylinder test and the rotarod test. They performed better than male mice treated with Mn directly in water in all three tests after six weeks of exposure despite having the same total amount of Mn in the drinking water. The female Sed_Mn group did not develop a phenotype after six weeks of exposure. However, female Mn mice only performed worse than controls in one test suggesting a possible resistance of females to manganese treatment. This is supported by the literature in which multiple studies have reported an increased sensitivity of males compared to females possibly due to estrogen inhibition of the NFKB inflammatory pathway involved in neurodegeneration (Moreno 2011; Gillies 2014).

We hypothesized that metal-sediment interactions may alter metal toxicity from ingestion of drinking water by changing metal behavior. Manganese bioavailability and uptake across physiological membranes depends heavily on its oxidation state. Manganese speciation can also alter metal behavior in intracellular fluids. Intracellular divalent cations including Mn^{2+}, the most common free cytosolic manganese species, can

interact with proteins and effect the function of metabolic enzymes. Divalent manganese may also complex with amyloid fibrils, prion proteins, and Lewy body inclusion bodies that are highly prevalent in neurodegenerative diseases including Parkinson's disease (Choi 2006; Chartlet 2012). These complexes are associated with the observed perturbation of intracellular degradation systems such as the ubiquitin-proteasome complex but whether divalent metal ion complexes cause or are an effect of misregulated protein oligomerization remains uncertain.

Current animal studies analyzing heavy metal toxicity do not consider the microenvironment of the metals in the aquatic environment or the complex interactions that occur within sediments. Our study provides an *in-vivo* model to expose mice to water contaminants that simulates sediment interactions. We supported our hypothesis that sediment interactions alter metal toxicity in mammals. Future studies should include more complex sediments including those with microorganisms that can metabolize metals and affect metal behavior in water. Additionally, phenotypic tests may be altered and should be selected based on predicted metal contaminants and their target organ systems. Heavy metal contamination of drinking water is a global public health issue and mechanistic insights into the effects of metal contaminants is needed for the protection of human health. Our exposure model can be used to improve toxicity testing on single metal contaminants and metal mixtures that are present in water systems.

Funding Sources and Acknowledgements

This project is made possible with support from the Johns Hopkins Environmental Health & Engineering Chen Award (ZW and EB) and the Johns Hopkins University Catalyst Award (ZW). Experimental disposals and salaries were partially supported by the U.S. National Institutes of Health R01ES25761, U01ES026721 Opportunity Fund and R21ES028351 (ZW). The student author was supported by the U.S. National Institutes of Health T32 Training Grant 5T32ES007141 (DMF). We also thank Dr. Jiou Wang and student Reham Aljumaah for their generous help with the accelerating rotarod.

References

1. Alsulimani HH, Ye Q, Kim J. 2015. Effect of hfe deficiency on memory capacity and motor coordination after manganese exposure by drinking water in mice. Toxicol Res 31(4):347-54.
2. Anderson JG, Fordahl SC, Cooney PT, Weaver TL, Colyer CL, Erikson KM. 2008. Manganese exposure alters extracellular GABA, GABA receptor and transporter protein and mRNA levels in the developing rat brain. Neurotoxicology 29(6):1044-53.
3. Avila DS, Colle D, Gubert P, Palma AS, Puntel G, Manarin F, Noremberg S, Nascimento PC, Aschner M, Rocha JB. 2010. A possible neuroprotective action of a vinylic telluride against mn-induced neurotoxicity. Toxicological Sciences 115(1):194-201.
4. Blamey F, McKenna BA, Li C, Cheng M, Tang C, Jiang H, Howard DL, Paterson DJ, Kappen P, Wang P. 2018. Manganese distribution and speciation help to explain the effects of silicate and phosphate on manganese toxicity in four crop species. New Phytol 217(3):1146-60.
5. Bouabid S, Tinakoua A, Lakhdar-Ghazal N, Benazzouz A. 2016. Manganese neurotoxicity: Behavioral disorders associated with dysfunctions in the basal ganglia and neurochemical transmission. J Neurochem 136(4):677-91.
6. Brooks SP and Dunnett SB. 2009. Tests to assess motor phenotype in mice: A user's guide. Nature Reviews Neuroscience 10(7):519.
7. Bryan G and Langston W. 1992. Bioavailability, accumulation and effects of heavy metals in sediments with special reference to united kingdom estuaries: A review. Environmental Pollution 76(2):89-131.
8. Cannon JR, Tapias V, Na HM, Honick AS, Drolet RE, Greenamyre JT. 2009. A highly reproducible rotenone model of parkinson's disease. Neurobiol Dis 34(2):279-90.
9. Chandra S and Shukla G. 1981. Concentrations of striatal catecholamines in rats given manganese chloride through drinking water. J Neurochem 36(2):683-7.
10. Charlet L, Chapron Y, Faller P, Kirsch R, Stone AT, Baveye PC. 2012. Neurodegenerative diseases and exposure to the environmental metals mn, pb, and hg. Coord Chem Rev 256(19-20):2147-63.
11. Choi CJ, Kanthasamy A, Anantharam V, Kanthasamy AG. 2006. Interaction of metals with prion protein: Possible role of divalent cations in the pathogenesis of prion diseases. Neurotoxicology 27(5):777-87.
12. Chowdhury S, Mazumder MJ, Al-Attas O, Husain T. 2016. Heavy metals in drinking water: Occurrences, implications, and future needs in developing countries. Sci Total Environ 569:476-88.
13. Gillies GE, Pienaar IS, Vohra S, Qamhawi Z. 2014. Sex differences in Parkinson’s disease. Front Neuroendocrinol 35(3):370-84.
14. Graham AM, Wadhawan AR, Bouwer EJ. 2009. Chromium occurrence and speciation in baltimore harbor sediments and porewater, baltimore, maryland, USA. Environmental Toxicology and Chemistry 28(3):471-80.
15. Guilarte TR, Gonzales KK. Manganese-Induced Parkinsonism Is Not Idiopathic Parkinson's Disease: Environmental and Genetic Evidence. Toxicol Sci. 2015;146(2):204-12.
16. Islam MS, Ahmed MK, Raknuzzaman M, Habibullah-Al-Mamun M, Islam MK. 2015. Heavy metal pollution in surface water and sediment: A preliminary assessment of an urban river in a developing country. Ecol Ind 48:282-91.

17. Krishna S, Dodd CA, Hekmatyar SK, Filipov NM. 2014. Brain deposition and neurotoxicity of manganese in adult mice exposed via the drinking water. Arch Toxicol 88(1):47-64.
18. Moreno JA, Streifel KM, Sullivan KA, Hanneman WH, Tjalkens RB. 2011. Manganese-induced NF-κB activation and nitrosative stress is decreased by estrogen in juvenile mice. Toxicological Sciences 122(1):121-33.
19. National Research Council. 2010. Guide for the care and use of laboratory animals. National Academies Press.
20. Nicolau R, Galera-Cunha A, Lucas Y. 2006. Transfer of nutrients and labile metals from the continent to the sea by a small mediterranean river. Chemosphere 63(3):469-76.
21. O'Neal SL and Zheng W. 2015. Manganese toxicity upon overexposure: A decade in review. Current Environmental Health Reports 2(3):315-28.
22. Sarkar S, Malovic E, Harischandra DS, Ngwa HA, Ghosh A, Hogan C, Rokad D, Zenitsky G, Jin H, Anantharam V. 2018. Manganese exposure induces neuroinflammation by impairing mitochondrial dynamics in astrocytes. Neurotoxicology 64:204-18.
23. United States Environmental Protection Agency. 2015. Regulated drinking water contaminants.
24. Online database. Available at: https://www.epa.gov/sites/production/files/2015-05/documents/environments-contaminants-drinking-water.pdf (Accessed on Dec 20, 2018).
25. Wadhawan AR, Stone AT, Bouwer EJ. 2013. Biogeochemical controls on hexavalent chromium
26. formation in estuarine sediments. Environ Sci Technol 47(15):8220-8.
27. World Health Organization. 2011. Guidelines for drinking-water quality. WHO Chron 38(4):104-8.

Figures

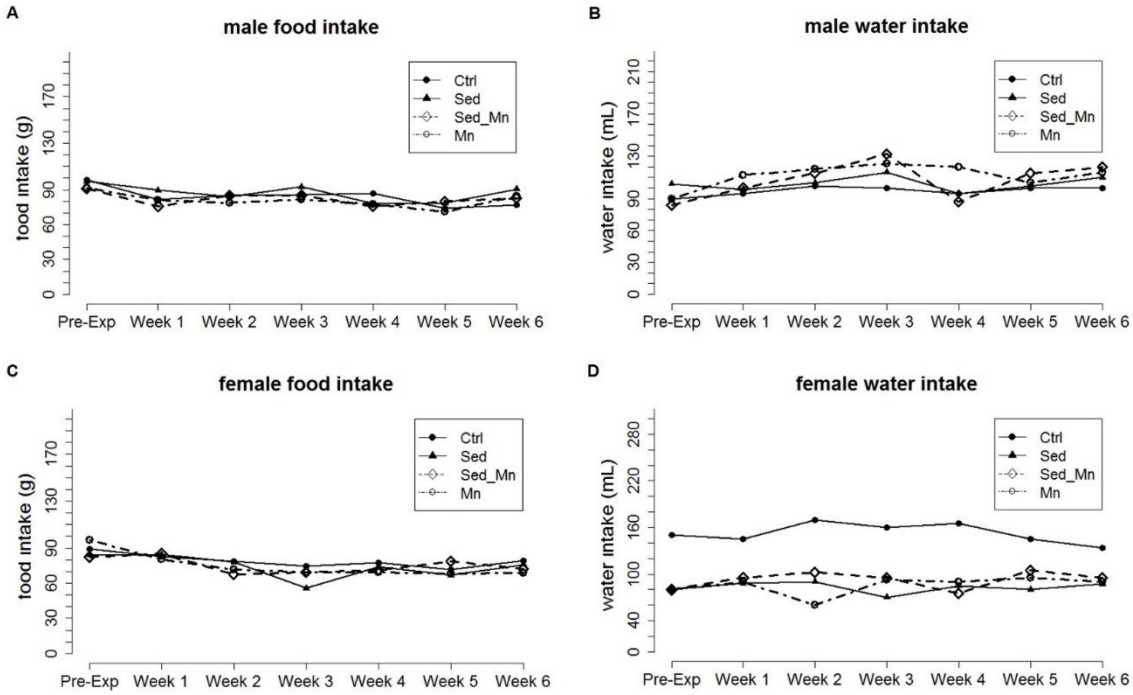

Figure 1. Weekly food and water intake changes in response to manganese exposure.
A-B) Male weekly food and water intake rate by cage from week 0 (pre-exposure) to week 6. C-D) Female weekly food and water intake rate by cage from week 0 (pre-exposure) to week 6.

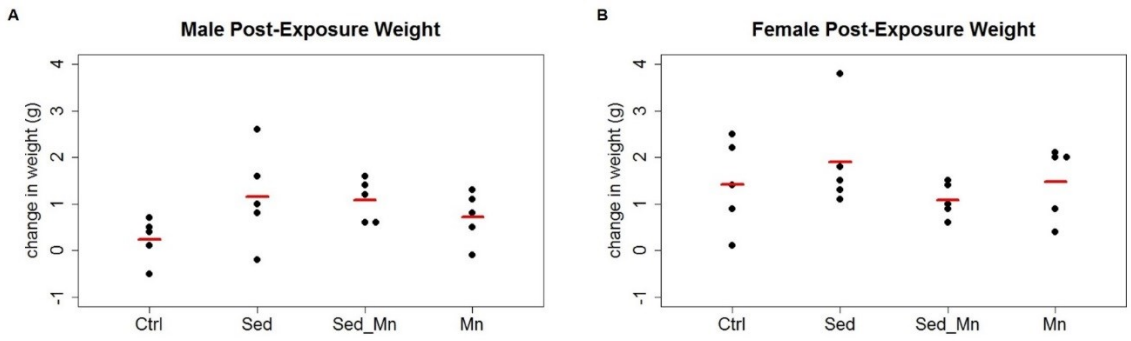

Figure 2. Mouse weight change after six weeks of manganese exposure.
A-B) Male and female total change in weight at week 6 from week 0 (pre-exposure). Red bar indicates mean for each group (n=5) (ANOVA, p>0.05).

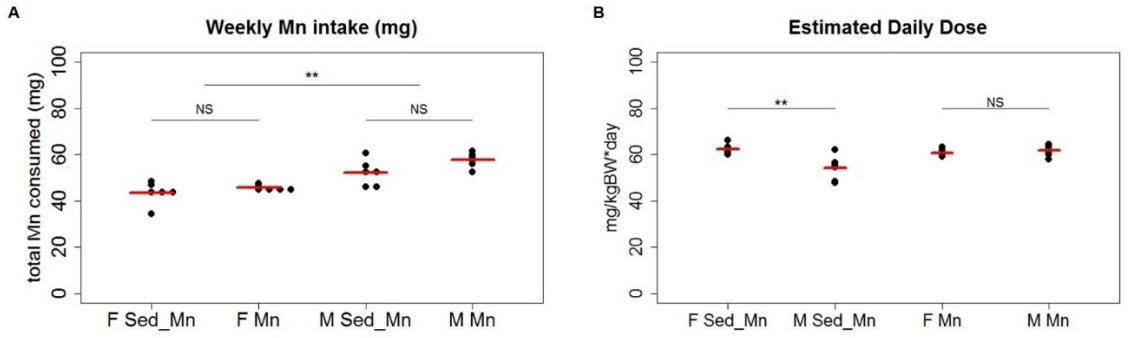

Figure 3. Weekly manganese intake and estimated daily dose did not change between treatment groups.

A) Weekly manganese intake (mg) of female and male mice exposed to sediment manganese water (Sed_Mn) versus manganese water (Mn). Red bar indicates mean (n=6 weeks). There was no difference in the total manganese consumed from water between Sed_Mn and Mn treatment groups (ANOVA, p>0.05, not significant NS). Male treatment groups consumed higher amounts of manganese than female groups (ANOVA, p<0.01, **).

B) The estimated daily exposure dose for all groups. Males exposed to sediment water (Sed_Mn) had a lower daily exposure than females (ANOVA, p<0.01, **). Males and females exposed to manganese directly in water (Mn) both had an estimated daily exposure of 61 mg/kg (ANOVA, p>0.05).

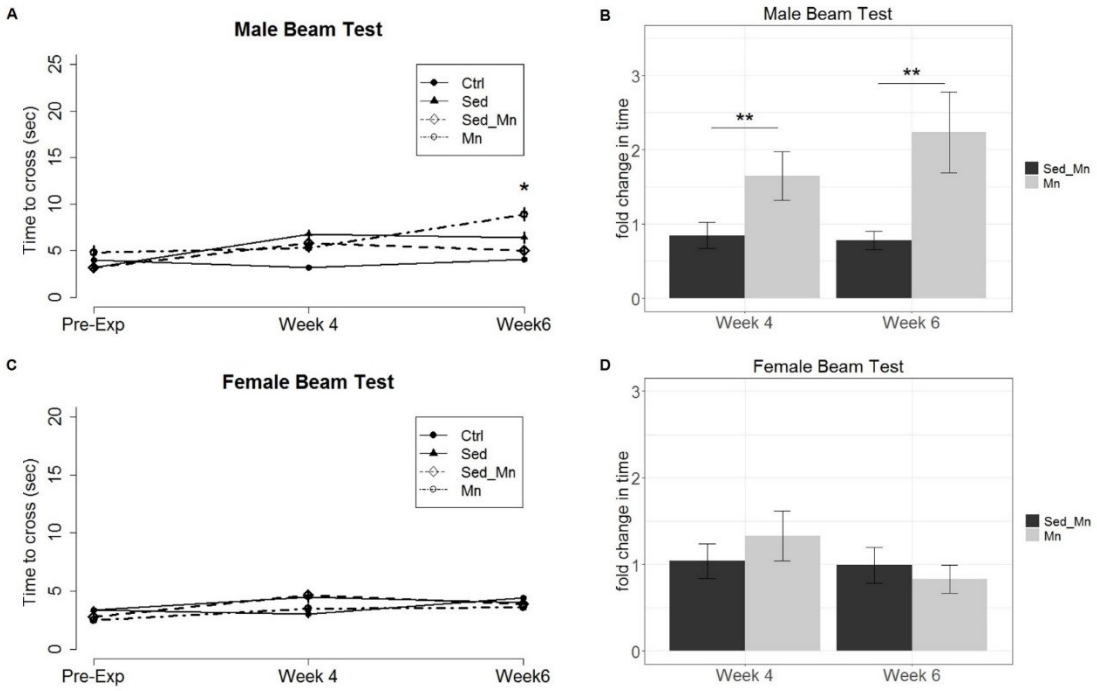

Figure 4. Examination of the average time to complete the beam traversal test between manganese treatment groups at week 4 and week 6 revealed that sediment interaction decreased effect on motor coordination in males.

A) Average time to cross beam (seconds) ±SEM at week 0 (pre-exposure), week 4, and week 6. Male Mn but not Sed_Mn mice took significantly longer to cross the beam than control mice at week 6 (ANOVA, $p<0.05$, *).

B) Average fold change in time to cross beam ± SEM compared to respective controls (Mn/Ctrl; Sed_Mn/Sed). Fold change in time was altered with manganese sediment interaction but no significant effect of exposure duration was observed (two-way ANOVA, $p<0.01$, **).

C) Average time to cross beam (seconds) ±SEM at week 0 (pre-exposure), week 4, and week 6. Female mice exposed to manganese did not take longer to cross the beam than control mice.

D) Average fold change in time to cross beam ± SEM compared to respective controls (Mn/Ctrl; Sed_Mn/Sed). Fold change in time was not significantly altered in either treatment group and there was no observed effect of exposure duration.

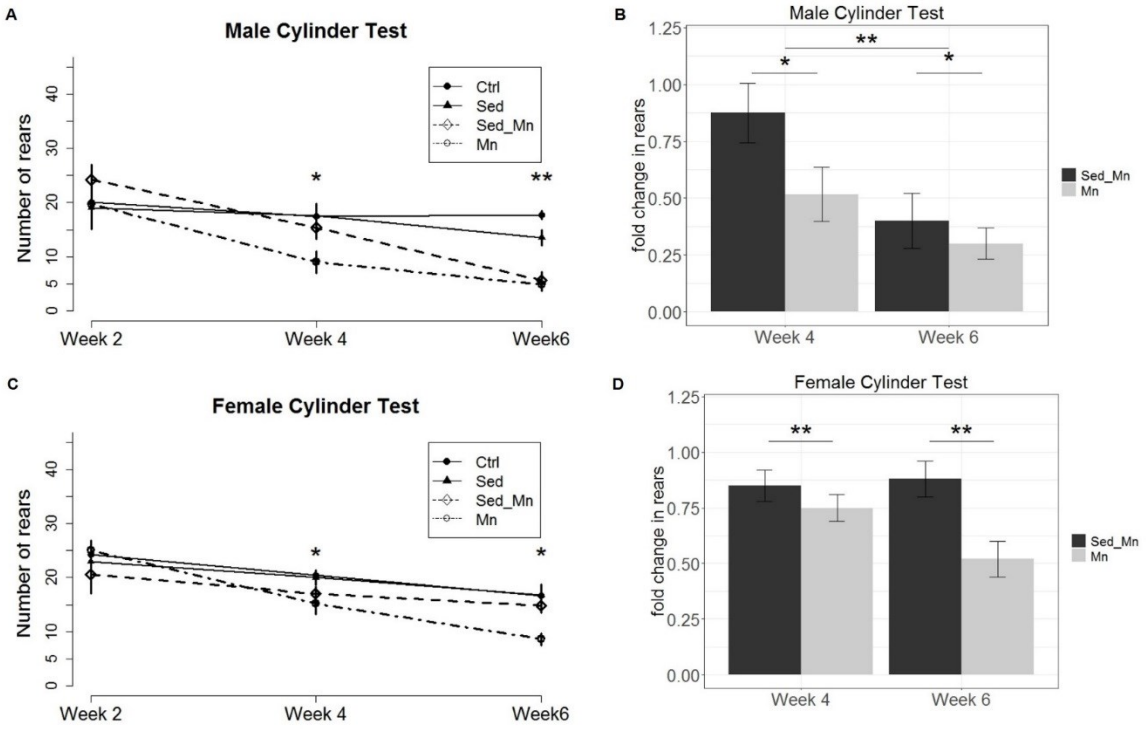

Figure 5. Examination of exploratory rearing behavior between manganese treatment groups at week 4 and week 6 revealed that sediment decreased effect on rearing activity in males and females.

A) Average number of rears ±SEM at week 0 (pre-exposure), week 4, and week 6. Male Mn mice had significantly reduced rearing behavior compared to control mice at week 4 (ANOVA, $p<0.05$, *) and week 6 (ANOVA, $p<0.01$, **). Male Sed_Mn mice had significantly reduced rearing behavior at week 6 only (ANOVA, $p<0.01$, **)

B) Average fold change in rearing ± SEM compared to respective controls (Mn/Ctrl; Sed_Mn/Sed). Fold change in rearing was altered with manganese sediment interaction (two-way ANOVA, $p<0.05$) and with exposure duration (two-way ANOVA, $p<0.01$, **).

C) Average number of rears ±SEM at week 0 (pre-exposure), week 4, and week 6. Female Mn mice had significantly reduced rearing behavior compared to control mice at week 4 (ANOVA, $p<0.05$, *) and week 6 (ANOVA, $p<0.05$, *). Female Sed_Mn mice did not show reduced rearing behavior compared to control mice.

D) Average fold change in rearing ± SEM compared to respective controls (Mn/Ctrl; Sed_Mn/Sed). Fold change in rearing was altered with manganese sediment interaction (two-way ANOVA, $p<0.01$, **) but not with exposure duration.

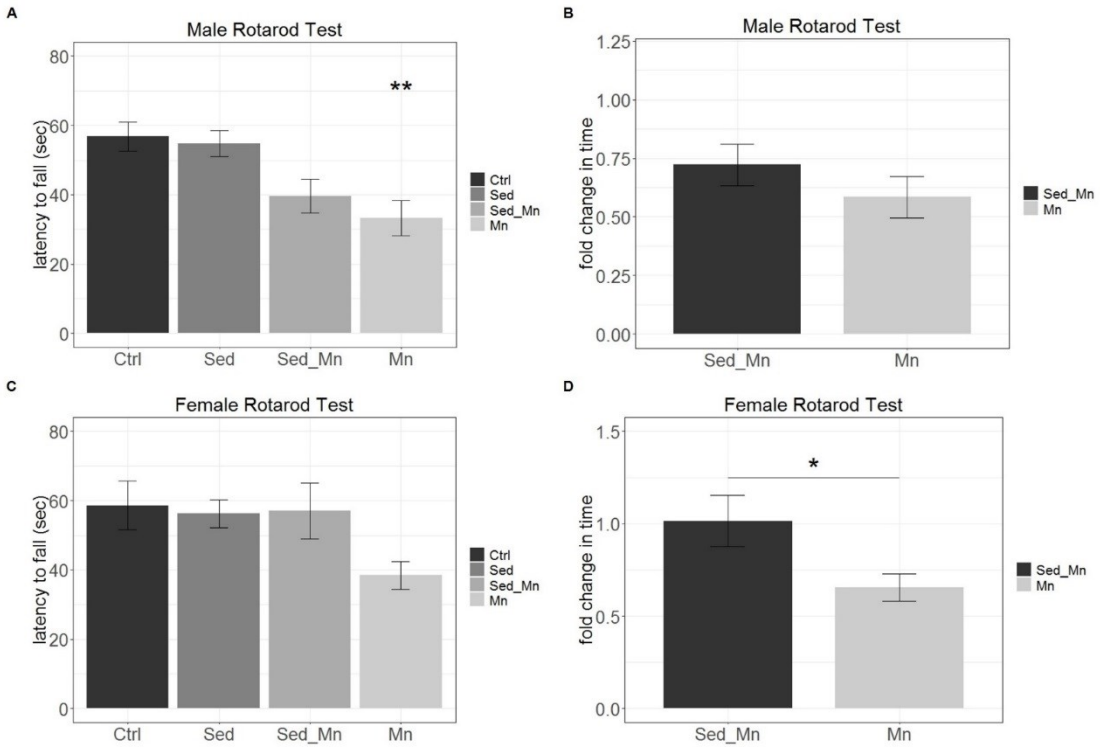

Figure 6. Examination of the average time on the accelerating rotarod between manganese treatment groups after six weeks of exposure reveals decreased effect on motor coordination in females.

A) Average time to fall (s) ±SEM at week 6. Male Mn mice remained on the rotarod for significantly less time than control mice at week 6 (ANOVA, $p<0.01$, **). Male Sed_Mn mice also spent less time on the rotarod but it was not significant (ANOVA, $p=0.065$).

B) Average fold change in time ± SEM compared to respective controls (Mn/Ctrl; Sed_Mn/Sed). Fold change in time was not significantly altered with manganese sediment interaction (Student's t-test, $p>0.05$).

C) Average time to fall ±SEM at week 6. There was no significant difference in the average time to fall in manganese exposed female groups (ANOVA, $p>0.05$).

D) Average fold change in time ± SEM compared to respective controls (Mn/Ctrl; Sed_Mn/Sed). Fold change in time was altered with manganese sediment interaction (Student's t-test, $p<0.05$).

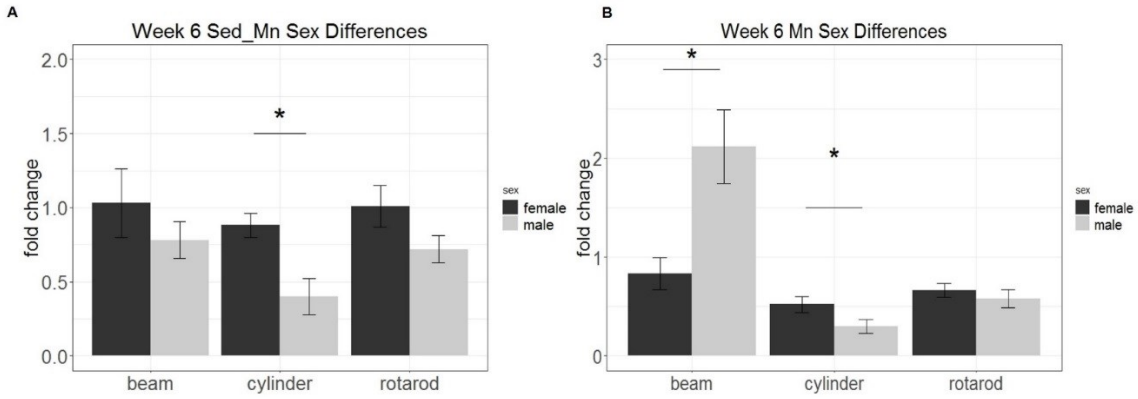

Figure 7. Examination of sex differences in behavioral testing reveals increased sensitivity of males in at least one behavioral test in both manganese treatment groups.

A) Average fold change of the Sed_Mn treated male and female mice compared to the sediment control (Sed) ± SEM at week 6 (Student's t-test, $p<0.05$).

B) Average fold change of the Mn treated male and female mice compared to the control ± SEM at week 6 (Student's t-test, $p<0.05$).

Dana M. Freeman

CURRICULUM VITAE

Contact Information:

Email: dfreem20@jhmi.edu; dmfreeman09@gmail.com

Mobile: (478)361-8195

Current Address: 2924 N. Calvert St Apt 1 Baltimore, MD. 21218

Education:

Johns Hopkins University- Bloomberg School of Public Health- Baltimore, MD
PhD candidate in Environmental Health & Engineering
Molecular Toxicology Physiology & Molecular Mechanisms Track
GPA: 3.73
August 2015- Present

Georgia Institute of Technology - Atlanta, GA
Bachelor of Science in Biochemistry
Graduated: May 2013
Highest Honors Distinction, GPA: 3.77

Awards/Honors:

Frederik B. Bang Award- May 2018

NCEH/ATSDR Director's Award for Excellence in Innovation- January 2015

President's Undergraduate Research Award- Spring 2013

Summa Cum Laude, Georgia Institute of Technology- Spring 2013

Work Experience:

Johns Hopkins Bloomberg School of Public Health- Baltimore, MD

August 2015- Present

Graduate Research Assistant and Teaching Assistant

- Studying epigenetic patterns in exposure induced *in-vitro* and *in-vivo models* of Parkinson's Disease for my dissertation.
- Collaborate with the Center for Alternatives to Animal Testing to test epigenomic responses to Parkinson's disease associated chemicals using their complex *in-vitro* neurological models.
- Provide teaching assistance to multiple classes including *Principles of Environmental Health*, *Introduction to Molecular Toxicology*, *Clinical and Occupational Toxicology*.

U.S. Centers for Disease Control and Prevention- Chamblee, GA

August 2013- August 2015 Oak Ridge Institute for Science and Education Fellowship

- Studied the presence of carcinogenic metabolites known as tobacco-specific nitrosamines (TSNAs) in both users of tobacco products and people regularly exposed to secondhand smoke.

- Collaborated in the development of a sample preparation method which would enable the detection of TSNAs in human urine samples.
- Contributed to the national public health studies, National Health and Nutrition Examination Survey (NHANES) and Population Assessment of Tobacco and Health (PATH), by preparing thousands of human urine samples for LC/MS/MS analysis.

Dr. Raquel Lieberman Research Laboratory- Atlanta, GA

May 2011-August 2013 Georgia Tech Undergraduate Research Assistant and Laboratory Technician

- Characterized the calcium binding stabilization of myocilin, an ocular protein whose misfolding mutations have been associated with glaucoma.
- Successfully crystallized myocilin single nucleotide polymorphisms which ultimately led to the solution of the unknown protein structure by means of X-ray crystallography.
- Collaborated with Kimberly Clark to improve the isolation of an enzyme in the folate pathway with antimicrobial potential as well as assess the accuracy of a newly developed computational model with results from experimental stability studies.

SASCO Chemical Group, Inc. – Macon, GA

August 2011- December 2012 Research and Development Laboratory Technician Intern

- Assisted in the development and testing of release chemicals used in the manufacture of various elastomeric compounds targeted for application in tires, belts, tubing, seals and hoses.
- Assisted in the development of a new platen release agent based on the saponification of a novel combination of unsaturated fatty acids that is currently being commercialized.
- Tested new release agent products for quality control properties including pH, Brookfield viscosity, specific gravity, and solids content via moisture analyzers.

Publications:

First author publications:

- Freeman, D. M., & Wang, Z. 2019. Towards the molecular mechanisms of transgenerational epigenetic inheritance: insights from transgenic mice. In *Transgenerational Epigenetics* (pp. 137-156). Academic Press.
- Freeman, D.M., Lou,D., Li, Y., Martos, S.N., Wang,Z. 2020. The conserved DNMT1 dependent methylation regions in human cells are vulnerable to environmental rotenone. Epigenetics & Chromatin 13, 17 (2020). https://doi.org/10.1186/s13072-020-00338-8.
- Freeman, D. M., O'Neal, R., Zhang, Q., Bouwer, E. J., & Wang, Z. 2019. Manganese-induced Parkinsonism in mice is reduced using a novel contaminated water sediment exposure model. *bioRxiv*, 541664. Environmental Toxicology and Pharmacology. doi:10.1016/j.etap.2020.103399
- Freeman, D.M., Wang, Z. 2020. Epigenetic vulnerability of insulator CTCF motifs at Parkinson's disease-associated genes in response to neurotoxicant rotenone. Under Review: Frontiers in Genetics.

Co-authored in publications:

- Chesnut, M., Munoz, L.S., Harris, G., Freeman, D., Gama, L. Pardo, C.A., Pamies, D. 2019. A Roadmap for 21st Century Models to Study Mosquito-Borne Flavivirus Neuropathogenesis, Prevention, and Treatment. Accepted June 11, 2019. *Front. Cell. Infect. Microbiol.*
- Harris, G., Eschment, M., Orozco, S.P., McCaffery, J.M., Maclennan, R., Severin, D., Leist, M., Kleensang, A., Pamies, D., Maertens, A., Hogberg, H.T., Freeman, D., Kirkwood, A., Hartung, T., Smirnova, L. 2018. Toxicity, recovery and resilience in a 3D

dopaminergic neuron in vitro model exposed to rotenone. *Archives of Toxicology, 92(8)*, 2587-2606.

- Hill, S. E., Nguyen, E., Ukachukwu, C. U., Freeman, D. M., Quirk, S., & Lieberman, R. L. 2017. Metal ion coordination in the E. coli Nudix hydrolase dihydroneopterin triphosphate pyrophosphatase: New clues into catalytic mechanism. *PloS one*, *12*(7), e0180241.
- Donegan, R. K., Hill, S. E., Freeman, D. M., Nguyen, E., Orwig, S. D., Turnage, K. C., & Lieberman, R. L. 2014. Structural basis for misfolding in myocilin-associated glaucoma. *Human molecular genetics*, *24*(8), 2111-2124.

Received an academic acknowledgement in publication:

- Donegan, R. K., Hill, S. E., Turnage, K. C., Orwig, S. D., & Lieberman, R. L. (2012). The glaucoma-associated olfactomedin domain of myocilin is a novel calcium binding protein. *Journal of Biological Chemistry*, *287*(52), 43370-43377.

Presentations:

Oral Presentations:

- *The toxic effects of MnCl2 on motor function are reduced in mice using a contaminated water sediment exposure model.*
  International Congress of Toxicology XV- Honolulu, HI July 2019

- *The Development of an Environmental Parkinson's Disease Model using Manganese Contaminated Water Sediment*
  Johns Hopkins Environmental Health & Engineering Symposium- Baltimore, MD January 2018

- *TSNA Sample Preparation: The Challenges of Applying Automation to a Robust Analytical Method*
  Co-presented with Keegan Nicodemus; U.S. Centers for Disease Control Tobacco and Volatiles Meeting- Atlanta, GA May 2015

- *The Crystallization of Myocilin Mutations K398R and E396D*
  Georgia Institute of Technology Research Symposium- Atlanta, GA May 2013

Poster Presentation:

- *Human allele-specific methylated regions have increased resilience to rotenone exposure in α-Synuclein knockdown neurons.*
  - Johns Hopkins Environmental Health & Engineering Retreat- Baltimore, MD January 2020
    - Received 1st place overall in poster competition
  - Society of Toxicology Annual Meeting- Anaheim, CA March 2020 (cancelled)
    - Received 1st place in SOT-National Capital Area Chapter Student Award

- *Rotenone and Paraquat target non-imprinted DNMT1 dependent loci in a human in-vitro model of neurodegeneration.*
  - Johns Hopkins Environmental Health & Engineering Retreat- Baltimore, MD January 2019
  - Society of Toxicology Annual Meeting- Baltimore, MD March 2019
  - Delta Omega Poster Competition-Baltimore, MD March 2019
    - Received 2nd place in Laboratory Sciences Category

- *Rotenone Reduces Global DNA Methylation and Alters the Expression of Parkinson's Disease Associated Genes*
  - Johns Hopkins Environmental Health & Engineering Retreat- Baltimore, MD January 2018
    - Received 1st place in Toxicology Poster Competition
  - Delta Omega Poster Competition -Baltimore, MD February 2018
    - Received 2nd place in Laboratory Sciences Category
  - Society of Toxicology Annual Meeting- San Antonio, TX March 2018
    - Received Johns Hopkins School of Public Health Student Travel Award

- *Transcriptome Characterization for a Rotenone – Induced Human In-Vitro Model of Parkinson's Disease*
  - Society of Toxicology National Capital Area Symposium- Washington D.C. April 2017
    - Received Honorable Mention in Poster Competition

- *Oxidative Stress Induced α-Synuclein Alters Global DNA Methylation Patterns in an In-Vitro Model of Parkinson's Disease*
  - Johns Hopkins Environmental Health & Engineering Retreat- Baltimore, MD January 2017

Professional Affiliations/Activities:

- Johns Hopkins Environmental Health & Engineering Steering Committee
  Bloomberg School of Public Health Student Representative

- Johns Hopkins Environmental Health & Engineering Student Organization
  President 2018-2019
  President-Elect 2017-2018
  Research Committee Student Representative 2016-2017

- Society of Toxicology National Capital Area Regional Chapter
  Graduate Student Representative 2018-2019
  Vice Graduate Student Representative 2017-2018

- Society of Toxicology Graduate Student Leadership Committee
  Programming Committee Member 2018-2019
  Programming Committee Member 2017-2018

- Alpha Chi Sigma Professional Chemistry Fraternity, Alpha Omega Chapter, Georgia Institute of Technology.
  Brotherhood Chair 2012-2013

Skills:

- **Laboratory**
  - Mastered various molecular biology techniques in cells and tissues including nucleic acid extraction, histone extraction, human cell transfection, site directed mutagenesis, bacterial expression, chromatin immunoprecipitation PCR (CHIP-PCR), and quantitative PCR (qPCR).
  - Managed multiple cell cultures including immortalized mammalian cells, undifferentiated neuronal cells, fully differentiated dopaminergic neurons in 2D and 3D cultures, and mammalian embryonic stem cells.
  - Utilized *in-vitro* toxicological assays measuring viability, intracellular oxidative stress, and mitochondrial damage.

- Prepared high-quality next generation sequencing libraries for RNA-sequencing, whole genome Bisulfite sequencing, targeted Bisulfite- amplicon sequencing, Assay for Transposase-Accessible Chromatin (ATAC) sequencing, and chromatin immunoprecipitation (CHIP) sequencing.
- Conducted an *in-vivo* exposure study in mice and analyzed motor function with a battery of behavioral tests.
- Investigated protein dynamics with Western blots, co-immunoprecipitation, ELISA, and immunofluorescence.
- Performed analytical chemistry techniques including titration, liquid- liquid extraction, solid phase extraction, and high-performance liquid chromatography.

- **Software**
  - Designed primers for qPCR, CHIP-PCR, and targeted Bisulfite sequencing using primer design software.
  - Analyzed Bisulfite sequencing and RNA sequencing data using Galaxy and R statistical software.
  - Examined whole genome next generation sequencing data in UCSC, WashU, and IGV genome browsers.
  - Performed gene enrichment analyses and statistical analyses in R Statistical software.
  - Taken classes on HTML and Python coding languages.
  - Programmed sample preparation methods on automated liquid handling robotic systems using C++ language.
- **Interpersonal/Leadership:**
  - Developed research ideas and secured funding for those ideas through institutional research awards.
  - Established the first student travel award as President of the departmental student organization.
  - Selected to speak at scientific meetings including at the International Congress of Toxicology XV.
  - Received high marks on all evaluations for courses I taught or served as the teaching assistant.
  - Trained lab technicians, undergraduates, and graduate students in molecular biology and epigenetics.
  - Organized several large networking events, educational workshops, and professional development activities.
  - Served on several educational and research committees for Johns Hopkins School of Public Health.
  - Mentored youth in Baltimore City and volunteered as a judge in Maryland regional science fairs.

References:

- Zhibin Wang, PhD
  Advisor/ Associate Professor- Johns Hopkins University, Baltimore, MD
  410-955-7840; zwang47@jhu.edu

- Winnie Tang, PhD
  Associate Professor- Johns Hopkins University, Baltimore, MD
  410-614-3910; wtang10@jhu.edu

- Jim Yager, PhD
  Professor Emeritus- Johns Hopkins University, Baltimore, MD
  410-955-3695; jyager1@jhu.edu